ISSN number 0971 - 9709

The Journal of Indian Geophysical Union

AN OPEN ACCESS BIMONTHLY JOURNAL OF IGU

VOLUME 27, ISSUE 2, MARCH 2023

EDITORIAL OFFICE

Indian Geophysical Union, NGRI Campus, Uppal Road, Hyderabad- 500 007
Telephone: 91-4027012739, 27012332; Telefax:+91-04-27171564
Email: jigu1963@gmail.com, website: http://iguonline.in/journal/

The Journal with six issues in a year publishes articles covering
Solid Earth Geosciences; Marine Geosciences; and Atmospheric, Space and Planetary Sciences.
The Journal is Financially supported by MoES, Govt. of India.

Annual Subscription

Individual Rs -1000/- per issue and Institutional Rs- 5000/- for six issues
Payments should be sent by DD drawn in favour of "The Treasurer, Indian Geophysical Union", payable at Hyderabad,
Money Transfer/NEFT/RTGS (Inter-Bank Transfer), Treasurer, Indian Geophysical Union, State Bank of India, Habsiguda Branch,
Habsiguda, Uppal Road, Hyderabad- 500 007
A/C: 52191021424, IFSC Code: SBIN0020087, MICR Code: 500002318, SWIFT Code: SBININBBHO9.
For correspondence, please contact, Hon. Secretary, Indian Geophysical Union, NGRI Campus, Uppal Road,
Hyderabad - 500 007, India; Email: igu123@gmail.com; Ph: 040 27012332

ISSN: 0257-7968 (Clarivate Analytics)
ISSN: 0971-9709 (NISCAIR)
Approved as bimonthly ESCI journal by Clarivate Analytics
Cited in Indian Citation Index (ICI), New Delhi
Evaluated by NISCAIR, New Delhi
UGC Approved Journal

CONTENTS

Research Articles

J. Ind. Geophys. Union, 27(2) (2023), 62-83

Volume, mass of sediments and igneous crustal thickness below the Arabian Basin, northwest Indian Ocean

Shravan Kumar[1*], A.K. Chaubey[2], Uma Shankar[1], Akhil Mishra[3] and Jensen Jacob[4]

[1]Department of Geophysics, Institute of Science, Banaras Hindu University, Varanasi-221005, India.
[2]Department of Applied Geophysics, Indian Institute of Technology (Indian School of Mines), Dhanbad-826004, India.
[3]CSIR- National Geophysical Research Institute, Hyderabad-500007, India
[4]CSIR-National Institute of Oceanography, Dona Paula, Goa-403004, India.
*Corresponding author: sk.bhu89@gmail.com

ABSTRACT

Evolutionary history of the Arabian Basin has been complex. It has evolved due to complex processes of seafloor spreading and ridge propagation along the paleo Carlsberg Ridge in the early Tertiary under the influence of Reunion hotspot. Although the crystalline crust of the basin is considered similar to a normal oceanic crust, basement depth anomalies are reported in the basin. Above complexity necessitates estimation of sediment and igneous crustal load below the seafloor of the basin in order to provide constraints for the evolution of the basin. In order to do so, ship-borne as well as satellite altimetry derived bathymetry and free-air gravity anomaly data, have been analyzed in the light of available seismic information. The purpose is to investigate spatial distribution of sediment thickness, igneous crustal thickness and depth to the Moho derived from 2D forward gravity modeling as well as 3D gravity inversion. The study shows that northwestern region of the Arabian Basin is carpeted with thick Indus fan sediments (~3.5 km), whereas northeastern flank of the Carlsberg Ridge is covered with a thin veneer of sediments (~500 m). Sediment gravity values are calculated from the parabolic density function obtained from P-wave seismic velocities. The Moho depth in the basin ranges from 9 km near the flanks of the Carlsberg Ridge to 13 km in northern part of the basin filled with thick sediments, whereas igneous crustal thickness varies between 3 km and 8 km. These results can be used as constraints to refine the tectonic evolution of the basin. These results may also be useful for investigating thermal subsidence in the oceanic lithosphere as well as paleo-bathymetry of the basin.

Keywords: Arabian Sea Basin, Sediment thickness, Igneous crustal thickness, Gravity inversion, Gravity modeling, Moho depth.

INTRODUCTION

The Arabian Basin is a triangular basin bounded by various morphological features (Figure 1). To the northwest, it is bounded by the Owen fracture zone which offsets the Carlsberg and Sheba ridges. In the northwards, it is bounded by the Murray Ridge which is considered as an extension of the Owen fracture zone, although it shows a slightly different orientation. To the south-west, it is bounded by the active Carlsberg Ridge which acts as a barrier to the sediments flow and is segmented by a NE-SW oriented fracture zones. To the northeast, the basin is bounded by the aseismic Laxmi and Laccadive ridges. Seabed topography undulations have shown that the bathymetry in the basin varies from ~3.4 km in the north to ~4.4 km in the south. The basin is covered by huge amounts of sediments deposited by the Indus River which shows continuous progradation of the Indus fan southward. Several studies (Naini and Talwani, 1983; Miles and Roest, 1993; Miles et al., 1998; Chaubey et al., 1993, 1995, 1998, 2002a; Dyment, 1998; Royer et al., 2002) have identified well developed sea-floor spreading type magnetic anomalies in the basin and concluded that the basin is underlain by oceanic crust.

There are several studies about the evolutionary history of the basin. It is well established that Arabian and Eastern Somali basins are conjugate basins, created by seafloor spreading along the paleo Carlsberg Ridge in the early Tertiary (McKenzie and Sclater, 1971; Whitmarsh, 1974; Norton and Sclater, 1979; Naini and Talwani, 1983; Chaubey et al.,1993, 1995; Miles and Roest, 1993). More recent research advancements in these basins have accentuated the theory of the evolution of the basins and explained that the evolution was primarily dominated by a complex pattern of spreading-ridge propagation between ~63 and 42 Ma (Dyment, 1998; Chaubey et al., 1998, 2002a; Royer et al., 2002). The systematic episodes of propagation of spreading ridges have resulted in an asymmetric crustal accretion in conjugate basins. Evolutionary episodes of these basins were also affected by two major geodynamic events- movement of Indian plate over Reunion hotspot and the Indo-Eurasian continental collisions.

Indus Fan, which extends from continental shelf off Pakistan in the north to the active Carlsberg Ridge in the south, is the second largest deep-sea fan and one of the largest sediments bodies in modern ocean basins (Kolla and Coumes, 1987). The fan mainly comprises material which got deposited due to erosion from the western Himalaya, Karakoram and Hindu Kush (Clift et al., 2002). Huge amounts of sediments deposited by the Indus River shows continuous progradation of the Indus Fan southward. The sediments, in general, are thicker in the western part of the Arabian Basin than that of eastern part.

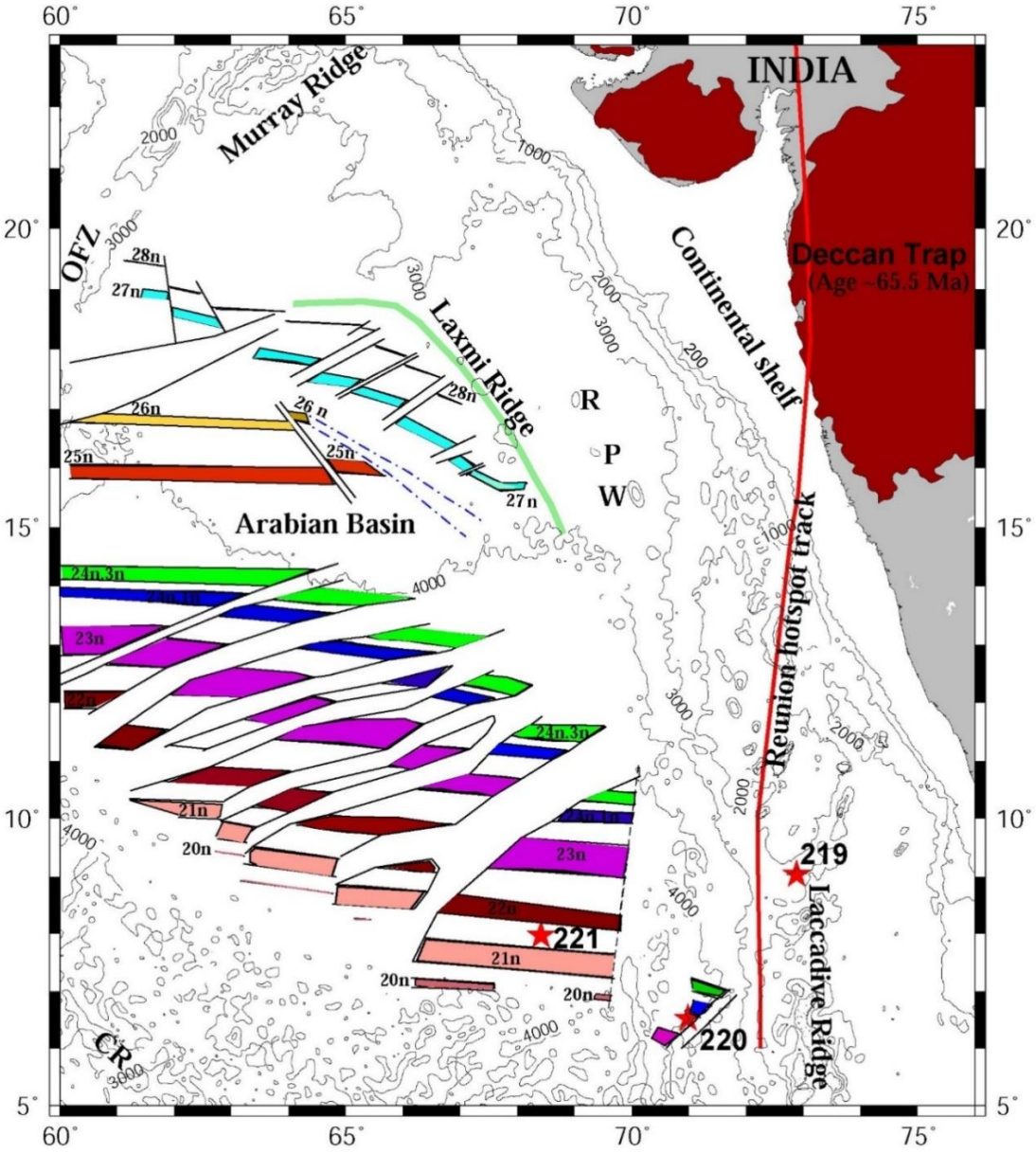

Figure 1. Tectonic map of the Arabian Basin and adjoining region, showing magnetic isochrons (coloured blocks), pseudo faults (black colour lines), super psuedofaults (blue colour dotted and dashed line), fracture zones (dashed black lines) and structural features (Chaubey et al., 2002a). Solid thick red colour line represents the computer-modelled Reunion hotspot track. CR: Carlsberg Ridge; OFZ- Owen Fracture Zone; R: Raman Seamount; P: Panikkar Seamount; W: Wadia Guyot. The dark red and light green colour mark the onshore outcrop of Deccan flood basalts and Laxmi Ridge gravity low, respectively. Bathymetric contours are in meters. Solid red-colour stars are DSDP drill sites annotated with site numbers.

Thus, the complex breakup history together with the northward movement of Indian subcontinent and its passage over the Reunion hotspot, large-scale sedimentation processes and collision of Indian plate with Eurasia, may all have significantly impacted the crustal structure of the basin.

Previous investigations in the region have mainly been focused on the nature of basin crust, its evolution, sedimentation history and occurrences of seamounts (Ewing et al., 1969; Naini and Kolla, 1982; Naini and Talwani, 1983; Kolla and Coumes, 1987; Chaubey et al., 1993, 1995, 1998, 2002a; Miles and Roest, 1993; Miles et al., 1998; Clift et al., 2001, 2002, 2019; Ferrier et al., 2015; Sreejith et al., 2016). Since knowledge of sediment thickness is critical in understanding geological evolution and processes involved, the correct estimation of sediment thickness becomes very important parameter. In Arabian Sea,

sediment thickness maps presently available are given by Naini and Kolla (1982), and Kolla and Coumes (1987) which is poorly resolved. Apart from this, a global sediment thickness grid with 5 arc-minute resolution (Straume et al., 2019) is also available at National Centers for Environmental Information (NCEI). Since global sediment thickness grids often result from the insufficient data coverage at several places, it causes uncertainties in sediment thickness due to insufficient seismic reflection and refraction profiles. This data deficiency problem mostly occurs in the deeper part of the ocean. In this study, our focus is to refine/update the distribution of sediment thickness in the Arabian Basin by modeling several profiles using gravity data along with available seismic refraction as well as seismic multi-channel and single-channel reflection data. As the evolution of the study region is complex in nature, estimates of sediment load as well as igneous crustal thickness can provide some constraints to refine its tectonic evolution.

The present study is aimed to provide an updated isopach map, depth to the Moho and igneous crustal thickness with 2'x2' grid resolution for the region 60°E-70°E, 7°N-19°N with estimates of volume and mass of sediments and igneous crust lying beneath the seafloor of the Arabian Basin.

TECTONIC AND GEOLOGICAL SETTINGS

The Western Continental Margin of India (WCMI) and adjacent oceanic regions were evolved due to multi-stage rifting and drifting during the geological past. The main stages are (i) rifting and subsequent drifting of Madagascar from India during the Late Cretaceous under the influence of Marian hotspot, which resulted the in the formation of south-western continental margin of India, (ii) short span of rifting between Seychelles-Laxmi Ridge and India at the end of Cretaceous, causing evolution of the Laxmi Basin, and (iii) rifting and subsequent drifting of Seychelles from India-Laxmi Ridge during the Early Tertiary, creating the conjugate Arabian and Eastern Somali basins along paleo-Carlsberg Ridge (Norton and Sclater, 1979; Courtillot et al., 1988; White and McKenzie, 1989; Bhattacharya et al., 1994; Storey, 1995; Chaubey et al., 1998, 2002a; Dyment, 1998; Royer et al., 2002; Krishna et al., 2006; Yatheesh et al., 2006; Collier et al., 2008; Minshull et al., 2008; Bhattacharya and Yatheesh, 2015). It is observed that the last two phases of rift/drift scenario were contemporaneous with the volcanic eruption by the Reunion mantle plume, which resulted in eruption of continental flood basalts on central-western India and Seychelles at ~65 Ma (Fisk et al., 1989). The Reunion mantle plume interacted initially with the continental lithosphere of the central-western India, followed by stretched continental lithosphere of the western margin of India and finally with oceanic lithosphere during the rapid northward drift of the Indian Plate.

Three major phases for evolution of the Arabian and its conjugate Eastern Somali basins have been suggested by Chaubey et al. (2002a) which is based on magnetic anomaly identification. This shows that evolutionary period of both the basins lasted between magnetic chrons 28n (~63 Ma) and 20n (~43 Ma) which involved different episodes of eastward and westward spreading ridge propagations. The first phase was characterized by westward propagation between chrons 28n (~63 Ma) and 27n (~61 Ma) near the Laxmi Ridge (Figure 1). The second phase shows a general eastward propagation between chrons 26n (~57.7 Ma) and 25n (~56.2 Ma). In last and third phase, a systematic westward propagation was observed between chrons 24r (~55 Ma) and 20n (~43 Ma). The major consequence of ridge propagations was observed as asymmetric crustal accretion in the conjugate basins between chrons 28n (~63 Ma) and 20n (~43 Ma) during different episodes. ~65% of the crust formed at the Carlsberg Ridge between chrons 26n (~57.7 Ma) and 25n (~56.2 Ma) was accreted in the Eastern Somali Basin (African Plate), whereas about 75% of the crust formed between chrons 24r (~55 Ma) and 20n (~43 Ma) was accreted in the Arabian Basin (Indian Plate).

Indian plate started moving after the breakup of Madagascar from India by Marion plume around 90 Ma with super mobile phase between 80 and 53 Ma (Negi et al., 1986; Agrawal et al., 1992). During this phase, the Deccan volcanic eruptions occurred mainly in <1 My (Courtillot et al., 1986, Kumar and Chaubey, 2019, 2022) during magnetic chron 29r (~65.6-64.8 Ma) by the Reunion plume at the Cretaceous-Tertiary (K-T) boundary. This event probably triggered the rapid northward motion of the Indian plate (Cande and Stegman, 2011) which abruptly got flagging after the start of India-Eurasia collision. Initial collision occurred at ~52 Ma (Early Eocene) when continental India came into contact with Kohistan-Ladakh Island Arc (KLA) system closing the Neo-Tethys along the Indus-Tsangpo Suture Zone. Then, India including the KLA collided with Eurasia mainland at ~44 Ma. This continent-continent collision event (~44 Ma) is termed as *'soft collision'* (Gibbons et al., 2015). The soft collision resulted in considerable slowing down of the spreading rates at the Carlsberg Ridge from chron 21n onward (Chaubey et al., 1993). It also resulted reorganization of spreading geometry in the Indian Ocean (Mckenzie and Sclater, 1971; Chaubey et al., 1993; Royer et al., 2002). During chron 18n,

spreading along the Carlsberg Ridge became indiscernible due to continued collision (Chaubey et al., 1993). When the entire oceanic crust north of Indian Plate subducted, i.e. complete closure of Tethys Sea, continental crust of Indian and Eurasian plates came into complete-contact at ~34 Ma. This complete continent-continent contact is known as *'hard collision'* (Gibbons et al., 2015). Consequently, rapid rise of the Himalayas continued and by the Late Miocene (~11.2-5.3 Ma), it took a form of lofty mountain range. Indus River came into existence after the Early Eocene. Subsequently the Indus River with its tributaries emanating from Himalaya started bringing large volume of eroded sediments by Early Oligocene time and started debouching it into the Arabian Sea as Indus Fan. Indus Fan sedimentation probably initiated with the Himalayan uplift combined with the Middle Oligocene-Early Miocene sea-level lowering. According to the results of the DSDP Site 221 (Figure 2), it has been observed that illite-rich clayey sediments, characteristic of Indus Fan sedimentation, started depositing in distal part of the Arabian Basin by the Middle-Late Oligocene (Weser, 1974). Channel and levee complexes are most pronounced after the early Miocene which is coincident with an increase in sedimentation rates (Clift et al., 2001). Erosional record of Indus Fan is necessary to understand the links between the tectonic evolution of the region, and the regional climate, most notably the monsoon and the erosion of the Himalayas, Karakoram and the Tibetan Plateau.

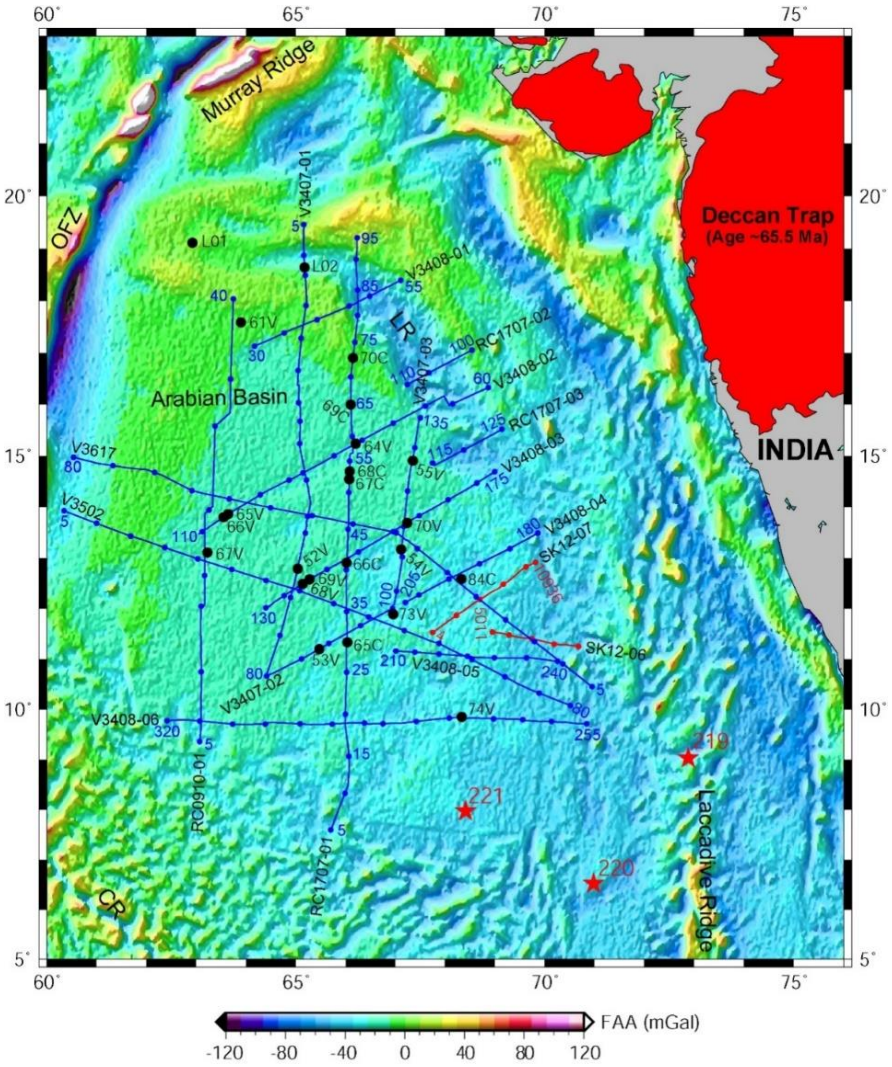

Figure 2. Map showing dataset of single channel seismic reflection and multi-channel reflection tracks used in this study. Single channel seismic data tracks are shown with blue lines, whereas multi-channel seismic data tracks are shown with red lines. Black circles denote the refraction stations, whereas dark-red stars denote DSDP drilled well sites. Numerals on the single channel tracklines denote the fix numbers, whereas numerals on the multi-channel lines denote shot points. CR: Carlsberg Ridge; OFZ: Owen Fracture Zone; LR: Laxmi Ridge. FAA contours are drawn in background for reference.

GEOPHYSICAL DATA

Bathymetry and Free-air gravity anomaly data

'Bedrock' version of ETOPO1, high resolution 1'x1' global relief model are used for bathymetry data and preparation of maps. This dataset are generated from global and regional digital datasets (Amante and Eakins, 2009). The gravity data are obtained from satellite altimetry-derived global marine gravity data (grav.img.29.1) of Sandwell et al. (2014) as shown in Figure 2. This dataset is derived by amalgamation of CryoSat-2 and Jason-1 satellite data with earlier existed gravity data from GEOSAT and ERS-1 satellite altimetry, resulting two times more accurate than the earlier gravity datasets of Sandwell and Smith (2009). This gravity data is mainly effective to understand the regional tectonic processes and mapping thousands of previously uncharted seamounts (Sandwell et al., 2014). In addition to these data, ship-borne bathymetry and free-air gravity data were also utilized for the present study. The accuracy of satellite derived bathymetry and gravity data has been tested by comparing with several ship-borne bathymetry and gravity profiles. It is found that both the datasets match very well. Average Root Mean Square (RMS) errors between satellite altimetry derived bathymetry and ship-borne bathymetry, and between satellite altimetry derived gravity and ship-borne gravity data are ~53 m and 3.4 mGal, respectively. In view of this, ship track data along SK12-07 have been extended with satellite bathymetry and gravity data to fill the data gaps within the limit of the basin.

P-wave velocity and density

We have utilized all available seismic refraction data in the present study (Figure 2). The seismic velocity structure underlying the Arabian Basin was first given by Naini and Talwani (1983). The data indicate that the velocities, in general, vary from 1.7 km/s to 3.8 km/s in sedimentary layers above acoustic basement. The crust underlying the sediment is represented by velocities that range between 5-7 km/s. This velocity range results in two discontinuities. The first has a velocity range of 5.5-6.0 km/s, whereas the second one ranges between 6.5-7.0 km/s. Moho velocity of 7.9-8.3 km/s has been observed at several locations in the basin (Naini and Talwani, 1983).

Density of each layer is necessary to interpret the gravity anomalies into crustal mass anomalies. For this purpose, Brocher (2005) formula was used to calculate density values in each layer from the observed average P-wave velocity data. In the study area, computed density for sediments is taken as a uniform value of 2.2 g/cm^3, whereas two layered oceanic crust are considered to have the density values as 2.62 g/cm^3 and 2.88 g/cm^3 for layer 2 and layer 3, respectively. A uniform density value of 3.33 g/cm^3 has been taken for the upper mantle (Table 1). These density values in each layer have been used while performing the forward gravity data modeling.

Table 1. Average P-wave velocity in different crustal layers. Brocher (2005) formula is used for density conversion of each layer**.**

Crustal layers	Avg. P-wave velocity (km/s)	Density (g/cm^3)
Sediments	2.72	2.20
Basalt flow	4.46	2.46
Crustal Layer-1	5.43	2.60
Crustal Layer-2	6.30	2.78
Underplated Layer	7.20	3.03
Oceanic Layer-2	5.51	2.62
Oceanic Layer-3	6.67	2.88
Upper Mantle	8.10	3.33

Seismic reflection data

Published seismic sections from Chaubey et al. (2002b) along track SK12-07 (Figure 3) and Sreejith et al. (2016) along track SK12-06 in the Arabian Basin have been used for imaging subsurface layers viz. seabed and igneous basement as constraints in performing forward gravity data modeling. Multi-Channel Seismic (MCS) data along tracks SK12-06 and SK12-07 collected onboard ORV Sagar Kanya during 1984-85 are used in the present study. The data were acquired using DFS-V (Digital Field System-V) seismic system with 24-channel seismic streamer at a ship speed of 4-5 knots. A record length of 8 s and a sampling interval of 4 ms were chosen to achieve a 12-fold coverage. The seismic source consisted of a D-type air gun array – combination of 7 air guns spaced at varied intervals – with 7.98 litre total capacity. In addition, Single Channel Seismic (SCS) data from NCEI, earlier known as National Geophysical Data Centre, have also been utilized in the present study. There are several surveyed tracks along which SCS data were collected from various cruises onboard the Lamont-Doherty Geological Observatory research vessels such as R/V Vema (cruise V34 in 1977, cruise V35 in 1978 and cruise V36 in 1980) and R/V Robert D. Conrad (cruise RC09 in 1965 and cruise RC17 in 1974). The tracks within the limit of the study area were compiled and utilized in the present study. Seismic section along RC1707-01 is shown in Figure 4 which has been used to prepare the sediment thickness map.

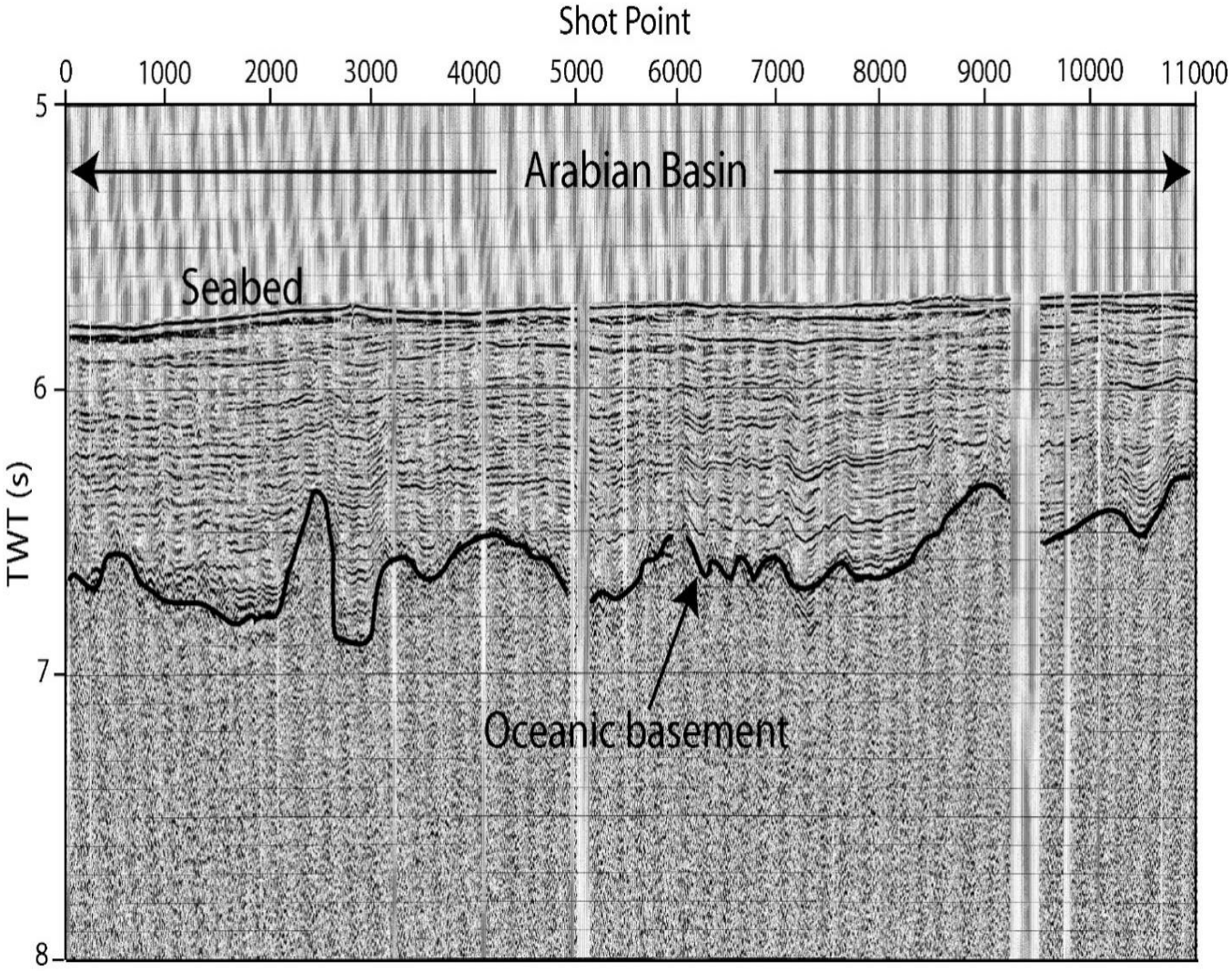

Figure 3. Seismic section along track SK12-07. Interpreted basement is shown with solid black curve.

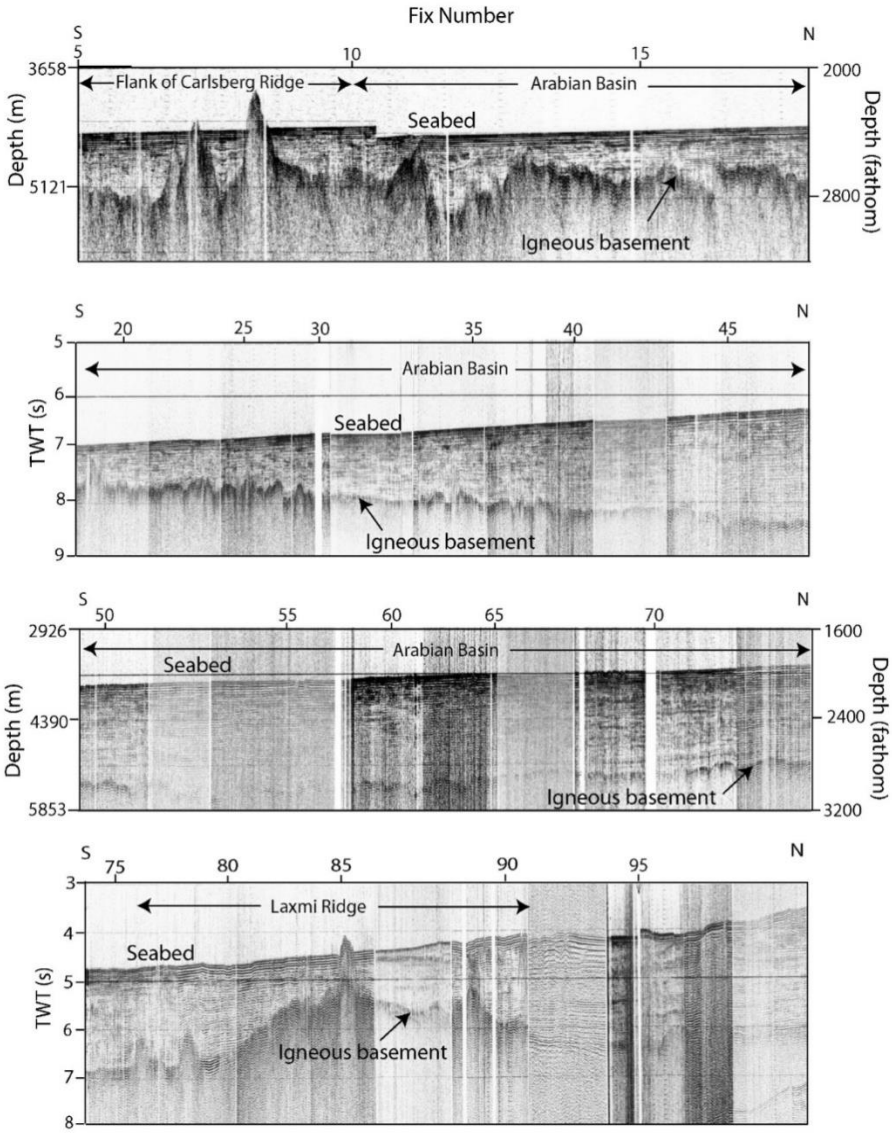

Figure 4. Seismic section along track RC1707-01.

METHODOLOGY

Forward modeling of gravity anomaly data

As a first step, available MCS time sections and refraction data were analysed for identification and understanding of main crustal layers and thickness of each layer. Once the basic knowledge of the study area is gained, 2D forward gravity modeling was performed using GM-SYS module of Oasis Montaj Geosoft software which is based on the algorithm developed by Talwani et al. (1959). Density values for gravity modeling (Table-1) were computed from the average seismic P-wave velocities with the formula given by Brocher (2005). Then trial and error method have been used until calculated gravity anomaly due to an assumed structure is matched with the observed anomaly. This process is continued till the discrepancy becomes minimum between observed and calculated anomalies. Modelling of anomaly data was performed assuming Airy-type isostatic equilibrium.

3D gravity inversion

In present study, gravity data was inverted after incorporating all the corrections by using a MATLAB code developed by Gomez-Ortiz and Agarwal (2005). Inversion scheme described by Oldenburg (1974) was used to determine the depth to the undulating interface from the Residual Mantle Bouguer Anomaly (RMBA) by means of an iterative process which is as follows:

$$F[h(x,y)] = -\frac{F[\Delta g(x,y)]e^{|k|z}}{2\pi G\rho} - \sum_{n=2}^{\infty}\frac{|k|^{n-1}}{n!}F[h(x,y)^n] \quad \ldots\ldots (1)$$

where, F [ ] stands for 2D discrete Fourier transform,

G is the universal gravitational constant,

ρ denotes the density of the interface,

Δg (x,y) is the gridded gravity anomaly,

h(x,y) is the depth to the interface,

z is the mean reference depth of the horizontal interface,

and |k| is for absolute value of the wave vector. It is not easy to decide the wavelengths to be filtered out and the range of wavelengths which will be used in inversion process because it depends on target depth and spectrum analysis of the gravity anomaly (Gomez-Ortiz et al., 2011). In this study, the filtering technique used in Parker-Oldenburg gravity inversion scheme is 69tilized. RMBA data was filtered before downward continuation by a cosine taper in a wavelength range 60-100 km. The intermediate wavelengths are partially passed.

ANALYSIS AND RESULTS

Sediment thickness gridded data

2D forward gravity data modeling was performed along several profiles considering the basin, seamounts and Laxmi Ridge (Figure 5). Several profiles were modeled for the entire basin but here we have presented only four profiles namely,

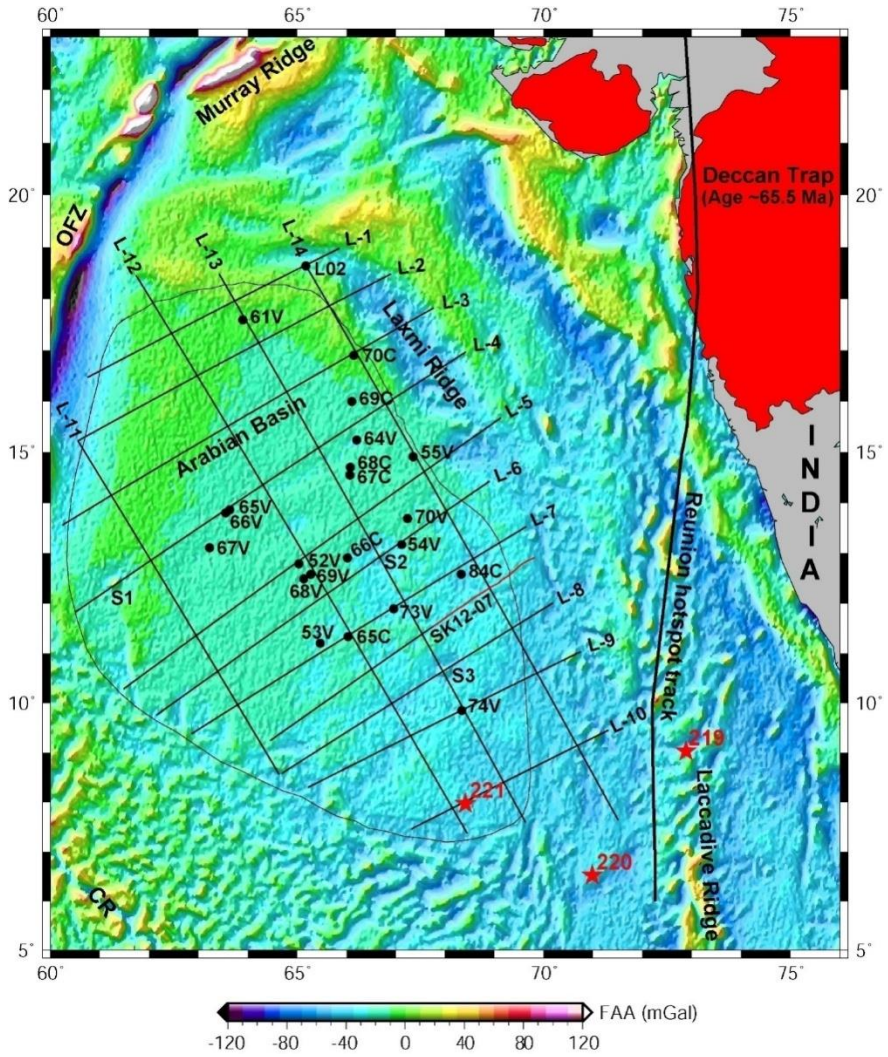

Figure 5. Colour shaded map of free air gravity anomalies in Arabian Basin prepared from 1-minute high resolution satellite altimetry derived data. Black filled circles in the offshore areas show locations of seismic refraction stations from Naini and Talwani (1983). S1, S2, S3 are the three identified seamounts. CR: Carlsberg Ridge; OFZ: Owen fracture zone. All the lines show the locations of regional traverses utilized for structural modeling in this study.

L2, L4, SK12-07 and L10 with some profiles crossing the Laxmi Ridge (Figures 6a-d) for understanding the crustal architecture beneath the basin. Forward modeling along these profiles has been carried out using the constraints available from published velocity model (Naini and Talwani, 1983). Available MCS (SK12-06 and SK12-07) as well as SCS sections were used as constraints for seabed and basement, wherever found necessary. SK12-07 seismic track line is extended to the Carlsberg Ridge flank and is modeled as a whole (Figure 6c). Likewise, in RC1707-01 seismic section annotated with fix numbers, sediment thickness variation is clearly visible from Carlsberg Ridge flank to Laxmi Ridge boundary (Figure 4).

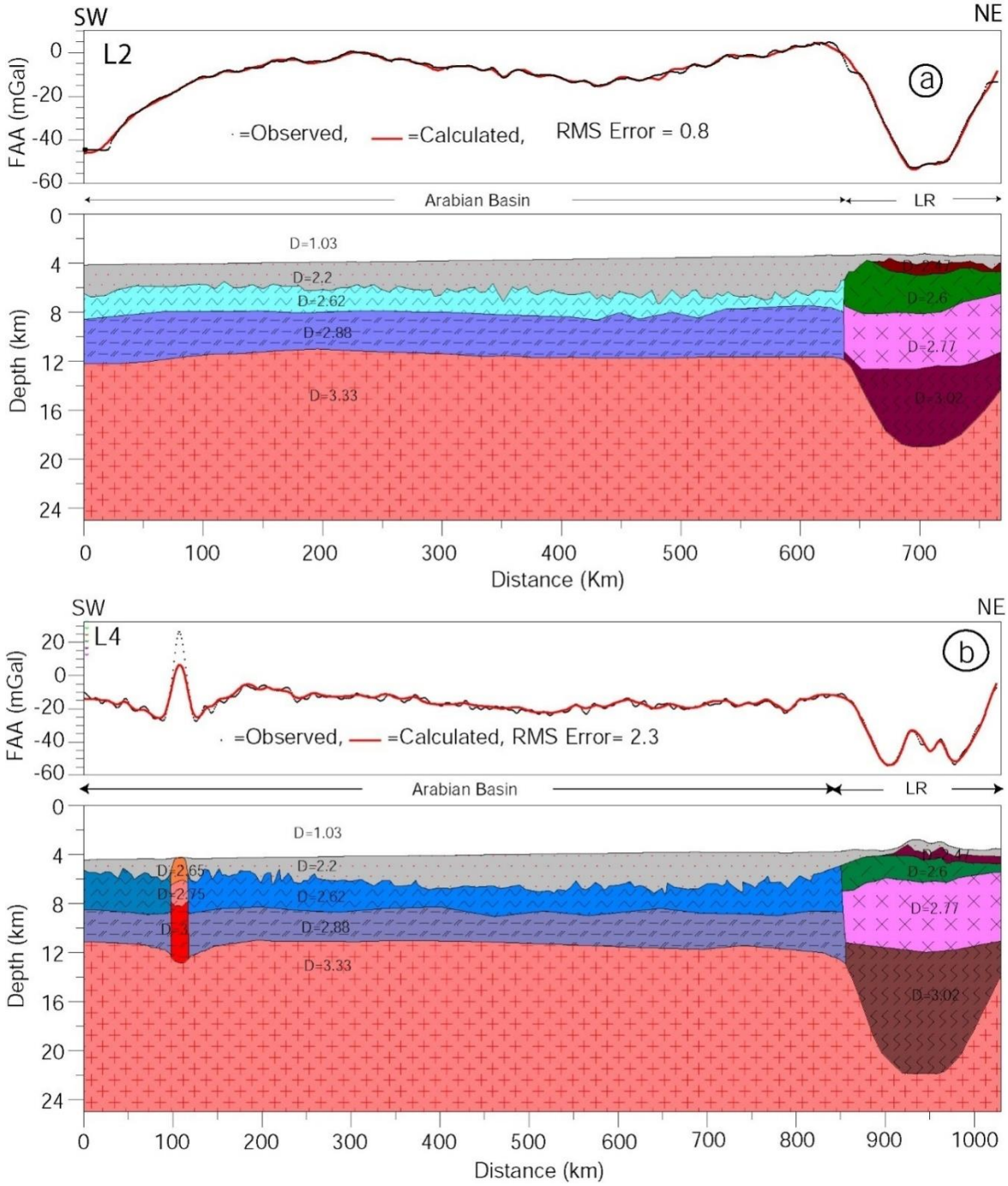

(Contd.)

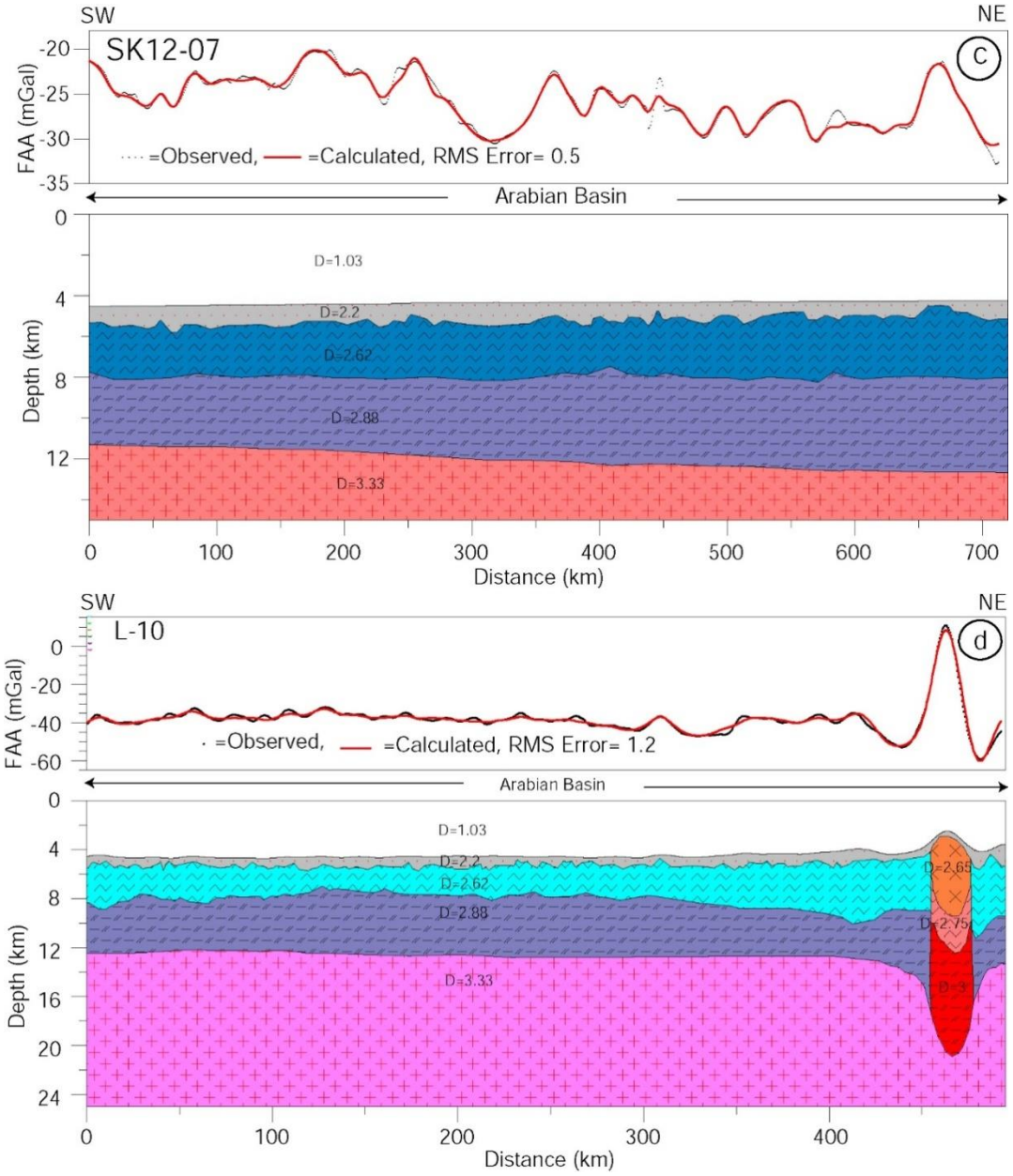

Figure 6. 2D gravity crustal models along profiles L2, L4, SK12-07 and L10 respectively (a-d). Location of profiles are shown in Figure 5.

Both the bathymetry and gravity data along these selected profiles are filtered using a Gaussian filter of width 20 km before resampling it to an interval of 1 minute. The crossover error analysis at different interfaces was also performed for the intersecting lines and corrected accordingly. For modeling in oceanic Arabian Basin, the density for sediments, oceanic layer-2 and oceanic layer-3 has been taken as 2.2 g/cm^3, 2.62 g/ cm^3 and 2.88 g/ cm^3, respectively. For modeling over Laxmi Ridge, five crustal layers have been considered and densities for these layers have been taken as 2.2 g/ cm^3, 2.46 g/ cm^3, 2.60 g/ cm^3, 2.78 g/ cm^3 and 3.03 g/ cm^3 (Table 1). In all crustal models, the layer of density 2.46 g/ cm^3 corresponds to basaltic flow (Kumar and Chaubey, 2019, 2022). Though this study is mainly focused in the Arabian Basin west of Laxmi-Laccadive Ridge system, the Laxmi Ridge is also modelled (Figure 6a,b) for its crustal architecture. Since nature of the crust of the Laxmi Ridge is debated, it is here modelled with layers as sediments, basaltic flow layer, crustal layer-1, crustal layer-2 and an underplated layer (Pandey et al., 1995; Mishra et al., 2018, 2020; Vasanthi, 2022).

For obtaining sediment thickness data, it is necessary to subtract the depth of seabed from the depth of basement. The data was further smoothened by calculating 10*10 km block medians to remove short wavelengths and spatial aliasing during gridding. To fill the data gaps between the points, the dataset was gridded using continuous curvature spline algorithms (Smith and Wessel, 1990). Tension factor of 0.2 was taken to suppress local maxima and minima. Short range variations from the sediment thickness grid were removed by non-convolution median filter with a cutoff wavelength of 100 km (Wobbe et al., 2014). The 2-minute gridded sediment thickness map shows the variation of sediments from less than 1 km near the flanks of the Carlsberg Ridge to more than 3 km in the Indus Basin (Figure 7). This sediment thickness map is further used for the calculation of gravity effect of sedimentary layers.

Above generated map was compared to NCEI world's sediment thickness map (Divins, 2003; Whittaker et al., 2013) shown in Figure 8a and a good correlation was found. The difference in sediment thickness is shown in Figure 8b which reveals ~800 m more thickness in Indus Fan region and ~300 m more in south-east part of the study region as compared to NCEI estimated thickness. In regions along Owen fracture zone, thickness of sediments has been found ~200 m lesser.

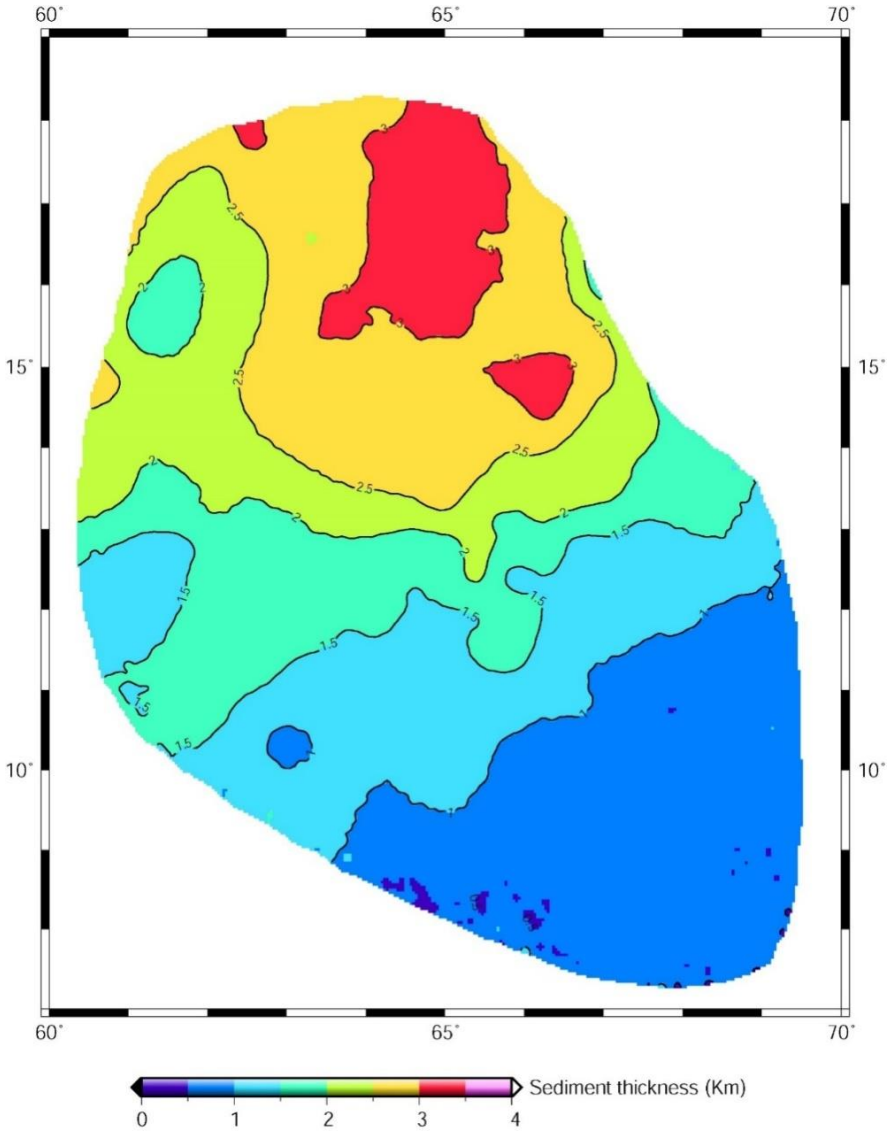

Figure 7. Colour shaded contour map of sediment thickness generated from gravity modelling with available seismic constraints. Thickness is in kilometers.

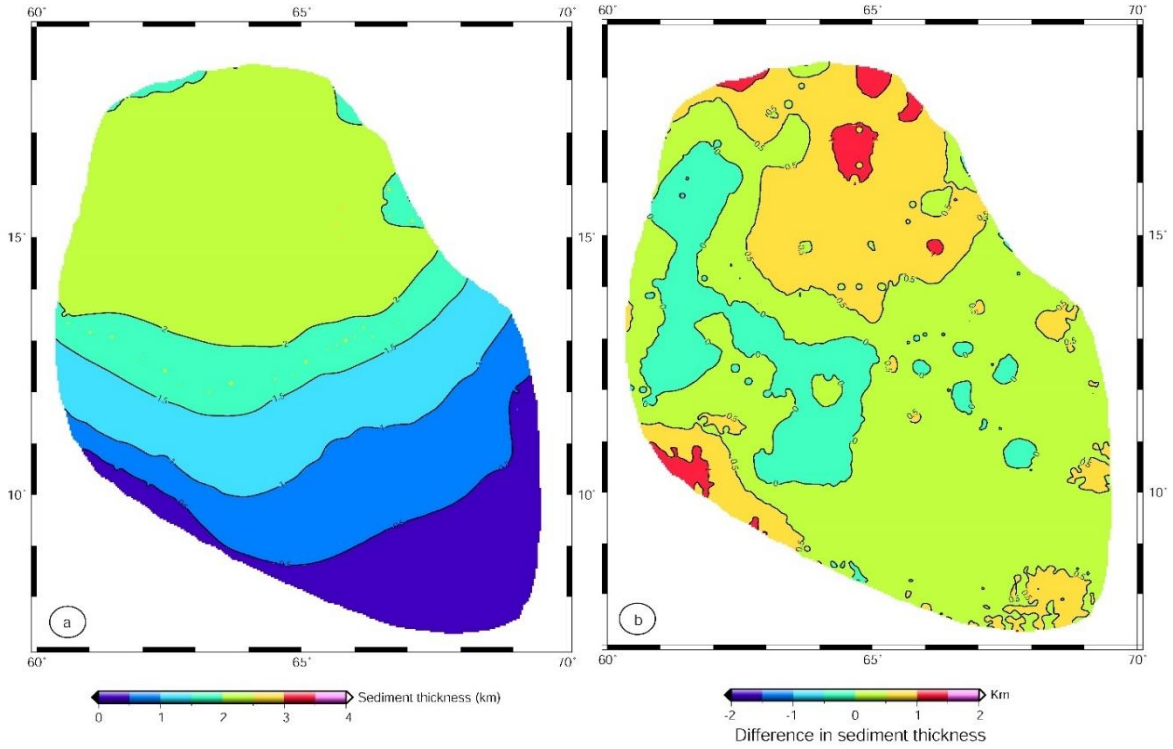

Figure 8. (a) Colour shaded contour map of sediment thickness for the same region obtained from NCEI world sediment thickness data. Thickness is in kilometers**, (b)** Colour shaded contour map showing difference between the sediments thickness derived from this study (Figure 7) and obtained from NCEI world sediment thickness data (Figure 8a).

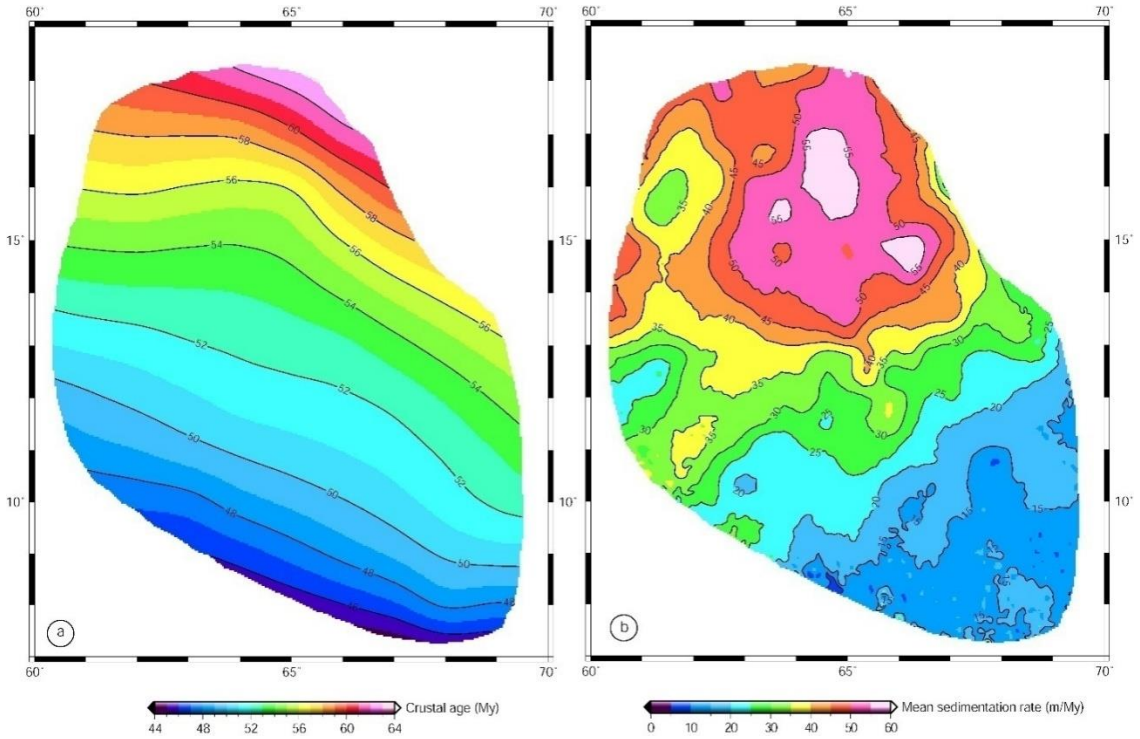

Figure 9. (a) Crustal age map based on regional magnetic isochron map of Chaubey et al. (2002a), **(b)** Map showing the mean sedimentation rate (m/My) within the basin.

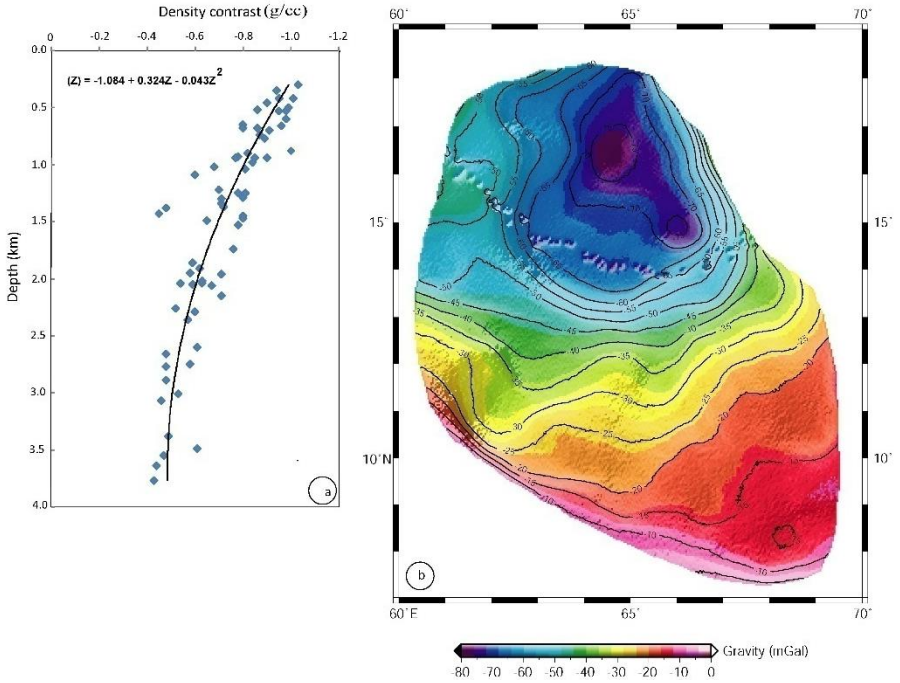

Figure 10. (a) Map showing the decrease in density contrast with depth of burial defined by a quadratic density function in the Arabian Basin obtained by sediment seismic velocities, **(b)** Gravity effect of sedimentary layer in the Arabian Basin considering the sediment thickness and density contrast vs. depth relation from Figures. 7 and 10a, respectively.

Sedimentation rate gridded data

For computation of age of the ocean crust, we considered the normal oceanic lithosphere of the basin. Age grid data is necessary to compute sedimentation rate in the basin. For the present study magnetic isochron map by Chaubey et al. (2002a) and geomagnetic reversal timescale by Cande and Kent (1995) have been used for age determination. The age interval of igneous crust in the Arabian Basin varies from ~63.1 Ma in the northern part to ~44.5 Ma in the southern part (Figure 9a). In the present study, the computed sedimentation rate is almost continuously decreasing from north to south in the basin with an average rate as ~30 m/My. It is maximum (~50 m/My) in Indus Fan region located south-west of the Laxmi Ridge, whereas north-east flank of the Carlsberg Ridge shows least sedimentation rate (~10 m/My) as shown in Figure 9b.

Sediment gravity gridded data

Density-depth relationship for sediments

The density-depth relation for the Arabian Basin sediments is required for quantitative estimation of gravity effect of the sedimentary layers. Since density of deeper layers increases due to compaction in case of sedimentary basins, we generated a map between density contrast and depth in the entire basin sediments with respect to oceanic basement (Figure 10a). The graph shows a decrease of density contrast with respect to underlying basement and shows parabolic variation with depth (Bhaskara Rao, 1986; Radha Krishna et al., 2010). For gravity computation due to the entire sedimentary layer, entire sedimentary layer is divided into four sub-layers with stepwise density values. In the present study, a quadratic density function method is adopted for fitting the depth dependent density distribution in the basin which is as follows:

$$\Delta\rho(z) = a_0 + a_1 z + a_2 z^2 \qquad \ldots\ldots (2)$$

where, z denotes the depth below seabed, a_0 denotes the extrapolated density contrast at the surface and a_1 & a_2 are the constants of the quadratic function.

Gravity effect of sediment

Whatever gravity values we observe at the surface, is the aggregate of all the underlying layers. Sediment load has its own gravity contribution in the observed values. To compute the gravity effect of sediments, sedimentary layer was considered as a number of adjacent regular prismatic bodies that stretch down to the oceanic basement with the dataset interpolated onto a 2'x2' sediment thickness grid. The dataset was extended beyond the study area to avoid the edge effects in gravity calculation of the sedimentary layer. Gravity anomaly of these prismatic bodies with known

density values across each sedimentary layers is defined by a quadratic density function. A function subprogram from Bhaskara Rao and Ramesh Babu (1991) was used for computation of gravity anomaly at each grid and is shown in Figure 10b. The map shows variations in gravity value due to uneven deposits of sediments. It ranges from -10 mGal near the north-eastern flank of the Carlsberg Ridge where sediment thickness is less than 1 km, to as low as -80 mGal in Indus fan region having maximum sediment thickness off India-Pakistan shelf region. The deep basinal parts of central Arabian Basin show gravity low of ~ -50 mGal.

Moho depth grid data

Gravity inversion technique has been used to map the depth to the Moho in present study. For that, crustal gravity effects are to be subtracted above Moho interface. To get that, the following necessary computations are required which are summarized as follows:

Sediment corrected basement and Mantle Bouguer Anomaly (MBA)

It is necessary to correct observed sea floor depths for the effect of sediment loading while examining the uplift and subsidence of the oceanic lithosphere. Indus fan sediment has a significant role in subsidence of the crust in northern part of the study area. Therefore, the effect of sediment load was removed after multiplying by a correction factor value of 0.48 to sediment thickness map (Crough, 1983) to get the sediment corrected basement. Computation of gravity anomaly from bathymetry and density contrast is carried out using an algorithm developed by Parker (1972). Since free air gravity map is mainly governed by gravity attraction of density contrast at the seafloor, MBA map is generated which reflects the deeper subsurface structure. For this purpose, gravity attractions for seafloor topography, sediments and crustal thickness were subtracted from free air anomaly.

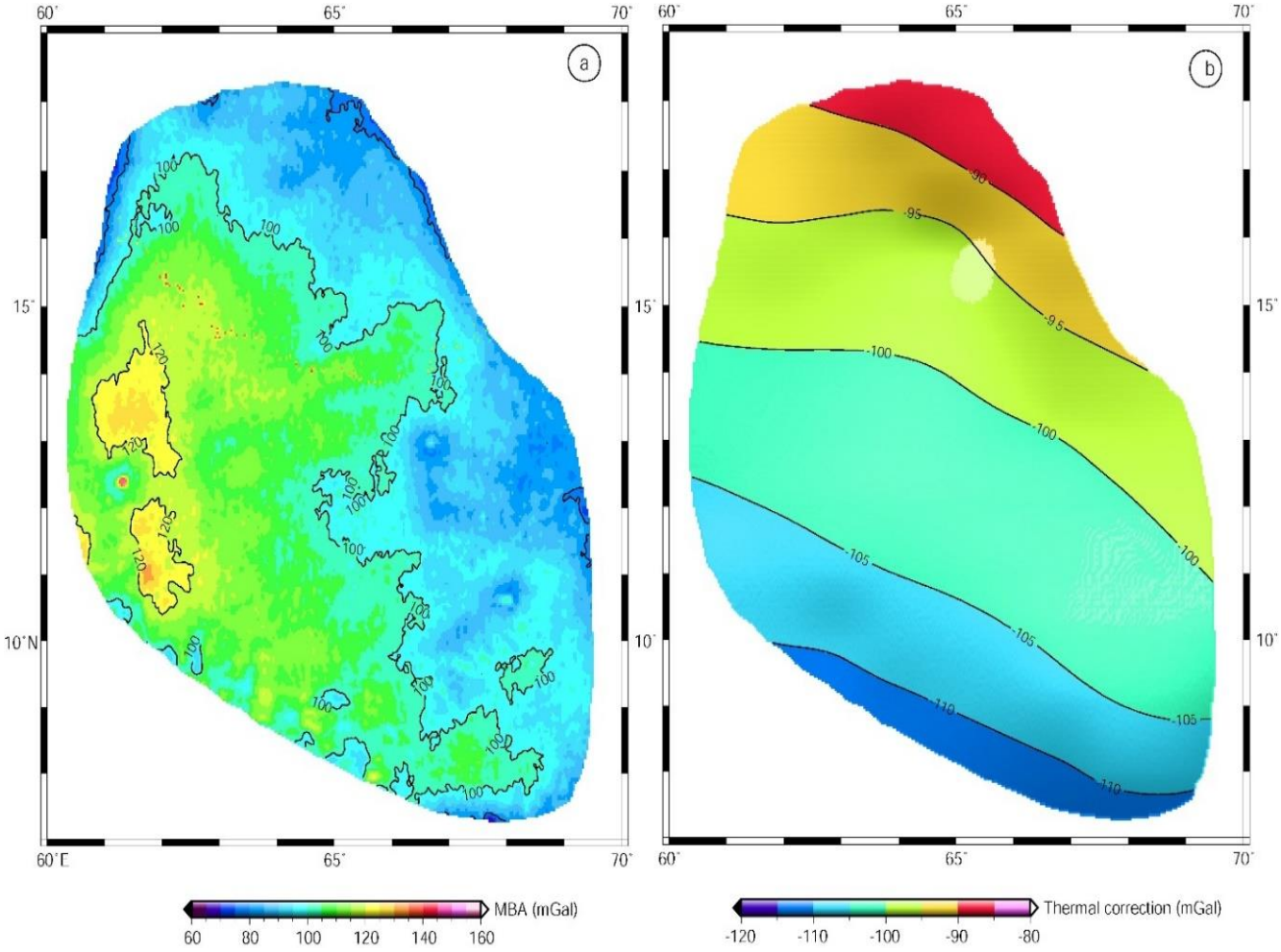

Figure 11. (a) Mantle Bouguer Anomaly (MBA) map of the basin, **(b)** Colour shaded contour map showing lithospheric thermal gravity value within the study area.

After subtracting these effects, resultant map gives information about deeper crust as well as undulations in Moho. MBA map of the study area is shown in Figure 11a which shows that relatively smaller MBA values indicate deeper regions, whereas more positive MBA values indicate shallower regions.

Lithospheric thermal gravity correction

It is reported that oceanic lithosphere is associated with elevated geotherms. The lithosphere thermal gravity anomaly is an important factor in active seafloor spreading oceanic regions as it generates a large negative anomaly at the oceanic ridges (Greenhalgh and Kusznir, 2007). It is clear that maximum lithospheric thermal gravity correction is required near the ridge crest. Therefore, correction for lithospheric thermal gravity is necessary to be computed as it compensates for large negative anomaly from oceanic lithosphere (Cowie and Kusznir, 2012). For this purpose, following formula was used for thermal gravity anomaly calculations. Crustal age data was used from Chaubey et al. (2002a) and the thermal structure was calculated from 0 to 100 km depth based on the plate cooling model of Mckenzie (1978). Δg_t is caused by the density contrast arising from lateral variations in lithospheric temperatures and is evaluated using $\Delta\rho_t = \rho\alpha\Delta T$.

$$\Delta g_t = \frac{(8G\alpha\rho aTm)}{\pi} \cdot \sum_{m=0}^{\infty} \frac{1}{(2m+1)2} \left[\frac{\beta}{(2m+1)\pi} \sin\frac{(2m+1)\pi}{\beta}\right] \cdot \exp\left(-\frac{(2m+1)2t}{\tau}\right) \quad \ldots\ldots (3)$$

The parameters used in calculation of lithospheric thermal gravity correction are given in Table 2. For oceanic lithosphere, lithosphere stretching factor, $\beta = \infty$ and t denotes the oceanic crustal age as defined by magnetic isochrons. For the present study, thermal gravity correction is computed as ~ -120 mGal near the north-eastern flank of the Carlsberg Ridge and it continuously keeps on decreasing but with still substantial values away from the ridge-flank (Figure 11b).

3D inversion of Residual Mantle Bouguer anomaly data

As oceanic lithosphere gets cooled by the passage of time away from the ridge crest, it generates a thermal anomaly. If we invert MBA to get the Moho topography with an appropriate value of crust-mantle density contrast and mean Moho depth, we get relatively deeper Moho (Chappell and Kusznir, 2008). Therefore, thermal structure based on Mckenzie plate model (Mckenzie, 1978) was calculated for 0 to 100 km with the use of oceanic age grid to compensate the lithospheric cooling effects. Further, computed thermal gravity effect due to cooling of lithosphere was subtracted from MBA to give RMBA as shown in Figure 12a. This map was further detrended with a linear fit as shown in Figure 12b. This figure shows RMBA values vary from -30 to 60 mGal, indicative of nearly flat and regular Moho. It also reflects well in terms of Moho variations across the basin. Positive values indicate regions of shallower Moho, whereas negative values show regions of relatively deeper Moho.

In this study, the Moho reference depth has been determined using available seismic refraction stations in the basin that corresponds to the thickness of crust that has zero bathymetry (Mooney et al., 1998; Alvey et al., 2008). We calculated a series of the Moho depth models for the study area, corresponding to assumed crust-mantle density contrast in 0.05 g/cm^3 steps, while fixing mantle density at 3.3 g/cm^3. RMBA values were downward continued to a constant depth before the calculations.

Table 2. Parameters used in calculation of lithospheric thermal gravity**.**

Parameter	Definition	Value
G	Universal gravitational constant	6.67x 10^{-11} Nm^2/Kg^2
ρ	Mantle density	3300 kg/m^3
a	Plate thickness	100 km
T_m	Temperature at the bottom of the plate	1300 ˚C
α	Volumetric coefficient of thermal expansion	3.0 x 10^{-5} $˚C^{-1}$
τ	Lithosphere cooling thermal decay constant	65 Ma

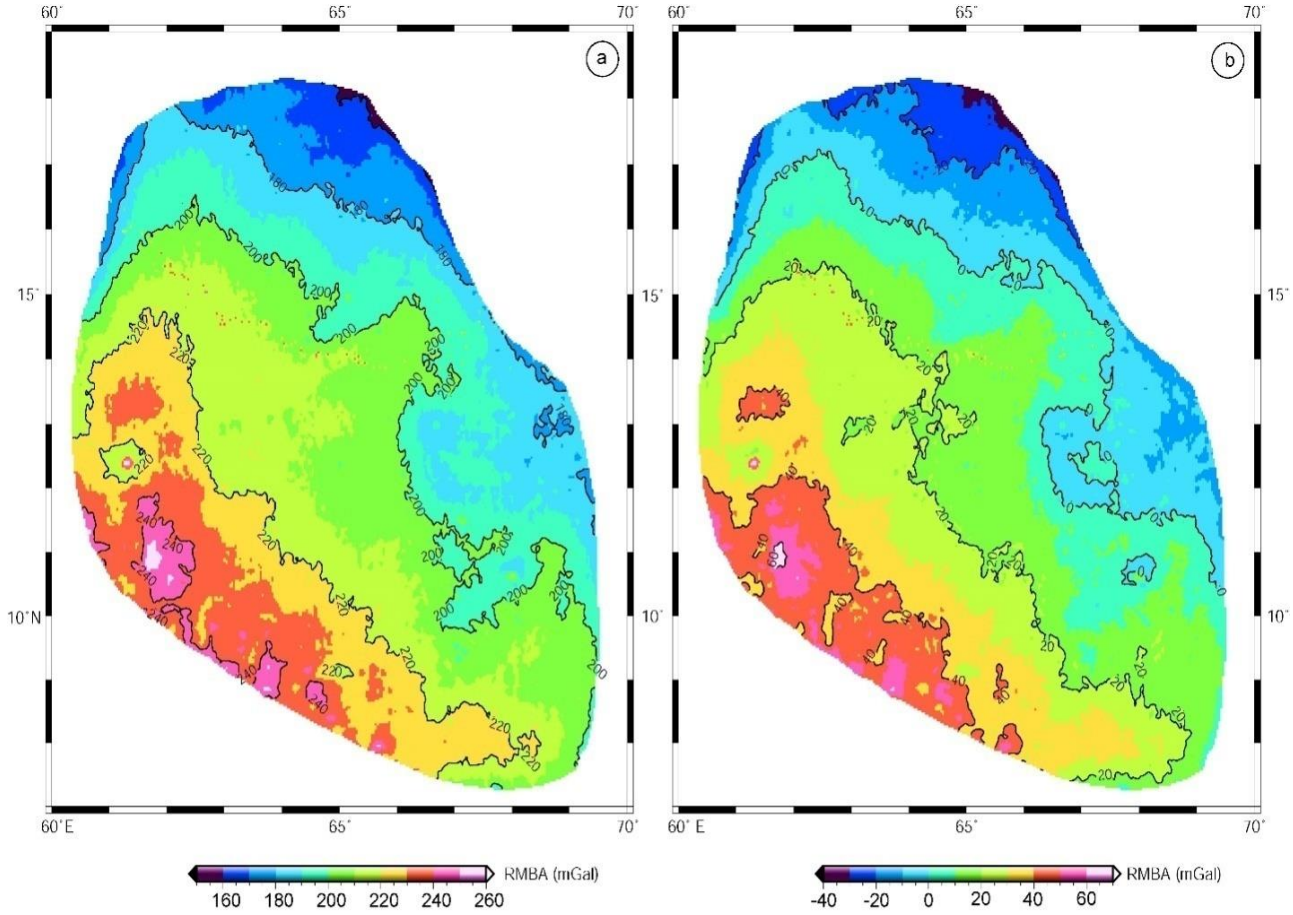

Figure 12. (a) Residual Mantle Bouguer Anomaly (RMBA) map of the basin, **(b)** RMBA map of the study area after detrending it by a linear fit.

Table 3. Sensitivity of inversion results to assumed density contrast at crust-mantle interface.

Assumed density contrast (g/cc)	Best fitting slope*	RMS (km)#
0.40	0.41	1.01
0.45	0.53	0.95
0.50	0.62	0.92
0.55	0.72	0.90
0.60	0.81	0.89

*Fit to the data using the relationship: seismic refraction Moho, Mseism = Mc + R × Mgrav, where Mc is the y-axis intercept, R is the best fitting slope, and Mgrav is gravity-derived Moho.

#Root mean square for the difference between gravity-derived and seismically determined Moho.

We have tested downward continuation depths at 11, 11.5 and 12 km. In the present study, results from downward continuation depths of 12 km are presented. Since inversion results are greatly affected by the crustal-mantle density contrast and the reference Moho depth, we took the best suited combination of crust-mantle density contrast and the reference Moho depth for this study as 0.6 g/cm^3 and 12 km respectively after exercising several combinations (Table 3).

Above analysis shows the variation in the Moho depth across the basin (Figure 13a). The depth to the Moho in entire basin varies from 9-13 km. The average Moho depth in northern part of the basin as well as in south-eastern part is ~12 km, whereas it is ~10.5 km near the flank of the Carlsberg Ridge. Deeper Moho over seamounts was observed with an average value of 13-14 km.

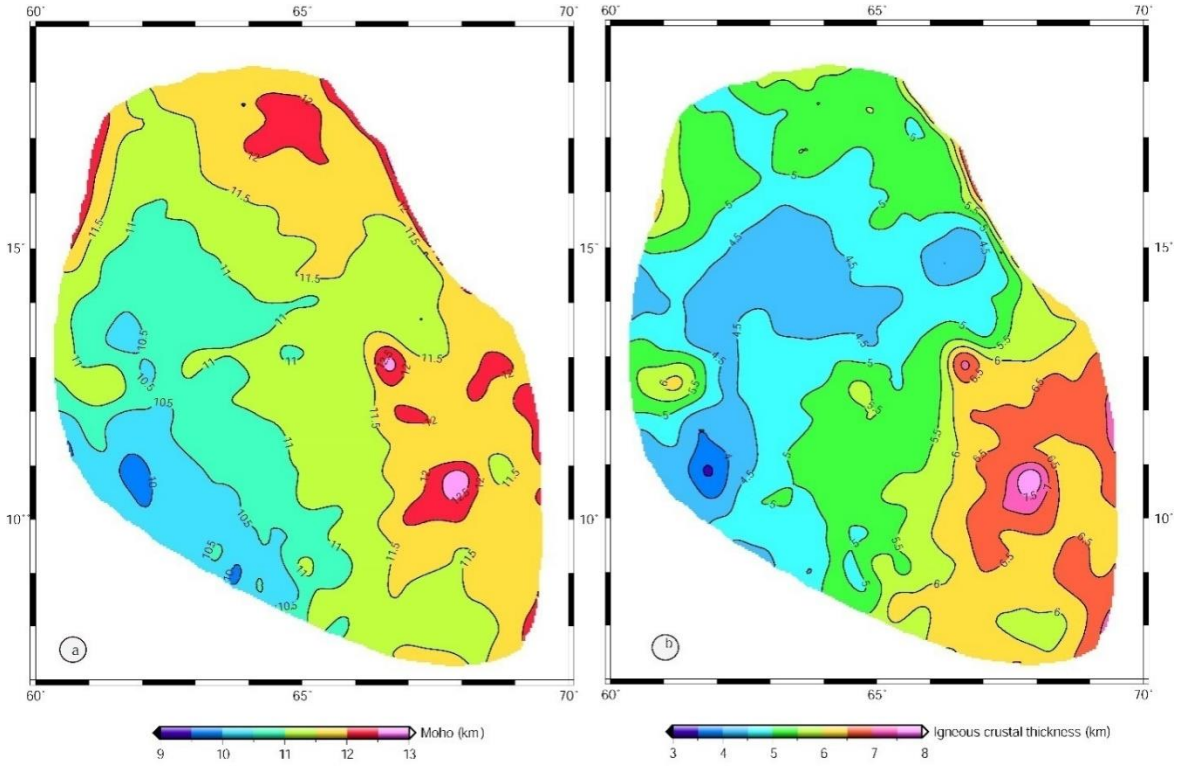

Figure 13. (a) Map showing the Moho variations of the basin obtained from the inversion of RMBA data, **(b)** Igneous crustal thickness map of the Arabian Basin.

Igneous crustal thickness grid data

Igneous crustal thickness map is generated after subtracting the water and sedimentary layer from the Moho depth. The data has been used to generate gridded database of igneous crustal thickness, and finally igneous crustal thickness map of the basin is generated (Figure 13b). RMBA map mimics the igneous crustal thickness variations. In RMBA, crust and mantle density variations both contribute to RMBA together with mean Moho depth (Magde et al., 1995; Canales et al., 2002). Igneous crustal thickness variations across the basin caused due to variation in observed RMBA signal are shown in Figure 13b. For the same RMBA, a larger density contrast at Moho produces a smaller lateral change in crustal thickness and vice versa. In addition to this, gravity inversion results depend on the age of oceanic lithosphere which is included as the lithospheric thermal gravity correction. Igneous crustal thickness variations are in range of 3-8 km (Figure 13b). The average igneous crust in northern part of the basin is 5 km, whereas it is 6 km in south-eastern part of the basin. It is ~4.5 km near the Carlsberg Ridge. Thicker igneous crust over the seamounts is observed with an average value of 6.5 km.

The free air gravity anomaly map of the Arabian Basin also reveals three seamounts that are associated with high gravity values. Deeper Moho and thicker igneous crust are observed below seamounts due to isostatic compensation. It is clearly visible that the Moho depth and crustal thickness under a seamount along profile L4 are deeper than the surroundings (Figure 13a, b), so as in 2D forward gravity model along profile L4 at ~100 km distance (Figure 6b).

Volume, mass of sediments and igneous crust

Sedimentation is second most important mechanism which controls the volume of ocean basins after seafloor spreading. As it is evident that huge sediment deposition in the Arabian Basin is mainly due to Indus derived sediments which is eroded from the Himalayan region, correct estimate of volume will be beneficial/required to understand the tectonic evolution of the basin in greater detail. The limits of sediment thickness map coincide with the north-eastern flank of the Carlsberg Ridge and western end of the Laxmi and Laccadive ridges. Polygon-shaped sediment thickness map was converted to volume by interpolating the thickness values at the intersections of 2-minute grid for a total of 66117 points, superimposed over the sediment thickness map. The resulting volume is estimated as 1.48×10^6 km^3. Further, a weightage density was calculated from velocity-density relationship for the sedimentary layer and mass of the sediments was computed. The estimated

mass of sediments is 3.2x 10^{18} kg. Likewise, estimated volume and mass of igneous crust beneath the basin are 4.87x 10^6 km^3 and 1.36x10^{19} kg, respectively.

DISCUSSION

Spatial distribution of sediment thickness and sedimentation rate

For the present study, total thickness of sediments is considered irrespective of their origin. It contains sources of fluvial, aeolian, biogenous, and authigenic origin all together. However, fluvial detritus is one of the major sources of sediments in Arabian Sea. Indus River solely contributes ~440 million tons of sediment annually among several sediment contributors (Holeman, 1968). Clayey minerals are deposited by several major drainage areas with its erosional products. Clear identification of illite rich sediments at DSDP site 221 has been dated as Middle Oligocene which confirms that it got transported to down south from Himalayas to its present location.

Although Indus River is the main source of sedimentation in the basin, some continental rivers viz Narmada and Tapti also play some role in sedimentation. The northwestern region of the basin is dominantly covered with the Indus fan sediments with maximum thickness (~3.5 km) and clearly demonstrates in sediment thickness map, whereas in southern and south-eastern region, thickness of sediments is continuously getting thinner. On the north-eastern flank of the Carlsberg Ridge, thickness is observed as ~500 m. Since Carlsberg Ridge is still active, sediment accumulation at the ridge axis is negligible but increases off the flanks due to cooling of the lithosphere. Apart from this, source of the sediment in Indus Fan lies in western Himalayan belt which continuously feed sediment materials to the fan. Sedimentary fill shows continuous progradation of the Indus Fan southward. In overall, sedimentation rate within the basin also follows the same trend as the thickness of sediments. It suggests that sedimentation in the basin almost follow a direct correlation between the thickness of sediments and the crustal age. Rate of sediment accumulation and the amount of sediment in depocentres can provide some insight into tectonics and geological history of the basin. In case of Bay of Bengal, sediment deposit is extremely high due to continuous denudation of Himalayan rocks by several rivers. Curray (1994) proposed the volume of Bengal Fan as 12.5 x 10^6 km^3 mostly post collision sediments and sedimentary rocks. Contrary to this, volume of sediments in present study for the Arabian Basin is calculated as 1.48x10^6 km^3. Several researchers have discussed about a distinct increase in sediment discharge during the Oligocene-Miocene (~23 Ma) and the start of turbidity system. This provides an important age marker which corresponds to rapid erosion of the Himalayan rock materials, responsible for commencement of Indus Fan sedimentation. As the fan progrades, pelagic sediments are overlain by turbidites of the fan. It is shown by 'R' reflector (Chaubey et al., 2002b) which probably demarcates pre-collision sediments dominated with aeolian sources, to post-collision sediments dominated with fluvial and monsoonal sources.

Collision of Indo-Eurasian plates caused a significant uplift of the Himalayas by about early Oligocene (Molnar and Tapponnier, 1975) and this activity initiated the formation of the Indus River after millions of years. Upliftment of Himalayan mountains occurred several times in geological past which subsequently became the source of monsoonal activity. Consequently, Indus River drainage system was originated by Oligocene time as suggested by Weser (1974) by studying sediments at the DSDP site 221 with sedimentation rate 3-5 m/My. However, sedimentation rates at site 221 are fairly uniform which suggests that such distal sites are not good records of temporal variations. Thus, to address the mass flux issues, a thick, proximal fan is required to analyze that can clearly give sedimentation rates in different times. In the present study, sedimentation rate is almost continuously decreasing from north to south with an average rate as ~30 m/My with a maximum rate (~50 m/My) in Indus Fan region located south-west of the Laxmi Ridge forming a depocenter, whereas north-east flank of the Carlsberg Ridge shows least sedimentation rate (~10 m/My). Though Indus River is the main source of sediment deposit in the basin, sea level changes in different geological time intervals have also affected sedimentation rate. This possibly implies that climatic and sea level changes along with tectonic processes have played a major role in erosion and sediment transportation to basin.

Tectonic controls on sedimentation

The evolutionary history of WCMI and its adjoining ocean basins has been very complex. Later on, it became more complex after Indian plate passed over the Reunion hotspot which changed the structural configuration of the region thoroughly. Likewise, basin also has complex sedimentary history since its creation. Passive continental margins always get more sediment in comparison to deep sea because of its proximity to coastal rivers. Apart from this, there are several other factors that influence sediment deposition in the basin. Climatic conditions over landmasses adjoining the Arabian Sea also provide the type of material and sediment volume transported into the sea. India's

eastern margin is having a humid climate that provides the necessary rainfall for abundant river run-off. This river run-off eventually empties into the sea. Even if a large portion of it drains into the Bay of Bengal, a significant amount of water body with loaded sediments still enters the Arabian Sea. If we analyze the type of sediments transported to the sea, India's northern and western margins are specified by a desert climate where sediment supply is strongly influenced by aeolian processes but if it is observed on a year-round basis, a considerable quantity of aeolian detritus is supplied to the Arabian Sea.

Another reason for varying sediment thickness in the basin could be the basement depth anomaly. Western part of the Arabian Basin exhibits zone of positive depth anomalies, which indicate excess subsidence of the oceanic crust that has resulted into deeper basement depth causing more sediment thickness in this region (Ajay and Chaubey, 2008). On contrary to this, eastern part of the basin is dominated with negative depth anomalies which indicate vertical upwelling due to convection. This resulted the shallower basement in eastern part of the basin, causing less sediment thickness in this part. Basement over the active Carlsberg Ridge has been observed very rugged over the flank of the ridge generating basement highs and lows and therefore less sedimentation is clearly observed in RC1707-01 seismic section (Figure 4).

Moho and igneous crustal thickness variations

To calibrate the inversion results with available seismic refraction data, we compared our results to Moho depth observed at seven refraction stations in the study area. RMS error was calculated for every case between Moho derived from inversion results and seismically derived refraction Moho. A best fitting slope between inversion Moho and seismically derived refraction Moho was computed for each case (Table 3). We observe that the result with average crustal density of 2.7 g/cm^3 has both the smallest RMS as well as best fitting slope that approaches to unity (Table 3). Since available seismic refraction data are limited and scattered at long distances, it is not easy to get an ideal correlation, which has best fitting slope 1, between inversion derived Moho and seismic refraction Moho. Gravity inversion results broadly agree with seismic refraction data for the Moho variations. However, Moho with inversion result and seismically constrained crustal layers rarely correlate closely. At refraction stations 70V and 55V, difference in Moho is nearly 1 km. Since these refraction stations fall near the Laxmi Ridge, it can be justified that the Moho values would be more than 11 km because at any profiles shown in Figures 6a-d, Moho variations will not abruptly change but will gradually vary near the edges. The reason of these differences arises from a number of effects. Like, the lateral density variations between crust and upper mantle during inversion process is not considered. This may account for much of the variation in the Moho. Several other reasons for the Moho differences are resolutional differences among bathymetry, gravity and sediment thickness data used in inversion process (Wang et al., 2011; Dwivedi et al., 2019). After analyzing these aspects, it is clear that inversion results do not accurately predict local Moho but they provide important information about variations at regional scale.

Since deep seismic refraction surveys are expensive, gravity inversion technique proves a more practical approach for mapping the Moho topography over regional scale. Integration with available ship-borne gravity and seismic data within the region gives better picture of the study area. The present study proposes that average Moho depth in northern and south-eastern part of the Arabian Basin is ~12 km. In order to examine the Moho undulations in the basin, we compared the Moho results estimated in present work with the available seismic refraction Moho. Depth to Moho beneath the seamounts does not match well in results generated from inversion and forward 2D gravity data modeling because seamount features have been modeled considering the Airy Type isostatic compensation. Therefore, the Moho undulations derived from gravity inversion technique are smaller in amplitude than those of derived from isostatically compensated seismically constrained 2D crustal modelling. However, crustal thickness derived from inversion of RMBA mainly depends on the density contrast at Moho as well as mean Moho depth.

In northern part of the study area, sediment deposition has profoundly taken place with excess influx of sediments from Indus River causing subsidence of the underlying crust. On contrary to this, thickness of sediments in eastern part of study area near the Laccadive ridge is relatively less and the basement depth is shallower. It can be inferred that depth anomalies across the Arabian Basin are responsible for the variations in basement but it doesn't show any significant effect over Moho undulations. If we analyze the available MCS reflection time sections viz. SK12-06, SK12-07 in eastern part of the study area, we observe the Moho being deeper near the Laccadive Ridge in comparison to western part of the study area. As eastern part of the basin is in proximity to aseismic ridges, tectonic processes such as rifting and drifting with the onset of Reunion hotspot has an impact to certain extent over this part. There may be several

interpretations for this but magmatic emplacement during the northward movement of Indian plate may have caused subsidence in subsequent years after the major catastrophic volcanic event occurred ~65 Ma. It may have affected the nearby region of the basin. Therefore, crustal thickness in south-eastern region of the study area are thicker as compared to the northern part. It is interesting to note that sediment load due to Indus Fan sediment deposit does not play a significant role in subsidence of the Moho in the northern part of the study area as this region is cold and underlain by high density materials. Overall, the Moho variations in the basin was found to be regular and flat except at the seamounts. The seismic refraction stations, too, don't provide any evidence of magmatic underplating material in the basin which can cause increased crustal thickness in the region.

CONCLUSIONS

(i) The northern region of the Arabian Basin is dominantly covered with the Indus Fan sediments having maximum sediment thickness (~3.5 km), whereas the minimum thickness is observed near north-eastern flank of the Carlsberg Ridge (~500 m).

(ii) Gravity value due to varying sediments ranges from -10 mGal near the north-eastern flank of the Carlsberg Ridge having sediment thickness less than 1 km, to as low as -80 mGal in Indus fan region having maximum sediment thickness off India-Pakistan shelf region.

(iii) Thermal gravity correction is computed as ~ -120 mGal near the north-eastern flank of the Carlsberg Ridge and it continuously decreases away from the ridge-flank.

(iv) The Moho depth and igneous crustal thickness in the basin vary between 9-13 km and 3-8 km, respectively.

(v) The estimated volume and mass of the basinal (a) sediments are ~1.48×10^6 km^3 and 3.2×10^{18} kg, whereas (b) igneous crust are ~4.87×10^6 km^3 and 1.36×10^{19} kg, respectively.

Availability of data and material: Bathymetry and gravity data employed in this work were obtained from https://www.ngdc.noaa.gov/mgg/global/global.html and https://topex.ucsd.edu/marine_grav/mar_grav.html, respectively.

Code availability: 3DINVER.M program can be obtained from the website http://www.escet.urjc.es/dgomez/, or from the IAMG server at http://www.iamg.org/CGEditor/index.htm.

ACKNOWLEDGEMENTS

Leading author is thankful to Department of Geophysics, Institute of Science, Banaras Hindu University for providing the basic research facilities. Authors are also grateful to Prof. Sunil Kumar Singh, Director, CSIR-National Institute of Oceanography for his encouragement, support and permission to publish this work. Authors are very thankful to reviewers for their constructive comments and suggestions. Authors would also like to sincerely thank Dr. O.P. Pandey, Chief Editor, JIGU for his input and positive suggestions, which have improved the quality of the manuscript enormously. Figures were generated using GMT software of Wessel and Smith (1998).

Compliance with Ethical Standards

The authors declare no conflict of interest and adhere to copyright norms.

REFERENCES

Agrawal, P.K., Pandey, O.P. and Negi, J.G., 1992. Madagascar: A continental fragment of the paleo super Dharwar craton of India. Geology, 20, 543-546.

Ajay, K.K. and Chaubey, A.K., 2008. Depth anomalies in the Arabian Basin, NW Indian Ocean. Geo-Mar. Lett., 28(1), 15-22.

Alvey, A., Gaina, C., Kusznir, N.J. and Torsvik, T.H., 2008. Integrated crustal thickness mapping and plate reconstructions for the high Arctic. Earth Planet Sci. Lett., 274 (3-4), 310-321.

Amante, C. and Eakins, B.W., 2009. ETOPO1 1 Arc-Minute Global Relief Model: Procedures, Data Sources and Analysis. NOAA Technical Memorandum NESDIS NGDC-24. National Geophysical Data Center, NOAA. http://dx.doi.org/10.7289/V5C8276M.

Bhattacharya, G.C., Chaubey, A.K., Murty, G.P.S., Srinivas, K., Sarma, K.V.L.N.S., Subrahmanyam, V. and Krishna, K.S., 1994. Evidence for seafloor spreading in the Laxmi Basin, northeastern Arabian Sea. Earth Planet. Sci. Lett., 125(1-4), 211-220.

Bhattacharya, G.C. and Yatheesh, V., 2015. Plate-tectonic evolution of the deep ocean basins adjoining the western continental margin of India - a proposed model for the early opening scenario. Pet. Geosci. Indian Contexts, Springer Geology, 1-61.

Bhaskara Rao, D., 1986. Modelling of sedimentary basins from gravity anomalies with variable density contrast. Geophys. J. R. Astron. Soc., 84(1), 207-212.

Bhaskara Rao, D. and Ramesh Babu, N., 1991. A FORTRAN-77 computer program for three-dimensional analysis of gravity anomalies with variable density contrast. Comput. and Geosci., 17, 655-667.

Brocher, T.M., 2005. Empirical relations between elastic wavespeeds and density in the Earth's crust. Bull. Seismol. Soc. Am., 95(6), 2081-2092.

Canales, J.P., Ito, G., Detrick, R.S. and Sinton, J., 2002. Crustal thickness along the western Galápagos Spreading Center and the compensation of the Galápagos hotspot swell. Earth Planet. Sci. Lett., 203(1), 311-327.

Cande, S.C. and Kent, D.V., 1995. Revised calibration of the geomagnetic polarity timescale for the Late Cretaceous and Cenozoic. J. Geophys. Res., 100, 6093-6095.

Cande, S. and Stegman, D.R., 2011. Indian and African plate driven by the push force of the Reunion plume head. Nature, 475 (7354), 47-52.

Chappell, A.R. and Kusznir, N.J., 2008. Three-dimensional gravity inversion for Moho depth at rifted continental margins incorporating a lithosphere thermal gravity anomaly correction. Geophys. J. Int., 174(1), 1-13. http://dx.doi.org/10.1111/j.1365-246X.2008.03803.x.

Chaubey, A.K., Bhattacharya, G.C., Murty, G.P.S. and Desa, M., 1993. Spreading history of the Arabian Sea: some new constraints. Mar. Geol., 112(1-4), 343-352.

Chaubey, A.K., Bhattacharya, G.C. and Rao, D.G., 1995. Seafloor spreading magnetic anomalies in the southeastern Arabian Sea. Mar. Geol., 128 (1-2), 105-114.

Chaubey, A.K., Bhattacharya, G.C., Murty, G.P.S., Srinivas, K., Ramprasad, T. and Rao, D.G., 1998. Early Tertiary seafloor spreading magnetic anomalies and paleo-propagators in the northern Arabian Sea. Earth Planet. Sci. Lett., 154 (1-4), 41-52.

Chaubey, A.K., Dyment, J., Bhattacharya, G.C., Royer, J.Y., Srinivas, K. and Yatheesh, V., 2002a. Paleogene magnetic isochrons and palaeo-propagators in the Arabian and eastern Somali basins, northwest Indian Ocean. In: The tectonic and climatic evolution of the Arabian sea region (eds), Clift, P.D., Kroon, D., Gaedicke, C. and Craig, J., Geol. Soc. London, Spec. Publ., 195(1), 71-85.

Chaubey, A.K., Rao, D.G., Srinivas, K., Ramprasad, T., Ramana, M.V. and Subrahmanyam, V., 2002b. Analyses of multichannel seismic reflection, gravity and magnetic data along a regional profile across the central-western continental margin of India. Mar. Geol., 182 (3-4), 303-323.

Clift, P., Gaedicke, C., Edwards, R., Lee, J., Hildebrand, P., Amjad, S., White, R.S. and Schlüter, H.U., 2002. The stratigraphic evolution of the Indus Fan and the history of sedimentation in the Arabian Sea. Mar. Geophys. Res., 23(3), 223-245.

Clift, P.D., Shimizu, N., Layne, G.D., Blusztajn, J.S., Gaedicke, C., Schluter, H.U., Clark, M.K. and Amjad, S., 2001. Development of the Indus Fan and its significance for the erosional history of the Western Himalaya and Karakoram. Geol. Soc. Am. Bull., 113 (8), 1039-1051.

Clift., P.D., Zhou, P., Stockli, D.F. and Blusztajn, J., 2019. Regional Pliocene exhumation of the Lesser Himalaya in the Indus drainage. Solid Earth, 10(3), 647-661.

Collier, J.S., Sansom, V., Ishizuka, O., Taylor, R.N., Minshull, T.A. and Whitmarsh, R.B., 2008. Age of Seychelles-India break-up. Earth Planet. Sci. Lett., 272(1-2), 264-277.

Courtillot, V., Besse, J., Vandamme, D., Montigny, R., Jaeger, J.J. and Cappetta, H., 1986. Deccan flood basalts at the Cretaceous/Tertiary boundary?. Earth Planet. Sci. Lett., 80, 361-374.

Courtillot, V., Feraud, G., Maluski, H., Vandamme, D., Moreau, M. and Besse, J., 1988. Deccan flood basalts and the Cretaceous/Tertiary boundary. Nature, 333(6176), 843-846.

Cowie, L. and Kusznir, N., 2012. Mapping crustal thickness and oceanic lithosphere distribution in the Eastern Mediterranean using gravity inversion. Pet. Geosci., 18(4), 373-380.

Crough, S.T., 1983. The correction for sediment loading on the seafloor. J. Geophys. Res. Solid Earth, 88 (B8), 6449-6454.

Curray, J.R., 1994. Sediment volume and mass beneath the Bay of Bengal. Earth Planet. Sci. Lett., 125, 371–383.

Divins, D., 2003. Total sediment thickness of the world's oceans and marginal seas. Boulder, CO: NOAA National Geophysical Data Center.

Dyment, J., 1998. Evolution of the Carlsberg ridge between 60 and 45 Ma: Ridge propagation, spreading asymmetry and the Deccan-Reunion hotspot. J. Geophys. Res., 103(B10), 24067-24084.

Dwivedi, D., Chamoli, A. and Pandey, A.K., 2019. Crustal structure and lateral variations in Moho beneath the Delhi fold belt, NW India: Insight from gravity data modeling and inversion. Phys. Earth Planet. Inter., 297, 106317.

Ewing, M., Eittreim, S., Truchan, M. and Ewing, J.I., 1969. Sediment distribution in the Indian Ocean. Deep Sea Research and Oceanographic Abstracts, 16(3), 231-248.

Ferrier, K.L., Mitrovica, J.X., Giosan, L. and Clift, P.D., 2015. Sea-level responses to erosion and deposition of sediment in the Indus River basin and the Arabian Sea. Earth Planet. Sci. Lett., 416, 12-20.

Fisk, M.R., Duncan, R.A., Baxter, A.N., Greenough, J.D., Hargraves, R.B. and Tatsumi, Y., 1989. Reunion hotspot magma chemistry over the past 65 my: Results from Leg 115 of the Ocean Drilling Program. Geology, 17(10), 934-937.

Gibbons, A.D., Zahirovic, S., Müller, R.D., Whittaker, J.M. and Yatheesh, V., 2015. A tectonic model reconciling evidence for the collisions between India, Eurasia and intra-oceanic arcs of the central-eastern Tethys. Gondwana Res., 28, 451-492.

Greenhalgh, E.E. and Kusznir, N.J., 2007. Evidence for thin oceanic crust on the extinct Aegir Ridge, Norwegian Basin, NE Atlantic derived from satellite gravity inversion. Geophys. Res. Lett., 34(6).

Gómez-Ortiz, D. and Agarwal, B.N.P., 2005. 3DINVER. M: a MATLAB program to invert the gravity anomaly over a 3D horizontal density interface by Parker-Oldenburg's algorithm. Comput. and Geosci., 31(4), 513-520.

Gomez-Ortiz, D., Agarwal, B.N.P., Tejero, R. and Ruiz, J., 2011. Crustal structure from gravity signature in the Iberian Peninsula. Geol. Soc. Am. Bull., 123(7–8), 1247-1257.

Holeman, J.N., 1968. The Sediment Yield of Major Rivers of the World. Water Resour. Res., 4(4), 737-747.

Kolla, V. and Coumes, F., 1987. Morphology, Internal Structure, Seismic Stratigraphy and Sedimentation of Indus Fan. AAPG Bulletin., 71(6), 650-677.

Krishna, K.S., Gopala Rao, D. and Sar, D., 2006. Nature of the crust in the Laxmi Basin (14°-20°N), western continental margin of India. Tectonics, 25, TC1006. https://doi.org/10.1029/2004TC001747.

Kumar, P. and Chaubey, A.K., 2019. Extension of flood basalt on the northwestern continental margin of India. J. Earth Syst. Sci., 128, 81.

Kumar, P. and Chaubey, A.K., 2022. Réunion plume associated flood basalt volcanism on the northwestern continental margin of India and related tectonics. J. Asian Earth Sci., 237, 105352. https://doi.org/10.1016/j.jseaes.2022.105352.

Magde, L.S., Detrick, R.S. and TERA group, 1995. Crustal and upper mantle contribution to the axial gravity anomaly at the southern East Pacific Rise. J. Geophys. Res., 100 (B3), 3747-3766.

McKenzie, D., 1978. Some remarks on the development of sedimentary basins. Earth Planet. Sci. Lett., 40(1), 25-32.

McKenzie, D. and Sclater, J.G., 1971. The Evolution of the Indian Ocean since the Late Cretaceous. Geophy. J. Int., 24(5), 437-528.

Miles, P.R. and Roest, W.R., 1993. Earliest sea-floor spreading magnetic anomalies in the north Arabian Sea and the ocean-continent transition. Geophys. J. Int., 115(3), 1025-1031.

Miles, P.R., Munschy, M. and Segoufin, J., 1998. Structure and early evolution of the Arabian Sea and East Somali Basin. Geophys. J. Int., 134(3), 876-888.

Minshull, T.A., Lane, C.I., Collier, J.S. and Whitmarsh, R.B., 2008. The relationship between rifting and magmatism in the northeastern Arabian Sea. Nat. Geosci., 1(7), 463-467.

Mishra, A., Chaubey, A.K., Sreejith, K.M. and Kumar, S., 2018. Crustal underplating and effective elastic plate thickness of the Laxmi Ridge, northern Arabian Sea. Tectonophysics, 744, 82–92.

Mishra, A., Chaubey, A.K., Kumar, S., Kumar, P.V., Kumar, P. and Dubey, K.M., 2020. Does the Laxmi Ridge continue towards the Laccadive Ridge? New insights from an integrated geophysical study. J. Asian Earth Sci., 201, 104491.

Molnar, P. and Tapponnier, P., 1975. Cenozoic tectonics of Asia: Effects of a continental collision. Sci., 189, 419-426.

Mooney, W.D., Laske, G. and Masters, T.G., 1998. CRUST 5.1: A global crustal model at 5 x 5. J. Geophys. Res. Solid Earth, 103 (B1), 727-747.

Naini, B.R. and Kolla, V., 1982. Acoustic character and thickness of sediments of the Indus Fan and the continental margin of western India. Mar. Geol., 47(3-4), 181-195.

Naini, B.R. and Talwani, M., 1983. Structural framework and the evolutionary history of the continental margin of western India; In: Studies in continental margin geology (eds) Watkins, J.S., Drake, C.L., Am. Assoc. Pet. Geol. Memoir, 34, 167-191.

Negi, J.G., Pandey, O.P. and Agrawal, P.K., 1986. Super-mobility of hot Indian lithosphere. Tectonophysics, 131, 147-156.

Norton, I.O. and Sclater, J.G., 1979. A model for the evolution of the Indian Ocean and the breakup of Gondwanaland. J. Geophys. Res. Solid Earth, 84(B12), 6803-6830.

Oldenburg, D.W., 1974. The inversion and interpretation of gravity anomalies. Geophysics, 39(4), 526-536.

Pandey, O.P., Agrawal, P.K. and Negi, J.G., 1995. Lithospheric structure beneath Laxmi Ridge and late Cretaceous geodynamic events. Geo-Mar. Lett., 15, 85-91.

Parker, R.L., 1972. The rapid calculation of potential anomalies. Geophys. J. R. Astr. Soc., 31(4), 447-455.

Radhakrishna, M., Subrahmanyam, C. and Damodharan, T., 2010. Thin oceanic crust below Bay of Bengal inferred from 3-D gravity interpretation. Tectonophysics, 493, 93-105. doi:10.1016/j.tecto.2010.07.004

Royer, J.Y., Chaubey, A.K., Dyment, J., Bhattacharya, G.C., Srinivas, K., Yatheesh, V. and Ramprasad, T., 2002. Paleogene plate tectonic evolution of the Arabian and eastern Somali basins. Geol. Soc. London, Spec. Publ., 195(1), 7-23.

Sandwell, D.T. and Smith, W.H.F., 2009. Global marine gravity from retracked Geosat and ERS-1 altimetry: ridge segmentation versus spreading rate. J. Geophys. Res. Solid Earth, 114(B1). http://dx.doi.org/10.1029/2008JB006008.

Sandwell, D.T., Müller, R.D., Smith, W.H.F., Garcia, E. and Francis, R., 2014. New global marine gravity model from CryoSat-2 and Jason-1 reveals buried tectonic structure. Science, 346(6205), 65-67.

Smith, W.H.F. and Wessel, P., 1990. Gridding with continuous curvature splines in tension. Geophysics, 55(3), 293-305.

Sreejith, K.M., Chaubey, A.K., Mishra, A., Kumar, S. and Rajawat, A.S., 2016. Pseudofaults and associated seamounts in the conjugate Arabian and eastern Somali basins, NW Indian Ocean-New constraints from high-resolution satellite-derived gravity data. J. Asian Earth Sci., 131, 1-11.

Storey, B.C., 1995. The role of mantle plumes in continental breakup: case histories from Gondwanaland. Nature, 377(6547), 301-308.

Straume, E.O., Gaina, C., Medvedev, S., Hochmuth, K., Gohl, K., Whittaker, J.M., Abdul Fattah, R., Doornenbal, J.C. and Hopper, J.R., 2019. GlobSed: Updated total sediment thickness in the world's oceans. Geochem. Geophys., 20(4), 1756-1772. http://dx.doi.org/10.1029/2018GC008115.

Talwani, M., Worzel, J.L. and Landisman, M., 1959. Rapid gravity computations for two-dimensional bodies with application to the Mendocino submarine fracture zone. J. Geophys. *R*., 64(1), 49-59.

Vasanthi, A., 2022. Lithospheric structure and geodynamical evolution of the Laxmi Ridge: new inferences from satellite gravity studies. Geo-Mar. Lett., 42, 14. https://doi.org/10.1007/s00367-022-00737-8

Wang, T., Lin, J., Tucholke, B. and Chen, Y.J., 2011. Crustal thickness anomalies in the North Atlantic Ocean basin from gravity analysis. Geochem. Geophys, 12(3).

Weser, O.E., 1974. Sedimentological aspects of strata encountered on Leg 23 in the northern Arabian Sea**.** Init. Rep. DSDP, 23 (1974), 503-519.

Wessel, P. and Smith, W.H., 1998. New, improved version of Generic Mapping Tools released. Eos, Transactions AGU, 79(47), 579-579.

White, R. and McKenzie, D., 1989. Magmatism at rift zones: The generation of volcanic continental margins and flood basalts. J. Geophys. Res. Solid Earth, 94(B6), 7685-7729.

Whittaker, J.M., Goncharov, A., Williams, S.E., Müller, R.D. and Leitchenkov, G., 2013. Global sediment thickness data set updated for the Australian-Antarctic Southern Ocean. Geochem. Geophys., 14(8), 3297-3305.

Whitmarsh, R.B., 1974. Some aspects of plate tectonics in the Arabian Sea. Init. Rep. DSDP, 23, 527-535.

Wobbe, F., Lindeque, A. and Gohl, K., 2014. Anomalous South Pacific lithosphere dynamics derived from new total sediment thickness estimates off the West Antarctic margin. Glob. Planet. Change, 123, 139-149.

Yatheesh, V., Bhattacharya, G.C. and Mahender, K., 2006. The terrace like feature in the mid-continental slope region off Trivandrum and a plausible model for India-Madagascar juxtaposition in immediate pre-drift scenario. Gondwana Res., 10 (1-2), 179-185.

Received on: 05.11.2022; Revised on: 23.01.2023; Accepted on: 26.01.2023

J. Ind. Geophys. Union, 27(2) (2023), 84-95

Geophysical investigation for lead and zinc and associated minerals around Phophonga Hill, Goalpara District, Assam

Ashish Kumar*[1, 3], Om Prakash[2] and Uma Shankar[3]
[1]Geological Survey of India, Northern Region, Lucknow-226024
[2] Ex, Geological Survey of India, Northern Region, Lucknow-226024
[3]Department of Geophysics, Institute of Science, Banaras Hindu University, Varanasi-221005
*Corresponding author: akumar282@gmail.com

ABSTRACT

The detailed geophysical survey comprising self-potential (SP), induced polarization (IP) time domain (TD) and magnetic vertical field (VF) has been carried out in and around Phophonga hill, Goalpara district (Assam) in an area of 1.9 sq. km in order to delineate the subsurface extension of the anomalous body. The area is mainly occupied by Assam-Meghalaya Gneissic Complex rocks. These rocks of Archaean to Proterozoic age are deeply weathered. They are comprised of banded biotite hornblende gneiss and quartzo-feldspathic gneiss with pegmatite and schist. The geophysical data were processed and interpreted for the identification of lithological contacts, as well as a favourable zone for mineralization. Magnetic and apparent resistivity maps reveal a wide range of variation in magnetic and resistivity values over the exposed formation. The smooth variation in magnetic and resistivity values is recorded in the central part, occupied by soil/cultivated land. The contacts of exposed formation on either side of the study area and soil/cultivated land in the central part, have been demarcated by magnetic and resistivity methods. Some important anomalies have been delineated by the geophysical investigations (W200/N240, 0/N190, E200/N190, E400/N120, and W2600/N200) from Phophonga hill area to Satbaini area for possible lead, zinc, and iron sulphide mineralization. These anomalous zones have been recommended for the verification of the causative sources.

Keywords: Self potential; Induced polarization; Magnetic vertical field; Resistivity; Self-Potential anomalous zone; Mineralized body; Assam-Meghalaya Gneissic Complex

INTRODUCTION

Lead (Pb) and zinc (Zn) are the minerals that mainly occur in sulphide mineralization like galena (PbS) and sphalerite (ZnS). It is found in association with iron sulphide and also occur in its oxides. Iron sulfides are conducting in nature and can be helpful to detect Pb-Zn deposits (Evrard et al., 2018). The western Indian craton of Rajasthan remains the main attraction of base metal exploration (Imam et al., 2014; Bhadra et al., 2021). The lead and zinc are first reported by the Geological Survey of India (GSI) in the Rajpura-Dariba-Bethumni and Pur-Banera belt of western Indian craton of Rajasthan (Gupta, 1934; Imam et al., 2014). Geochemical mapping (Bora and Baruah, 2011) by GSI in Assam has reported higher concentrations of REE, Be, Ti, V, Rb, Sr, and Y in the inselbergs and isolated hillocks in and around the study area. Based on the anomalous values obtained during the geochemical mapping, a preliminary investigation for REE in the southern part of Agia around Sujukona Hill and Tukureswari Hill, was taken up during field session 2013-14 of GSI. The detailed mapping has delineated a shear zone controlled mineralization in the area (Bora et al., 2014). Given the presence of sulphide mineralization in the weak planes with quartz veins and fracture planes, as well as the high values of Zn and Pb in the samples taken along the shear zone, the detailed geophysical surveys (SP, IP, and magnetic) have been carried out along the shear zone to delineate the sub-surface extension and the sub-surface depth continuity of the anomalous body in and around Phophonga hill area (Figure 1). A total area of 1.9 sq. km has been covered with 10 line km from traverses E800 to W3000. Twenty (20) traverses were laid with a 200 m traverse interval with each traverse having length of 500 m with a station interval of 10 m.

GEOLOGY

The area is mainly covered by Assam-Meghalaya Gneissic complex rocks of Archaean to Proterozoic age, surrounded by Quaternary sediments of Late Pleistocene to Late Holocene age. The survey area is the northern extension of the Shillong/Meghalaya plateau, occupied by isolated hills and small hillocks (Baruah and Hazarika, 2008; Kumar et al., 2022). The inselbergs are isolated hills and ridges of Precambrians of the gneissic complex i.e. granite gneiss, hornblende biotite gneiss and migmatites. The gneissic complex has structural relation with the Shillong massif and basement (Bhagabaty et al., 2017). They form the oldest components of the basin and the rocks are deeply weathered, which include high-grade metamorphic rock granitoid gneisses, banded biotite hornblende gneisses with pink granitic injections and pegmatite and quartz veins. The meta-sediments and banded magnetite quartzite of the Shillong group are intruded by grey granite and pink porphyritic granite, pegmatite, quartz veins, basic intrusive and overlain by the Quaternary sediments of the Brahmaputra valley (Bora and Barua, 2011). The depositional landscape of the valley took its present shape during Quaternary era. Its origin and development are

linked to the history of the Himalayas in the north and the Shillong plateau in the south. The Quaternary sediments are identified by four depositional surfaces i.e. Barpeta Formation, Hauli Formation, Sorbhog Formation, and Chapar formation. The detailed geological map of the Phophonga hill area, Goalpara district, Assam is shown in Figure 2 (Poddar et al., 1979; GSI, 1984).

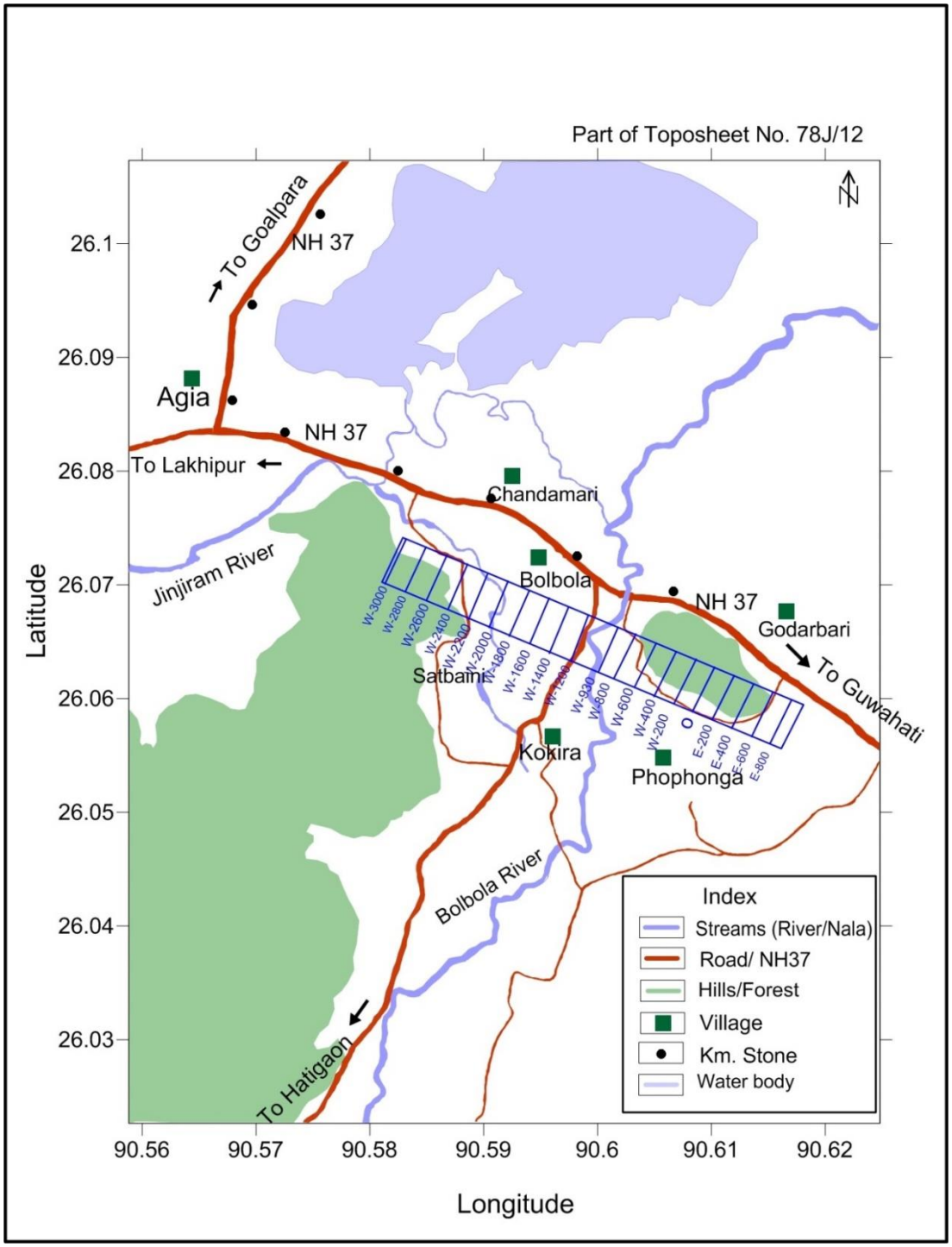

Figure 1. Location and geophysical layout map of Phophonga hill area, Goalpara district, Assam.

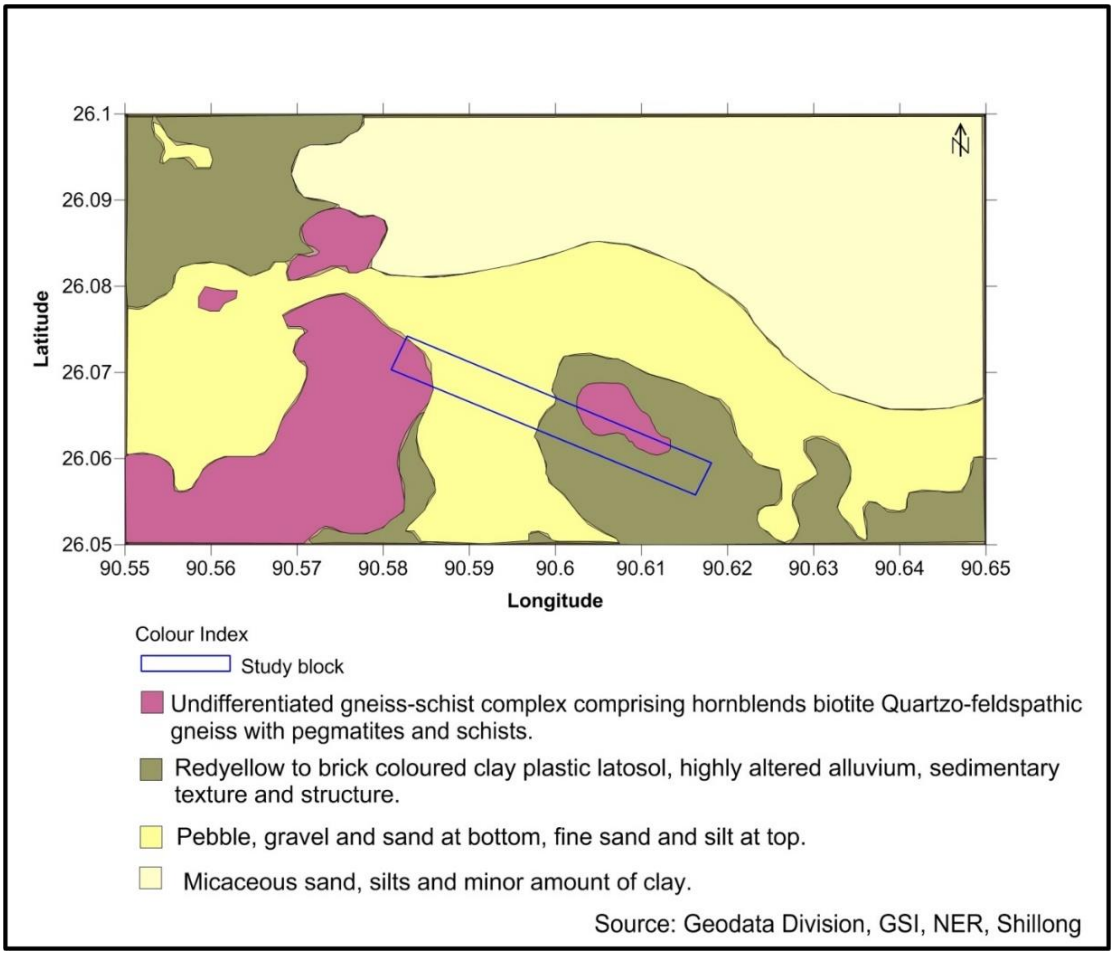

Figure 2. Geology map of Phophonga hill area, Goalpara district, Assam.

METHODOLOGY

The detailed self-potential (SP), induced polarization (IP) time domain (TD) and magnetic anomaly maps have been prepared using Geosoft and profiles by Grapher software to interpret the maps to identify the sulfide mineralization. Sulfide mineralization may have a naturally occurring negative electrical potential with respect to the surrounding country rock (Han et al., 2022; Turan-Karaoglan and Gokturkler, 2021). It is very common in pyrite, chalcopyrite, pyrrhotite, sphalerite, galena, and graphite (Abedi and Norouzi, 2012; Telford et al., 1990). The SP technique has been widely employed in geothermal exploration, cavity detection, and environmental issues in addition to sulfide mineralization (Abdelrahman et al., 2008; Upadhyay et al., 2020). The IP technique is a crucial tool for locating sulfide minerals (Irvine and Smith, 1990; Alilou et al., 2014). When using an IP approach in the time domain, the rate of IP voltage decay caused by the disconnection of induced current in the subsurface is dependent on the metallic grain size of the rock (Seigel et al., 1997; Mao et al., 2016; Srigutomo et al., 2016). The SP observations are taken at 10 m station intervals with reference to several auxiliary bases and the base correction was applied to tie up the SP readings with the master base established at the beginning of the survey work near reference point 0/0 (zero by zero) line. IP (TD) chargeability cum resistivity survey has been carried out using a dipole-dipole array with electrode separation (a) of 20 m and inter-electrode spacing n= 2 and 3. The apparent resistivity is given by the following equation

$$\rho = \pi n\,(n+1)(n+2)a\frac{\delta V}{I} \ldots\ldots\ldots\ldots\ldots\ldots\ldots\ldots (1).$$

where δV is potential difference and I is current

The observed magnetic anomaly is due to the magnetic susceptibility variation in the subsurface geological rocks (Murthy and Rao, 2001), which are recorded at all the stations along each traverse with reference to the base established in the area.

RESULTS AND DISCUSSION

Self-Potential

The Self-Potential (SP) contour map (Figure 3) shows a color display of a single grid image with the lowest value indicating deep blue colour and the highest value as red and dark pink colors. The SP values are affected by the hydraulic gradient/concentration of chemical content in the groundwater and subsurface geological variation (Buselli and Lu, 2001). The total variation in the SP values from -20 to +60 mV has been observed in the area. The SP contours are trending in NEE-SWW, N-S and E-W directions depending upon the anomaly variations. The qualitative analysis of the SP contour map reveals a feeble SP anomaly zone from traverse 0 to E400, which is more or less coincide with the shear zone. Another moderate SP anomalous zone has been observed in the northern end of the traverses 0 to W400. The change in contours pattern near traverses W600 and W2400 reflects the formational contact. The central part of the study area is occupied by soil and cultivated land which reveals positive variation in SP values (pink and red color) but has no importance from the mineralization point of view.

Magnetic

The magnetic map is prepared using Geosoft software as shown in Figure 4 by reducing the raw magnetic data and finding wide variations in the magnetic data over the present area. In order to identify various lithological formations and sulphide mineralization, the magnetic data are evaluated and categorized. According to the magnetic signatures, the study area may be separated into three magnetic domains: the southeast, the middle, and the northwest. Over the southeasterly region dropping over the Phophonga hills, the variations in magnetic response are often smooth. The northern end of the southeast section from traverses E400 to W800, displays moderate to high magnetic changes over exposed granite which may be related to ferruginous minerals in the subsurface. Over the central portion of the area, which is made up of cultivated land and soil cover, a smooth fluctuation of 100 to 200 nT has been observed. Due to the occurrence of amphibolites that include magnetite and banded magnetite quartzite (BMQ), as well as other ferruginous minerals, substantial magnetic fluctuations have been observed along the over W2600 and W3000 profiles in the northwest

.

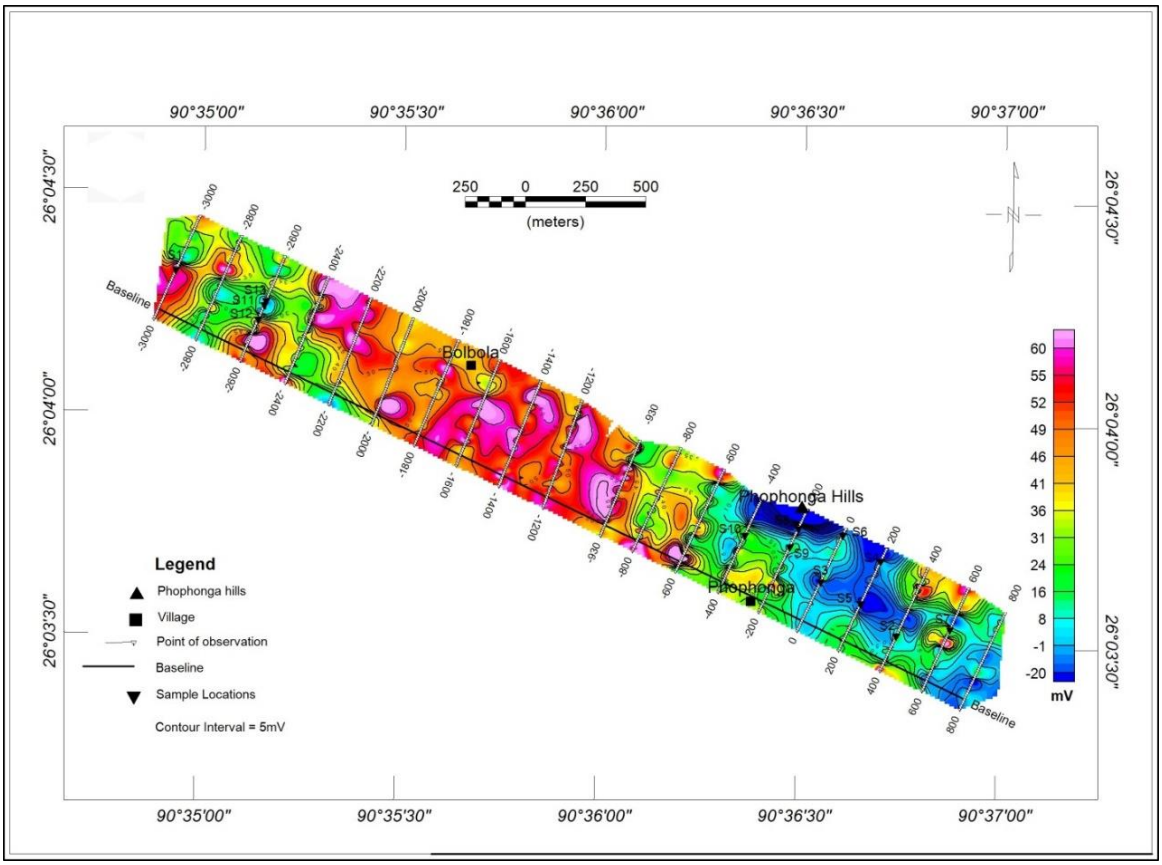

Figure 3. Self-Potential (SP) anomaly contour map over the Phophonga hill area, Goalpara district, Assam.

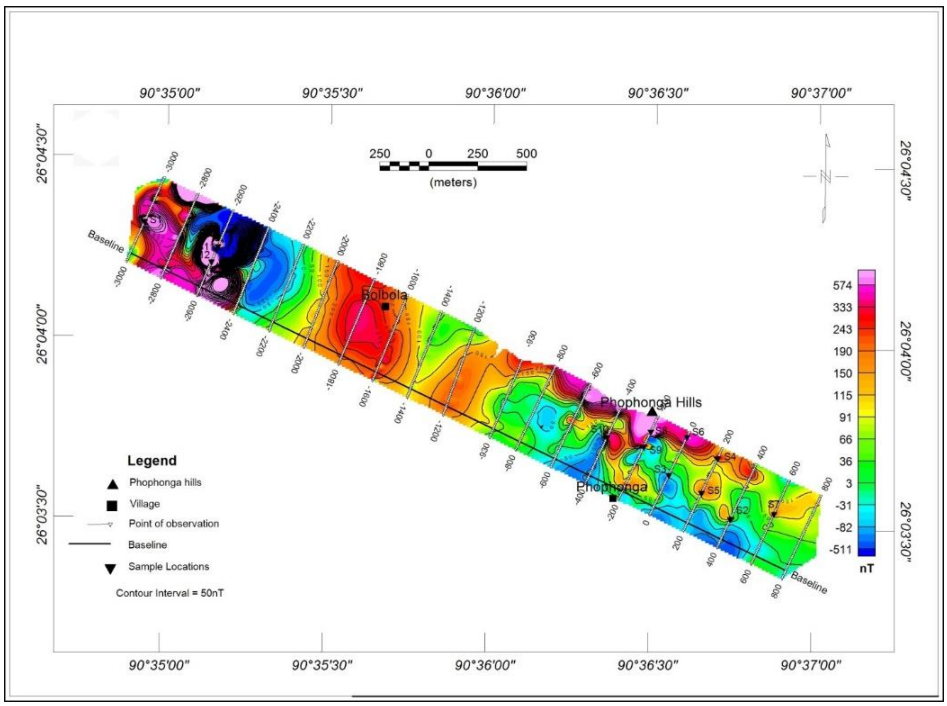

Figure 4. Magnetic (VF) anomaly contour map over the Phophonga hill area, Goalpara district, Assam.

Induced Polarization

The IP chargeability contour maps are shown in Figures 5 and 6 for dipole-dipole arrays n=2 and 3, respectively and the apparent resistivity contour maps are shown in Figures 7 and 8 for dipole-dipole arrays n=2 and 3, respectively. Both the chargeability maps for a=20 m and n=2 and 3 are showing similar responses. Three moderate to high chargeability anomaly zones have been recorded over the study area. The centers of these anomaly zones are lying near traverses 0, E200, E600, W400, W600, and W2600. These high zones are lying over high resistive formations except traverses 0, E400 and W2600. The contact of various lithologies may be easily distinguished by the resistivity maps. While the central region's resistivity is low over an area that is cultivated or covered with soil, the southeast and northwestern regions represent strong resistive zones. The contacts of two high-resistive formations with the low-resistive formation in the central part, are clearly demarcated nearby traverses W600 and W2200.

Integrated geophysical approach

Some representative geophysical profiles of the survey area comprising SP, IP (chargeability and apparent resistivity) and magnetic values are shown in Figures 9, 10 and 11, respectively. The geophysical responses along traverse 0 to E600 have reflected a feeble SP anomaly of about -30 mV, which has been recorded along traverses 0 and E200 near station N190 which is well corroborated with moderate to high chargeability and low resistivity with small magnetic variations. These responses are almost falling over the reported shear zone, may be favorable from the mineralization point of view. Over traverse E400 at station N120, a strong magnetic anomaly that is corroborated by a strong chargeability, decreasing resistivity and a feeble SP anomaly has been seen. Geophysical responses along traverses W200 to W600 are shown in Figure 10. The change in magnetic response with chargeability, resistivity, and SP along traverse W200 at station N240 exposes a contact/shear zone. The end of W200 over granite exposure has seen the occurrence of yet another broad high magnetic anomaly with broad SP low, rising chargeability and descending resistivity trends. This may be due to the presence of sulphide minerals bearing magnetite/ferruginous material below the granite formation. A similar trend has been recorded over traverses W400 and W600. The geophysical profiles W2400 to W3000 (Figure 11) lye over the northwestern side of the area. The formational contact observed near stations N160 and N200 along the traverses W2400 and W3000 respectively have been delineated by resistivity survey. A broad magnetic zone across traverse W2600 indicates a causative body that contains magnetite and has a high chargeability and low resistivity with a low SP trend. Other than a high magnetic value at the profile's northern end, there was no informative response above W2800. The rock samples from the western portion of the region were found to include banded magnetite quartzite

(BMQ), magnetite-bearing amphibolites, banded gneiss and biotite-hornblende-gneiss that had high-density values (3.3 to 3.5 gm/cc), may be the reason for the strong magnetic responses.

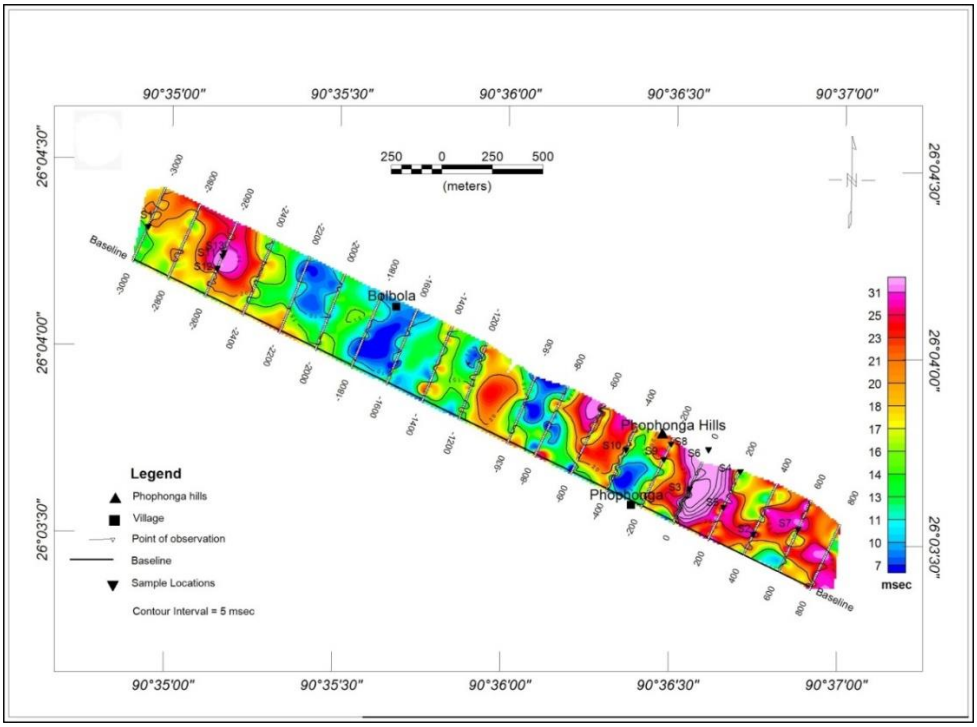

Figure 5. IP chargeability contour map (dipole-dipole array, a=20 m and n=2) over the Phophonga hill area, Goalpara district, Assam.

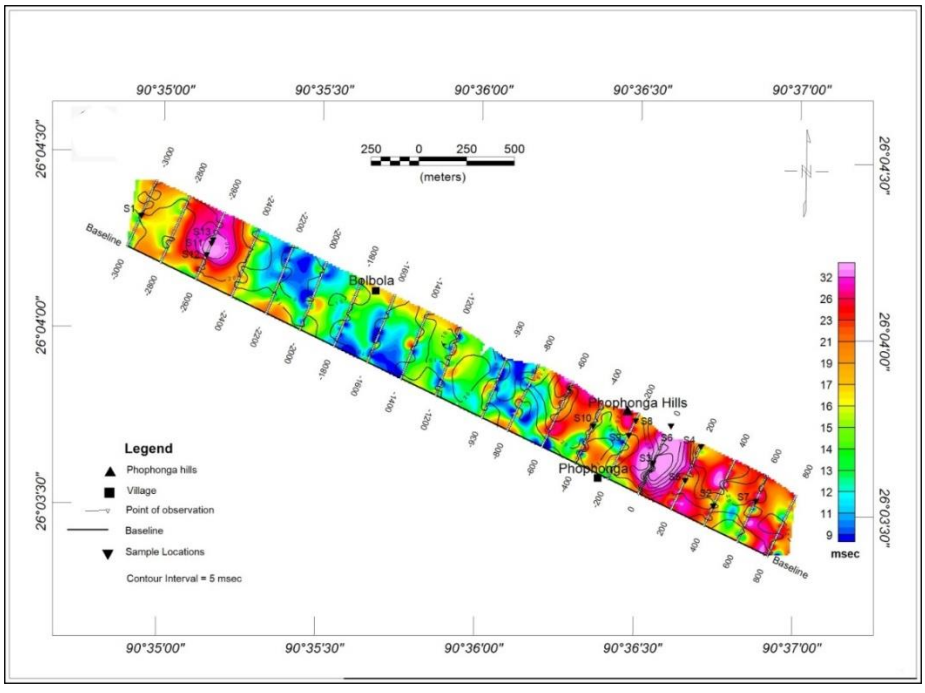

Figure 6. IP chargeability contour map (dipole-dipole array, a=20 m and n=3) over the Phophonga hill area, Goalpara district, Assam.

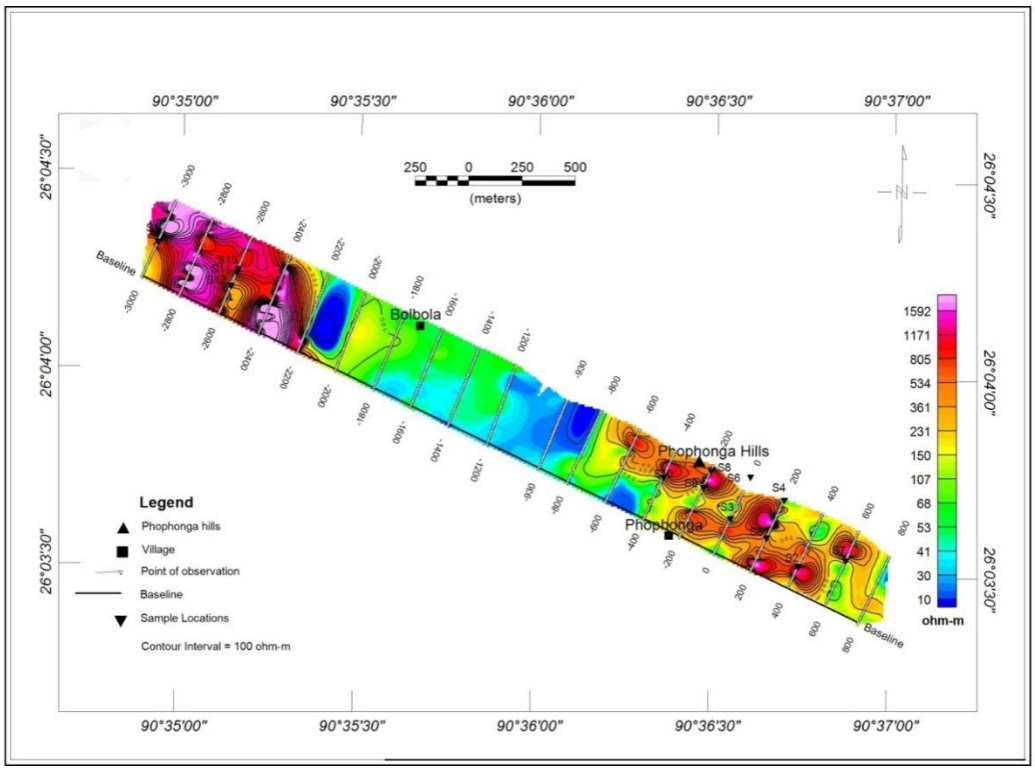

Figure 7. Apparent resistivity contour map (dipole-dipole array, a=20 m and n=2) over the Phophonga hill area, Goalpara district, Assam.

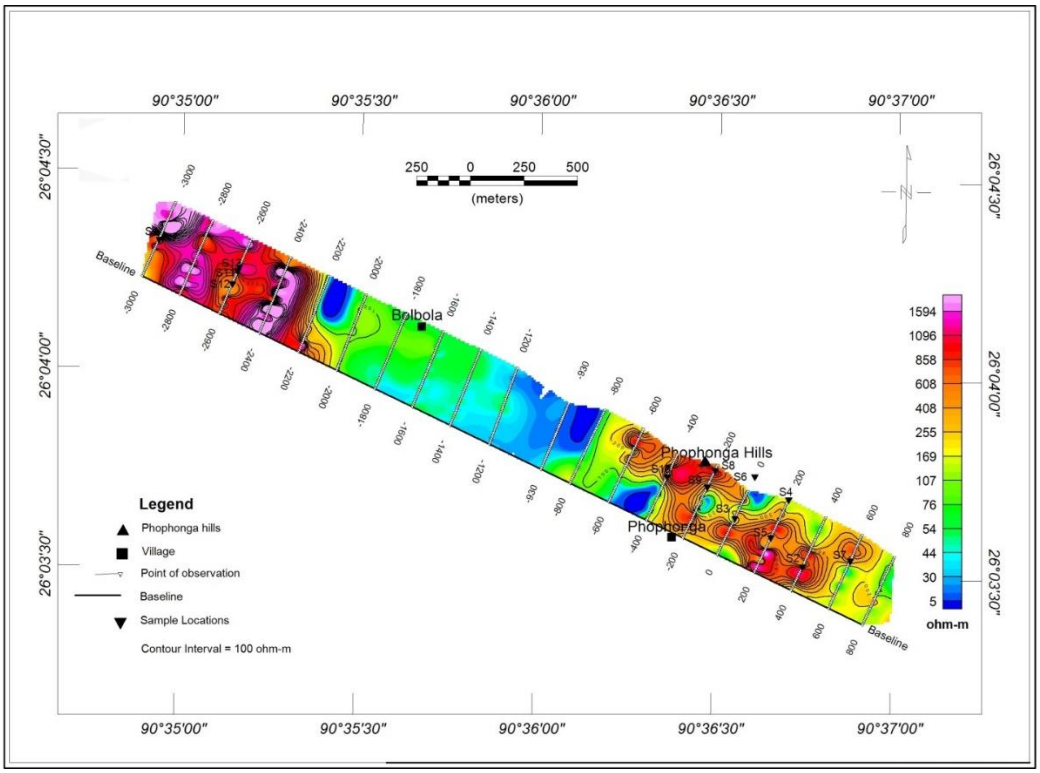

Figure 8. Apparent resistivity contour map (dipole-dipole array, a=20 m and n=3) over the, Phophonga hill area, Goalpara district, Assam

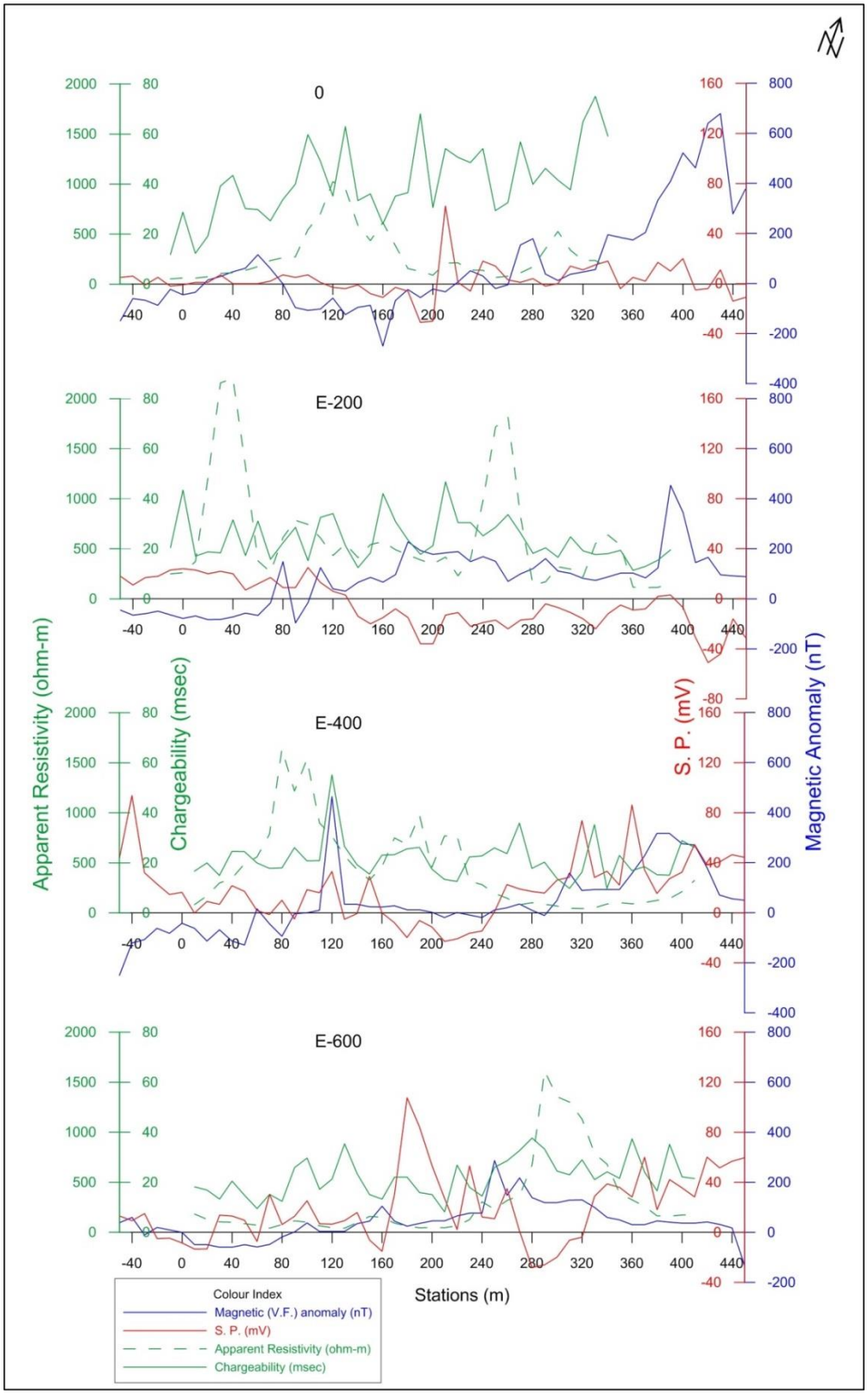

Figure 9. SP, IP (chargeability and apparent resistivity) and magnetic profile lines (0, E-200, E-400, and E-600) over the Phophonga hill area, Goalpara district, Assam.

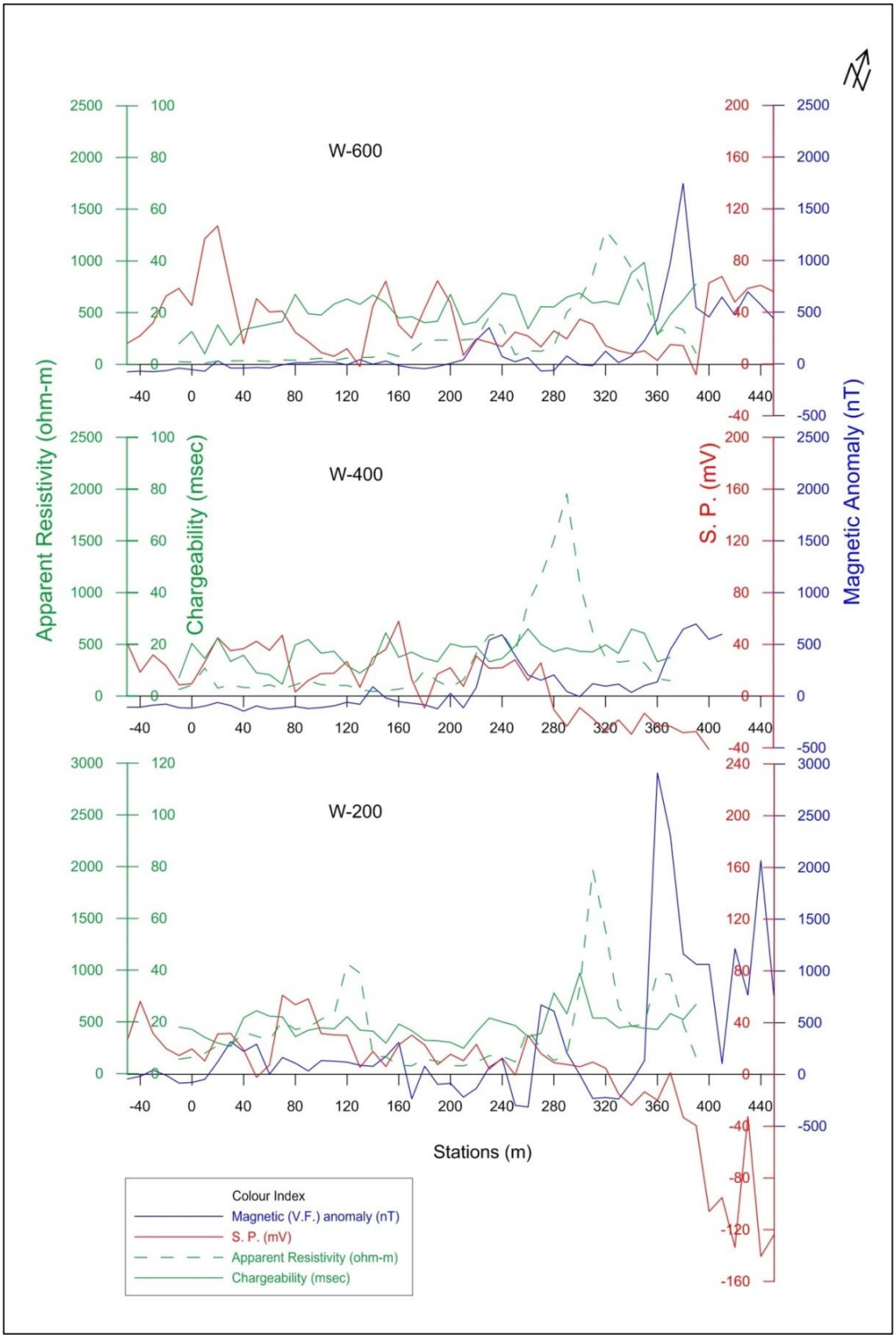

Figure 10. SP, IP (chargeability and apparent resistivity) and magnetic profile lines (W-200, W-400, and W-600) over the Phophonga hill area, Goalpara district, Assam.

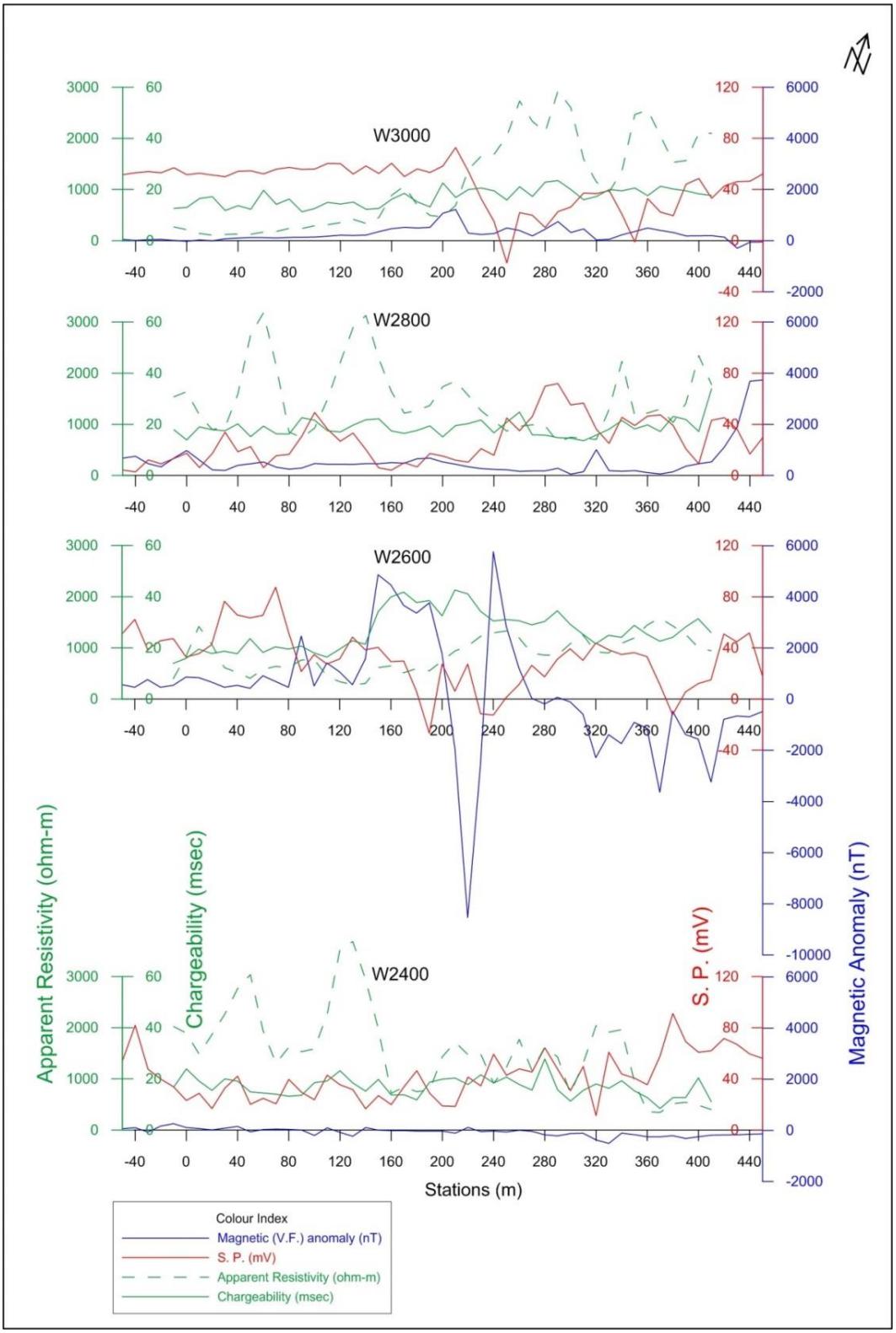

Figure 11. SP, IP (chargeability and apparent resistivity) and magnetic profile lines (W-2400, W-2600, W-2800, and W-3000) over the Phophonga hill area, Goalpara district, Assam.

CONCLUSION

The following conclusions have been drawn from the present study:

(i) Geophysical studies have identified the lithological connections between exposed strata in the northwest and southeast and soil/cultivated land in the center.

(ii) Few feeble SP anomalous zones of limited areal extent have been delineated, which are also supported by isolated moderate to high chargeability anomalies with decreasing trends of resistivity and magnetic responses.

(iii) Some geophysical anomalies have been recorded over W200/N240, 0/N190, E200/N190 and E400/N120. These anomalous zones have been recommended for drilling to verify the nature of the causative body. Integration of geophysical and geological investigation suggests the area near profile lines 0, E-200, and W-200 may be important for lead and zinc mineralization.

(iv) Another broad high magnetic anomaly with broad SP low, rising trend of chargeability and decreasing trend of resistivity has been recorded at the end of W200 over granite exposure. The anomaly may be due to the magnetite-bearing sulphide mineralization in the subsurface below the granite exposure. Since the anomaly is open, it is therefore recommended to trace out the lateral as well as the subsurface extension of the anomalous body.

(v) A broad magnetic zone with high chargeability and supporting low resistivity with a low SP trend over traverse W2600 reveals magnetite bearing causative body.

ACKNOWLEDGEMENTS

The authors are thankful to the reviewers for their valuable suggestions that significantly improve the quality of the manuscript. The authors express their sincere thanks to the then ADG & HOD, Shri Amarjeet Singh, DDG M-II, Shri S. Y. Katti G.S.I, NER, Shillong and Shri S. N. Meshram, DDG SU: Assam for providing the logistic and administrative support. The authors sincerely thank Shri Narendra Singh, the then Director (GP), Dr. N. B. Singha and Shri S. P. Bhutia, the then Senior Geologists, State Unit: Assam, Guwahati for technical discussions.

Compliance with Ethical Standards

The authors declare no conflict of interest and adhere to copyright norms.

REFERENCES

Abdelrahman, E.M., Essa, K.S., Abo-Ezz, E.R., Sultan, M., Sauck, W.A. and Gharieb, A.G., 2008. New least-squares algorithm for model parameters estimation using self-potential anomalies. Comp. Geosci., 34, 1569–1576.

Abedi, M. and Norouzi, G., 2012. Integration of various geophysical data with geological and geochemical data to determine additional drilling for copper exploration. J. Appl. Geophy., 83, 35–45.

Alilou, S.K, Norouzi, G.H., Doulati, F. and Abedi M., 2014. Application of Magnetometery, Electrical Resistivity and Induced Polarization for Exploration of Polymetal Deposits, A Case Study: Halab Dandi, Zanjan, Iran. 2nd Intl' Conference on Advances in Engineering Sciences and Applied Mathematics, May 4-5, 2014 Istanbul (Turkey).

Baruah, S. and Hazarika, D., 2008. A GIS based tectonic map of north-eastern India. Curr. Sci., 95(2), 176–177.

Bhadra, B.K., Jain A.K., Karunakar, G., Meena, H., Rehpade, S.B. and Rao S.S., 2021. Integrated remote sensing and geophysical techniques for shallow base metal deposits (Zn, Pb, Cu) below the gossan zone at Kalabar, Western Aravalli Belt, India. J. Appl. Geophys., 191, 104365.

Bhagabaty, B., Mazumdar, M.K., Mazumdar, A.C. and Borah, P., 2017. Geochemical Characteristics of Tukureswari and Barbhita Granitoid in Goalpara District, Assam. J. Geol. Soc. India, 89, 532–540.

Bora, A.K., Singha, N.B. Th. and Singh, M.S., 2014. Final report on Preliminary Investigation for REE in southern part of Agia around Sujukona Hill in parts of Goalpara district, Assam. GSI unpublished report.

Bora, A.K. and Baruah, B., 2011. Interim report on National Geochemical Mapping in parts of Goalpara and Bongaigaon districts, Assam Toposheet no. 78J/12. GSI unpublished report.

Buselli, G. and Lu, K., 2001. Groundwater contamination monitoring with multichannel electrical and electromagnetic methods. J. Appl. Geophys., 48, 11–23.

Evrard, M., Dumont, G., Hermans, Th., Chouteau, M., Francis, O., Pirard, E. and Nguyen, F., 2018. Geophysical Investigation of the Pb–Zn Deposit of Lontzen–Poppelsberg, Belgium. Minerals, 8, 233, MDPI, Basel, Switzerland.

GSI, 1984. Geological Survey of India, 1: 50, 000 Geological map series of Toposheet no. 78J/12.

Gupta, B.C., 1934. The Geology of Central Mewar. Mem. Geol. Soc. India, 65, 107–168.

Han Z., Kang X., Wu. and Shi X., 2022. Characterization of the non-Gaussian hydraulic conductivity field via deep learning-based inversion of hydraulic-head and self-potential data. J. Hydrology, 610, 127830.

Imam, N., Sahu, M. and Singh, C., 2014. Exploration and mining trend of lead and zinc, Rajpura-Dariba, Rajasthan, India. Int. J. Technical Res. Appl., 2(2), 40–41.

Irvine, R.J. and Smith, M.J., 1990. Geophysical exploration for epithermal gold deposits. J. Geochem. Expl., 36, 375–412.

Kumar, A., Murmu, C., Vemula, R., Shankar, U. and Majumdar, N., 2022. Delineation of subsurface geological structures in parts of Bongaigaon, Kokrajhar and Dhubri districts of Assam by gravity and magnetic methods. J. Ind. Geophys. Union, 26(2), 78–93.

Mao, D., Revil, A. and Hinto J., 2016. Induced polarization response of porous media with metallic particles-Part 4: Detection of metallic and nonmetallic targets in time-

domain induced polarization tomography. Geophysics, 81(4), d359–d375.

Murthy, I.V. R. and Rama Rao, P., 2001. Magnetic Anomalies and Basement Structure Around Vizianagaram, Visakhapatnam and Srikakulam Districts of Andhra Pradesh, India. Gondwana Res., 4(3), 443–454.

Poddar, B.C., Chakrabarti, C., Duara, B.K., Chakravarti, P. and Banerjee, S.N., 1979. A Preliminary Geological appraisal of parts of Ganga-Brahmaputra basin, Brahmaputra Basin Studies Unit, GSI unpublished report.

Seigel, H.O., Vanhala, H. and Sheard S.N., 1997. Some case histories of source discrimination using time-domain spectral IP. Geophysics, 62(5), 1394–1408.

Srigutomo, W., Trimadona, and Pratomo, P.M., 2016. 2D Resistivity and Induced Polarization Measurement for Manganese Ore Exploration. J. Phys., Conference Series 739, 012138.

Telford, W.M., Geldart, L.P. and Sheriff, R.E., 1990. Applied Geophysics. Second Edition, Cambridge University Press.

Turan-Karaoglan, S. and Gokturkler, G., 2021. Search Algorithm for model parameter estimation from self-potential data. J. Appl. Geophys., 194, 104461.

Upadhyay, A, Singh, Panda, K.P. and Sharma, S.P., 2020. Delineation of gold mineralization near Lawa village, North Singhbhum Mobile Belt, India, using electrical resistivity imaging, self-potential and very low frequency methods. J. Appl. Geophys., 172, 103902.

Received on: 29.11.2023; Revised on: 21.02.2023; Accepted on: 27.03.2023

J. Ind. Geophys. Union, 27(2) (2023), 96-108

Effects of artificial boundaries on SH-waves propagation in a Weiskopf type anisotropic liquid-filled porous medium

Vijay Kumar Kalyani*, Kajal Naik, Prashant Malavadkar and Shubhalaxmi Joshi
School of mathematics and statistics, Dr. Vishwanath Karad MIT-World Peace University,
Pune, Maharashtra-411038, India.
*Corresponding author: vijaykumar.kalyani@mitwpu.edu.in

ABSTRACT

Reported in the present paper are the results of the study of SH-waves propagation in a Weiskopf-type anisotropic porous medium. The finite difference method has been applied with artificial absorbing and reflecting boundaries to model the wave propagation and to study the reflections at the boundaries. Stability criteria have also been developed to make the finite difference scheme convergent and stable. Numerical values of the reflection coefficients are calculated at the left and right boundaries for different values of angle of incidence, anisotropic parameter and porosity parameter. A source term is considered to generate a wave field in the medium. Two-dimensional SH-waves profiles are generated and are depicted graphically to study the absorbing capabilities of the non-reflecting boundaries at different propagation times.

Keywords: Finite difference method, SH-Waves propagation, Artificial boundaries, Anisotropic liquid-filled porous medium, Earthquakes

INTRODUCTION

Earthquakes occur due to the movement and collision of tectonic plates inside the earth which generate two types of seismic waves. The first which travels through the earth's inner layers are body waves and the second surface waves move through the earth's crust. These surface waves, which propagate through the earth's crust, are mostly responsible for the damage and destruction during earthquakes. The geological structure of earth's surface may be presumed as a liquid-saturated anisotropic porous medium. Biot (1956) in his well-known work presented the idea of seismic wave propagation in an anisotropic porous media. Based on the theory of Biot (1956), the problems of wave propagation in porous media in different structures have been discussed by several authors, including Deresiewicz (1961), Bose (1962), Chakraborty and Dey (1982), Chattopadhyay and De (1983), Kalyani and Kar (1986) and others.

Many authors have developed various techniques to study seismic wave propagation in different media. Among them, the finite difference methods are mostly used because these methods are stable and converge to the exact solution rapidly. During the earthquakes, seismic waves are generated and propagate through an infinite medium. In the implementation of finite difference methods, computation is limited to a finite domain only, as it is restricted by artificial boundaries. Reynolds (1978) in his well-known research work showed that Dirichlet and Neumann boundary conditions cause reflection of the waves from the boundaries. Whereas, in the actual phenomenon, seismic waves propagate through these boundaries without reflection. To reduce edge reflections at the boundaries, the author implemented absorbing boundary conditions by factorizing second-order differential operators into first-order differential operators and showed a considerable reduction in edge reflection using synthetic seismograms. In related work, Zhang et. al. (1993) discussed the effects of absorbing boundary conditions near a free surface and at the corners of the computational domain in a 2D transversely isotropic (TI) medium by factorizing a second-order differential operator. Clayton and Engquist (1977) implemented absorbing boundary conditions with a finite difference method successfully for waves travelling with an incident angle less than 45^0. Based on this concept, Keys (1985), Cerjan et al. (1985), Sochacki et al. (1987) and Burns (1992) suggested an improved absorbing boundary condition by extending the computational domain. Further, Grote and Keller (2000) implemented absorbing boundary conditions for the time-dependent elastic wave equation in three dimensions using a finite difference scheme showing the superiority of their method over other existing finite difference methods.

Alpert et al. (2002) described a new approach to study scalar wave equations wherein they used non-reflecting boundary conditions. Comparing their numerical results with the various existing methods, they revealed that their proposed methods achieved superiority in terms of accuracy. Peng and Toksoz (1994) used a finite difference method to model 2D and 3D acoustic and elastic wave propagation by developing optimal absorbing boundary conditions. Tsynkov (2003) in his work numerically simulated time-dependent acoustic waves for unbounded unobstructed space implemented for non-local artificial boundary conditions. Further, Ju and Wang (2001), applied the concept of Higdon's one-way first-order boundary operator, to model unbounded elastic wave problems using a time-dependent absorbing boundary condition. Givoli and Neta (2003) proposed a high-order non-reflecting boundary condition for time-dependent wave problems in an unbounded domain. Hagstrom et al. (2008) improved and extended high-order local absorbing boundary conditions for two-dimensional waveguides. Hall and Wang

(2009) discussed both reflecting and absorbing boundary conditions in two-dimensional models of heterogeneous, anisotropic and fractured media. Burgos and Santos (2016) presented a finite element technique based on Deslauriers-Dubuc interpolating scaling functions for simulation and analysis of wave propagation. Results obtained by them are successfully validated by comparing with the standard Finite Difference Method. Alam et al. (2021), in their paper, used a finite difference scheme to model time-dependent wave propagation based on absorbing and reflecting boundaries to demonstrate the boundary effects and absorption of spurious reflection boundaries.

Until now, the finite difference technique has been successfully used to analyse the propagation of seismic waves in different media of the earth's interior. However, so far author's knowledge, no work has been done on finite difference modelling of seismic wave propagation in Weiskopf type anisotropic porous media, having absorbing boundary conditions. Studies of such a problem will help to understand and interpret the effects of absorbing boundary conditions on the finite difference modelling of seismic wave propagation in Weiskopf-type anisotropic porous medium. This encouraged us to develop finite difference modelling of SH-waves propagation in a Weiskopf-type anisotropic porous media with absorbing and reflecting artificial boundaries to evaluate the edge reflection at the boundaries. Furthermore, the results obtained with absorbing boundaries are compared with the reflecting boundary condition for different values of anisotropy and porosity parameters of the medium. Also, the reflection coefficients have been developed and plotted with respect to the angle of incidence of the SH waves for different values of porosity and anisotropic parameters. We have also developed the stability criteria for the finite difference method to minimize the exponential growth of the error by finding the valid range of the parameters. The stability criteria ensure a feasible solution for the system representing the propagation of seismic waves in a Weiskopf-type anisotropic porous medium with absorbing boundary conditions.

PROBLEM FORMULATION IN AN ANISOTROPIC POROUS MEDIA

A two-dimensional liquid-filled anisotropic porous medium of the earth is considered with an x-axis along the horizontal at the free surface of the earth, a y-axis normal to the plane and a z-axis directed vertically downwards as shown in Figure 1. A source "S" of SH waves at a depth "d" from the free surface is considered in the half-space to generate the wave field.

Equations of the motion in a liquid-filled porous medium are given by Biot (1956) as

$$\frac{\partial \tau_{xx}}{\partial x} + \frac{\partial \tau_{xy}}{\partial x} + \frac{\partial \tau_{xz}}{\partial x} = \frac{\partial^2}{\partial t^2}(\rho_{11}\, u_x + \rho_{12}\, U_x)$$

$$\frac{\partial T}{\partial x} = \frac{\partial^2}{\partial t^2}(\rho_{11}\, u_x + \rho_{12}\, U_x)$$

where $\tau_{xx}, \tau_{xy}, \ldots$ are the stress tensor components. The pressure p of the fluid and the force T applied by the fluid on the fraction of an area of the unit cross-section of the aggregate is related to β, the measure of the porosity by

$$-\mathrm{T} = \beta \mathrm{p}.$$

The mass coefficients $\rho_{11}, \rho_{12}, \rho_{22}$ associated with a mass of solid $\rho(s)$ and mass of the liquid $\rho(f)$, each measured per unit volume of the aggregate, are related by:

$$\rho(s) = \rho_{11} + \rho_{12} \quad \text{and} \quad \rho(f) = \rho_{12} + \rho_{22}$$

satisfying

$$\rho_{11} > 0,\ \rho_{22} > 0,\ \rho_{12} < 0$$

$$\rho_{11}\ \rho_{22} - \rho_{12}^{\ 2} > 0$$

Also, if ρ_s and ρ_f represent mass densities of solid and liquid respectively, then as per Biot (1956)

$$\rho(s) = (1-\beta)\rho_s \quad and \quad \rho(f) = (\beta)\rho_f .$$

Further, the mass density of the aggregate ρ in terms of mass coefficients $\rho_{11}, \rho_{12}, \rho_{22}$ is given by

$$\rho = \rho_{11} + 2\rho_{12} + \rho_{22} .$$

Using the theory of Biot (1956) and Weiskopf (1945), the stress-strain relations for the liquid filled Weiskopf type anisotropic porous medium can be expressed as:

$$\left.\begin{aligned} \tau_{xx} &= 2Ne_{xx} + Ae + Q\,\Theta \\ \tau_{yy} &= 2Ne_{yy} + Ae + Q\,\Theta \\ \tau_{zz} &= 2Ne_{zz} + Ae + Q\,\Theta \\ \tau_{xy} &= Ne_{xy} \\ \tau_{yz} &= Ge_{yz} \\ \tau_{zx} &= Ge_{zx}\ and\ \mathrm{T} = \mathrm{Q\,e} + \mathrm{R}\,\theta \end{aligned}\right\} \quad \ldots(1)$$

where $e = Div\,\bar{u}$ and $\theta = Div\bar{U}$ and A, N are Lame coefficients. (u_x, u_y, u_z) and (U_x, U_y, U_z) represent displacement component vectors of the solid and the liquid respectively. The coefficient R represents pressure on the liquid keeping total volume constant, wherein, the coefficient Q measures the coupling between the volume change of the solid and that of liquid.

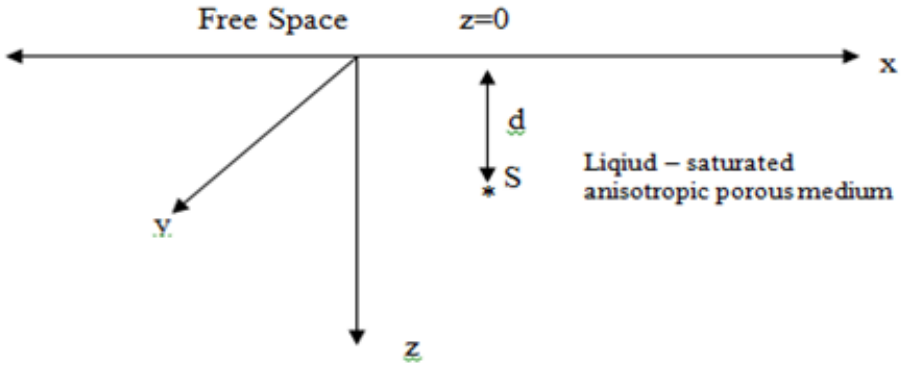

Figure 1. Geometry of the problem

For a SH waves propagating in x-direction and causing displacement in the y-direction only, we have

$$u = w = 0 \; and \; v = v(x, z, t).$$

In the absence of body forces, equation of motion for the propagation of SH-waves parallel to x-axis in a liquid-filled porous medium having Weiskopf type anisotropy, is given by Kar and Kalyani (1986, 1989)

$$\mathrm{N}\frac{\partial^2 \mathrm{v}}{\partial \mathrm{x}^2} + \mathrm{G}\frac{\partial^2 \mathrm{v}}{\partial \mathrm{z}^2} = \mathrm{d}\frac{\partial^2 \mathrm{v}}{\partial \mathrm{t}^2}, \qquad \ldots(2)$$

where N and G are shear moduli and

$$d = \rho_{11} - \frac{\rho_{12}^{\ 2}}{\rho_{22}}. \qquad \ldots(3)$$

FINITE DIFFERENCE METHODOLOGY

The finite difference methods are important and effective techniques in finding solutions of wide varieties of problems related to engineering and science. Most of these problems reduces to linear, non-linear, anisotropic, non-homogeneous and time dependent with different types of boundary conditions. The exact solution of differential equations in these classes may not always exist. Most of the authors are using various finite-difference methods to solve differential equations by approximating derivatives with finite differences.

For the development of a finite-difference model, we subdivide xz-plane in to a finite number of rectangles with uniform increments $\Delta x, \Delta z$ along the x, z axes respectively and increment in time is Δt. Assuming $v(x, z, t)$ be approximate solution of equation (2) at a finite set of $x, z \; and \; t$ with the notation

$$v_{i,j}^{k} = v\left(x_i, z_j, t_k\right), \qquad \ldots (4)$$

the two-dimensional wave equation (2) with source term (f) can be discretized as

$$d\left(\frac{v_{i,j}^{k+1} - 2v_{i,j}^{k} + v_{i,j}^{k-1}}{\Delta t^2}\right) = N\left(\frac{v_{i+1,j}^{k} - 2v_{i,j}^{k} + v_{i-1,j}^{k}}{\Delta x^2}\right) + G\left(\frac{v_{i,j+1}^{k} - 2v_{i,j}^{k} + v_{i,j-1}^{k}}{\Delta z^2}\right) + \mathrm{f} \qquad \ldots(5)$$

Assuming $\Delta x = \Delta z$ for constant mesh spacing, the numerical scheme (5) can be reduced to

$$\mathrm{v}_{\mathrm{i,j}}^{\mathrm{k+1}} = 2\mathrm{v}_{\mathrm{i,j}}^{\mathrm{k}} - \mathrm{v}_{\mathrm{i,j}}^{\mathrm{k-1}} + \left(\frac{\mathrm{c}\Delta \mathrm{t}}{\Delta \mathrm{x}}\right)^2 \left[\left(\mathrm{v}_{\mathrm{i+1,j}}^{\mathrm{k}} - 2\mathrm{v}_{\mathrm{i,j}}^{\mathrm{k}} + \mathrm{v}_{\mathrm{i-1,j}}^{\mathrm{k}}\right) + \frac{\mathrm{G}}{\mathrm{N}}\left(\mathrm{v}_{\mathrm{i,j+1}}^{\mathrm{k}} - 2\mathrm{v}_{\mathrm{i,j}}^{\mathrm{k}} + \mathrm{v}_{\mathrm{i,j-1}}^{\mathrm{k}}\right)\right] + \mathrm{f}_{\mathrm{i}}^{\mathrm{n}} \left(\frac{\Delta \mathrm{t}^2}{\mathrm{d}}\right),$$

which gives,

$$\mathrm{v}_{\mathrm{i,j}}^{\mathrm{k+1}} = 2\mathrm{v}_{\mathrm{i,j}}^{\mathrm{k}} - \mathrm{v}_{\mathrm{i,j}}^{\mathrm{k-1}} + (\mathrm{CFL})^2\left[\left(\mathrm{v}_{\mathrm{i+1,j}}^{\mathrm{k}} - 2\mathrm{v}_{\mathrm{i,j}}^{\mathrm{k}} + \mathrm{v}_{\mathrm{i-1,j}}^{\mathrm{k}}\right) + \frac{\mathrm{G}}{\mathrm{N}}\left(\mathrm{v}_{\mathrm{i,j+1}}^{\mathrm{k}} - 2\,\mathrm{v}_{\mathrm{i,j}}^{\mathrm{k}} + \mathrm{v}_{\mathrm{i,j-1}}^{\mathrm{k}}\right)\right] + \mathrm{f}_{\mathrm{i}}^{\mathrm{n}} \left(\frac{\Delta \mathrm{t}^2}{\mathrm{d}}\right), \qquad \ldots (6)$$

where, $\mathrm{CFL} = \frac{\mathrm{c}\,\Delta t}{\Delta x}$ and

$$c^2 = \frac{N}{d} = \frac{\mathrm{N}}{\rho_{11} - \frac{\rho_{12}^{\ 2}}{\rho_{22}}} = \frac{\mathrm{N}}{\rho}\,\frac{\Upsilon_{22}}{\Upsilon_{11}\Upsilon_{22} - \Upsilon_{12}^2} = \frac{\mathrm{N}}{\rho}\,\Upsilon$$

in which $\Upsilon_{ij} = \frac{\rho_{ij}}{\rho}$, where ρ measures the total mass of the fluid-solid aggregate per unit volume and $\Upsilon = \frac{\Upsilon_{22}}{\Upsilon_{11}\Upsilon_{22} - \Upsilon_{12}^2}$ is the dynamical parameter of the fluid-solid aggregate depends on porosity and density of the fluid.

STABILITY ANALYSIS

For the finite difference modelling of seismic waves propagation in time domain, the finite difference scheme must satisfy stability condition. The approximate solution obtained by using finite difference scheme should be bounded and converge to exact solution as time progresses. Alford et al. (1974) developed implicit finite difference method and obtained very accurate solution for elastic wave equation. Holberg (1987) discussed stability criteria for 3-D scalar wave equation. Cao and Greenhalgh (1998) studied 2.5-D finite difference scheme for simulation of seismic wave propagation and revealed that stability criteria and boundary conditions of 2-D finite difference methods are not enough for 2.5-D scheme. In equation (6) the finite difference scheme developed for the analysis of seismic waves in an anisotropic porous medium will be stable if

$$\left(2(1-\mathrm{CFL}^2-\frac{\mathrm{G}}{\mathrm{N}}\,\mathrm{CFL}^2)\right)\geq 0$$

which gives, $\mathrm{CFL}\leq\pm\frac{1}{\sqrt{1+\frac{\mathrm{G}}{\mathrm{N}}}}$

Neglecting negative value of CFL, the finite difference scheme (6) will be stable, if

$$\mathrm{CFL}\leq\frac{1}{\sqrt{1+\frac{\mathrm{G}}{\mathrm{N}}}}$$

BOUNDARY CONDITIONS

In the present study, a two-dimensional finite plane in the form of square represented by $\Omega=[-L,L]\times[-L,L]$ is assumed for numerical study. The objective is to determine the displacement v that satisfies some boundary conditions on the boundary of the domain. Here, we consider two types of boundary conditions to investigate the seismic wave behaviour in an anisotropic liquid filled porous medium. First, the Dirichlet boundary condition represented by

$$\mathrm{v}(0,\mathrm{z},\mathrm{t})=0,\ \mathrm{v}(\mathrm{L_x},\mathrm{z},\mathrm{t})=0\ \text{and}\ \ \mathrm{v}(\mathrm{x},0,\mathrm{t})=0,\ \mathrm{v}(\mathrm{x},\mathrm{L_z},\mathrm{t})=0 \qquad \ldots (7)$$

is used to formulate the model. In general, the seismic wave propagates in an infinite media.

However, implementation of these Dirichlet boundary conditions with finite difference method to solve seismic wave propagation, produces reflection of the waves at the boundaries. Secondly, to reduce reflections at the boundaries, we have used absorbing boundary conditions developed by Mur (1981), and are given by:

$$\left.\begin{aligned}
\frac{\partial \mathrm{v}}{\partial \mathrm{t}}|_{\mathrm{x}=0}&=\mathrm{c}\frac{\partial \mathrm{v}}{\partial \mathrm{x}}|_{\mathrm{x}=0};\ \frac{\partial \mathrm{v}}{\partial \mathrm{t}}|_{\mathrm{x}=\mathrm{L_x}}=-\mathrm{c}\frac{\partial \mathrm{v}}{\partial \mathrm{x}}|_{\mathrm{x}=\mathrm{L_x}}\\
\frac{\partial \mathrm{v}}{\partial \mathrm{t}}|_{\mathrm{z}=0}&=\sqrt{\frac{\mathrm{G}}{\mathrm{N}}}\,\mathrm{c}\frac{\partial \mathrm{v}}{\partial \mathrm{z}}|_{\mathrm{z}=0}\\
\frac{\partial \mathrm{v}}{\partial \mathrm{t}}|_{\mathrm{z}=\mathrm{L_z}}&=-\sqrt{\frac{\mathrm{G}}{\mathrm{N}}}\,\mathrm{c}\,\frac{\partial \mathrm{v}}{\partial \mathrm{z}}|_{\mathrm{z}=\mathrm{L_z}}
\end{aligned}\right\}\ \ldots (8)$$

where, $\mathrm{c}=\sqrt{\frac{\mathrm{N}}{\mathrm{d}}}$.

To discretise the above absorbing conditions, both derivatives are approximated by averaging the derivatives at two different locations and are evaluated at the point $(x_n-\frac{\Delta x}{2},t_m-\frac{\Delta t}{2})$, we obtain

$$\left.\begin{aligned}
\mathrm{v}_{\mathrm{i,j}}^{\mathrm{k+1}}&=\mathrm{v}_{\mathrm{i+1,j}}^{\mathrm{k}}+\left(\frac{\mathrm{CFL}-1}{\mathrm{CFL}+1}\right)(\mathrm{v}_{\mathrm{i+1,j}}^{\mathrm{k+1}}-v_{i,j}^{k})\\
\mathrm{v}_{\mathrm{i,j}}^{\mathrm{k+1}}&=\mathrm{v}_{\mathrm{i-1,j}}^{\mathrm{k}}+\left(\frac{\mathrm{CFL}-1}{\mathrm{CFL}+1}\right)(\mathrm{v}_{\mathrm{i-1,j}}^{\mathrm{k+1}}-\mathrm{v}_{\mathrm{i,j}}^{\mathrm{k}})\\
\mathrm{v}_{\mathrm{i,j}}^{\mathrm{k+1}}&=\mathrm{v}_{\mathrm{i,j+1}}^{\mathrm{k}}+\left(\frac{\mathrm{CFL}\sqrt{\frac{\mathrm{G}}{\mathrm{N}}}-1}{\mathrm{CFL}\sqrt{\frac{\mathrm{G}}{\mathrm{N}}}+1}\right)(\mathrm{v}_{\mathrm{i,j+1}}^{\mathrm{k+1}}-\mathrm{v}_{\mathrm{i,j}}^{\mathrm{k}})\\
\mathrm{v}_{\mathrm{i,j}}^{\mathrm{k+1}}&=\mathrm{v}_{\mathrm{i,j-1}}^{\mathrm{k}}+\left(\frac{\mathrm{CFL}\sqrt{\frac{\mathrm{G}}{\mathrm{N}}}-1}{\mathrm{CFL}\sqrt{\frac{\mathrm{G}}{\mathrm{N}}}+1}\right)(\mathrm{v}_{\mathrm{i,j-1}}^{\mathrm{k+1}}-\mathrm{v}_{\mathrm{i,j}}^{\mathrm{k}})
\end{aligned}\right\}\ \ldots (9)$$

REFLECTION COEFFICIENTS

The existing two-dimensional dynamical equation (2) of the motion for the propagation of SH waves in a liquid-filled porous medium having Weiskopf type anisotropy, can be factorised as,

$$\frac{\partial^2\mathrm{v}}{\partial \mathrm{t}^2}-\frac{\mathrm{N}}{\mathrm{d}}\frac{\partial^2\mathrm{v}}{\partial \mathrm{x}^2}-\frac{\mathrm{G}}{\mathrm{d}}\frac{\partial^2\mathrm{v}}{\partial \mathrm{z}^2}=\left(\frac{\partial}{\partial \mathrm{t}}-\sqrt{\frac{\mathrm{N}}{\mathrm{d}}}\left(\frac{\partial^2}{\partial \mathrm{x}^2}+\frac{\mathrm{G}}{\mathrm{N}}\frac{\partial^2}{\partial \mathrm{z}^2}\right)^{\frac{1}{2}}\right)\cdot\left(\frac{\partial}{\partial \mathrm{t}}+\sqrt{\frac{\mathrm{N}}{\mathrm{d}}}\left(\frac{\partial^2}{\partial \mathrm{x}^2}+\frac{\mathrm{G}}{\mathrm{N}}\frac{\partial^2}{\partial \mathrm{z}^2}\right)^{\frac{1}{2}}\right) \qquad \ldots (10)$$

which implies,

$$\frac{\partial^2\mathrm{v}}{\partial \mathrm{t}^2}-\frac{\mathrm{N}}{\mathrm{d}}\frac{\partial^2\mathrm{v}}{\partial \mathrm{x}^2}-\frac{\mathrm{G}}{\mathrm{d}}\frac{\partial^2\mathrm{v}}{\partial \mathrm{z}^2}=\left(\frac{\partial}{\partial \mathrm{x}}-\mathrm{L}\right)\left(\frac{\partial}{\partial \mathrm{x}}+\mathrm{L}\right) \qquad \ldots (11)$$

where, $$\mathrm{L}=\sqrt{\frac{\mathrm{N}}{\mathrm{d}}}\frac{\partial}{\partial \mathrm{x}}\left(\mathrm{I}+\frac{\mathrm{G}}{\mathrm{N}}\left(\frac{\partial^2}{\partial \mathrm{z}^2}\Big/\frac{\partial^2}{\partial \mathrm{x}^2}\right)\right)^{\frac{1}{2}} \qquad \ldots (12)$$

in which, I is the identity operator.

To analyse the absorbing ability of the boundary conditions, we consider the plane waves represented by (Reynolds (1978))

$$v = e^{i(\omega t \pm kx\, cos\theta \pm kz\, sin\theta)} \quad \text{... (13)}$$

Using equation (13), equation (12) can be written as

$$\mathrm{Lv} = \mathrm{ki}\cos\theta\left(\frac{\mathrm{N}}{\mathrm{d}}\,\mathrm{I} + \frac{\mathrm{G}}{\mathrm{d}}\,\frac{sin^2\theta}{cos^2\theta}\right)^{\frac{1}{2}}\mathrm{v} \quad \ldots (14)$$

Using equation (9), the boundary conditions from equation (7), can be written as,

$$\left.\begin{aligned}\left(\frac{\partial}{\partial \mathrm{t}} - \frac{\partial}{\partial \mathrm{x}}\mathrm{L}\right)\mathrm{v} = 0, \mathrm{x} = -\mathrm{a}\\ \left(\frac{\partial}{\partial \mathrm{t}} + \frac{\partial}{\partial \mathrm{x}}\mathrm{L}\right)\mathrm{v} = 0, \mathrm{x} = \ \mathrm{a}\end{aligned}\right\} \quad \ldots (15)$$

Boundary conditions (15) are functions of wave number k represent reflection coefficient of magnitude zero, which cannot be applied for real problems. Using the concept of Reynolds (1978), we define $f(k_z)$ by

$$\mathrm{f(k_z)} = \sqrt{\frac{\mathrm{N}}{\mathrm{d}} + \frac{\mathrm{G}}{\mathrm{d}}\frac{\mathrm{k_z}^2}{\mathrm{k_x}^2}} \quad \ldots (16)$$

using Maclaurin series, we obtain

$$\mathrm{f(k_z)} = \frac{\mathrm{N}}{\mathrm{d}} + \frac{1}{2}\frac{\mathrm{G}}{\mathrm{d}}\frac{\mathrm{k_z}^2}{\mathrm{k_x}^2} \quad \ldots (17)$$

Using equation (12) and (10), boundary conditions (15) can be represented as,

$$\left(\frac{\partial}{\partial \mathrm{t}} \pm \frac{\partial}{\partial \mathrm{x}}\left(\frac{\mathrm{N}}{\mathrm{d}} + \frac{1}{2}\frac{\mathrm{G}}{\mathrm{d}}\left(\frac{\partial^2}{\partial \mathrm{z}^2}\Big/\frac{\partial^2}{\partial \mathrm{x}^2}\right)\right)\right)\mathrm{v} = 0 \quad \ldots (18)$$

On applying the operator $\frac{\partial}{\partial x}$ on (18), the boundary conditions in (18) can be rewritten as

$$\left.\begin{aligned}\frac{\partial}{\partial \mathrm{x}}\left(\frac{\partial \mathrm{v}}{\partial \mathrm{t}}\right) + \frac{\mathrm{N}}{\mathrm{d}}\frac{\partial^2 \mathrm{v}}{\partial \mathrm{x}^2} + \frac{1}{2}\frac{\mathrm{G}}{\mathrm{d}}\frac{\partial^2 \mathrm{v}}{\partial \mathrm{z}^2} = 0, \ \mathrm{x} = \mathrm{a}\\ \frac{\partial}{\partial \mathrm{x}}\left(\frac{\partial \mathrm{v}}{\partial \mathrm{t}}\right) - \frac{\mathrm{N}}{\mathrm{d}}\frac{\partial^2 \mathrm{v}}{\partial \mathrm{x}^2} - \frac{1}{2}\frac{\mathrm{G}}{\mathrm{d}}\frac{\partial^2 \mathrm{v}}{\partial \mathrm{z}^2} = 0, \ \mathrm{x} = -\mathrm{a}\end{aligned}\right\} \quad \ldots (19)$$

which can be expressed as

$$\left.\begin{aligned}\frac{\partial^2 \mathrm{v}}{\partial \mathrm{x}\,\partial \mathrm{t}} + \frac{\mathrm{N}}{\mathrm{d}}\frac{\partial^2 \mathrm{v}}{\partial \mathrm{x}^2} + \frac{\mathrm{p}}{\mathrm{p+1}}\frac{\mathrm{G}}{\mathrm{d}}\frac{\partial^2 \mathrm{v}}{\partial \mathrm{z}^2} = 0, \quad \mathrm{x} = \mathrm{a}\\ \frac{\partial^2 \mathrm{v}}{\partial \mathrm{x}\,\partial \mathrm{t}} - \frac{\mathrm{N}}{\mathrm{d}}\frac{\partial^2 \mathrm{v}}{\partial \mathrm{x}^2} - \frac{\mathrm{p}}{\mathrm{p+1}}\frac{\mathrm{G}}{\mathrm{d}}\frac{\partial^2 \mathrm{v}}{\partial \mathrm{z}^2} = 0, \ \mathrm{x} = -\mathrm{a}\end{aligned}\right\} \quad \ldots (20)$$

where $p = \frac{c\,\Delta t}{\Delta x} = 1$ yields low or zero reflection from the boundaries.

To calculate reflection coefficients at $x = a$ and $x = -a$, we take total wave displacement as,

$$\mathrm{v} = \mathrm{e}^{\mathrm{i(wt - kxcos\theta \pm kzsin\theta)}} + \mathrm{Re}^{\mathrm{i(wt + kxcos\theta \pm kzsin\theta)}} \quad \ldots (21)$$

Putting the above equation in (20), the reflection coefficient at $x = a$ is given by

$$|\mathrm{R1}| = \left|\frac{\mathrm{c}\cos\theta - \mathrm{V_{SH}}}{\mathrm{c}\cos\theta + \mathrm{V_{SH}}}\right| \quad \ldots (22)$$

Similarly, the reflection coefficient at $x = -a$ from (20) is given by

$$|\mathrm{R2}| = \left|\frac{\mathrm{c}\cos\theta + \mathrm{V_{SH}}}{\mathrm{c}\cos\theta - \mathrm{V_{SH}}}\right| \quad \ldots (23)$$

where, $\mathrm{V_{SH}} = \frac{\mathrm{N}}{\mathrm{d}}\cos^2\theta + \frac{\mathrm{p}}{\mathrm{p+1}}\frac{\mathrm{G}}{\mathrm{d}}\sin^2\theta$ … (24)

NUMERICAL SOLUTION

In the present section, we compare the results obtained using reflecting boundary condition with the results of absorbing boundary condition. We have modified the MATLAB code given by Stephen (2016) to numerically simulate the 2D wave propagation in an anisotropic porous medium. In order to find the effects of reflecting and absorbing boundary conditions on the wave displacement, we have used the following parameters for numerical calculations:

$\frac{\mathrm{G}}{\mathrm{N}} = 0.5, 1.0$ and 1.5; $\gamma = 0.5, 1.0$ and 1.5 and CFL=0.5

To find the absorbing effect of boundary condition on the propagation of SH-waves, source term

$$\mathrm{v}^{\mathrm{k}}_{50,50} = \Delta \mathrm{t}^{\,2}\, 20 \sin\left(\frac{30\pi \mathrm{t}}{20}\right)$$

is used to generate the SH-waves in the medium. From Figures 2 and 3, it is observed that the displacement of the wave decreases as anisotropic parameter $\frac{G}{N}$ increases from 0.5 to 1.5 in case of both absorbing boundary (ABC) and non-absorbing conditions (non-ABC) respectively. However, it is also observed that the displacement of the wave is less in absorbing boundary condition than the non-absorbing boundary condition.

From Figures 4 and 5, it is observed that the displacement of the waves decreases as porosity parameter γ increases from 0.5 to 1.5 in both non-absorbing and absorbing boundary conditions respectively. However, it is also observed from the same figures that the displacement of the waves decreases faster in absorbing boundary condition than the non-absorbing boundary condition when γ increases from 0.5 to 1.5.

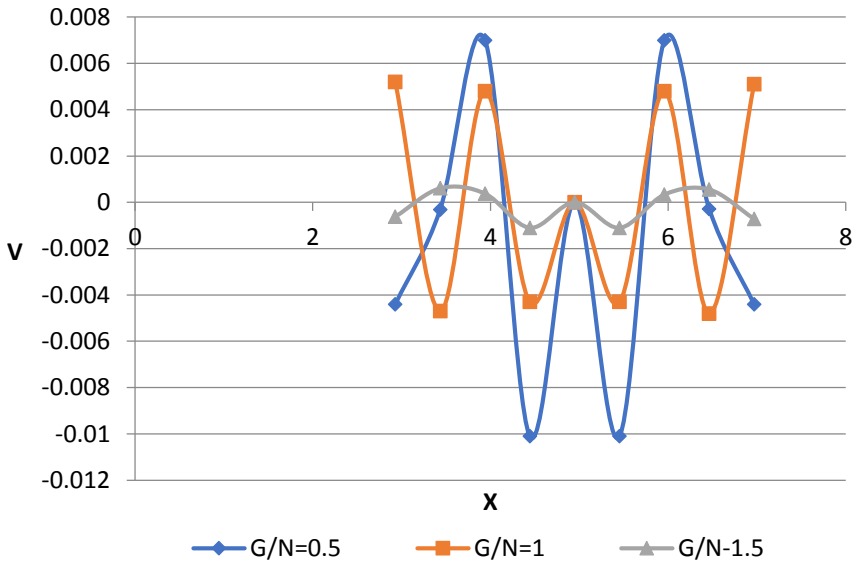

Figure 2. Variations of displacement with respect to x for G/N=0.5, 1.0, 1.5 with γ=1.0 for ABC.

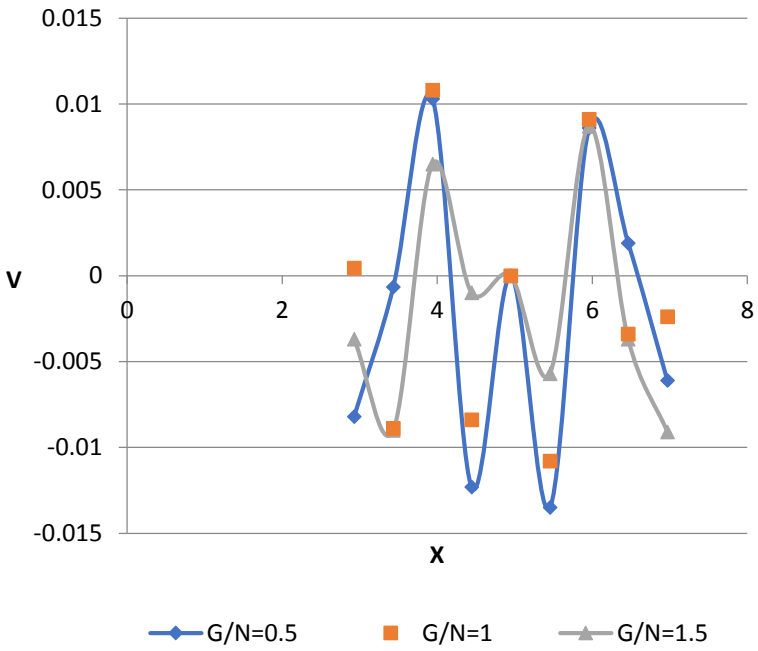

Figure 3. Variations of displacement with respect to x for G/N=0.5, 1.0, 1.5 with γ=1.0 for Non-ABC.

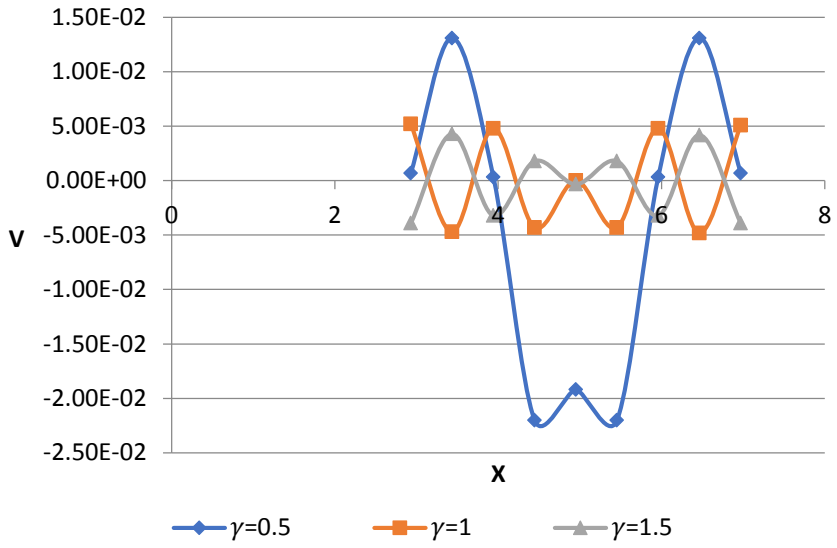

Figure 4. Variations of displacement with respect to x for γ=0.5, 1.0, 1.5 with G/N=1.0 for ABC

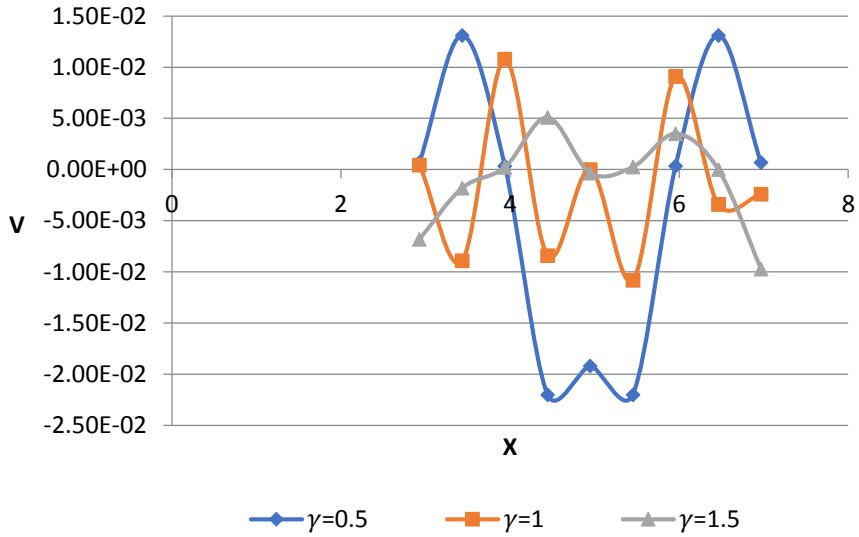

Figure 5. Variations of displacement with respect to x for γ=0.5, 1.0, 1.5 with G/N=1.0 for Non-ABC.

To implement numerically the absorbing boundary conditions to minimize the edge reflection from the boundaries, we use two types of stability conditions given by Mitchell (1969) and Reynolds (1978), first with $p = c\frac{\Delta t}{\Delta x} = 1$ and the second with $p = c\frac{\Delta t}{\Delta x} \leq \frac{1}{\sqrt{2}}$. The results are compared graphically in Figures 6 and 7 with $p = 1$ and in Figures 8 and 9 with $p = 1/\sqrt{2}$. From Figure 6, it is evident that the absolute value of the reflection coefficient R1 decreases with the increase in anisotropic parameter $\frac{G}{N}$ from 0.5 to 1.5. However, there exists a transition zone ($30^0 \leq \theta \leq 60^0$), where the change is irregular. Similarly, it is also observed from Figure 7 that the absolute value of the reflecting coefficient R1 decreases up to angle of incidence 60^0 and then increases for each value of γ. However, with the increase in the porosity parameter γ from 0.5 to 1.5, the reflection coefficient of the SH-wave decreases for all θ in $[0^0, 90^0]$.

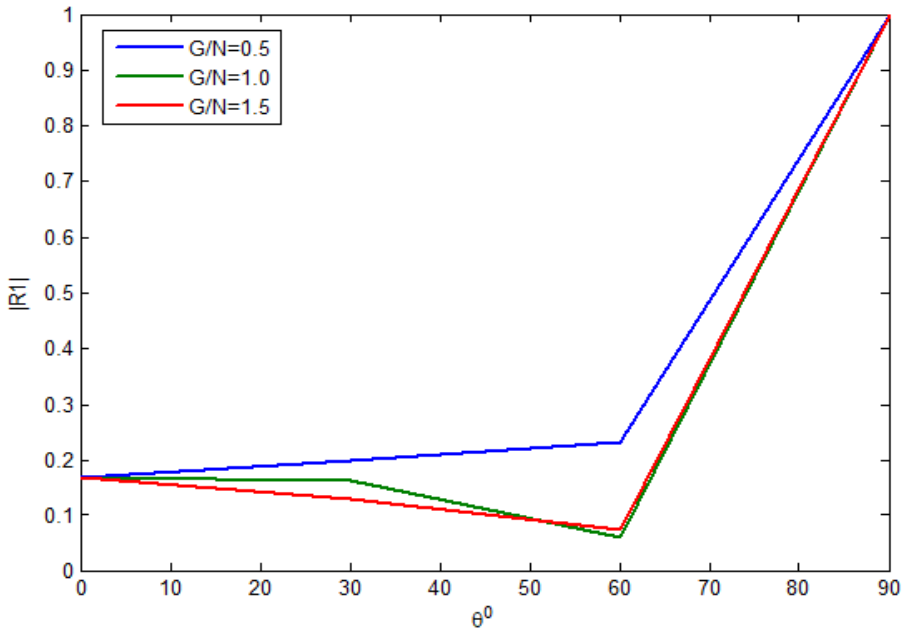

Figure 6. Variation of reflection coefficient at the right boundary for different values of G/N when γ =1 and p=1

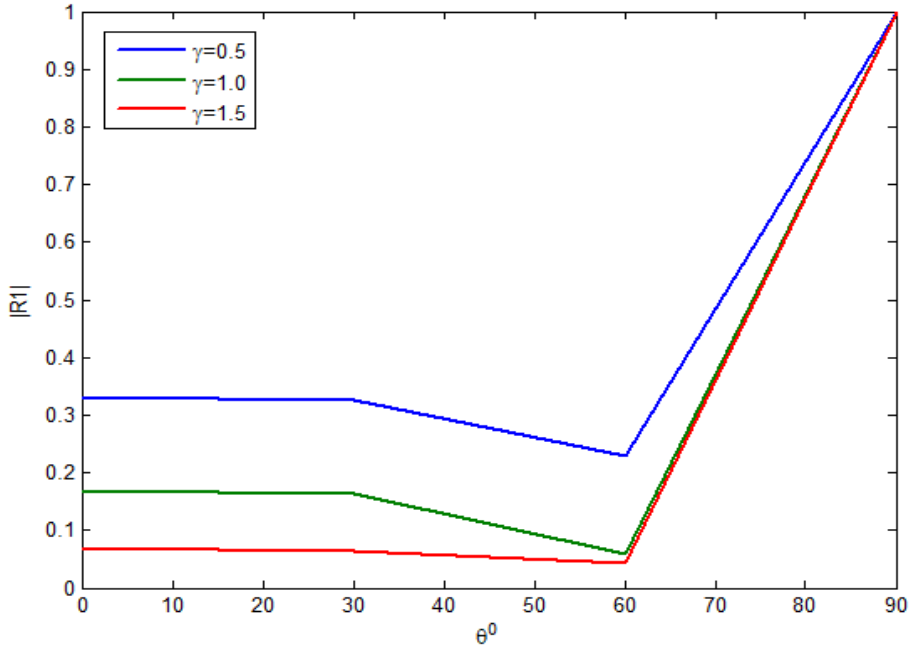

Figure 7. Variation of reflection coefficient at the right boundary for different values of γ when G/N = 1 and p=1

In Figures 8 and 9, variations of reflection coefficient for different values of Weiskopf type anisotropy parameter $\frac{G}{N}$ and porosity parameter γ with $p = 1/\sqrt{2}$ are presented. It is observed from Figure 8 that the absolute value of the reflecting coefficient R1 decreases with the increase in anisotropic parameter $\frac{G}{N}$. Also, the increase in porosity parameter γ for particular value of θ in [0^0, 90^0] shows decrease in the absolute value of the reflecting coefficient R1 as shown in Figure 9. It is also observed that the reflection coefficients are nearly zero at θ = 60^0 when $\frac{G}{N}$ = 1.5, γ =1, and for γ =1.5, $\frac{G}{N} = 1$ with $p = 1/\sqrt{2}$.

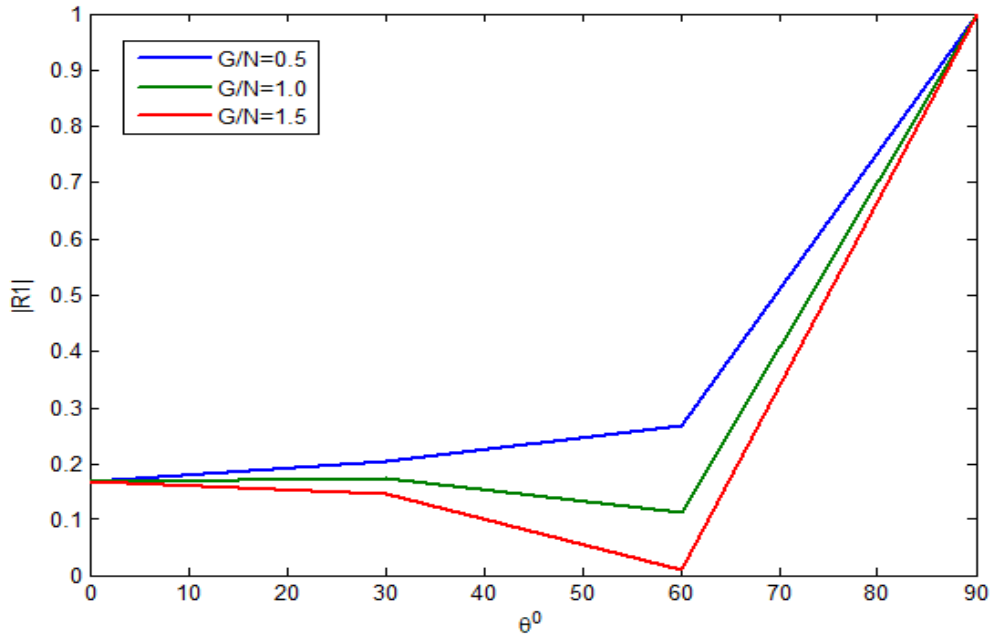

Figure 8. Variation of reflection coefficient at the right boundary for different values of G/N when γ = 1 and p=1/√2

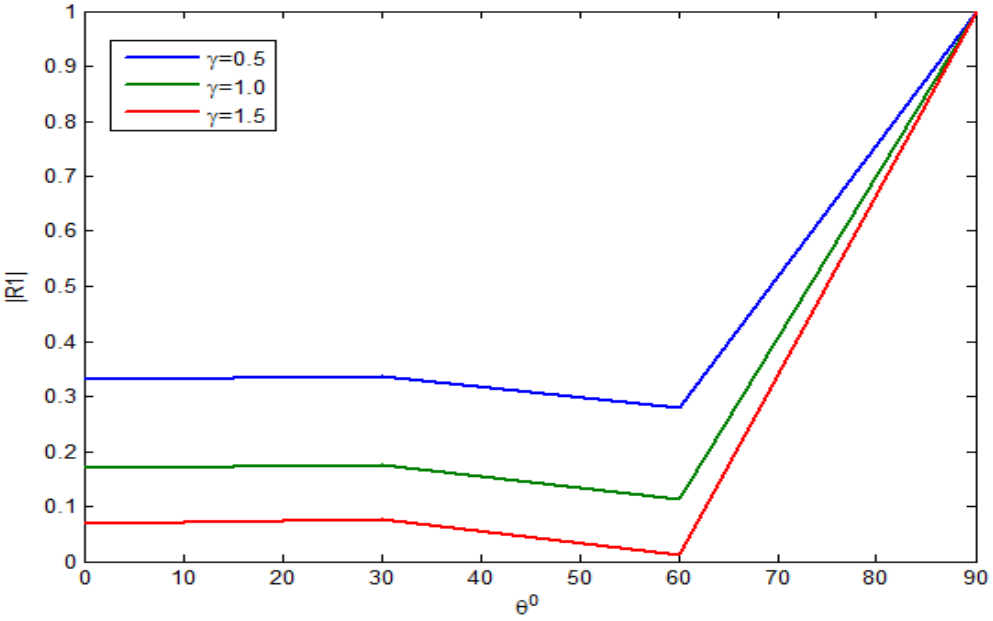

Figure 9. Variation of reflection coefficient at the right boundary for different values of γ when G/N =1 and p=1/√2

Figures 10 and 11 represent effects of anisotropic parameter $\frac{G}{N}$ and porosity parameter γ respectively on the absolute value of reflection coefficient at the left boundary. It is observed from Figure 10 that reflection at the left boundary decreases with the decrease in porosity parameter. However, the effect of anisotropic parameter on reflection at the left boundary is irregular. In the interval $(0^0,30^0)$ U $(60^0,90^0)$, reflection from the left boundary increases with the increase in anisotropic parameter $\frac{G}{N}$. But reflection is irregular in $(30^0,60^0)$ except for $\frac{G}{N}$ equals to 0.5 which is decreasing with the increase in angle of incidence of the SH-waves.

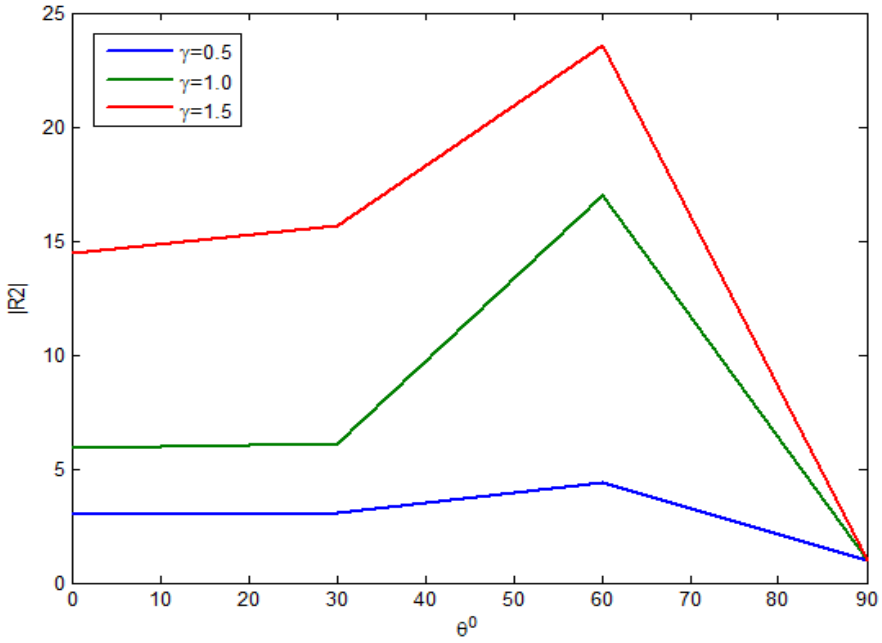

Figure 10. Variation of reflection coefficient at the left boundary for different values of γ when G/N=1 and p=1

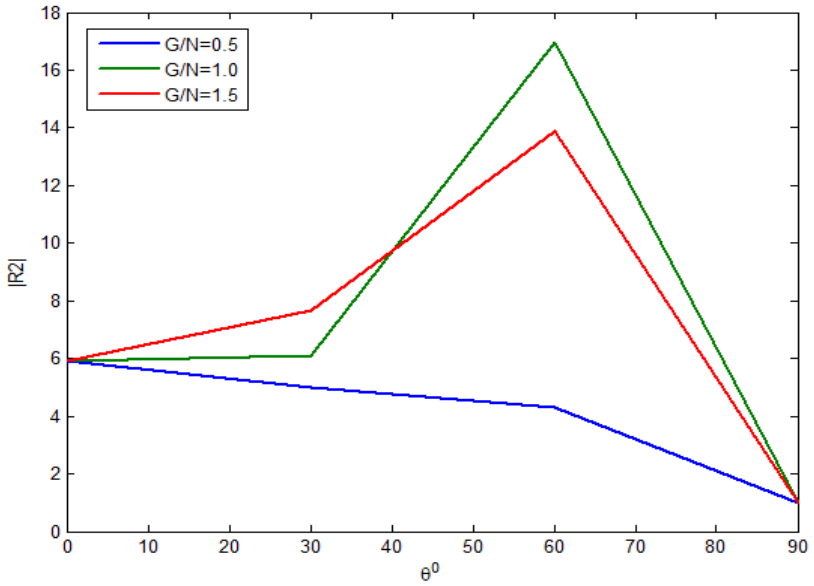

Figure 11. Variation of reflection coefficient at the left boundary for different values of G/N when γ =1 and p=1

Snapshots of two-dimensional SH-waves profile for the propagation time of 7s, 10s and 13s are presented in Figures 12 to 14 respectively. It is observed from the figures that as time increases the absorbing capability of the non-reflecting boundary also increases. In other words, reflection at the boundaries decreases with the increase in time.

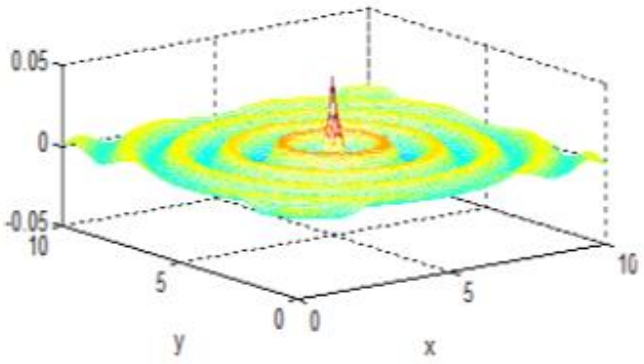

Figure 12. Two-dimensional SH-waves profile at t = 7s

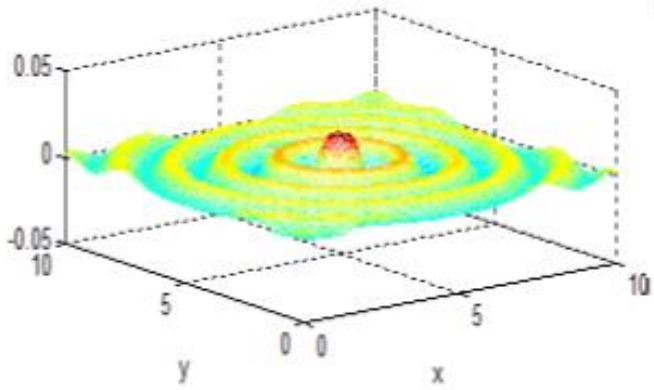

Figure 13. Two-dimensional SH-waves profile at t = 10s

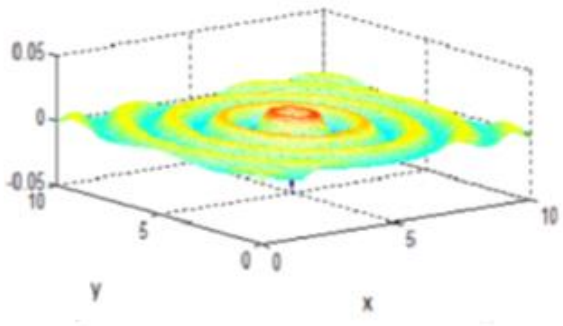

Figure 14. Two-dimensional SH-waves profile at t = 13s

CONCLUSIONS

From the above studies, it can be concluded that finite difference method is an important and effective technique to numerically model SH waves propagation in a liquid-filled anisotropic porous medium using reflecting and non-reflecting boundaries. The effects of variation of anisotropic and porosity parameters on the displacement of the wave have been studied using this technique. It is observed that absorbing boundary conditions are very effective in reducing reflection at the boundaries. Results of this study are summarised as follows:

1. Displacement of the waves decreases with the increase in anisotropic parameter $\frac{G}{N}$ in case of both absorbing and reflecting boundary conditions.
2. Displacement of the waves is less in absorbing boundary condition than the non-absorbing boundary condition for particular values of anisotropic parameter $\frac{G}{N}$ and porosity parameter γ.

3. Displacement of the waves decreases as porosity parameter γ increases in case of both absorbing and non-absorbing boundary conditions.
4. The absolute value of the reflection coefficient R1 decreases with the increase in anisotropic and porosity parameter for value of angle of incidence. However, at $p = 1$, there exists a transition zone near to the angle of incidence 60^0, where the change is irregular.
5. The absolute value of the reflection coefficient R2 is in direct proportion with the porosity parameter for particular value of angle of incidence. In particular when $p = 1$, the value of R2 first increases, attains maximum at $\theta=60^0$ and then decreases for each value of .
6. The absolute value of the reflection coefficient R2 increases with the increase in anisotropic parameter for particular value of angle of incidence θ, when $0 \leq \theta \leq 30$. In particular when $p = 1$, the value of R2 first increases, attains maximum at $\theta=60^0$ and then decreases for $\frac{G}{N} = 1$ and $\frac{G}{N} = 1.5$.
7. absorbing capacity of the non-reflecting boundary depends on the time for which wave propagates. Infact, reflection at the boundaries decreases with increase in time.

ACKNOWLEDGMENTS

Authors wish to thank Dr. Om Prakash Pandey, chief editor for his valuable suggestions to improve the article. Authors also acknowledges the support by Dr. Vishwanath Karad MIT World Peace University, Pune.

Compliance with Ethical Standards

The authors declare no conflict of interest and adhere to copyright norms.

REFERENCES

Alam, M. J., Loskor, W.Z. and Mohiuddin, M., 2021. Time dependent wave propagation modelling using finite difference scheme of 2D wave equation based on absorbing and reflecting boundaries. J. Applied Math. Phys., 9, 2334-2344

Alford, R.M., Kelley, K.R. and Boore, D.M., 1974. Accuracy of finite difference modelling of the acoustic Wave equation. Geophysics, 39, 834-842.

Alpert, B., Greengard, L. and Hagstrom, T., 2002. Nonreflecting boundary condition for the time- dependent wave equation. J. of Computational Phys., 180, 270-296.

Biot, M.A., 1956. Theory of propagation of elastic waves in a saturated porous solid, I, Low- frequency range. J. Acoust. Soc. Am., 28,168-178.

Bose, S.K., 1962. Wave propagation in marine sediments and water-saturated soil. Geofisica Pure Applicate, 52, 27-40.

Burgos, R.B. and Santos, M.A.C., 2016. Finite elements based on Deslauriers-Dubuc wavelets for wave propagation problems. Appl. Mathematics, 7, 1490-1497.

Burns, D.R.,1992. Acoustic and elastic scattering from seamounts in three dimensions: a numerical modelling study. J. Acoust. Soc. Am., 92, 2784–2791.

Cao, S. and Greenhalgh, S., 1998. 2.5-D modelling of seismic wave propagation: boundary condition, stability criterion, and efficiency. Geophysics, 63, 2082-2090.

Cerjan, C., Kosloff, D., Kosloff, R. and Reshef, M., 1985. A non-reflecting boundary condition for discrete acoustic and elastic wave equations. Geophysics, 50, 705–708.

Chakraborty, S. K. and Dey, S., 1982. The propagation of Love waves in water-saturated soil underlain by a heterogeneous elastic medium. Acta Mechanica, 44,169-176.

Chattopadhyay, A. and De, R.K., 1983. Love-type waves in a porous layer with irregular interface. Int. J., Engg. Sci., 21, 1295-1303.

Clayton, R. and Engquist, B., 1977. Absorbing boundary conditions for acoustic and elastic wave equations. Bull. Seism. Soc. Am., 67, 1529– 1540.

Deresiewicz, H., 1961. The effect of boundaries on wave propagation in a liquid- filled porous solid II, Love waves in porous layer. Bull. Seism. Soc. Am., 51, 51-59.

Givoli, D. and Neta, B., 2003. High-order non-reflecting boundary scheme for time-dependent waves. J. Computational Phys., 186, 24-46.

Grote, M.J. and Keller, J.B., 2000. Non-reflecting boundary conditions for elastic waves. SIAM J. Appl. Mathematics, 60, 803-819.

Hagstrom, T., Mar-Or, A. and Givoli, D., 2008. High-order local absorbing conditions for the wave equation: extensions and improvements. J. Computational Phys., 227, 3322-3357.

Hall, F. and Wang, Y., 2009. Elastic wave modelling by an integrated finite difference method. Geophys. J. Int.,177,104-114.

Holberg, O., 1987. Computational aspects of the choice of operator and sampling interval for numerical differentiation in large scale simulation of wave phenomena. Geophys. Prosp., 35, 629-655.

Ju, S.H., and Wang, Y.M., 2001. Time-dependent absorbing boundary conditions for elastic wave propagation. Int. J. Numer. Meth. Eng., 50, 2159–2174.

Kalyani, V.K. and Kar, B.K., 1986. Propagation of Love waves in a water-saturated soil lying between two semi-infinite homogeneous elastic media. Acta Geophysica Polonica, 34, 349-359.

Kar, B.K. and Kalyani, V.K., 1986. Reflection and refraction of SH-waves due to the presence of a sandwiched anisotropic liquid filled porous layer. Geophys. Res. Bull., 24(1), 30-37.

Kar, B.K. and Kalyani, V.K., 1989. Dispersion of Love waves in a multi-layered anisotropic porous crust. Gerlands Beitr. Geophysik, 98, 131-137.

Keys, R.G.,1985. Absorbing boundary conditions for acoustic media. Geophysics, 50, 892–902.

Mitchell, A.R., 1969. Computational methods in partial differential equations. John Wiley & Sons, Inc., 255 pages.

Mur, G., 1981. Absorbing Boundary Conditions for the finite-difference approximation of the time-domain electromagnetic field equations. IEEE Trans. Electromagnetic Compatibility, 23, 377-382.

Peng, C. and Toksoz, M.N., 1994. An optimal absorbing boundary condition for finite difference modelling of

acoustic and elastic wave propagation. J. Acoust. Soc. Am., 95, 733–745.

Reynolds, A.C., 1978. Boundary conditions for the numerical solution of wave propagation problems. Geophysics, 43, 1099-1110.

Sochacki, J., Kubichek, G.R.J., Fletcher, W.R. and Smithson, S., 1987. Absorbing boundary conditions and surface waves. Geophysics, 52, 60–71.

Stephen H., 2016. Video lectures CEE 709 Numerical methods in mechanics. http://hstephen.faculty.unlv.edu/teaching-2/cee-709/.

Tsynkov, S.V., 2003. Artificial boundary conditions for the numerical simulation of unsteady acoustic waves. J. Computational Phys., 189, 626-650.

Weiskopf, W.H., 1945. Stresses in soils under foundation. Journal of the Franklin Institute., 239(6), 445-465.

Zhang, Z.J., He, Q.D. and Xu, Z.X., 1993. The absorption of artificial boundary reflection in 2-D transversely isotropic media with FDM elastic wavefield modelling. Acta Geophys. Sinica, 36, 519-527.

Received on:13.02.2022; Revised on 23.03.2022; Accepted on: 26.03.2023

J. Ind. Geophys. Union, 27(2) (2023), 109-117

Application of Fuzzy graph theory in brittle plane network analysis - A potential method for carbon sequestration models

O.T. Manjusha[1] and Soumyajit Mukherjee[2]*

[1]Department of Mathematics, Govt. Arts and Science College, Kondotty, Malappuram- 673 041, Kerala, India
[2]Department of Earth Sciences, Indian Institute of Technology, Bombay (Powai), Mumbai-400 076, Maharashtra, India
*Corresponding author: soumyajitm@gmail.com, smukherjee@iitb.ac.in

ABSTRACT

Improved carbon sequestration (CCS) models with rocks as sinks require incorporation of uncertainty into the models. In such cases of uncertain geoscientific problems, fuzzy graph theory can be useful. Brittle shear plane network with indistinct shear planes is common in natural sheared rocks, and can be targeted for CCS. Due to non-unique possibility of continuity of P-planes, it is not possible to represent such networks as crisp graphs. We present few natural examples of the former type of P-planes in shear zones, and how fuzzy graph theory can represent the fracture network and fluid flow. The process involves assigning some sample numerical probability to represent the connectedness between the underdeveloped P-planes and the Y-planes. The presentation is a geometric exercise and does not extend to the genesis of the shear zones.

Keywords: Network, Fluid flow, Structural geology, Shear planes, Geoscientific uncertainty, Waste disposal, Carbon sequestration models

INTRODUCTION

Structural geological modeling requires representation of structures in some numerical form. When the structures are clearly decipherable, this is rather easy, for example, one can apply the graph theory (e.g., Sanderson et al., 2018; Mukherjee, 2019). Classical graph theory works when there is a full certainty that which nodes are connected by which vertices through edges.

Various brittle plane geometries develop in rocks at shallow crustal depths that undergo brittle shear (Figure 1a). In case the shear planes are clearly delineated (Figure 1b), one can use graph theory to represent the brittle plane network in terms of sigmoid shear bound by parallel planar shear planes commonly seen in sheared rocks. For example, in case of Figure 1b, the adjacency matrix is:

	a	b	c	d	e	f
a	0	0	0	0	1	0
b	0	0	0	0	0	1
c	0	0	0	0	0	1
d	0	0	0	0	0	1
e	0	0	0	0	0	1
f	0	0	1	1	0	0

Carbon sequestration (CCS) has recently been modeled in terms of extraneous CO_2 sources and CO_2 sinks in rocks and P-graph modeling approach has been undertaken (Chong et al., 2014). Fractured rocks especially coal has been targeted for CCS (e.g., Chen et al., 2020). However, since connectivity of fractures is uncertain at depth, establishing models on CCS becomes problematic (Figure 1 of Zhang et al., 2009). Pashin et al. (2008) presented a discrete fracture network model for CCS in coal. Such models would be possible when existence of the sink locations in the coal is fairly well understood. When the existence of the sinks is uncertain, models will nevertheless be required to be built in decision making. Other uncertainties can be *"unproven nature"* of the carbon sequestration technology, economic cost and life cycles of the CCS technologies and so on (Tan et al., 2010 and references therein). Researchers have identified CCS as one of the potential areas where graph theory concept needs more elaboration (e.g., Farid et al., 2021).

Anand et al. (2021) discussed various kinds of uncertainties in parameters in structural geological problems. The sigmoid planes can be indistinct due to *(i)* poor snap quality, *(ii)* they are indeed developed less prominently, or *(iii)* sometimes a part of them is below the ground surface hence not seen. For example, in seismic images, brittle planes may not always be clearly decipherable. This can be because of such brittle planes are below the seismic resolution (Misra and Mukherjee, 2018), and yet the modeler needs to make some presentation of the brittle plane network. In such cases, where the classical graph theory cannot represent the brittle plane network where uncertainty exists about continuation of fractures, fuzzy graph theory should be used.

The concept of fuzzy sets was introduced by Zadeh (1965), which later was well applied to solve several research problems that are uncertain in nature. Crisp set is a well-defined collection of distinct objects. If there is any uncertainty in the set boundaries of objects, the concept of fuzzy set is used. In other words, a fuzzy set is used to represent the degree of membership of any qualitative data. The crisp set is not able to work with scientific problems with inherent uncertainty because it consists of just two

truth values: 0 – false (no) and 1-true (yes). These single values of membership degree are unable to manage the uncertainties. Atanassov (1999) proposed the intuitionistic fuzzy set to manage uncertain situations using an extra degree of membership, defined as the *hesitation margin*. Intuitionistic fuzzy set, is as an extension of Zadeh's theory of fuzzy sets. Compared to classical fuzzy set, it is more flexible and efficient to work with uncertainty due to the presence of hesitation margin. Repository presents the fundamentals of the fuzzy graph theory. A fuzzy graph representing fracture network can constraints fluid flow through such a network.

METHODS

Figure 2a-c present a network of brittle shear planes where not all P-planes can be tracked with confidence. Here the curved P-plane AB joins two sub-parallel Y-planes. However, the other P-planes (CD, KZ, EF, GH and IJ) do not join both the C-planes. In some cases, the P-planes are too close-spaced in order to distinguish them confidently in naked eyes. A simplified situation can be thought in this case (Figure 3).

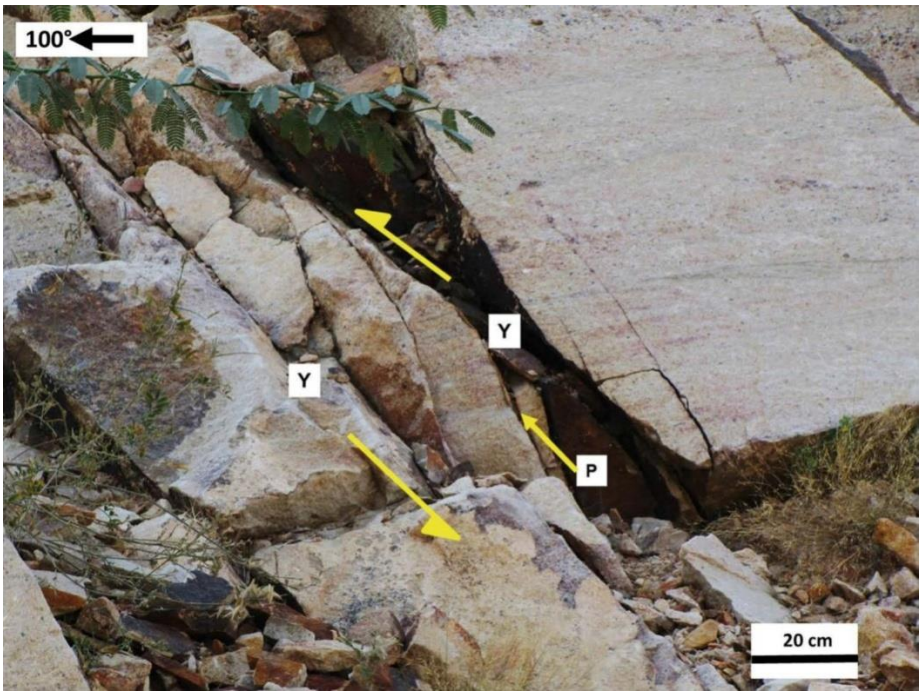

Figure 1(a). Clearly visible Y and P planes. Top-to-ESE brittle shear with distinct Y- and P-planes within fluvial sandstone of the Sarnoo hill area, observed on a sub-vertical section. Location: W of Sarnoo hill area, SE of the Sarnoo village, Barmer basin, India. Reproduced from figure 1.18 of Mukherjee et al. (2020).

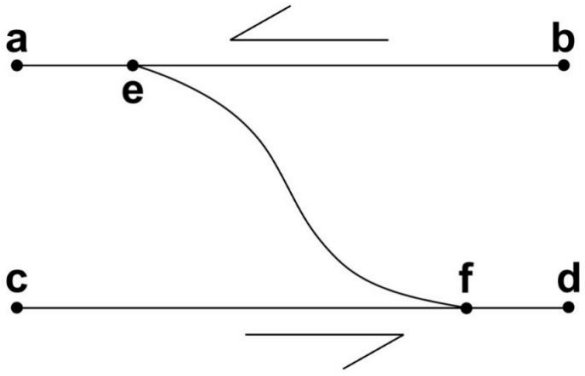

Figure 1(b). A brittle plane network in a brittle shear zone. Reproduced from Figure 2c of Mukherjee (2019).

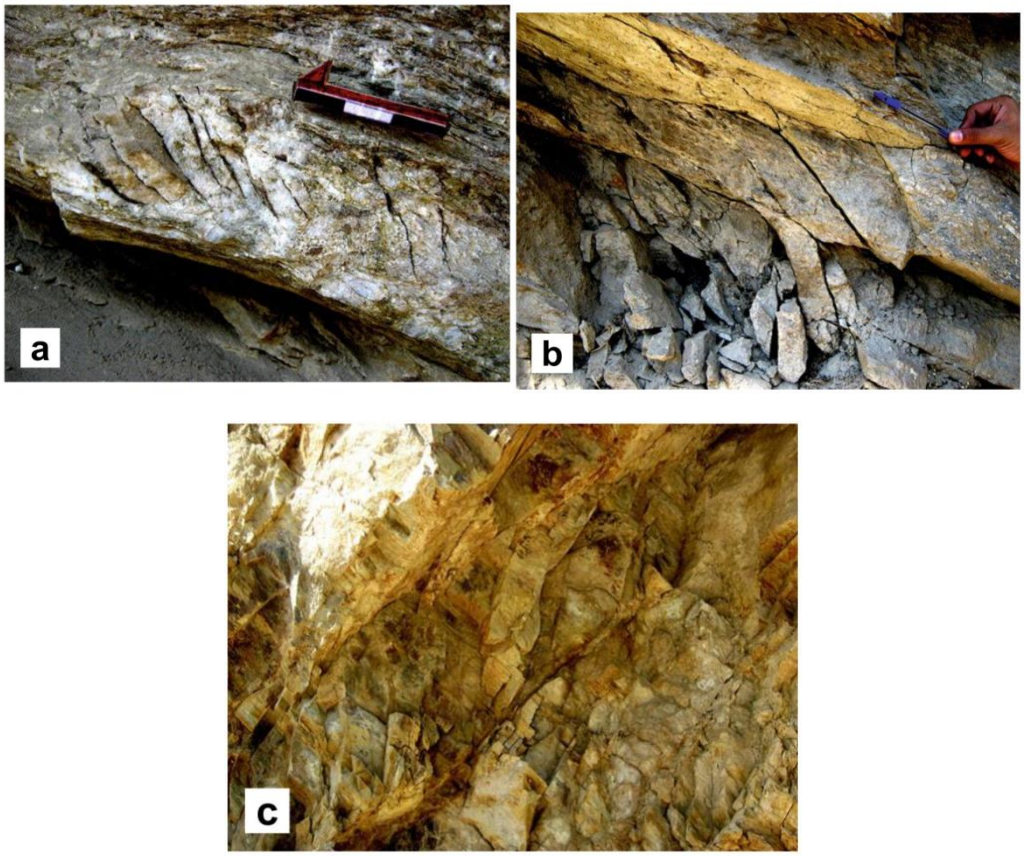

Figure 2. Brittle plane network consisting of Y and P planes. Here some of these planes cannot be traced continuously with full confidence, and hence a crisp graph cannot be visualized. Fuzzy graph theory can be applied in these cases. All examples from mylonitized gneiss in Greater Himalayan Crystallines, Bhagirathi section, Uttarakhand, India- **(a,b)** Top-to-left (up) shear. India; reproduced from figures. 5.15 and 5.20, respectively of Mukherjee (2014). **(c)** Top-to-right (up) shear; reproduced from figure 5.21 of Mukherjee (2014).

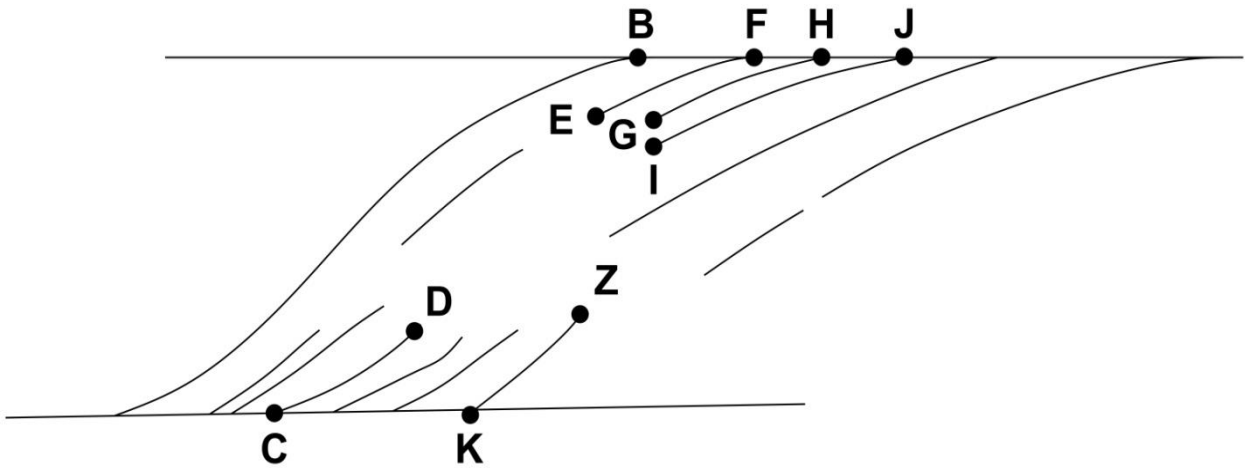

Figure 3. An idealized brittle shear plane network. Few sigmoid P-planes (e.g., AB) join the C-planes. The other P-plane, CD, KZ, EF, GH and IJ, are not fully developed and merge with just a single C-plane. In such a situation, fuzzy graph theory has been applied in this work.

We represent fracture network using intuitionistic fuzzy graph as follows (Figure 4). Points (nodes) A and B are certainly connected with AB as an arc. But it is uncertain for some reason whether point D connects with E, G or I by some arc. Connection between D and E or I, therefore can be represented as an intuitionistic fuzzy graph. Now if by zooming the image or by some image enhancement technique, a connection between D and G is established with some degree of confidence, it means that there is a much higher probability/possibility that they are connected, and therefore connections between D and E or D and I would be less likely/less probable. Putting some sample numerical probability values in a scale of 0 ("certainly not") to 1 ("certainly"), or using intuitionistic fuzzy graph enables one to represent the fracture network. In this graph, take the node set as V = {A, B, C, D, E, F, G, H, I, J, K, Z} and A (0.9, 0.1) denotes the degree of membership and degree of non-membership of the node *A* and similarly for all other nodes The ordered pair (0.7, 0.1) denotes the degree of membership and degree of non-membership of the arc relation $e_{FH}=(F,H)$ on $V \times V$and so on. These numerical values of possibilities are given according to the degree of confidence of the connection. The values are taken in the interval [0,1].

We will now get into further detail of fuzzy graph theory to tackle flow problems. The adjacency matrix of a fuzzy graph $G:(V,\sigma,\mu)$ is an $n\times n$ matrix defined as $A=[a_{ij}]$,

where $a_{ij}=\mu\ (v_i,v_j)$ (Anjali and Mathew, 2013). For example, consider the fuzzy graph in Figure 5 for a hypothetical data set. Its adjacency matrix is:

	v_1	v_2	v_3	v_4
v_1	0	0.1	0.9	0.4
v_2	0.1	0	0.6	0
v_3	0.9	0.6	0	0.2
v_4	0.4	0	0.2	0

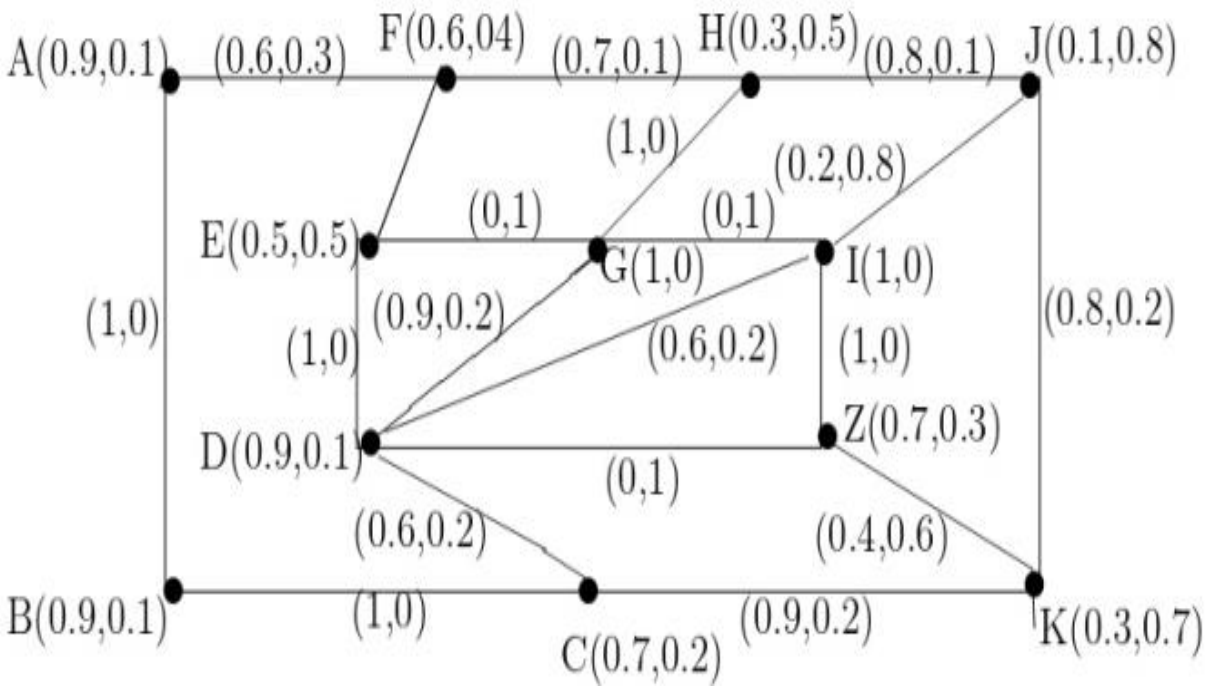

Figure 4. A fuzzy graph corresponding to the case of Figure 3.

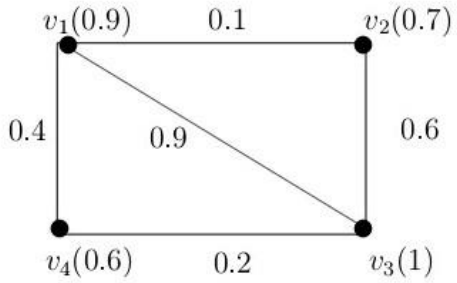

Figure 5. A fuzzy graph with nodes v_1, v_2, v_3 and v_4. Values inside brackets of the nodes are the fuzzy weights of the respective nodes. Fuzzy arc weights are represented by the values 0.1, 0.2, 0.4, 0.6, and 0.9.

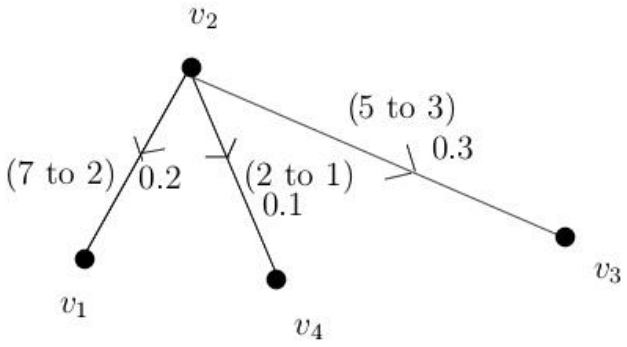

Figure 6. A network, from nodes v_2 to v_1 the flow can vary in magnitude from 7 to 2 units. Therefore, we take fuzzy weights 0.7 for v_2 and 0.2 for v_1. Similarly, one can take the fuzzy weight of v_3 as 0.3, v_4 as 0.1.

In this fuzzy graph, the numbers inside the first bracket represents the node weights, which do not appear in the adjacency matrix since. Instead, only the arc weights are used for the entries in the adjacency matrix. Such a presentation is as per Anjali and Mathew (2013). The entries in the adjacency matrix are obtained as follows. Since v_1 is not shown to be connected with itself by any edge, the entry is 0. Since v_1 is adjacent with v_2 with arc weight 0.1, the entry is 0.1 and so on.

Consider the network in Figure 6. From v_2 to v_1, the flow can vary in magnitude from 7 to 2 units. Therefore, we take fuzzy weights 0.7 for v_2 and 0.2 for v_1. Similarly, one can take the fuzzy weight of v_3 as 0.3, v_4 as 0.1. This is a first-time approach through this work. Suppose the fuzzy graph presented in Figure 6 has no arrows on edges. Then its corresponding adjacency matrix will differ.

That means flow can happen from one vertex to another and vice versa. The definition of a fuzzy graph allows us to give the arc weights in the following way. The arc (edge) weights are taken as the minimum among the corresponding node weights. This is logically true, since the maximum flow between two nodes is the minimum capacity between the two nodes. In that case, the adjacency matrix is:

$$A = \begin{array}{c} \\ v_1 \\ v_2 \\ v_3 \\ v_4 \end{array} \begin{array}{c} \begin{array}{cccc} v_1 & v_2 & v_3 & v_4 \end{array} \\ \begin{bmatrix} 0 & 0 & 0 & 0 \\ 0.2 & 0 & 0.3 & 0.1 \\ 0 & 0 & 0 & 0 \\ 0 & 0 & 0 & 0 \end{bmatrix} \end{array}$$

Suppose, instead of a range of flow, definite units of flow were given (e.g., 7, 5 and 2). We then assign fuzzy weights as 0.7, 0.5 and 0.2, respectively, for arcs. If a range of flow is given, we will get a freedom to take the minimum value amongst the range for representing the arc weight for the range of flow. As per the definition of adjacency matrix, one can represent these values by using their corresponding fuzzy weights. If 2, 1 and 3 are avoided, i.e., flow range 7 to 2 becomes 7, flow range 2 to 1 becomes 2 and flow range 5

to 3 becomes 5, the flow becomes exact, and one can assign the fuzzy weights. In fuzzy graph, we can give the maximum value of node weight and arc weight as 1 and minimum as 0. All other values are in between 1 and 0. A value equal to 1 means that the flow has fully happened. The intensity of the flow is represented by using these fuzzy weights.

Ramakrishnan and Lakshmi (2008) discussed how to fuse two nodes of the same fuzzy graph as follows. Let *G:* (*V, σ, μ*) be a fuzzy graph and let $u, v \in \sigma$. By the join (fusion) of two vertices *u* and *v*, the following is meant.

(i) Fuse (join) the vertices *u* and *v* as *uv* in the corresponding crisp graph $G^* = (\sigma^*, \mu^*)$ and then consider its underlying simple graph. A simple graph is the one without loops and possessing multiple edges.

(ii) The resulting fuzzy graph is $G_{uv}=(\sigma_{uv},\mu_{uv})$ where $\sigma_{uv}(x) = \{\max[\sigma(u), \sigma(v)]$ if $x = uv$

$\sigma(x)$ if $x \neq uv\}$

and $\mu_{uv}(x, y) = \{$ $\max[\mu(x, u), \mu(x, v)]$ if $y = uv$

$\max[\mu(u, y), \mu(v, y)]$ if $x = uv$

$\mu(x, y)$ if $x \neq uv$, $y \neq uv\}$

Consider the fuzzy graph in Figure 7. Figure 8 represents the fusing of the vertices *a* and *b*.

For instance,

$\mu_{ab}(ab,d)=Max\{\mu(a,d),\mu(b,d)\}=Max\{0.5,0\}=0.5$

$\sigma_{ab}(ab)=Max\{\sigma(a),\sigma(b)\}=Max\{1,0.8\}=1$

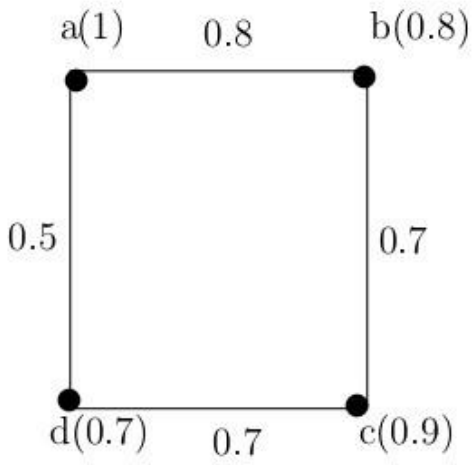

Figure 7. Example of a fuzzy graph with nodes a, b, c and d. Values inside the brackets of the nodes represent the fuzzy weights. Fuzzy arc weights are 0.5, 0.7 and 0.8.

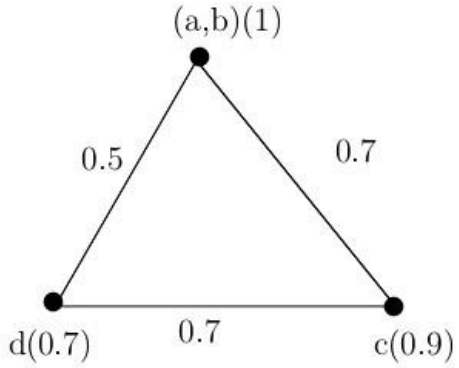

Figure 8. Fusing nodes *a* and *b* in the graph presented in Figure 7.

By using this idea, we can define the fusion of two vertices from two fuzzy graphs (Figure 9). Consider two fuzzy graphs G_1: (V_1, σ_1, μ_1) and G_2: (V_2, σ_2, μ_2). Let $u \in G_1$, $v \in G_2$. Fuse (join) the vertices u and v as uv in the corresponding crisp graph and then consider the underlying crisp simple graph. The resulting fuzzy graph is $G_{uv}=(\sigma_{uv},\mu_{uv})$ where:

$$\sigma_{uv}(x) = \{\max[\sigma_1(u), \sigma_2(v)] \text{ if } x = uv$$
$$\sigma_1(x) \text{ if } x \in G_1, \ x \neq uv$$
$$\sigma_2(x) \text{ if } x \in G_2, \ x \neq uv\}$$
$$\mu_{uv}(x,y) = \{\mu_1(x,u) \text{ if } y = uv, \ x \in G_1$$
$$\mu_2(x,v) \text{ if } y = uv, \ x \in G_2$$
$$\mu_1(x,y) \text{ if } x,y \in G_1$$
$$\mu_2(x,y) \text{ if } x,y \in G_2 \ \}$$

Coming to the case of a directed fuzzy graph or a fuzzy digraph, consider the network in Figure 10. The adjacency matrix of this new fuzzy graph is given below.

	A	BB_1	C	D
A	0	0.2	0	0
BB_1	0	0	0.1	0.1
C	0	0	0	0
D	0	0	0	0

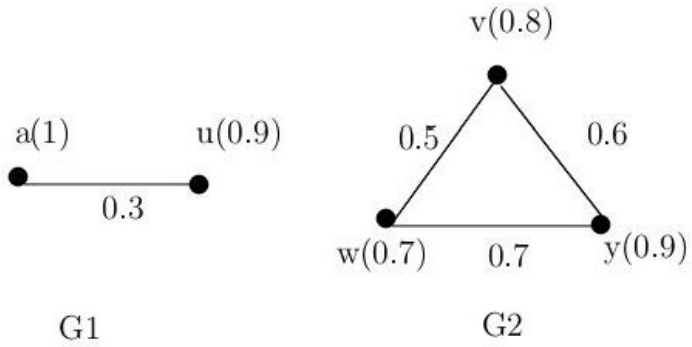

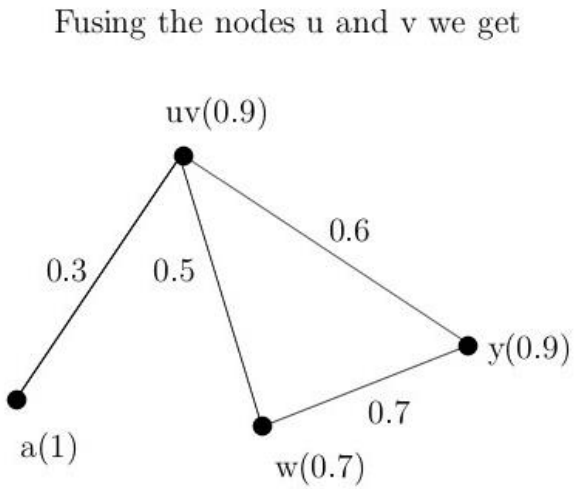

Figure 9. Fusion of two vertices u and v from two fuzzy graphs G_1 and G_2, respectively into uv. The fused vertex is assigned a weight 0.9, which is the maximum weight in between u and v.

7

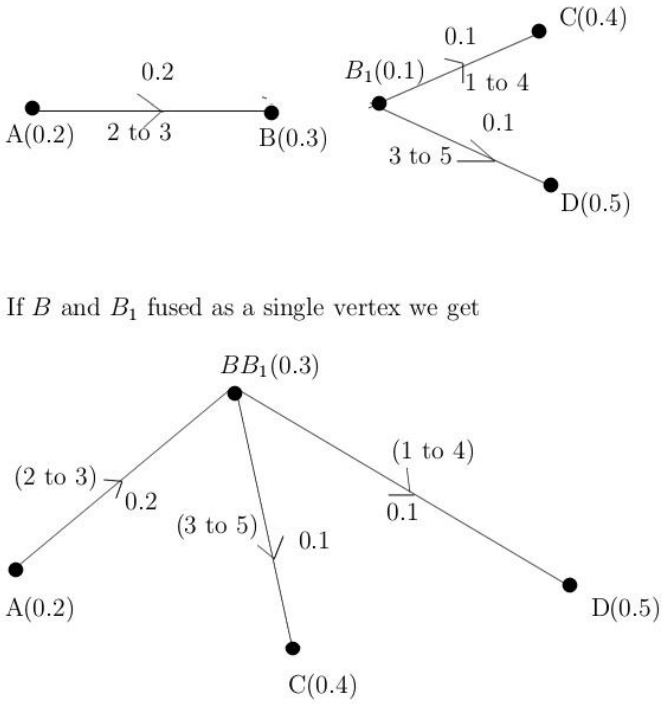

Figure 10. Fusing two nodes B and B_1 from two different networks. In the BB1 fused vertex, 0.3 is stated inside bracket. The magnitude is the maximum out of B (0.3) and B1 (0.1).

In the BB1 fused vertex, 0.3 is stated inside bracket. This means that the maximum out of B (0.3) and B1 (0.1) to be stated: "BB1 (0.3)". For the maximum taken, the logic is that the capacity elevates when nodes are fused (Ramakrishnan and Lakshmi, 2008).

The general expression for fusing *n* number of vertices is defined as follows. Fusing of *n* number of nodes within the same fuzzy graph: Let $G = (V,\sigma,\mu)$ be a fuzzy graph and let $u_1, u_2, \ldots u_n \in \sigma^*$. By the join of *n* vertices $u_1, u_2 \ldots, u_n$ we mean:

(i) Fuse the vertices u_1, u_2, u_n in the corresponding crisp graph $G^*=(\sigma^*,\mu^*)$

(ii) The resulting fuzzy graph is

$Gu_1u_2.....u_n=(\sigma u_1u_2 .....u_n, \mu u_1u_2.....u_n)$

Here, $\sigma_{u_1u_2.....u_n}(x) = \{\max[\sigma(u_1), \sigma(u_2), \ldots \ldots \sigma(u_n)]$

if $x = u_1u_2 \ldots \ldots \ldots u_n$

$\sigma(x)$ if $x \neq u_1u_2 \ldots \ldots \ldots u_n\}$ and

$\mu_{u_1u_2.....u_n}(x,y) = \{ \max[\mu(x,u_1), \mu(x,u_2),$
$\ldots \ldots \mu(x,u_n]$

if $y = u_1u_2 \ldots \ldots \ldots u_n$

$\max[\mu(u_1,y), \mu(u_2,y) \ldots \ldots \mu(u_n,y)]$

if $x = u_1u_2 \ldots \ldots \ldots u_n$

$\mu(x,y)$

if $x \neq u_1u_2 \ldots \ldots \ldots u_n$, $y \neq u_1u_2 \ldots \ldots \ldots u_n\}$

SUMMARY

Indistinct or poorly developed brittle plane networks are common in rocks. Their numerical representation can be important for modelers, such as in fluid flow, CCS and hydrocarbon reservoir studies. Hydrocarbon resources are depleting, and flow models realistic to geologic cases are of paramount importance. In this article we introduce the concept of fuzzy graph theory as a first step to fulfill such a far-reaching aim. An example of brittle shear planes consisting of Y and P-planes was considered with different degrees of connection between them**.** We further presented theoretical issues regarding fuzzy digraphs and joining / fusion of vertices.

ACKNOWLEDGEMENTS

CPDA grant supported SM. The Chief Editor and an anonymous reviewer are thanked for offering review comments.

Compliance with Ethical Standards

The authors declare no conflict of interest and adhere to copyright norms.

REFERENCES

Anand, P., Chakraverty, S. and Mukherjee, S., 2021. Fuzzy set concept in structural geology: Example of ductile simple shear. J. Earth System Sci., 130, 193.

Anjali, N. and Mathew, S., 2013. Energy of a fuzzy graph. Annals of Fuzzy Mathematics and Informatics. ISSN: 2093-9310.

Atanssov, K.T. 1999. Intuitionistic Fuzzy Sets. Springer.1-137.

Chen, J. et al., 2020. County-level CO2 emissions and sequestration in China during 1997–2017. Scientific data 7, 1-12.

Chong, F.K., Lawrance, K.K., Lim, P.P., Poon, M.C.Y., Foo, D.C.Y., Lam, H.L. and Tan, R.R., 2014. Planning of carbon capture storage deployment using process graph approach. Energy, 76, 641-651.

Farid, A.M., Thompson, D., Hegde, P. and Schoonenberg, W., 2021. A Tensor-Based Formulation of Hetero-functional Graph Theory. arXiv:2101.07220v1 [cs.AI]

Mukherjee, S., 2014. Atlas of Shear Zone Structures in Meso-scale. Springer Geology. Cham. 1-124, ISBN 978-3-319-0088-6.

Mukherjee, S., 2019. Using graph theory to represent brittle plane networks. In: Problems and Solutions in Structural Geology and Tectonics. Billi A, Fagereng A (Eds). Developments in Structural Geology and Tectonics Book Series. Vol. 5. Series Editor: Mukherjee S., Elsevier. 259-272., ISSN:2542-9000.

Mukherjee, S., Bose, N., Ghosh, R., Dutta, D., Misra, A.A., Kumar, M., Dasgupta, S., Biswas, T., Joshi, A. and Limaye, M. 2020. Structural Geological Atlas. Springer. ISBN: 978-981-13-9825-4.

Misra, A.A. and Mukherjee, S., 2018. Seismic Structural Analysis. In: Misra AA, Mukherjee S. (Eds) Atlas of Structural Geological Interpretation from Seismic Images. Wiley Blackwell. ISBN: 978-1-119-15832-5., 15-26.

Pashin, J.C., Jin, G., Zheng, C., Chen, S. and McIntyre, M.R., 2008. Discrete Fracture Network Models for Risk Assessment of Carbon Sequestration in Coal. Final technical report. URL: file:///F:/Manjusha_25Jan2022/READY%20TO%20SUBMIT/ee/Pashin.pdf (Accessed on 25-Jan-2022)

Ramakrishnan, P.V. and Lakshmi, T., 2008. A note on the fusion of two vertices in a fuzzy graph. Tsukuba J. Math., 32, 155-164.

Sandersons, D.J., Peacock, D.C.P., Nixon, C.W. and Rotevatn, A., 2018. Graph theory and the analysis of fracture networks. J. Struct. Geol., 125, 155-165.

Tan, R.R., Denny, K.S.N., Foo, D.C.Y. and Aviso, K.B., 2010. Crisp and fuzzy integer programming models for optimal carbon sequestration retrofit in the power sector. Chem. Engineering Res. and Design, 88, 1580-1588.

Zadeh, L.A., 1965. Fuzzy sets. Inf. Control, 8, 338-353.

Zhang, Y., Oldenburg, C.M., Finsterle, S., Jordan, P. and Zhang, K., 2009. Probability Estimation of CO2 Leakage Through Faults at Geologic Carbon Sequestration Sites. Energy Procedia, 1, 41-46.

Received on: 27.08.2022; Revised on: 21.12.2022; Accepted on: 24.12.2022

J. Ind. Geophys. Union, 27(2) (2023), 118-125

Study of a dumpyard fire in Perungudi and its effect on tropospheric ozone in an urban region of Chennai, India

S. Tamil Selvi *[1] and S. Najma Nikkath[2]

[1] Department of Physics, KCG College of Technology, Chennai-600 097, Tamil Nadu, India
[2] Department of Physics, Bhaktavasalam Memorial College for Women Chennai-600 080, Tamil Nadu, India
*Corresponding author: tssekar9773@gmail.com

ABSTRACT

The rise of ozone in the atmosphere and its effects on human health and the environment are one of the main concerns in urban areas. This paper examines the environmental threats with focus on concentration of ozone in association with the burning of household waste in open piles in Perungudi. The effects of ozone were investigated from daily values of Perungudi and nearby residential area of Velachery during and after the dumpyard fire for the period April 27, 2022 to July 27, 2022. This study is an effective step toward a better understanding of ozone changes in Perungudi under the changing influence of smoke during the dumpyard fire. Box plot analysis is used to find the nature of the ozone data by identifying mean and median in both the places. Histogram is used to explore the nature of the frequency distribution. Autocorrelation is employed to check the presence of trend or randomness. Results indicate presence of trend, which are not random. The Pearson correlation coefficient was applied to correlate the ozone (O_3) concentration in Velachery. The results show that the ozone concentration in Perungudi is higher when compared with the nearby residential area of Velachery.

Keywords: Dumpyard fire, Box-plot, histogram, Autocorrelation, Pearson correlation coefficient, Perungudi (Chennai, Tamil Nadu)

INTRODUCTION

The quality of air is adversely hit by the aerosol released due to garbage burning, which can be assessed by measuring the concentration of atmospheric pollutants like ozone (O_3). Atmosphere constitutes of various components such as PM_{10}, $PM_{2.5}$, NO_2, SO_4 ground ozone and lead, not to forget to mention the water vapour which plays a key role in the climate of a region. There are other dynamical factors which is more significant in affecting climate (Tamil Selvi et al., 2022). After carbon dioxide and methane, tropospheric ozone is the third leading cause of global warming (Stevenson et al., 2006; Fowler et al., 2008). Tropospheric ozone plays an important role in atmospheric chemistry, air quality, and climate change and is harmful to human health and agricultural production (WHO, 2003; Zeng et al., 2008; Monks et al., 2015; Agathokleous et al., 2020). In recent years, high levels of ozone (O_3) and its effect on air quality have become a global challenge (Paoletti et al., 2014; Li et al., 2019). It has been suggested that for every 10 μg/m^3 increase in ozone concentration, the daily human death rate increases by about 0.3% and the death rate of heart patients by about 0.4% (Colls and Tiwary, 2009).

Tropospheric ozone (O_3) is a very strong oxidant that is an indicator of photochemical oxidants. Ozone is a summer pollutant and an important short-lived climate pollutant (Faridi et al., 2018). Ozone has an associated radiative forcing of 0.35 W/m^2, but its maximum concentrations on the ground rarely last more than two to three hours (Cross and Pierson, 2013). The half-life of tropospheric ozone at 20 degrees Celsius is about three days (Shindell et al., 2012). Tropospheric ozone is produced by chemical reactions between Volatile Organic Compounds (VOCs) and carbon monoxide (CO) and hydroxyl radicals (OH) in the presence of nitrogen oxides in the atmosphere. Therefore, nitrogen oxides and VOCs (as well as CO) are precursors of tropospheric ozone (Crutzen, 1974; Retama et al., 2015). In other words, ozone is formed when pollutants react chemically in the presence of sunlight (Sudo and Akimoto, 2007; Cao et al., 2019). They are typically enhanced by increased atmospheric temperatures. (Zhang et al., 2019).

Garbage burning in the residential areas emits substantial amount of pollutants and toxins, and this is a source with the most uncertainty in the inventories (Sarath, et al., 2015). The massive landfill in Perungudi, a locality in South Chennai, caught fire on April 27, 2022 and continued for three days. With Perungudi as the centre, solid waste is dumped within Chennai city's limits. Around 4,500 tonnes of solid waste is dumped every day by the city Corporation. Concentrated toxic fumes spread over a radius of 6 km above the burning debris. The Velachery neighbourhood near Perungudi and the Pallikaranai marshland were the most affected. The smoke has the potential to affect the native flora and fauna and the health of the urban residents. Children below the age of five, persons with cardio-respiratory conditions, asthmatic patients, people with weak immunity, etc., are affected by the smoke. The smoke enveloped the residential area. The air was thick with ash and smoke. Burnt particulate matter from the dumpyard was suspended in the air around most of the residential neighborhoods in the area (www.the hindu.com).

According to Central Pollution Control Board, detrimental air pollution in Chennai district is a significant problem. Due to severe air pollution people suffered from respiratory problems and other relentless health effects (Sunyer et al., 1997; Nyberg et al., 2000). Except other metropolitan cities, Chennai district is facing a different scenario on pollution harm effects. The monsoon and sea breeze of the coastal regions, makes the peak of the harmful effects to be in moderation. Even when it exceeds the critical level, the coastal air in Chennai helps the situation to be under control (Guttikunda et al., 2014).

STUDY AREA

Chennai city, situated on the shores of the Bay of Bengal, is the capital of Tamil Nadu and the fourth largest metropolis in India. Perungudi lies in the neighborhood of Chennai in the state of Tamil Nadu. It is amidst the IT Estate India expressway. It is bordered on two sides by the famous Old Mahabalipuram road and Perungudi Lake (Tamil Selvi et al., 2021). The strategic location of Perungudi had made the place to transform from a small village to a vibrant commercial and residential hub. Being one of the two major land-fifills in Chennai, the Perungudi dumpyard is always in news for its frequent fires. This causes complaints from the residents about the air pollution and health issues. Tamil Nadu Pollution Control Board has installed real time continuous air quality monitoring station at Perungudi.

The dumpyard in Perungudi also extends its hands till Pallikaranai marsh land, which is aesthetically a beautiful home for rare and local migratory birds. It is desirable to analyze the concentration of ozone in this area during the dumpyard fire. The location of Perungudi in Chennai, India is shown in Figure 1.

DATA AND METHODOLOGY

The study aimed to analyse the ozone data by comparing Perungudi and Velachery data for the period 27th April–27th July, 2022. An assessment of the Perungudi ozone status was studied by comparing with the nearest residential area Velachery, during and after the dumpyard fire. The data was obtained from Central pollution control board. The data spread is analysed using box plot and histogram. Autocorrelation method is used to identify the randomness of the data. The association of ground level ozone was compared using the Pearson correlation coefficient (r) for the study period to find the nature of the trend present in the area. Pearson's correlation coefficient is a statistical measure of the strength of a linear relationship between paired data. Positive values denote positive linear correlation, while negative values denote negative linear correlation and a value of 0 denotes no linear correlation. The Figures 2 and 3 represent the time series plot for Perungudi and Velachery regions of Chennai.

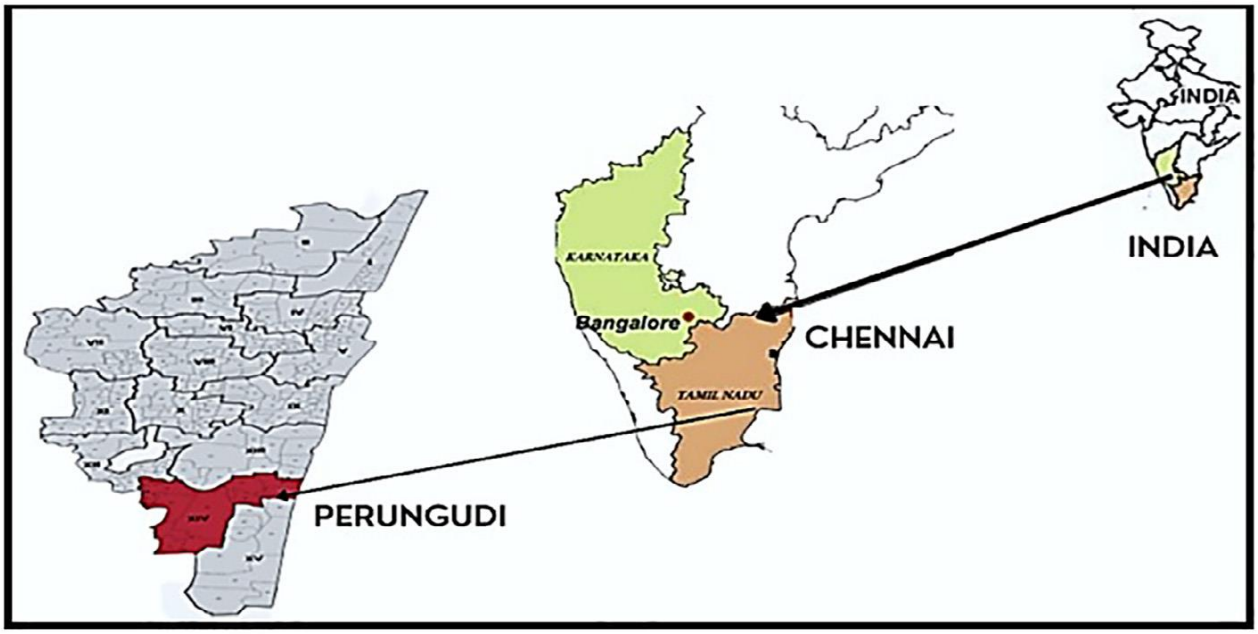

Figure 1. Location of Perungudi in Chennai, India.

BOX- PLOT METHOD

The box - plot is one of the easiest method for visualizing a data set without listing the individual values. The box-plots are also named as the Whisker diagram. The box- plot represents the numerical data in a graphical way. It is a way to show the data distribution systematically. The minimum, lower quartile, Median, Upper Quartile and Maximum value of our statistical data can be found using this method. Although box- plots are more primitive than histograms, they do have a number of advantages. First, the box-plot enables statisticians to do a quick graphical examination on one or more data sets. Box-plots also take up less space and are therefore particularly useful for comparing distributions between several groups or sets of data in parallel (https://en.m.wikipedia.org/wiki/Box_plot). This is a standardized way of displaying the distribution of data, which are shown in Figures 4 and 5 for Perungudi and Velachery data, respectively.

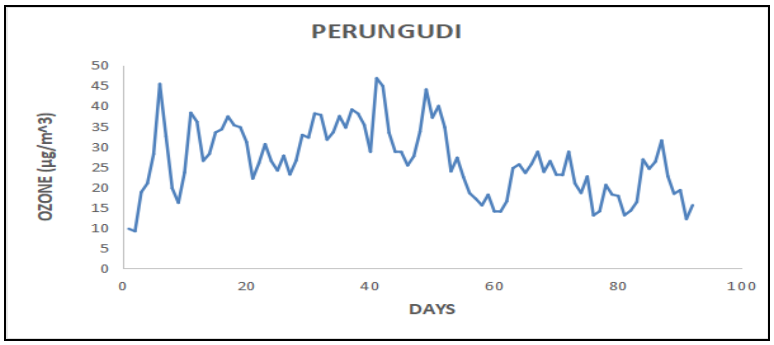

Figure 2. Time series graph for the Perungudi ozone concentration

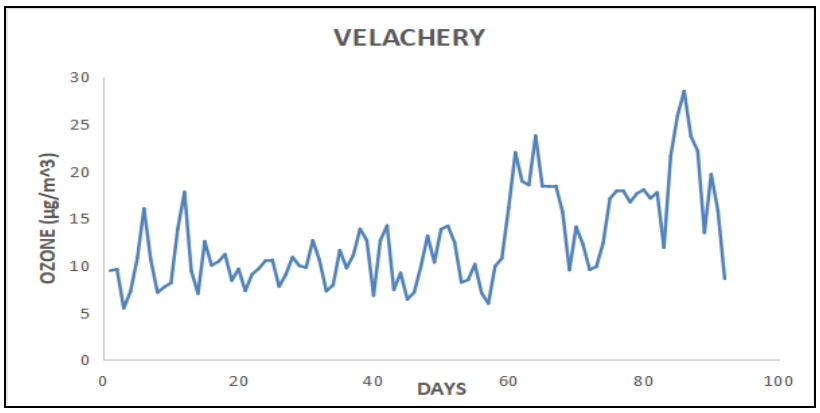

Figure 3. Time series graph for the Velachery ozone concentration

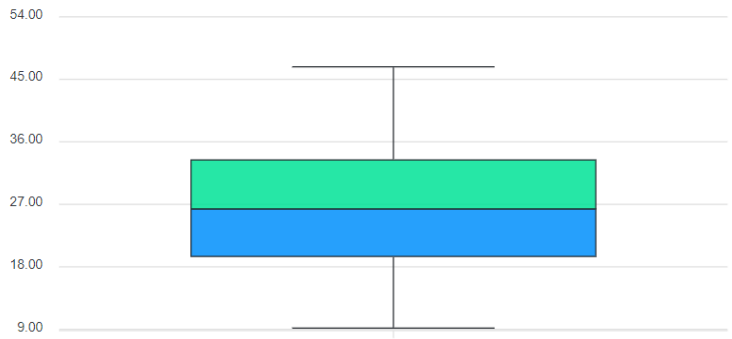

Figure 4. Box-plot for ozone concentration (µg/m^3) at Perungudi

HISTOGRAM METHOD

A histogram depicts the spread and the shape of the continuous given data set and displays the frequency of the data values. It helps in determining the median and the distribution of the given data set. It also display if any gaps or outliers found in the given set of data. If the shape looks like a bell curve, it reveals that the frequencies are equally distributed. The normal distribution is a distribution that has most of the data in the center with decreasing amounts evenly distributed to the left and the right. If one side of the average also falls on the other side of the average, which is the sign of normal distribution.

The histogram is a very familiar graphical tool for a single set of data. The area under the series of rectangles represents the frequency of each value of the ozone (Zai, et al., 2013). Skewed Distribution is the distribution with data clumped up on one side or the other with decreasing amounts trailing off to the left or the right. The graph is biased towards the left side, which is right-skewed distribution and will have the mean to the right of the median. A large number of data values occur on the left side and fewer data on the right side. Histogram of Perungudi and Velachery are depicted in the Figures 6 and 7.

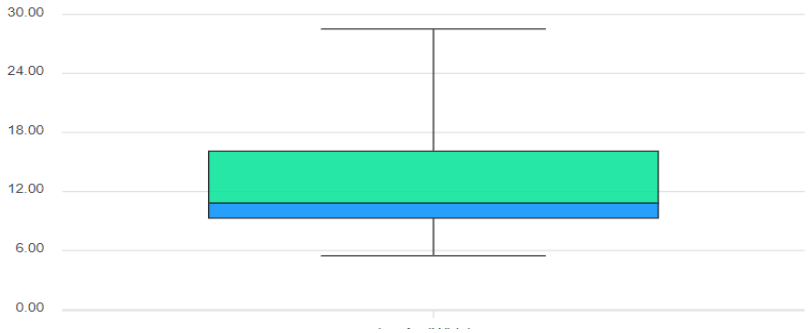

Figure 5. Box-plot for ozone concentration (µg/m^3) at Velachery

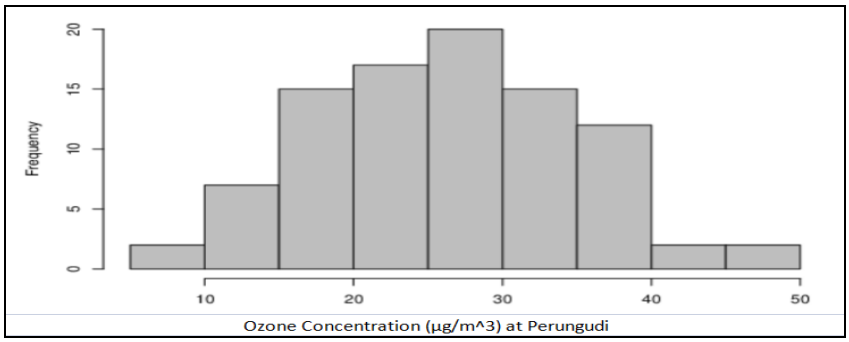

Figure 6. Histogram of ozone concentration at Perungudi

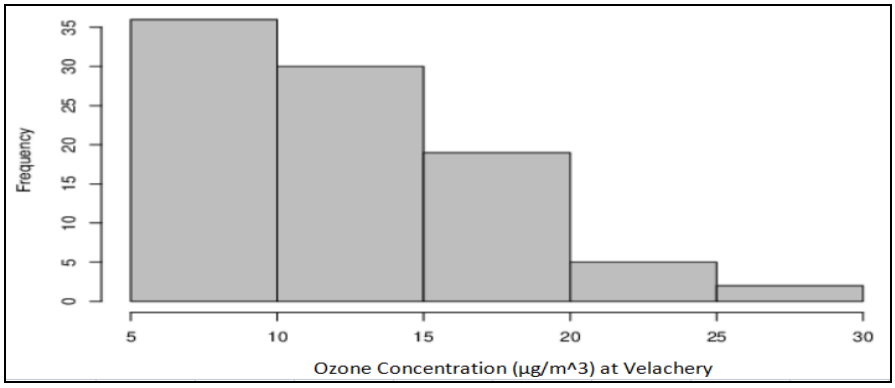

Figure 7. Histogram of ozone concentration at Velachery

AUTOCORRELATION METHOD

The correlogram is a widely used tool for checking the randomness in a data set. Autocorrelations should be near to zero for any and all time lag separations if the data is random. One or more of the autocorrelations will be significantly non-zero, if the data is not random. The Autocorrelation at lag 1 is very high but the other values at lags greater than 1 are relatively small but not zero. It can be confirmed that the data is not random and stationary. The time lag do not fall to zero within few lags rather decays slowly which shows non stationarity in it (Tamil Selvi et al., 2021). Correlogram shows slow decrease as the lags increase is due to the presence of trend while the shape is due to seasonality. The maximum peaks are found at lag 1 in both the data. The correlogram graphs for Perungudi and Velachery are represented in Figures 8 and 9.

PEARSON CORRELATION COEFFICIENT

Testing the degree of correlation between two or more variables is one of the most widely used statistical procedures. Pearson correlation coefficient ('r') is used to determine the strength of linear relationship between two variables (Hashim et al., 2018). The Pearson correlation coefficient, r, can take a range of values from +1 to -1. The correlation coefficient value r = 1 represents a perfect positive correlation and r = -1, indicates a perfect negative correlation. A value of 0 indicates that there is no association between the two variables. A value greater than 0 indicates a positive association; that is, as the value of one variable increases, so does the value of the other variable. A value less than 0 indicates a negative association; that is, as the value of one variable increases, the value of the other variable decreases.

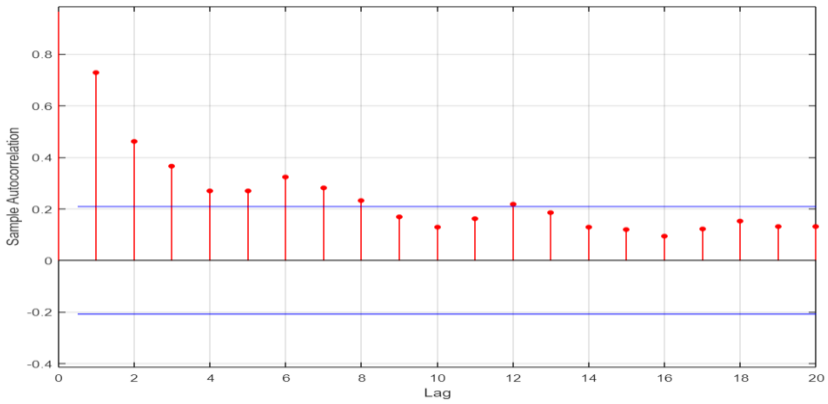

Figure 8. Autocorrelation plot for ozone at Perungudi

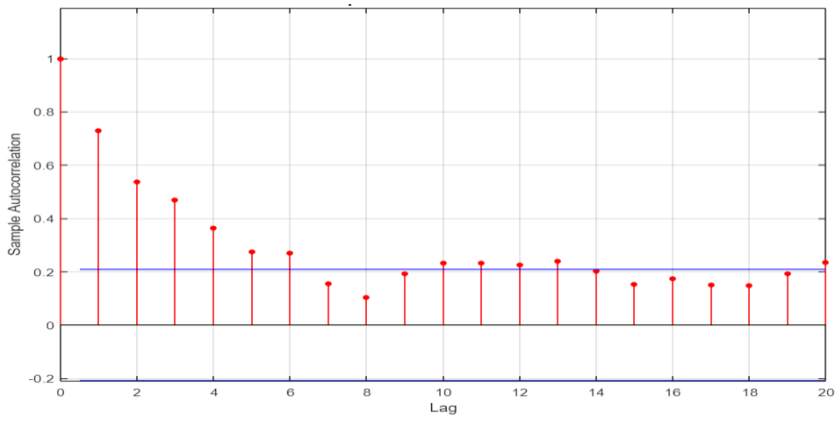

Figure 9. Autocorrelation plot for ozone at Velachery

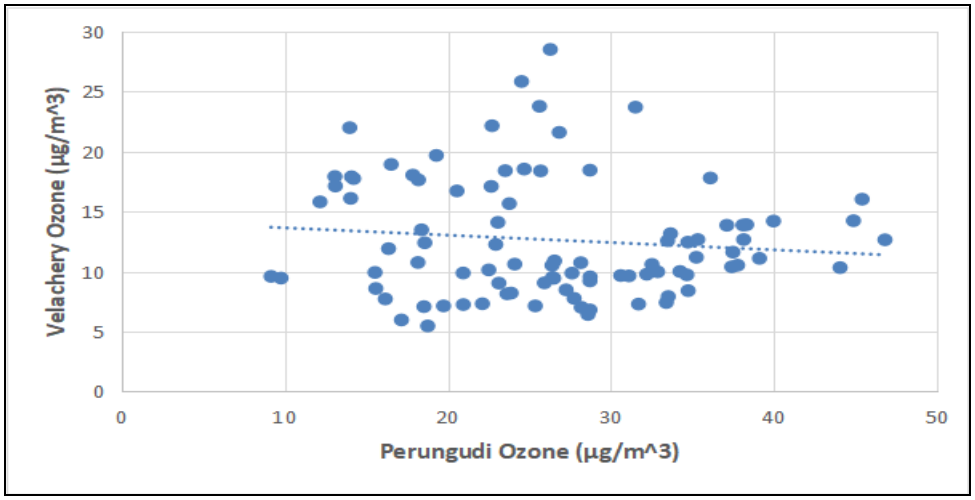

Figure 10. Scatter plot for Perungudi Ozone Vs Velachery Ozone

In the present study, the Pearson correlation method was applied to determine whether there is a statistically significant positive or negative relationship between Perungudi and Velachery ground level O_3 data. The scatter plot for Perungudi Ozone Vs Velachery Ozone are represented in the graph as shown in Figure 10.

RESULTS AND DISCUSSIONS

Velachery is the nearest neighbourhood of Perungudi and a residential area. The smoke from the Perungudi dumpyard fire continuously moved and surround the neighbourhood areas. The box-plot in Figure 4, summarize the median value for Perungudi ozone concentration as 26.335. The maximum ozone is found to be 46.79 and the minimum is 9.17. The mean ozone concentration is 26.005. Similarly, the box- plot in Figure 5 reveals that the median value for Velachery ozone concentration as 10.825. The maximum ozone is found to be 28.51 µg/m^3 and the minimum is 5.47 µg/m^3. The mean ozone concentration is 12.635 µg/m^3. The mean and median is approximately the same for Perungudi as it follows the normal distribution curve in histogram. The mean ozone concentration for Velachery is found to be greater than the median value. The mean value lies to the right of median as it clearly shows the right skewed distribution from the histogram analysis.

In Perungudi correlogram, notable peaks are observed till lag 8 and in Velachery notable peaks are observed till lag 6. The lag doesn't decay and become zero. There exist notable peaks on all the lags. This shows the presence of trend in both the ozone data. After the identification of trend in the ozone series, the nature of the trend is to be explored. Pearson correlation coefficient method is employed to identify the relationship of ozone concentration in both the places. The value of r is found to be -0.1073, which is a negative correlation. The relationship between the variables is weak as the value is nearer to zero. The sign of the Pearson correlation coefficient represents the direction of the relationship. Positive coefficients indicate that when the value of one variable increases, the value of the other variable also tends to increase. Positive relationships produce an upward slope on a scatter plot. Negative coefficients represent when the value of one variable increases, the value of the other variable tends to decrease. Negative relationships produce a downward slope. The value of R^2, the coefficient of determination, is 0.0115, which shows 1.15% variation between the two variables as the sample size of the data taken in study was a small window. The present study provides new insights on the ozone concentration and could pave the way for new findings in the research.

CONCLUSION

The present study analysed the influence of the dumpyard fire episode on the distribution of ozone over the regions such as Perungudi and Velachery regions of Chennai. However, it adds limited evidence to the widely spread of dumpyard fire in a residential area. There is a negative trend associated between Perungudi and Velachery troposheric ozone concentrations. The fire in Perungudi dumpyard doesn't affect the nearby residential area like Velachery. Even though smoke spread over large area, there is no significant ozone formation. The lack of prominent association may be due to other meteorological parameters like temperature, humidity, wind direction etc., The elevated ozone concentration can be seen during the fire days in

Perungudi when compared to Velachery. Though the case study helps to understand the influence of stable burning on ozone at a regional scale for a shorter period of time, demands the insight into deeper understanding of such influences on ozone. The effect of dumpyard fire is a threat to human health and air pollution. The health effects should be carefully studied in further research and authorities should find a solution. This would encourage the development of plans and options to mitigate or adapt to the possible changes. The present study might be a useful supplement to the regulatory authorities in rethinking the existing regulatory plans in controlling the air pollution. The feedbacks and interactions between fire and humans, climate, the atmosphere and ecosystems need to be understood. As proposed by Lavorel et al. (2005), integrated fire research framework could be employed to address fire and climate change issues.

ACKNOWLEDGEMENTS

The authors are thankful to the reviewers who have given critical and valuable suggestions to improve the manuscript to the present form. The authors express sincere thanks to Dr. O.P. Pandey, Chief Editor, JIGU for continuous involvement, encouragement and provided an opportunity to publish this research in the journal.

Compliance with Ethical Standards

The authors declare no conflict of interest and adhere to copyright norms.

REFERENCES

Agathokleous, E., Feng, Z. and Oksanen, E. et al., 2020. Ozone affects plant, insect, and soil microbial communities: A threat to terrestrial ecosystems and biodiversity. Science advances, 6(33), DOI: 10.1126/sciadv.abc1176.

Cao, L., Gao, M., Li, S., Yi, Z., and Meng, X., 2019. Sensitivity analysis of the dependence of the carbon bond mechanism IV (CBM-IV) on the initial air composition under an urban condition. Atmospheric Environ., 215, 116860.

Colls, J., and Tiwary, A., 2009. Air pollution: Measurement, modelling and mitigation. CRC Press, 2-154.

Cross, J.M. and Pierson, R., 2013. Short-Lived Climate Pollutants: why are They Important. Washington: EESI (Environment and Energy Study Institute), 202, 628–1400.

Crutzen, P.J., 1974. Photochemical reactions initiated by and influencing ozone in unpolluted tropospheric air. Tellus, 26(1–2), 47–57.

Faridi, S., Shamsipour, M., Krzyzanowski, M., Ku¨nzli, N., Amini, H., Azimi, F., and Naddafifi, K., 2018. Long-term trends and health impact of PM2. 5 and O3 in Tehran, Iran, 2006–2015. Environment Int., 114, 37–49.

Fowler, D., Amann, M., Anderson, R., Ashmore, M., Cox, P., Depledge, M. and Stevenson, D., 2008. Ground-level ozone in the 21st century: future trends, impacts and policy implications. The Royal Society, London UK. 15/08, 132.

Guttikunda, S.K., Goel, R., and Pant, P., 2014. Nature of air pollution, emission sources, and management in the Indian cities. Atmos. Environ., 95, 501–510.

Hashim, N.I.M., Noor, N.M. and Yusof, S.Y., 2018. Temporal characterisation of ground-level ozone concentration in Klang Valley. In E3S web of conferences 34, 02047. EDP sciences. https://doi.org/10.1051/e3sconf/20183402047.
https://www.thehindu.com/news/national/tamil-nadu/wasted-fire-in-the-dump-yard/article65369820.ece
https://en.m.wikipedia.org/wiki/Box_plot

Lavorel, S., Flannigan, M.D., Lambin, E.F. and Scholes, M.C., 2005. Vulnerability of land systems to fire: Interactions between humans, climate, the atmosphere and ecosystems, Mitigation and Adaptation Strategies for Global Change, 12(1), 33-53.

Li, K., Jacob, D.J., Liao, H., Shen, L., Zhang, Q., and Bates, K.H., 2019. Anthropogenic drivers of 2013–2017 trends in summer surface ozone in China. Proc. National Acad. Sci., 116(2), 422–427.

Monks, P.S., Archibald, A.T., Colette, A., Cooper, O., Coyle, M. and Derwent, R., et al. 2015. Tropospheric ozone and its precursors from the urban to the global scale from air quality to short-lived climate forcer. Atmosph. Chem. Phys., 15(15), 8889.

Nyberg, F., Gustavsson, P., Jarup, L., Bellander, T., Berglind, N., Jakobsson, R., Pershagen, G., et al., 2000. Urban Air Pollution and Lung Cancer in Stockholm. Epidemiology, 11, 487-495. http://dx.doi.org/10.1097/00001648-200009000-00002

Paoletti, E., De Marco, A., Beddows, D.C., Harrison, R.M., and Manning, W.J. 2014. Ozone levels in European and USA cities are increasing more than at rural sites, while peak values are decreasing. Environ. Pollution, 192, 295–299.

Retama, A., Baumgardner, D., Raga, G.B., McMeeking, G.R., and Walker, J.W. 2015. Seasonal trends in black carbon properties and co-pollutants in Mexico City. Atmosph. Chem Physics Discussions, 15(8), 12539–12582.

Sarath, K., Guttikunda, Goel, R., Mohan, D., Tiwari, G. and Gadepalli, R., 2015. Particulate and gaseous emissions in two coastal cities- Chennai and Vishakhapatnam, India. Air Qual Atmos Health, 8(6), 559-572.

Shindell, D., Kuylenstierna, J.C., Vignati, E., van Dingenen, R., Amann, M. and Klimont, Z., et al. 2012. Simultaneously mitigating near-term climate change and improving human health and food security. Science, 335(6065), 183–189.

Stevenson, D.S., Dentener, F.J., Schultz, M.G., Ellingsen, K., Van Noije, T.P.C., Wild, O., et al. 2006. Multimodel ensemble simulations of present-day and near-future tropospheric ozone. J. Geophys. Res., Atmospheres, 111(D8), 1–23.

Sudo, K., and Akimoto, H. 2007. Global source attribution of tropospheric ozone: Long-range transport from various source regions. J. Geophys. Res., Atmospheres, 112(12), 1.

Sunyer, J., Spix, C., Quenel, P., Ponce de Leon, A., Ponka, A., Barumandzadeh, T., Touloumi, G., Bacharova, L., Wojtyniak, B., Vonk, J., Schwartz, J. and Katsouyanni, K. 1997. Urban air pollution and emergency admissions for asthma in four European cities: the APHEA project. Thorax, 52, 760-765.

Tamil Selvi, S., Najma Nikkath, S., and Mahalakshmi, N. 2021. Impact of COVID19 lockdown on the particulate matter over Perungudi, Chennai, India. Materials Today: Proceedings, 280-286. https://doi.org/10.1016/j.matpr.2021.07.296.

Tamil Selvi, S., Najma Nikkath, S., and Mahalakshmi, N. 2022. Analysis of particulate component PM10 over residential and commercial area in urban city of Chennai. Materials Today: Proceedings, 55(2). https://doi.org/10.1016/j.matpr.2022.01.478

World Health Organization. 2003. Health aspects of air pollution with particulate matter, ozone and nitrogen dioxide: report on a WHO working group, Bonn, Germany 13-15 January 2003 (No. EUR/03/5042688)., Copenhagen:WHO Regional Offifice for Europe.

Zai, M., Jan, B. and Rashid Kamal Ansari, M., 2013. Investigating Explorative Character of Ozone Layer Depletion between Pakistan and China: A Comparative Regional Study. J Basic. Appl. Sci., 9, 483-488

Zeng, G., Pyle, J.A. and Young, P.J., 2008. Impact of climate change on tropospheric ozone and its global budgets. Atmospheric Chem. Physics, 8(2), 369–387.

Zhang, J., Wei, Y. and Fang, Z., 2019. Ozone Pollution: A Major Health Hazard Worldwide, Frontiers in Immunology, 10, 2518. DOI: 10.3389/fimmu.2019. 02518

Received on: 29.09.2022; Revised on: 28.02.2023; Accepted on: 12.03.2023

J. Ind. Geophys. Union, 27(2) (2023), 126-136

Structural inferences from Bouguer gravity data analysis in and around Armoor area, southern part of the Godavari basin, Eastern Dharwar craton (India)

Telu Raju*, Udaya Laxmi G, Linga Swamy Jogu and Kolipaka Venu

Centre of Exploration Geophysics, Osmania University, Hyderabad-500 007, India.
*Corresponding author: teluraju50@gmail.com

ABSTRACT

The Gravity survey area is located south of the Godavari basin in Eastern Dharwar Craton. Bouguer gravity anomaly is prepared which is based on 965 observations acquired at 200-meter station interval in and around the Armoor region (18°30'N-19°00'N and 78°00'E–78°30'E) in Nizamabad district, Telangana state of India, covering an area of about 604 sq km. The Bouguer gravity anomaly reveals the variance from -33 mGal to -54 mGal. The qualitative analysis of the Bouguer gravity anomaly map, low-pass, high-pass filtered and tilt derivative maps, reveal a combination of E-W, N-S and NW-SE trends that coincide with the lineaments and deep-seated faults present in the region. Six highs (H1-H6), three lows (L1-L3), and four deep-seated faults (F1-F4) are identified in this area. The high anomalies are attributed to the basement rocks, basic dykes and mineralized zones (banded magnetite quartzite) while low anomalies correspond to the variations in the peninsular gneissic complex.

Keywords: Armoor area, Eastern Dharwar Craton, Bouguer gravity, Structures, Low pass and high pass filters, Tilt derivatives.

INTRODUCTION

The current research region is located in the eastern Dharwar craton (EDC) in southern part of the peninsular India, belonging to the Archean-Proterozoic age. It is confined between 18°30'N-19°00'N and 78°00'E-78°30'E and covers toposheets E44G1, E44G2, E44G5 and E44G6. The study area is approximately 604 square kilometers and is located in the Armoor (Armur) region to the south of the Godavari basin in Nizamabad district, Telangana state, India. Figure 1 shows the location map of the study area. EDC contains the lithologically oldest rock types of granites, schists and other intrusive igneous rocks that have been extensively studied. EDC evolved through many tectonic events, resulting in the development of secondary structures like faults and folds, that reallocated the basement configuration to the present shape. The various litho-units of the study area includes Archean granites. Gray granites are rich in hornblende and biotite and pink granites are associated with potash feldspar (orthoclase). Amphibolites and plagioclase with little quartz and igneous intrusive (quartz veins, pegmatites, dolerites) and a small portion of chlorite schist and banded magnetite quartzite (BMQ) are found in the study area. Geophysical studies were attempted to better understand the subsurface configuration. Early geophysical studies in this region includes regional gravity (Subramanyam and Verma, 1982; Ramadass et al., 2003; Mishra et al., 2008; Sunil et al., 2010), heat flow (Gupta, 1982; Gupta et al., 1987) and deep seismic profiling across the Dharwar craton (Kaila et al., 1979; Reddy et al., 2003). In recent times also, several parts of the South Indian Shield have been actively probed by the different geophysical methods (Anand and Rajaram, 2002; Ramadass et al., 2006; Mandal et al., 2018; Malleswari et al., 2019; Rama Rao et al., 2020, 2023; Raju and Udayalaxmi, 2021; Lingaswamy et al., 2022).

GEOLOGICAL SETTING

The area under consideration belongs to the eastern Dharwar craton. Detailed geology of the study area is shown in Figure 2. The area contains various litho-units of the oldest rock types belonging to the Dharwar supergroup. They are exposed widely in most parts of the studied area. The Peninsular Gneissic Complex (PGC) rock units are further identified and re-organized based on the variations in their mineralogical composition. Dark coloured or grey granites cover around 15-20% of the study area and contain quartz with plagioclase, chlorite schist, feldspars, amphiboles, hornblende, and biotite. Later on, these grey granites are metamorphosed to hornblende and biotite gneisses. Amphibolites and migmatites are intruded into these grey granites as veins and linear ridges. Pink granites are believed to be younger than the grey granites and are dominated by K-Feldspars of microcline, orthoclase and sanidine. Alkali feldspar granite is medium to coarse-grained, dominated primarily by alkali feldspar with few mafic minerals. The microcline phenocrysts have quartz and twinned plagioclase inclusions with occasional alkali feldspar (Ramakrishna et al., 2016; Praveen et al., 2018). The metamorphic rocks of the EDC show an increase in the grade of metamorphism to southward from greenschist to amphibolite's facies (Jayanada et al., 2013). Amphibolites and pegmatites are intruded into the pink granites. Small clusters of amphibolites and meta basalts are encompassed in to younger pink granites on the SE and SW corners of

the study area. Banded magnetite quartzites are found on the northern side of the study area (Figure 2). A long dolerite dyke intrusive traverses north to south and has a length of about 35-40 km. The area has various rocks accompanied by rich mineral resources (GSI, 2000, 2010).

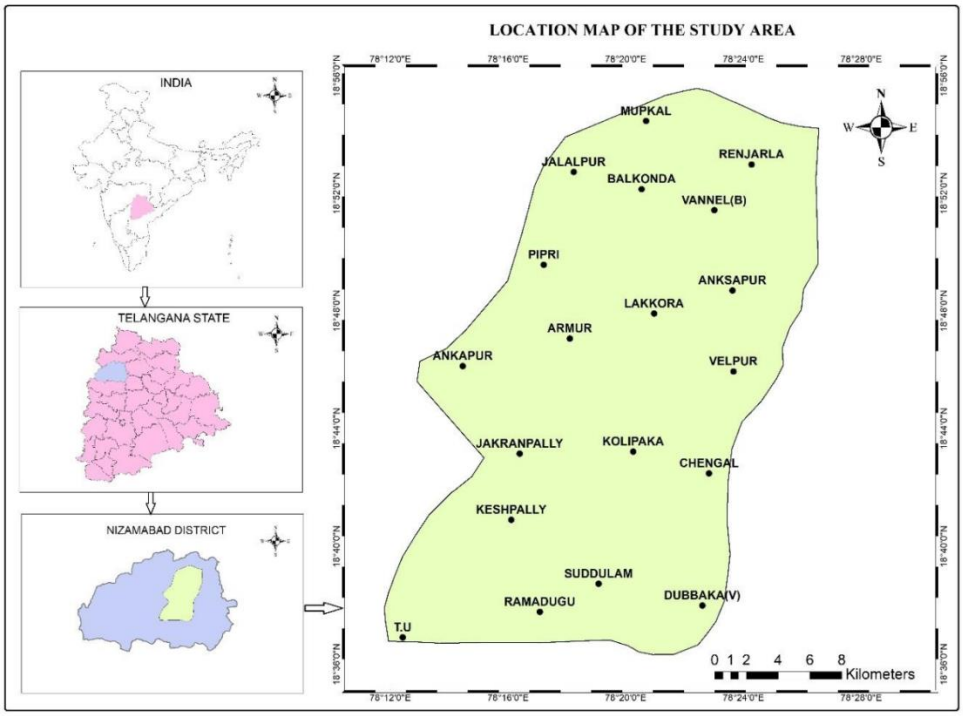

Figure 1. Location map of the study area

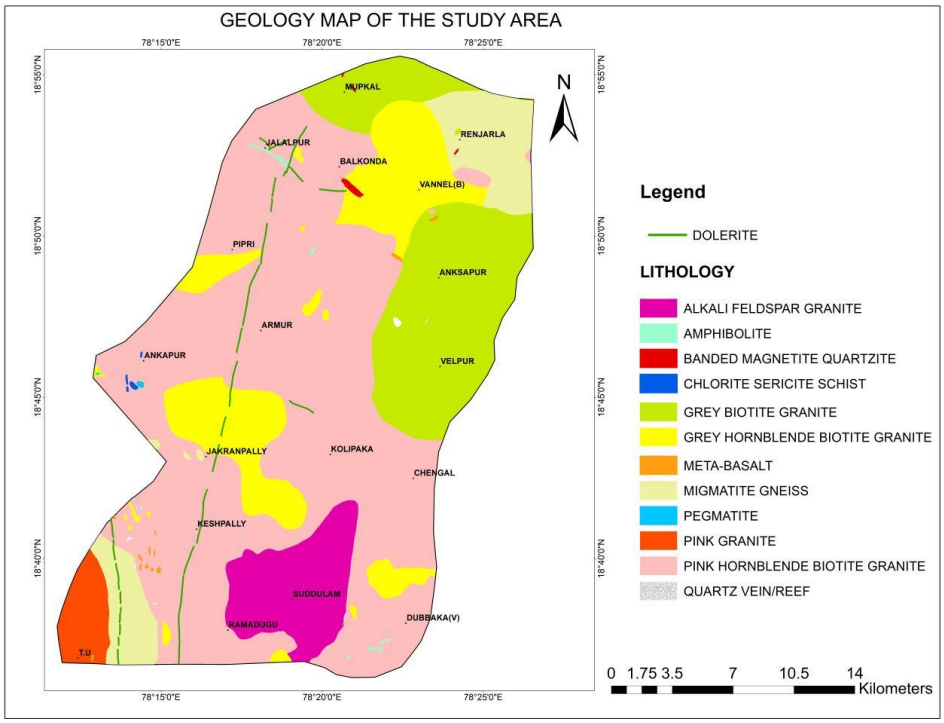

Figure 2. Geological map of the study area (Source: Bhukosh.gsi.gov.in)

DATA ACQUISITION AND METHODOLOGY

A total of 965 gravity measurements were taken, with a station interval of 200 m using a LaCoste Romberg (Model G-1106) gravimeter. Elevations are taken with the Arrow Gold-100 model DGPS instrument, the accuracy of the present DGPS is 10-15 cm and overall gravimeter sensitivity of 1 µgal and a range of 7500 mGals. There were a total of 11 traverses, the major traverse from Dichpally (Telangana University) to Mupkal, trending north-south is 40 km in length. Another major traverse is from Venchiryal (near Renjarla) to Dubbak village, which is 36 km long. All other traverses are nearly 10 to 20 km in length. In all, four traverses trend north to south, while remaining in different directions depending on road accessibility (Figure 3). The data is analyzed to study the natural configuration of geological structures such as faults and lithological boundaries (Jaques et al., 1984; Davis et al., 2004). Because of the large station interval, this can be considered a semi-detailed study. The surveys were directed towards tracing out and verifying the detailed geological setting and identifying different tectonic structures in the area that may have a bearing on subsurface structures and geological contacts.

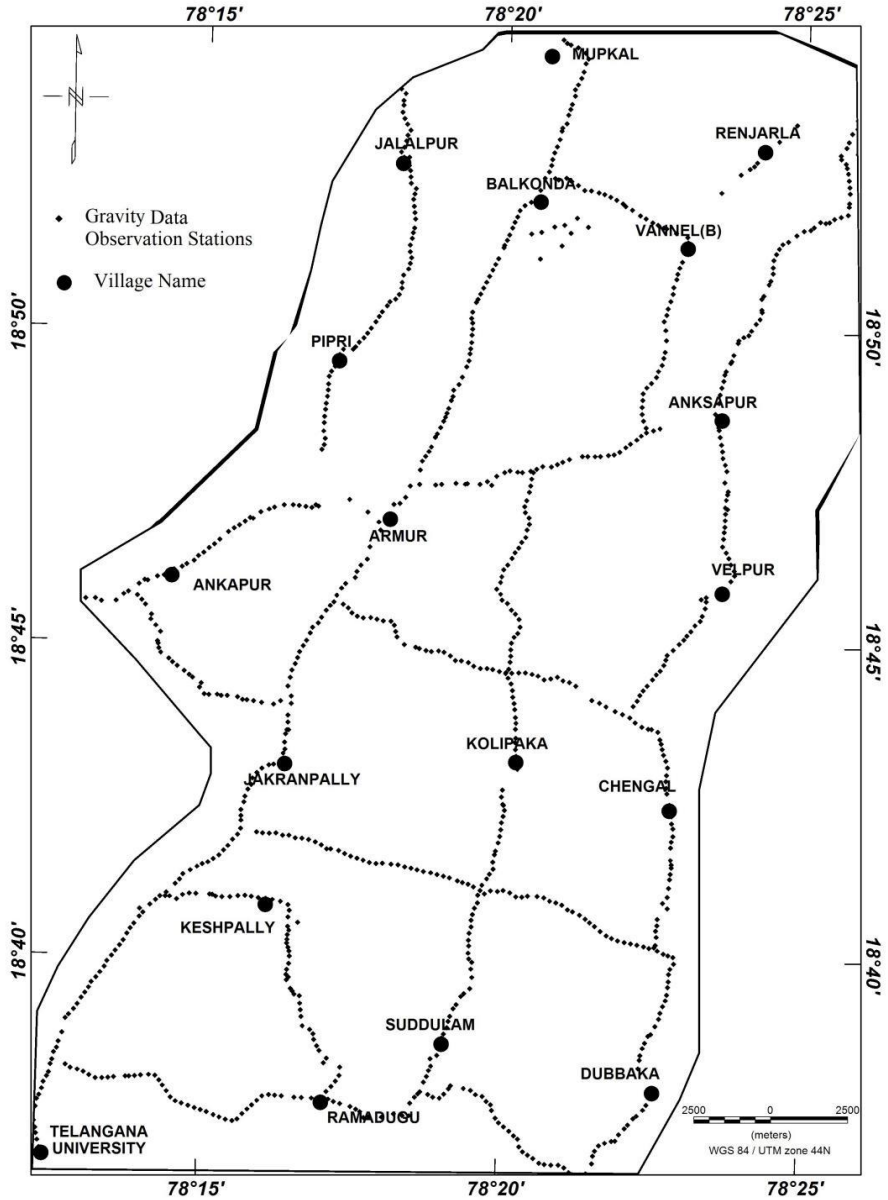

Figure 3. Location of gravity observations in the study area

GRAVITY DATA ANALYSIS

Qualitative analysis is an important tool to indicate and identify the geological formations. It can be accomplished by following the analogy to mathematical or experimental surveys of known structures (Al-Heety et al., 2017). Gravity data may be displayed as contour maps and profiles (Geosoft software, Oasis Montaj, 2016). Density is a physical feature of gravity and changes in density inside the earth at various depths lead to a wide range of gravity anomalies (Peterson and Reeves, 1985). Gravity data analysis includes creating gravity anomaly maps, upward continuations, derivative, regional and residual maps. Fourier transforms are very useful for converting from the frequency domain to the wave number domain and calculating derivatives (Blakely and Simpson, 1986; Ates et al., 1999). Then the major structural direction and trends may be identified by comparing gravity maps, geology maps and structural maps of the study area.

BOUGUER GRAVITY ANOMALY

The Bouguer anomaly map, which reflects the combined effects of lateral density heterogeneities at depth, is widely used in resource mapping and geodynamic studies (Agarwal et al., 1994). Short-wavelength anomalies are typically associated with surface geology, whereas long-wavelength anomalies reflect deeper structures. The Bouguer anomaly map was generated after applying the corrections to the gravity data as shown in Figure 4. It reveals that the variance in Bouguer anomaly is from -33 mGal to -54 mGal. The conspicuous and interesting zones of the area were determined using this anomaly map. Gravity highs are indicated as H1 to H6, while gravity lows by L1 and L2. F1, F2 and F3 are a subsurface inferred faults. H1 and H3 high anomalies are correlated with the stretched long dolerite dyke, the direction of the dolerite dyke is north to south (N-S), occupying the areas of Jalalpur to Dichpally (Telangana University). H2 is another prominent high, which is correlated with high density granites and migmatite gneisses. At Renjarla, Balkonda and Mupkal, H4, H5, and H6 gravity high closures are identified as mineralized zones, correlated geologically with banded magnetite quartzite (BMQ). Similarly, L1 is identified as low anomalous zone, which has been correlated with alkali feldspar and hornblende biotite granites at Ramadugu, Suddullam, Kolipaka and Lakkora areas; the other low anomaly L2 is identified at Ankapur and Munipally areas, correlated by small amount of pegmatite and chlorite schist in the western part of the study area. The area between high and low anomalous zones is identified as a subsurface inferred fault from the Bouguer anomaly map (Figure 4), F1, F2 and F3 can be traced based on nature of contours i.e. elongate crowded contours (Rao and Murthy, 1978).

LOW PASS AND HIGH PASS FILTERS

The residual (high pass) anomaly arises due to the geological features or ore deposits of interest which is defined by the survey's objective. Due to their deep–seated origin, the regional (low pass) anomalies exhibit broad and uniform variation in contrast to residuals (high pass) (Reynolds, 1997), which possess sharp anomalies with high curvature due to their relatively shallow origin. Thus, Low pass filtered anomalies should be determined to start with and subtracted from the Bouguer anomalies (Keary and Brooks, 1991). Small, localized gravity anomalies are less important for studying large-scale crustal structures than regional anomalies that could be recreated with a low-pass filter. On the other hand, a high-pass filter can decrease regional effects when investigating anomalies caused by shallow crustal bodies.

Low pass filtered Bouguer gravity anomaly

The regional features were observed in Figure 5. The northwestern part of the study area is a high anomaly zone due to the dolerite dyke in greater depth at Jalalpur, Pipri and Balkonda areas. The same features extend towards the south, like Jakranpally and Keshpally areas. Similarly, deep-seated features were identified in the study area's east and southeast zones. The middle part of the region, i.e., the Ramdugu and Kolipaka areas have low regional anomalies and similarly, the western part of the are has low regional anomaly at Ankapur.

High pass filtered Bouguer gravity anomaly

Figure 6 represents high pass filtered map reflecting the shallow depth local geological features. Banded magnetite quartzite was found at Mupkal, Balkonda and Renjarla, which are not regionally located; shallow depth dolerite dykes were discovered at Armur, Pipri, Jakranpally and Keshpally. Anksapur, Chengal and Dubbaka areas have high residual anomalies, while Vannel (B), Kolipaka, Jalalpur and Ankapur are characterized by low residual anomalies.

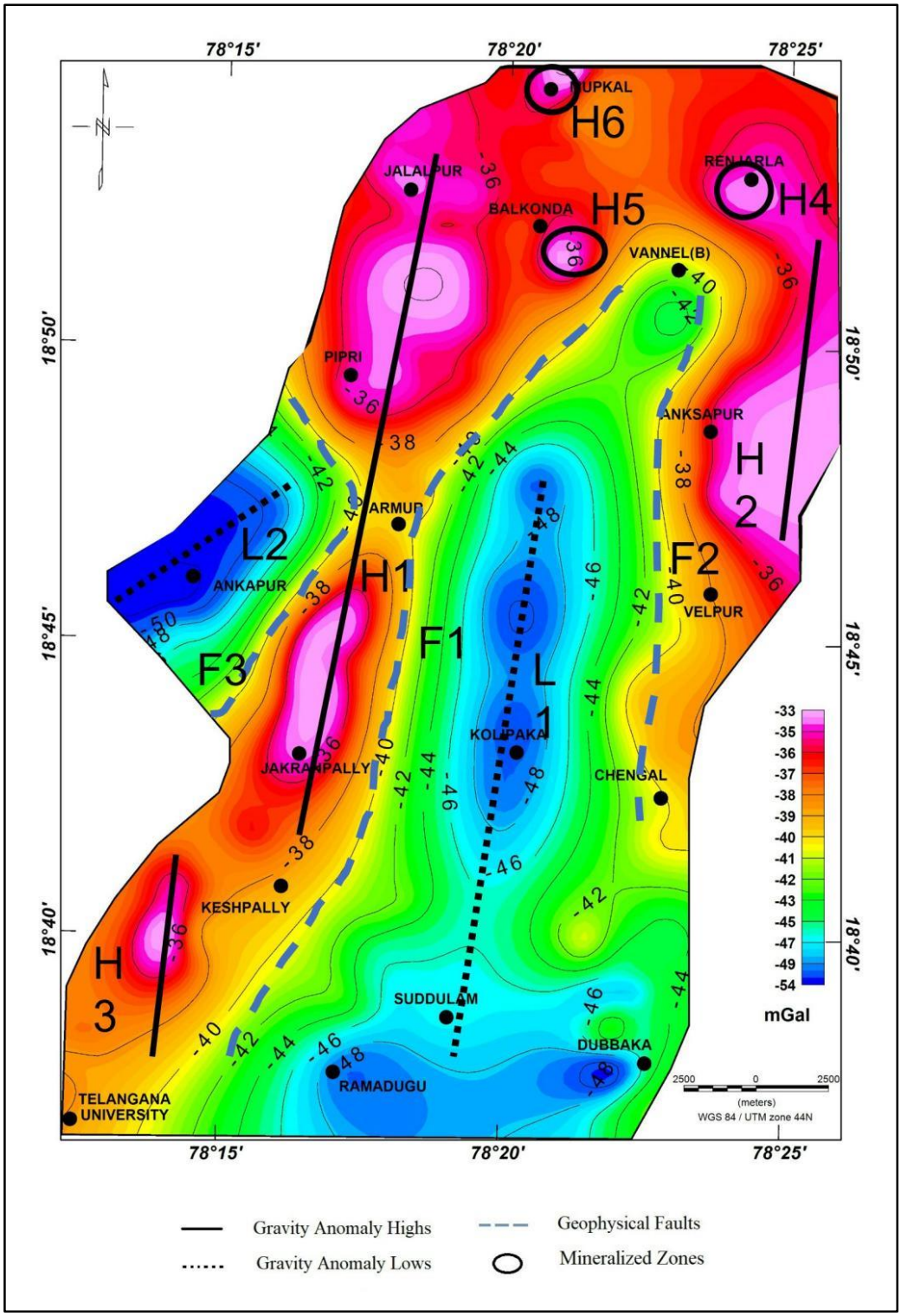

Figure 4. Bouguer gravity anomaly map of the study area

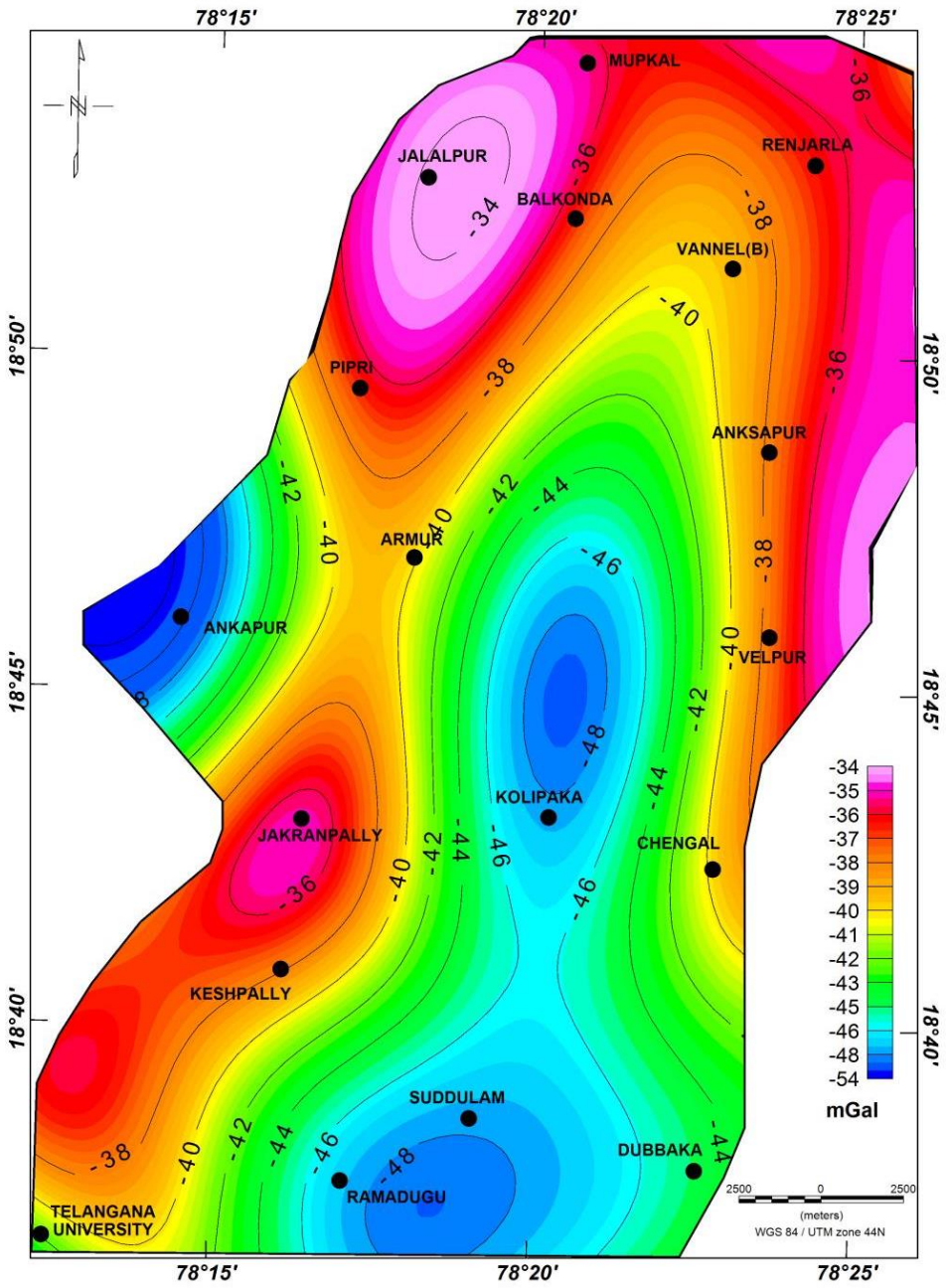

Figure 5. Low pass filtered Bouguer anomaly map of the study area

TILT DERIVATIVE ANALYSIS

The tilt derivative is the ratio between the vertical derivative and total horizontal derivative to the inverse of the tilt angle (Miller and Singh, 1994; Verduzco et al., 2004; Chowdari et al., 2017).

$$\Theta = \tan^{-1} \frac{\partial f / \partial z}{\partial f / \partial h}$$

Where, Θ = tilt angle and ∂f/∂h and ∂f/∂z are the total horizontal and first vertical derivatives of Bouguer gravity anomaly respectively.

The tilt derivative map had simplified the horizontal position with a stretch of edges from Figure 7. The highest value of the tilt angle derivative is -1.5524 rad and the lowest value of the tilt derivative is 1.5625 rad. H1 and H2 are the high anomalous trends observed from Jalalpur to

Dichpally (Telangana University), which were geologically correlated with dolerite dykes. In the eastern section of the study area, H3 was shown as a high anomalous zone. F1, F2, F3 and F4 are four geophysical subsurface interred faults observed over the investigation zone (Figure 7) as stated above. The faults trend NE-SW, E-W and in N-S in direction. Crowded contour elongation indicates fault or contact, faults can similarly be traced because beds of higher density may come into contact with beds of relatively lower density (Rao and Murthy, 1978). Tilt derivative highs H4 and H5 with positive values coincided with banded magnetite quartzites at Renjarla and Balkonda. In the observation, the Mupkal area was also identified as a high-anomaly zone, correlated by banded magnetite quartzite. Due to alkali feldspar granites and hornblende granites, the negative value of tilt derivative lows L1 and L3 could be seen from Ramadugu to Vannel (B). On the other hand, the western part of the study area have a low anomaly L2 in tilt angle due to a small amount of pegmatite and chlorite schist.

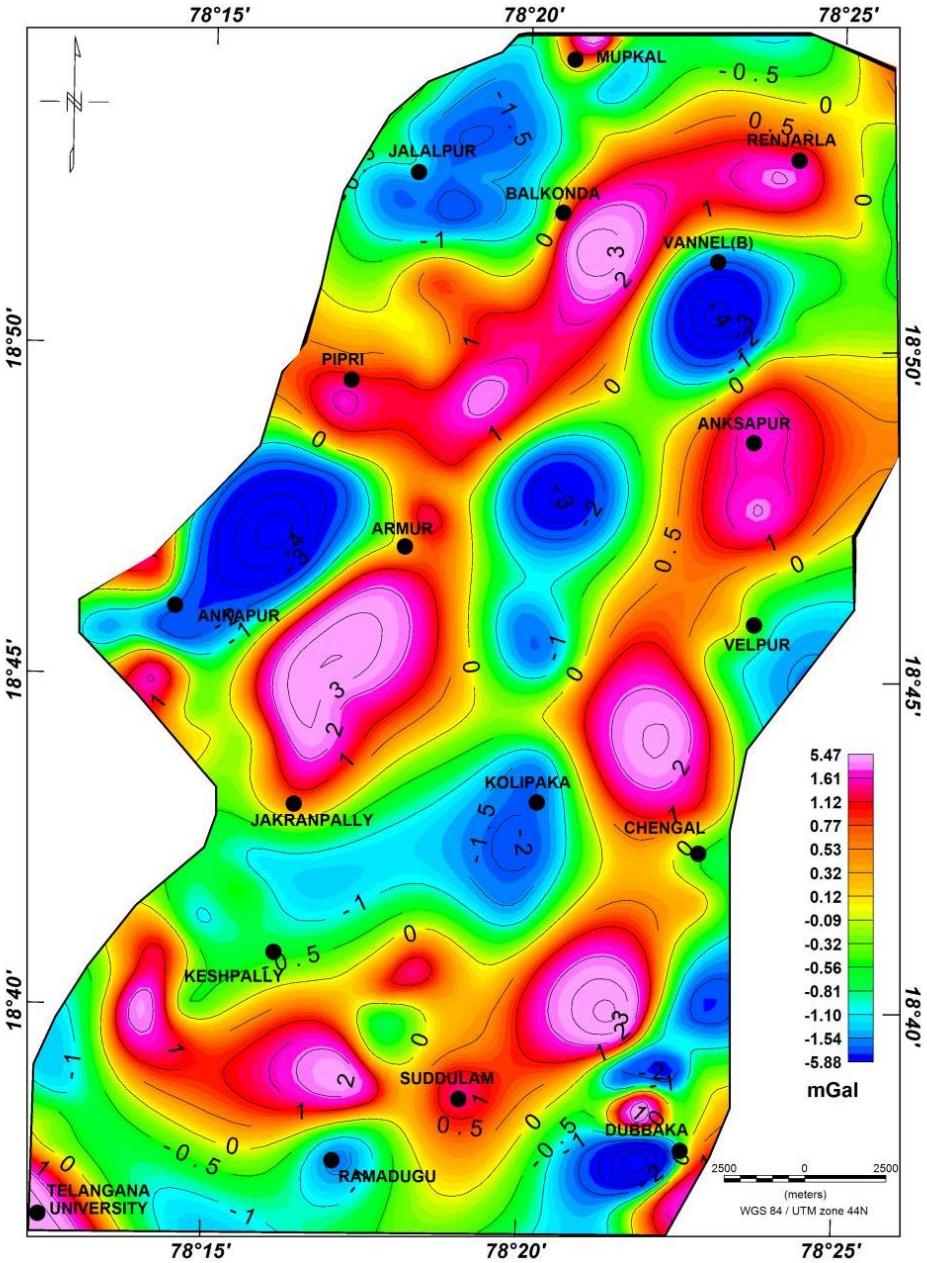

Figure 6. High pass filtered Bouguer anomaly map of the study area

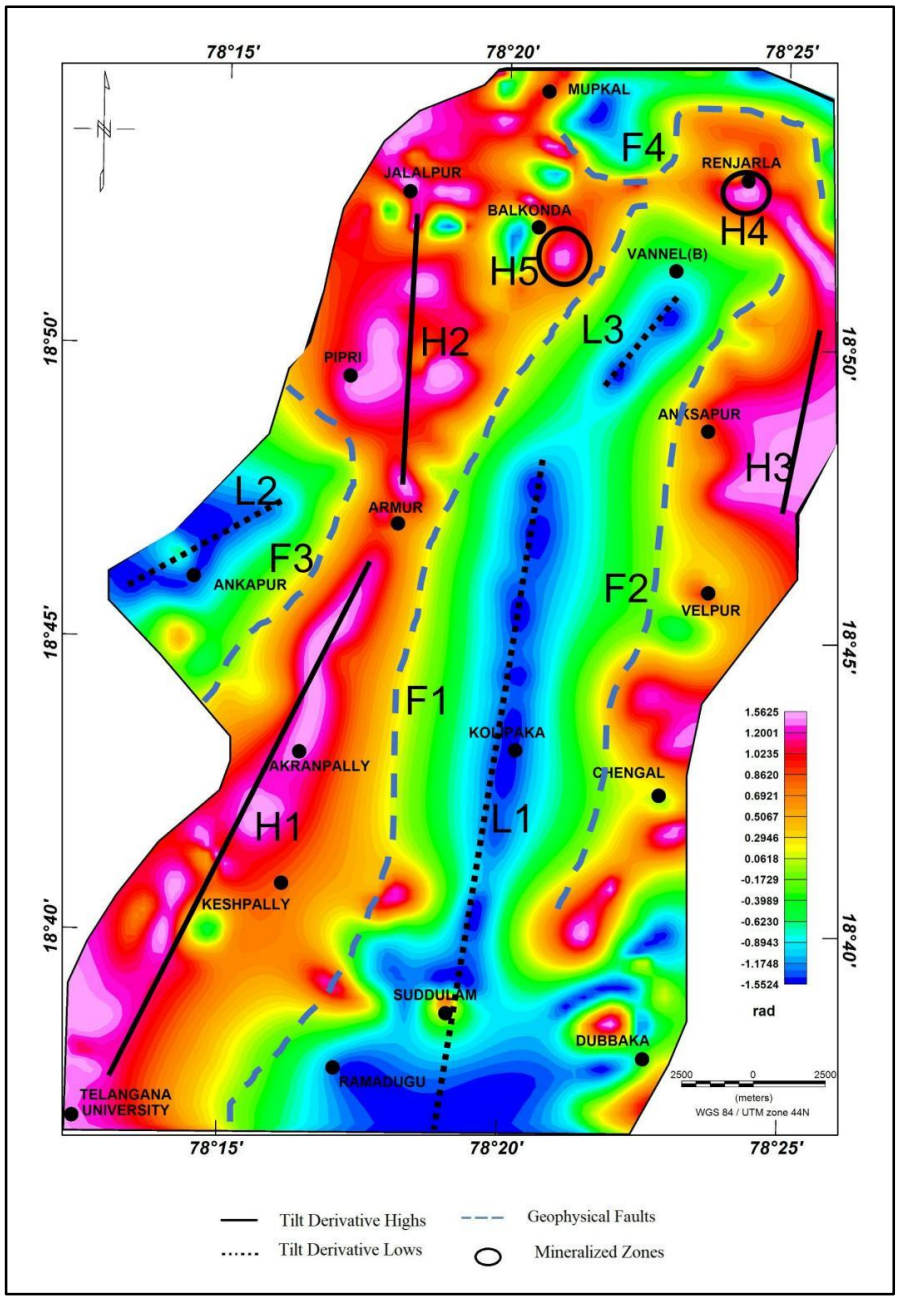

Figure 7. Tilt angle derivative Bouguer anomaly map of the study area

STRUCTURAL MAP

The structures have been delineated from a combination of Bouguer anomaly and tilt angle maps (Raju and Udayalaxmi, 2021; Lingaswamy et al., 2022) where the input of the tilt derivative is crucial (Oruc and Keskinsezer, 2008). Figure 8 shows the structural map resulting from the Bouguer gravity study. Black, thick lines H1, H2 and H3 are identified as positive anomaly areas. A large trend is noticed in the western side of the area as dyke (dolerite) and it has been tied up with geology. In the east, a trend might imply a highly dense body. Black-dot lines L1, L2 and L3 are indicated as low anomalous trends in the central part, which may cause alkali feldspar and biotite in granite. Blue dotted lines are indicated as subsurface inferred faults from the gravity studies, F1, F2, F3 and F4 are four inferred faults were identified geophysically by the gravity studies (Figure 8). Other high anomalies marked by black circles H4, H5 and H6 are identified as mineralized zones; three mineralized spots were identified in the study area at Balkonda, Mupkal and Reanjarla areas.

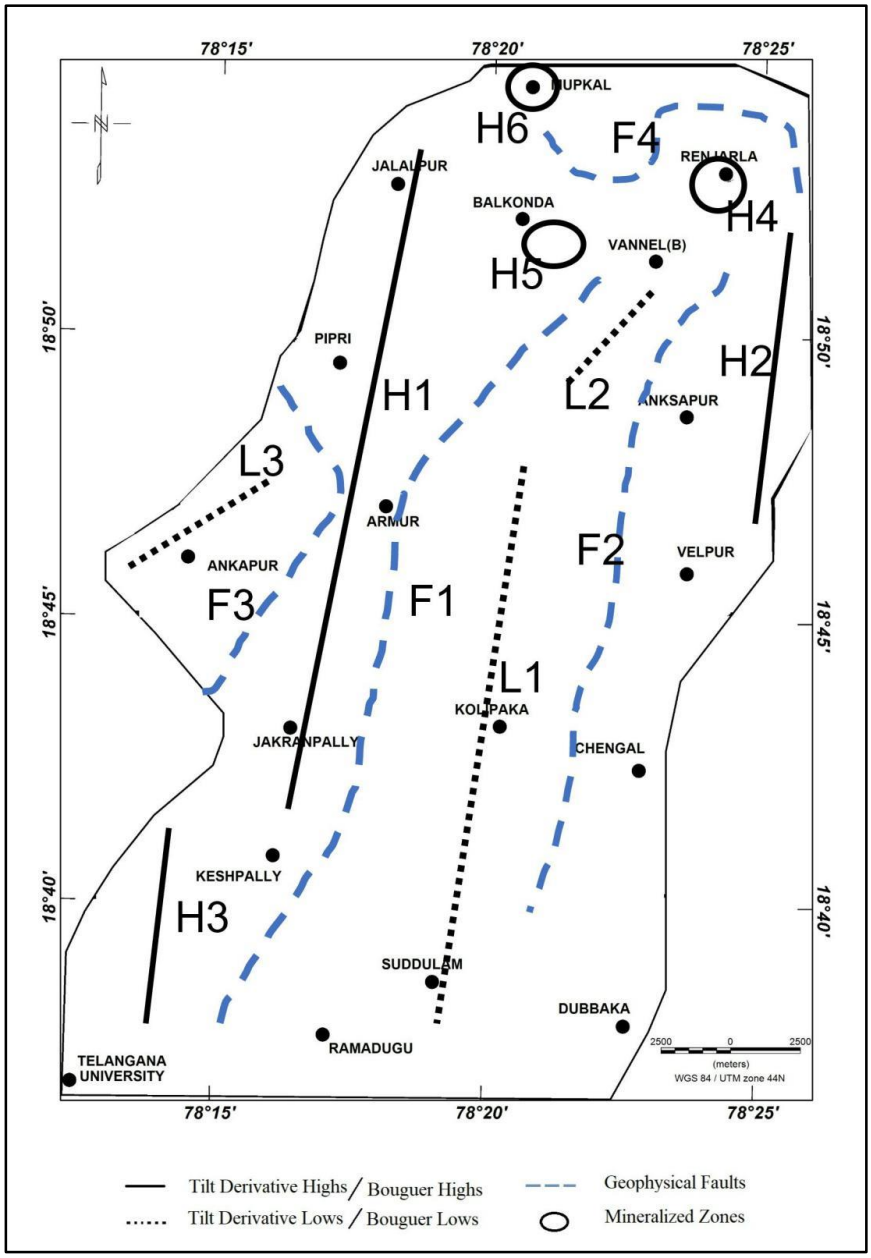

Figure 8. Structural map of the study area from Bouguer gravity data analysis

DISCUSSION

The identification of the research area's essential structural orientations and trends is made possible by comparing gravity maps and geology map. The variation in Bouguer gravity anomaly is -54 mGal to -33 mGal. From the Bouguer anomaly map (Figure 4), the prominent and interesting zones of the area were identified, high anomalies are correlated with the geology of long stretched dolerite dyke, whose direction is north to south (N-S), this feature was also identified in the regional anomaly map (Figure 5). The Bouguer map identifies the point of inflection (between high and low anomalous zones) as a subsurface inferred fault. The low anomalous zone, which is correlated geologically with alkali feldspar and hornblende biotite granites in the middle of the area and the other low anomalous zone, which is identified in the western part of the area, are correlated with small amounts of pegmatite and chlorite schist. Gravity highs are recognized mineralized zones associated geologically with banded magnetite quartzite (BMQ) at Renjarla, Balkonda and Mupkal regions in the northern section of the study area and these features were also observed in the residual anomaly map in Figure 6.

These structures have also been clearly delineated from the tilt angle map (Figure 7). The N-S direction of long stretched high anomalous trends from Jalalpur to Dichpally (Telangana University) has been observed. These were correlated geologically by dolerite dyke. The northern side highs coincide with banded magnetite quartzites at Renjarla and Balkonda. Geophysical subsurface interred faults are identified in the study area. The tilt derivative lows are noticed at Ramadugu to Vannel (B) and in the western part of the study area due to alkali feldspar granites, hornblende granites, little pegmatite and chlorite schist. From the structural map (Figure 8), faults, dykes, and mineralized zones were captured. Dykes and mineralized zones were correlated geologically.

CONCLUSIONS

Bouguer gravity surveys were conducted in and around Armoor region lying south of Godavari basin in Eastern Dharwar Craton. The structural fabric of the region was elucidated. the qualitative analysis of Bouguer gravity anomaly map, low pass, high pass and tilt derivative maps reveals a combination of E-W, N-W and NW-SE trends coinciding with the lineaments and deep-seated faults present in the region. The high anomalies are attributed to basement rocks containing basic dykes. Mineralized zones were identified in the northern part of the study area, near Balkonda (behind Model School), Renjarla (Gan Gutta) and Mupkal (Temple Gutta), that contain banded magnetite quartzite (iron ore). These anomalous zones signify variations in the peninsular gneissic compex.

ACKNOWLEDGEMENTS

The authors are very much thankful to the Head, Department of Geophysics, Centre of Exploration Geophysics, Osmania University, Hyderabad for providing necessary facilities to carry out the work and also acknowledge the UGC, New Delhi, India for their support to work and funding from the BSR- RFSMS Fellowship.

Compliance with Ethical Standards

The authors declare no conflict of interest and adhere to copyright norms.

REFERENCES

Agarwal, B.N.P., Das, L.K., Chakravorty, K. and Sivaji, C.H., 1994. Analysis of the Bouguer anomaly over central India: a regional perspective. Mem. Geol. Soc. India, 31, 469-494.

Al-Heetym E.M.S., Al-Mufarji, M.A. and Al Esho, L.H., 2017. Qualitative Interpretation of gravity and aeromagnetic data in west of Tikrit City and surroundings, Iraq. Int. J. Geosci. 8(02),151-166.

Anand, S.P. and Rajaram, M., 2002. Aeromagnetic data to probe the Dharwar craton. Curr. Sci., 83(2),162-167.

Ates, A., Kearey, P. and Tufan, S., 1999. New gravity and magnetic anomaly maps of Turkey. Geophys. J. Int. 136(2), 499-502.

Blakely, R.J. and Simpson, R.W., 1986. Approximating edges of source bodies from magnetic or gravity anomalies. Geophysics, 51(7), 1494-1498.

Chowdari, S., Singh, B., Rao, B.N., Kumar, N., Singh, A.P. and Chandrasekhar, D.V., 2017. Structural mapping based on potential field and remote sensing data, South Rewa Gondwana Basin, India. J. Earth System Sci., 126, 1-27.

Davis J., Mushayandebvu M.F., and Smith R., 2004. Magnetic detection and Characterization of Tertiary and Quaternary buried channels: SEG Expanded Abstracts, 23.

Geological Survey of India (GSI), 2000. Geology and Mineral Resources of India. GSI, Publication.

Geological Survey of India (GSI), 2010. Geology and Mineral Resources of India. GSI, Publication.

Geosoft (Oasis Montej and GMsys), 2016. Geophysical Processing and Analysis module of Geosoft.

Gupta, M.L., 1982. Heat flow in the Indian Peninsula-its geological and geophysical implications. Tectonophysics, 83(1-2), 71-90.

Gupta, M.L., Sharma, S.R., Sundar, A. and Singh, S.B., 1987. Geothermal studies in the Hyderabad granitic region and the crustal thermal structure of the Southern Indian Shield. Tectonophysics, 140(2-4), 257-264.

Jaques A.L., Lewis J.D., Smith C.B., Grocery G.P., Ferguson J., Chappell B.W. and Mc Culloch M.G., 1984. The diamond bearing ultrapotassic (lamporite) rocks of the west Kimberley region In: J. Kornprobst (Ed.), Kimberlites and related rocks, 1,225-244.

Jayananda, M., Tsutsumi, Y., Miyazaki, T., Gireesh, R.V., Kapfo, K.U., Hidaka, H. and Kano, T., 2013. Geochronological constraints on Meso-and Neoarchean regional metamorphism and magmatism in the Dharwar craton, southern India. J. Asian Earth Sci., 78, 18-38.

Kaila, K.L., Chowdhury, K.R., Reddy, P.R., Krishna, V.G., Narain, H., Subbotin, S.I.,Sollogub, V.B., Chekunov, A.V., Kharetchko, G.E., Lazarenko, M.A. and Ilchenko, T.V., 1979. Crustal structure along Kavali-Udipi profile in the Indian peninsular shield from deep seismic sounding. J. Geol. Soc. India, 20(7), 307- 333.

Keary, P. and Brooks, M. 1991. An introduction to Geophysical Exploration. Blackwell Scientific Publications, second edition, 254.

Linga Swamy, J., Udaya Laxmi,G., Chandrashekar, B. and Ravi Kumar, B., 2022. Subsurface structural features inferred from ground magnetic data in parts of Nagarkurnool and Wanaparthy districts, Telangana State (India) J. Ind. Geophys. Union, 26(5), 396-406.

Malleswari, D., Veeraswamy, K., Azeez, K.A., Gupta, A.K., Babu, N., Patro, P.K. and Harinarayana, T., 2019. Magnetotelluric investigation of lithospheric electrical structure beneath the Dharwar Craton in south India: Evidence for mantle suture and plume-continental interaction. Geosci. Front., 10(5), 1915-1930.

Mandal, B., Rao, V.V., Sarkar, D., Bhaskar Rao, Y.J., Raju, S., Karuppannan, P. and Sen, M.K., 2018. Deep crustal seismic reflection images from the Dharwar craton, Southern India-evidence for the Neoarchean subduction. Geophys. J. Int., 212(2), 777-794.

Miller, H.G. and Singh, V., 1994. Potential field tilt-a new concept for location of potential field sources. J. Appl. Geophys., 32(2-3), 213-217.

Mishra, D.C., Tiwari, V.M. and Singh, B., 2008. Geological Significance of Gravity Studies in India, Golden Jubilee Memoir Memoir, 66. J. Geol. Soc. India., pp.329-372.

Oruc, B and Keskinsezer, A., 2008. Structural setting of the Northeastern Biga Peninsula (turkey) from Tilt Derivatives of Gravity Gradient Tensors and Magnitude of Horizontal Gravity Components. Pure. Appl. Geophytes, 165, 1913-1927.

Paterson, N.R. and Reeves, C.V., 1985. Applications of gravity and magnetic surveys; the state-of-the-art in 1985. Geophysics, 50(12), pp.2558-2594.

Praveen, K., Anjaneyulu, M., Narshimha, C. and Reddy, U.V.B., 2018. Petrology and geochemistry data of the precambrian granitoids from the Hyderabad area, part of Eastern Dharwar Craton, Telangana state India. Data in Brief, 21, 1909-1917.

Raju, T. and Udaya Laxmi, G., 2021. delineation of subsurface Structures by using magnetic Studies in parts of Nizamabad District, Telangana state, India. J. Emerging Technologies and Innovative Res., 8(11), c24-c31.

Ramadass, G., Rao, I.R., Srinivasulu, N. and Himabindu, D., 2003. Density Studies in the Dharwar Craton along the Jadcharla-Goa Subtransect. J. Geol. Soc. India, 61(4), 439-448.

Ramadass, G., Rao, I.R. and Himabindu, D., 2006. Crustal configuration of the Dharwar craton, India, based on joint modeling of regional gravity and magnetic data. J. Asian Earth Sci., 26(5), 437-448.

Ramakrishna, C., Mallesh, G., Ravi, C. and Reddy, M.N., 2016. Petrological and Geochemical Studies on Granitoids in Bibinagar-Bhongir Area, Nalgonda District, Telangana, India. Int. J. Engineering Res. applications, 6, Issue 4(2), 57-63.

Rama Rao, J.V., Ravi Kumar, B., Kumar, M., Singh, R.B. and Veeraiah, B., 2020. Gravity of Dharwar craton, southern Indian shield. J. Geol. Soc. India, 96, 239-249.

Rama Rao, J.V., Kumar, B.R. and Veeraiah, B., 2023. A possible paleorift zone in the Central Dharwar Craton of South Indian Shield: Evidence from regional gravity anomalies. Geosyst. Geoenviron. 2(2), 100141.

Rao, B.S.R. and Murthy, I.V.R., 1978. Gravity and Magnetic methods of prospecting.

Reddy, P.R., Prasad, B.R., Rao, V.V., Sain, K., Rao, P.P., Khare, P. and Reddy, M.S., 2003. Deep seismic reflection and refraction/wide-angle reflection studies along Kuppam-Palani transect in the southern granulite terrain of India. Mem. Geol Soc. India, 50, 79-106.

Reynolds, J.M., 1997. An introduction to applied and environmental geophysics, John wiley and Sons Ltd, 1-796.

Subrahmanyam, C. and Verma, R.K., 1982. Gravity interpretation of the Dharwar greenstone-gneiss-granite terrain in the southern Indian shield and its geological implications. Tectonophysics, 84(2-4), 225-245.

Sunil, P.S., Radhakrishna, M., Kurian, P.J., Murty, B.V.S., Subrahmanyam, C., Nambiar, C.G., Arts, K.P., Arun, S.K. and Mohan, S.K., 2010. Crustal structure of the western part of the Southern Granulite Terrain of Indian Peninsular Shield derived from gravity data. J. Asian Earth Sci., 39(6), 551-564.

Verduzco, B., Fairhead, J.D., Green, C.M. and MacKenzie, C., 2004. New insights into magnetic derivatives for structural mapping. The leading edge, 23(2), 116-119.

Received on: 11.02.2023; Revised on:08.03.2023; Accepted on: 12.03.2023

J. Ind. Geophys. Union, 27(2) (2023), 137-152

Investigations of GPS-based total electron content (TEC) data at different low latitude IGS stations and its relevance to earthquake precursor studies

Manish Awasthi[1, 2], Raj Pal Singh[2] and Devbrat Pundhir[3*]

[1]Department of Electronics and Communication Engineering, GLA University, Mathura-281406
[2]Department of Physics, GLA University, Mathura. India-281406
[3]Seismo-electromagnetics and Space Research Laboratory, Department of Physics,
Raja Balwant Singh Engineering Technical Campus, Bichpuri, Agra, India-283105
*Corresponding author: devbratpundhir@gmail.com

ABSTRACT

In the present paper, IGS-TEC data of five low latitude stations which include Lucknow (26.9ºN, 80.96ºE), Bangalore (13.02^{0}N, 77.57^{0}E), Hyderabad (17.42^{0}N,78.55^{0}E), Port Blair (11.64ºN, 92.71ºE), and Lhasa (29.66ºN, 91.10ºE) are analyzed during high and low solar activity periods i.e. period-I and period-II, respectively to check its usefulness for earthquake precursory studies. The durational variations show that peak VTEC lies between 08:00 and 10:00 hrs (UT) at all the stations and ranges 25-50 TECU during period-I, it lies at the same time interval but within the range of 14-20 TECU during the period-II. The VTEC values are higher in the equinoctial months during both periods under consideration. In all seasons, seasonal peak VTEC values are noticed to vary between 14 and 42 TECU during period-I and 7 to 18 TECU during period-II. The influence of solar activity is studied on GPS-TEC in terms of sunspot numbers and solar flux index F10.7 cm and it is found that these solar indices are more fluctuating in the period-I than that period-II and attain peak values of ~ 175 and ~185 in period-I, and ~55 and ~85 during period-II. This enhanced solar activity causes more fluctuation in TEC data in period–I, compared to period -II. In addition, the effect of magnetic storms is also studied on GPS-TEC data and it is noticed that TEC is significantly affected in severe magnetic storms. This study provides a better understanding of the behavior of low latitude ionosphere during high and low solar activity periods.

Keywords: Ionosphere, IGS-TEC, Solar Activity, Solar Flux F10.7, Sunspot Numbers.

INTRODUCTION

In the recent era, the study of the ionosphere has become very important because of its wide area of applications, especially the low latitude ionosphere, which is affected by many geophysical phenomena such as magnetic storms, solar flares, and many anthropogenic sources which include nuclear explosions, dust storms, and volcanic activities. The ionospheric irregularities like Equatorial Ionization Anomaly (EIA), spread-F, and sporadic E, also affect the ionosphere which can be studied from the variation in ionospheric parameters (Pundhir et al., 2017a). So it is necessary to examine the effect of these factors on the ionosphere, which provides a better understanding of its structure and dynamics. For this, a diurnal, seasonal, and annual study of the ionosphere is inevitable. These studies are very important before examining the ionospheric data in earthquake precursory studies because the ionosphere is highly complex and variable and can be perturbed by a slight change in any of its parameters (Pundhir et al., 2017a).

Numerous researchers have studied the ionosphere morphologically by using TEC data that yielded remarkable findings (Natali and Meza, 2011; Wu et al., 2012; Akala et al., 2013; Huy et al., 2014). On account of the existence of EIA in India, extensive study of low latitude ionosphere is carried out by many workers using TEC observations based on global positioning system (GPS) measurements and have compared their findings with international reference ionospheric (IRI) models (Bhuyan and Borah., 2007; Mukherjee et al., 2010; Kumar et al., 2012; Prasad et al., 2012; Sharma et al., 2012; Chakraborty et al., 2014; Karia et al., 2015; Rathore et al., 2015; Pundhir et al., 2017b). The GPS-based TEC studies have succeeded in forecasting the ionosphere's behavior. In addition, these studies help detect the impact of solar activities on the ionosphere (Lastovicka, 2002; Dashora et al., 2009; Trivedi et al., 2011, 2013; Xu et al., 2012; Adebiyi et al., 2014). During space weather events like geomagnetic storms, the variation of TEC in the Indian region is studied at many low latitude stations namely; Rajkot (Bagiya et al., 2009), Varanasi (Kumar et al., 2012), Bhopal (Trivedi et al., 2011), Shimla (Rama Rao et al., 2009), and Agra (Pundhir et al., 2017a, b). The morphological studies by Kumar et al. (2012) have investigated the variations of vertical total electron content (VTEC) recorded during the low solar activity period extending from May 2007 to April 2009 at Varanasi (25.16^{0}N, 82.59^{0}E), located close to EIA crest and rest two International GNSS Service (IGS) stations Hyderabad (17.20^{0}N, 78.30^{0}E) and Bangalore (12.58^{0}N, 77.33^{0}E) in India. They have examined the diurnal and seasonal variations of TEC, and the effect of geomagnetic storms on it. It is reported that TEC is minimum during the winter months (November- February) and attains maximum during equinoctial months (March, April, September, and October) at all three stations. It assumed intermediate values during the summer months (May-August). Monthly, seasonal, and

annual variability of GPS-TEC has been compared with those derived from the IRI 2007 model with three different options of topside electron density, NeQuick, IRI01-corr, and IRI 2001. Results of GPS-TEC and IRI 2007 TEC models are found consistent for monthly, seasonal, and annual variations recorded at all three stations. Moreover, TEC variations are examined during geomagnetic quiet and disturbed days of all the months and seasons from May 2007 to April 2008 at Varanasi. It is observed that TEC variations are more affected during disturbed days in comparison to quiet periods.

Rathore et al. (2015) statistically compared total electron content (TEC) derived from the recent version of the IRI model (IRI 2012) with those recorded at Varanasi and results were found consistent with the correlation coefficient of 0.9 and root mean square deviations generally around 25-70% for diurnal comparisons. Pundhir et al. (2017b) carried out morphological studies of low latitude ionosphere using GPS-TEC data of Agra station for the years 2007 and 2011 and compared their results with the IRI-2012 Model and reported a good correlation (0.98) between two data sets during all the three seasons for both the years except for winter season of the year 2007. TEC values were higher the during equinox and lower during the winter seasons. Morphological spectral analysis of TEC data obtained at mid and high latitudes using GPS receivers was carried out by Yasyukevich et al. (2017). The harmonic variations of the varying time period in the TEC spectrum were found whose amplitude varies according to solar activity period. Considering the short-term TEC data (6 months, January 2016-December 2016) in relation to solar proxies, were studied by Parwani et al. (2019). They reported a sinusoidal pattern of diurnal TEC and semi-annual oscillation of seasonal TEC.

In this paper, TEC data recorded at five IGS stations Lucknow (LCK3), Banglore (IISC), Hyderabad (HYDE), Port Blair (PBRI), and Lhasa (LHAZ), have been analyzed for two years 2012 (period-I) and 2018 (period-II) during high and low solar activity respectively. The impacts of solar activity and magnetic storms have also been examined for both periods by using the variation of solar flux F10.7, sunspot numbers, and ∑Kp. The objective of the present work is to study the behavior of TEC during high and low solar activity to understand morphological variation in low latitude ionosphere. This paper provides a better understanding of TEC perturbations due to other activities except for earthquakes. So these investigations play a very important role to check their usefulness for earthquake precursory studies.

EXPERIMENTAL DETAILS

The electron density of the ionosphere is widely affected by solar activity, magnetic storms, and other geophysical phenomena like earthquakes, etc. For studying the spatial and temporal behaviour of the ionosphere globally, a network of 510 IGS stations has been established. At these stations, GPS receivers are deployed for recording the TEC data. Each of these receivers comprises an L_1/L_2 GPS antenna, a GPS receiver, connecting cables, and monitors two frequencies, f_1= 1.57545 GHz and f_2=1.2276 GHz, and 11 satellites can be tracked simultaneously. Receivers record the phase and amplitude and code/carrier divergence for each satellite being tracked. The satellites with elevation angles greater than 50^0 are tracked for avoiding the effect of multipath, troposcatter, and water vapours (Rama Rao et al., 2006). Receivers compute TEC from the carrier phase and combined frequency measurements in TEC units (1 TECU = 10^{16} electron/m^2). C/A code measurements are used on L_1 while on L_2 semi-codeless P-code measurements are taken in all the receivers. The biases induced in TEC values are eliminated using CP offset command on the GSV4004B installation by entering the biases in meters, for each pseudo-random noise (PRN). Further, the receiver's internal biases are also well taken care of prior to the final estimation of TEC data. Receivers estimate slant total electron content (STEC) by using the relation (Yadav et al., 2015)

$$\mathrm{STEC} = \frac{f_1^2 f_2^2}{f_1^2 - f_2^2}\left(\frac{P_1 - P_2}{40.3}\right) \qquad \text{.....(1)}$$

where f_1, f_2 are frequencies of satellite signal, P_1 and P_2 are pseudo ranges in meters

Vertical TEC (VTEC) is obtained from slant TEC by multiplying it by the suitable mapping function as given below (Mannucci et al., 1993)

$$S = \frac{1}{\cos z} = \left[1 - \left(\frac{r_e \cos\delta}{r_e + h_s}\right)^2\right]^{-\frac{1}{2}} \qquad \text{.....(2)}$$

where h_s, r_e, δ, and, z, stand for the effective height of the ionosphere, the mean radius of the earth in kilometers, elevation angle, and zenith angle (in degrees) respectively. For determining ionosphere price point (IPP) location, the

ionospheric effective height is considered as 350 km (Rama Rao et al., 2006).

This method is adopted for computing TEC at the site of all GPS receivers and is logged by employing suitable software. This GPS-TEC data is put in the public domain by many centers, e.g. Jet Propulsion Laboratory (JPL), Centre for Orbit Determination (CODE), Energy Mines and Resource Centre (EMR), European space agency (ESA), Script Orbit and Permanent Array Centre (SOPAC), and California Special Reference Centre (CSRC) through International GNSS Services (IGS), from where it can be downloaded.

We have downloaded GPS-TEC data measured at five IGS stations viz; Lucknow, Bangalore, Hyderabad, Port Blair, and Lhasa located at low latitudes obtained from the joint center of Script Orbit and Permanent Array Centre (SOPAC) and California Special Reference Centre (CSRC), through their website http://garner.ucsd.edu/pub for studying the diurnal, seasonal variation in the data during high and low solar activity period and for identifying the effect of magnetic storms on it.

METHODS OF PROCESSING THE TEC DATA

The GPS-TEC data obtained from IGS stations is in RINEX format which is converted into text format using the software developed by Seemala (2011). This software creates a time series of TEC data with a time resolution of 1 minute. The GPS-TEC data of each day of each station is averaged out and converted into hourly data. The monthly average value of VTEC for each hour is obtained by taking the mean of hourly values of VTEC of that hour for all the days of that month. Contour plots for the hourly average are obtained from MATLAB software. The seasonal mean value of TEC for each hour is estimated from the average hourly values of VTEC of that hour for all the days lying in that season. Similarly, the yearly mean of each hour is obtained by taking the average of all the TEC values of that hour for all the days in that year.

RESULTS AND DISCUSSION

Diurnal variations

The five contour plots are depicted in Figure 1a, b which show the hourly average variations of TEC data in different months for the Periods-I and II extending from 01 January to 31 December 2012 and 01 January to 31 December 2018 respectively at all five IGS stations i.e. Lucknow (LCK3), Bangalore (IISC), Hyderabad (HYDE), Port Blair (PBRI) and Lhasa (LHAZ). The gap in the contour plot of Hyderabad IGS station indicates the non-availability of VTEC data during May and June 2012. Looking at both of these figures it is clear that VTEC increases during sunrise to an afternoon maximum and after this, it reduces to its lowest level just before the setting of the sun. The common characteristics of low latitude ionosphere as noticed from the diurnal variation of TEC is that the VTEC variations attain minimum values during morning hours and then it enhances slowly with a time of day acquiring peak value in the afternoon and after this, it decreases steadily and attains a minimum value prior to sunset. These features of TEC variations are similar to those observed by other workers (Mukherjee et al., 2010; Kumar et al., 2012; Sharma et al., 2012; Pundhir et al., 2017b). The morning to midday values is highly useful in navigation and forecasting (Rama Rao et al., 2006; Bagiya et al., 2009). Monthly variations seen on all the IGS stations considered may be due to variations in the intensity of arriving solar radiations (Natali and Meza et al., 2011; Akala et al., 2013). The peak values of the VTEC at all the stations lie between 08:00 and 10:00 hrs (UT) and range of 25-50 TECU during the period-I, it lies at the same time interval but within a range of 14-20 TECU during the period-II. It is clear from the TEC variations of both periods that peak values are higher in the high solar activity period (2012) and lower in the low solar activity period (2018). The cause for this is that during high solar activity sun is more active in comparison to the low solar activity period and hence strong radiations are emitted during this period which causes additional ionization in comparison to the low solar activity period.

Contour plots give an approximate idea about TEC variation according to the variation of colors in them. Therefore, to get more information regarding TEC variation, the hourly and monthly average variations of VTEC data recorded at five IGS stations are shown in Figures 2a and b, respectively. The maximum values of VTEC variation are recorded at Hyderabad (≈50 TECU) in 2012 (period-I) and at Bangalore and Hyderabad (≈ 20 TECU) in 2018 (period-II). A minimum peak value is recorded at Lhasa, China (≈ 6 TECU and 4 TECU) in period-I and period-II, respectively. The VTEC variations at Lucknow are almost similar to those at Lhasa.

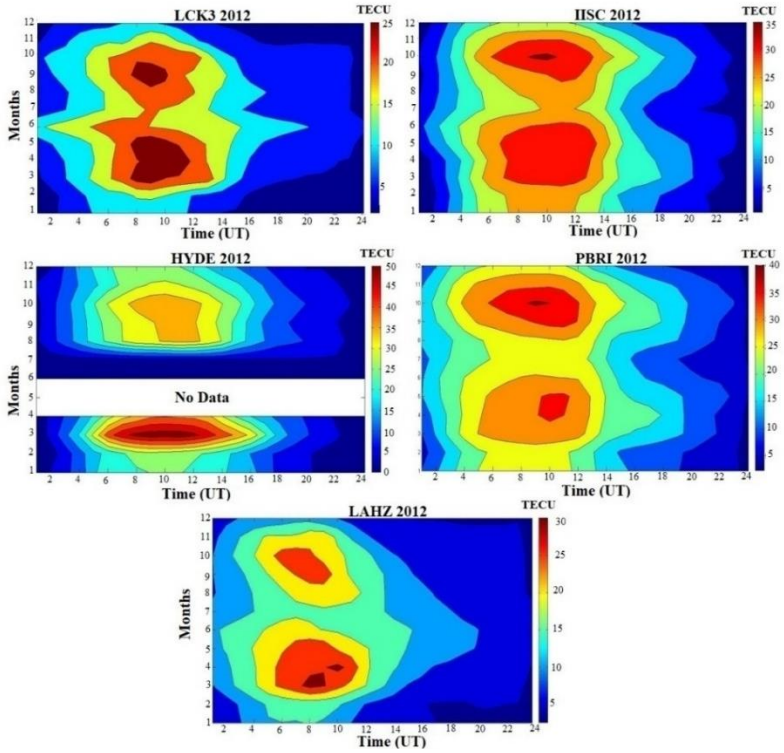

Figure 1a. Contour plots of the hourly average TEC variations (in TECU) at five IGS stations viz; Lucknow, IISC, Hyderabad, Port Blair, and Lhasa (China) for the year 2012.

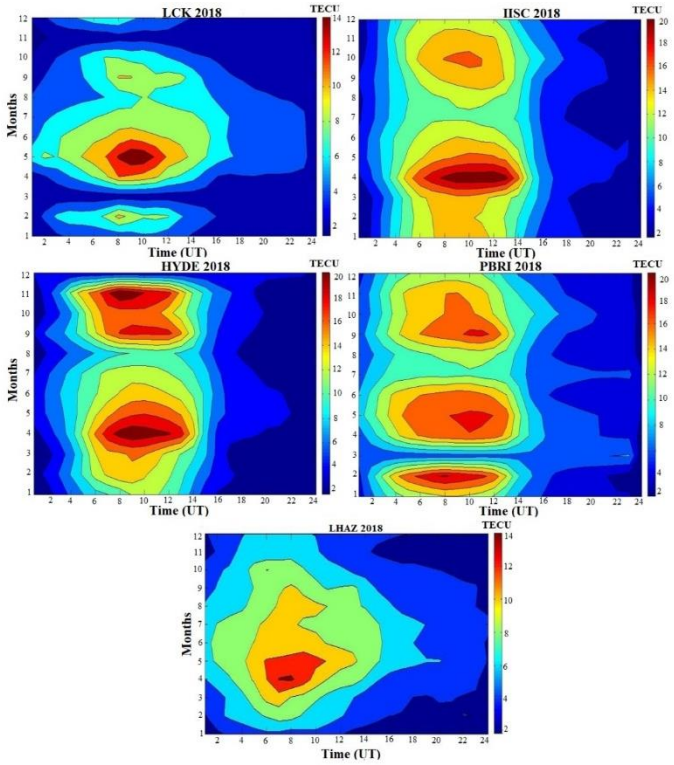

Figure 1b. Contour plots of the hourly average TEC (in TECU) variations at five IGS stations viz; Lucknow, IISC, Hyderabad, Port Blair, and Lhasa (China) for the year 2018.

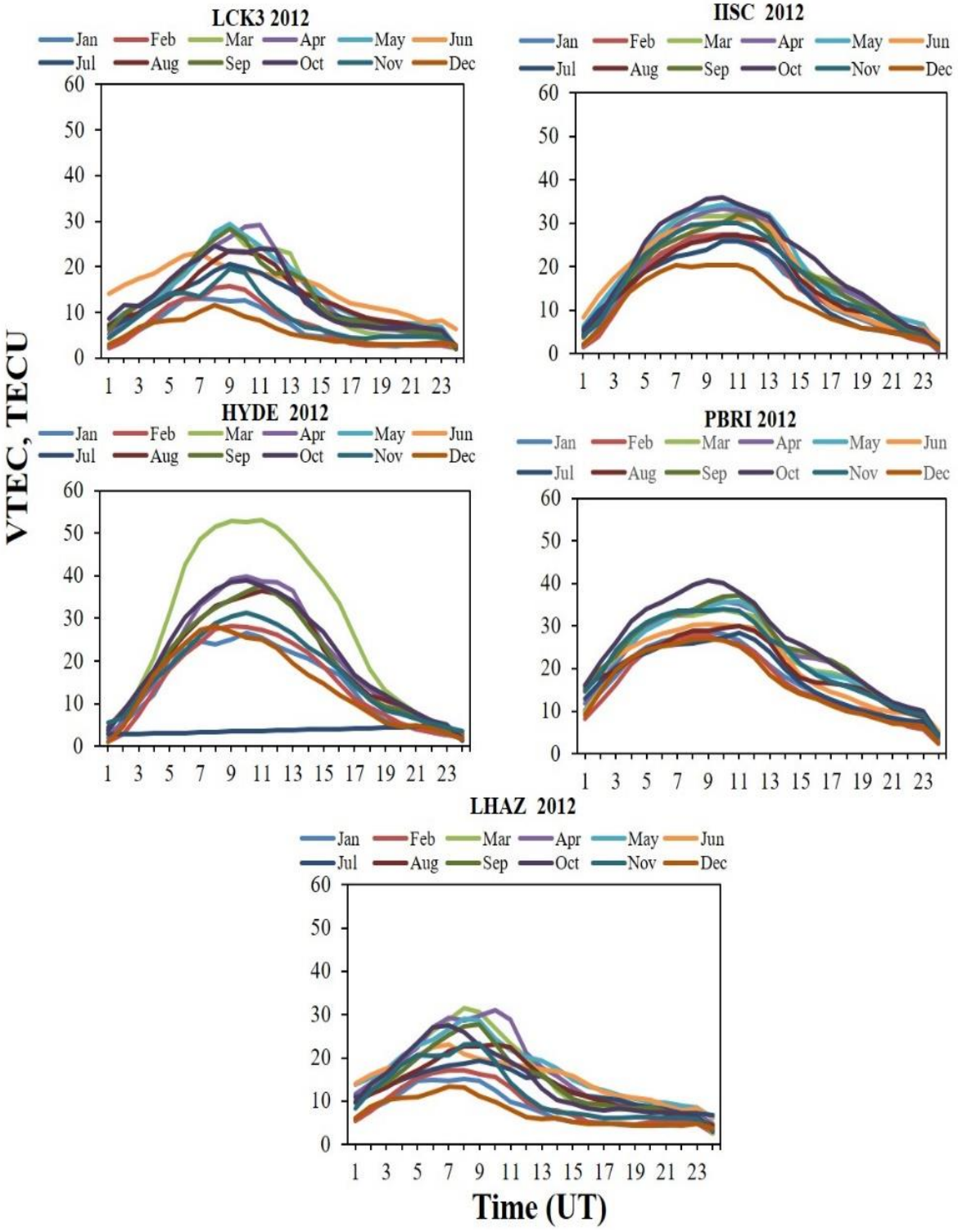

Figure 2a. Monthly VTEC (in TECU) variations (shown by solid curves of different colours) at five IGS stations for the year 2012.

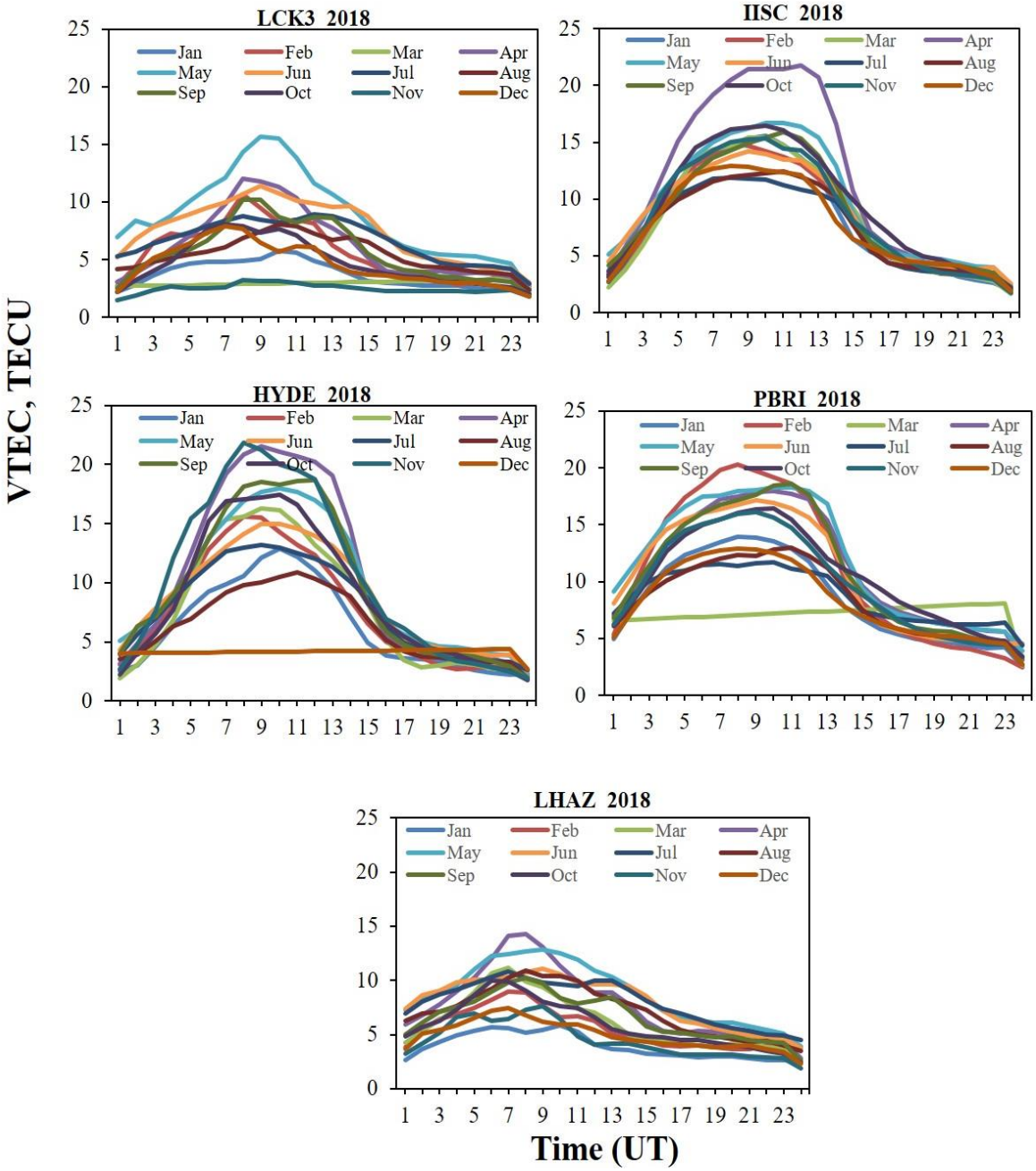

Figure 2b. Monthly VTEC (in TECU) variations (shown by solid curves of different colours) at five IGS stations for the year 2018.

The monthly average VTEC variations along with the yearly mean are plotted in Figures 3a and b for both periods under consideration to compare these variations. From these figures, it is clear that the maximum VTEC is recorded in March, April, May, September, and October (equinoctial months) at all the stations during both periods, except in March at Lucknow (period-II). The depletions in the monthly mean are also recorded at all the stations in December, January, and February in period-I, and at Lucknow and Lhasa, both in January and November. The same has also been recorded in the month of December at Lucknow for period-II. The highest GPS-TEC values are recorded in March (≈50 TECU) at Hyderabad and in April (≈20 TECU) at Bangalore in period-I and period-II, respectively. Thus, it may be inferred here that TEC values are higher in equinoctial months in comparison to the summer and winter seasons.

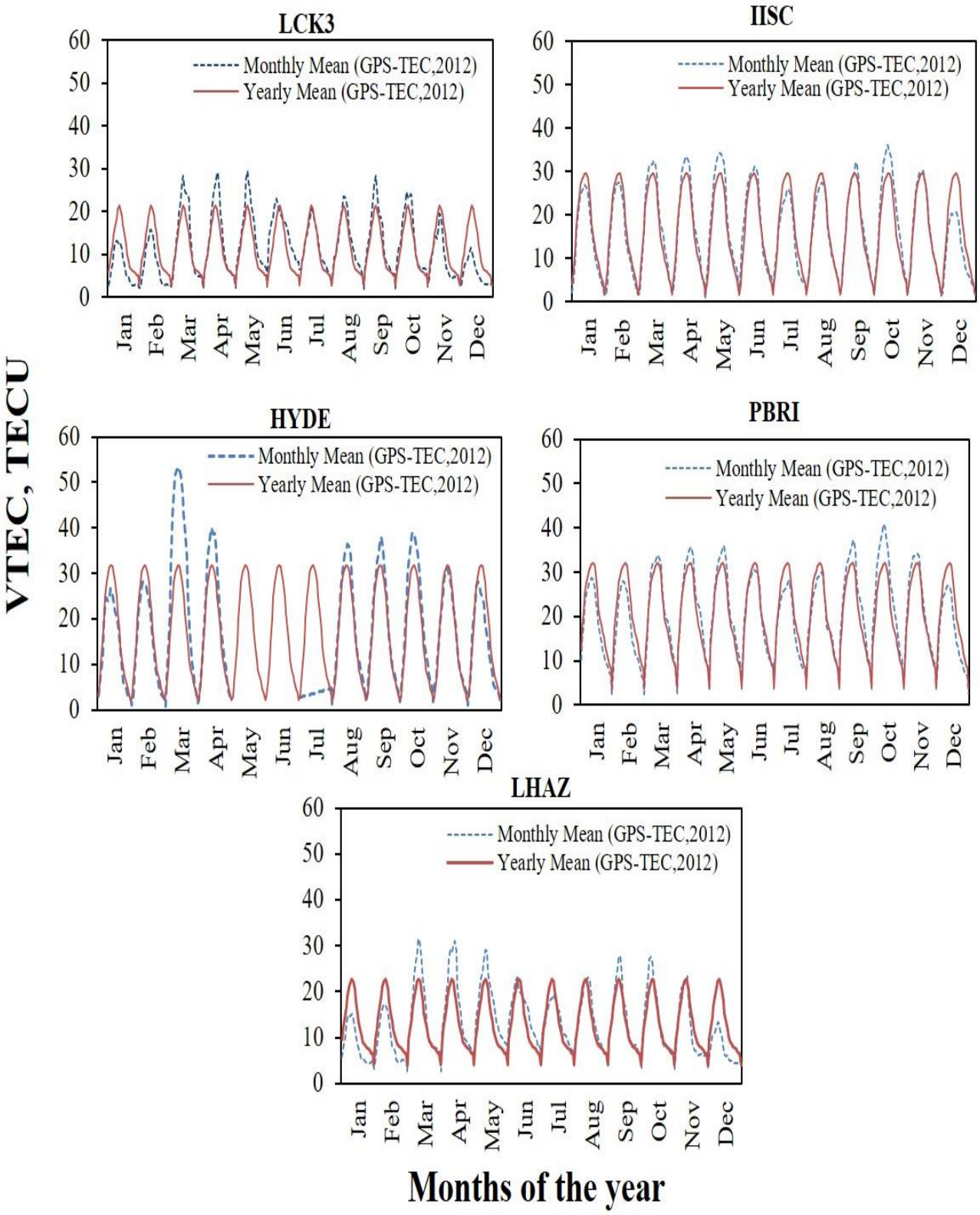

Figure 3a. Monthly TEC (in TECU) variations along with yearly mean at five IGS stations for the year 2012. The solid curve depicts the yearly mean and the dashed curve shows the monthly mean variation of VTEC data.

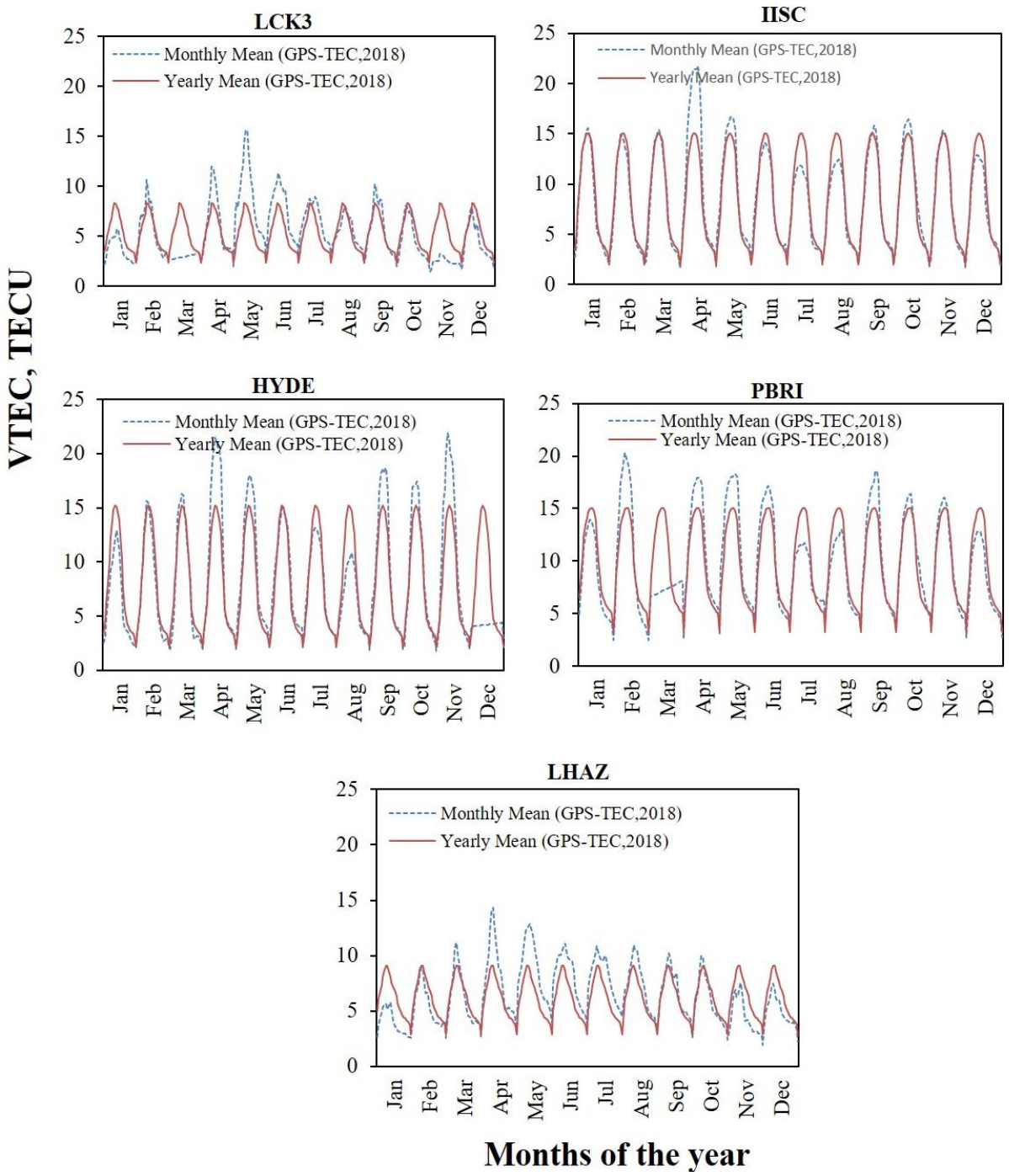

Figure 3b. Monthly TEC (in TECU) variations along with yearly mean at five IGS stations for the year 2018. The solid curve depicts the yearly mean and the dashed curve shows the monthly mean variation of VTEC data.

Seasonal variations

Here, we consider three seasons i.e. summer, equinox, and winter. The months of May to August lie in the summer solstice and the months of March, April, September, and October lie in the equinox, and the rest of the months i.e. January, February, November, and December, lie in the winter solstice. The average of each solstice is calculated for all five stations during both periods under consideration. These seasonal variations of VTEC and their seasonal means are shown in Figure 4a and b for the high and low activity years (i.e. 2012 and 2018), respectively. During all seasons, the seasonal peak VTEC values are noticed to vary between 14-42 TECU during period-I and 7-18 TECU

during period-II. In most of the cases, maximum values of TEC variations are recorded in equinoctial months during both periods, while at Lucknow and Port Blair, it is observed maximum during summer and winter in period-II. From the seasonal variations, it is clear that peak TEC values are higher in period-I than that in period-II. The direct impact of solar activity on electron density is the main cause for these variations in TEC data. This difference in the VTEC values may be due to variations in solar activity during both periods. The VTEC variations at all the stations assumed lower values in winter than that in summer and highest values during equinoxes for both periods except at Hyderabad and Bangalore in summer during period-I and II, respectively. Our findings are analogous to previous workers (Kumar et al., 2012; Sharma et al., 2012).

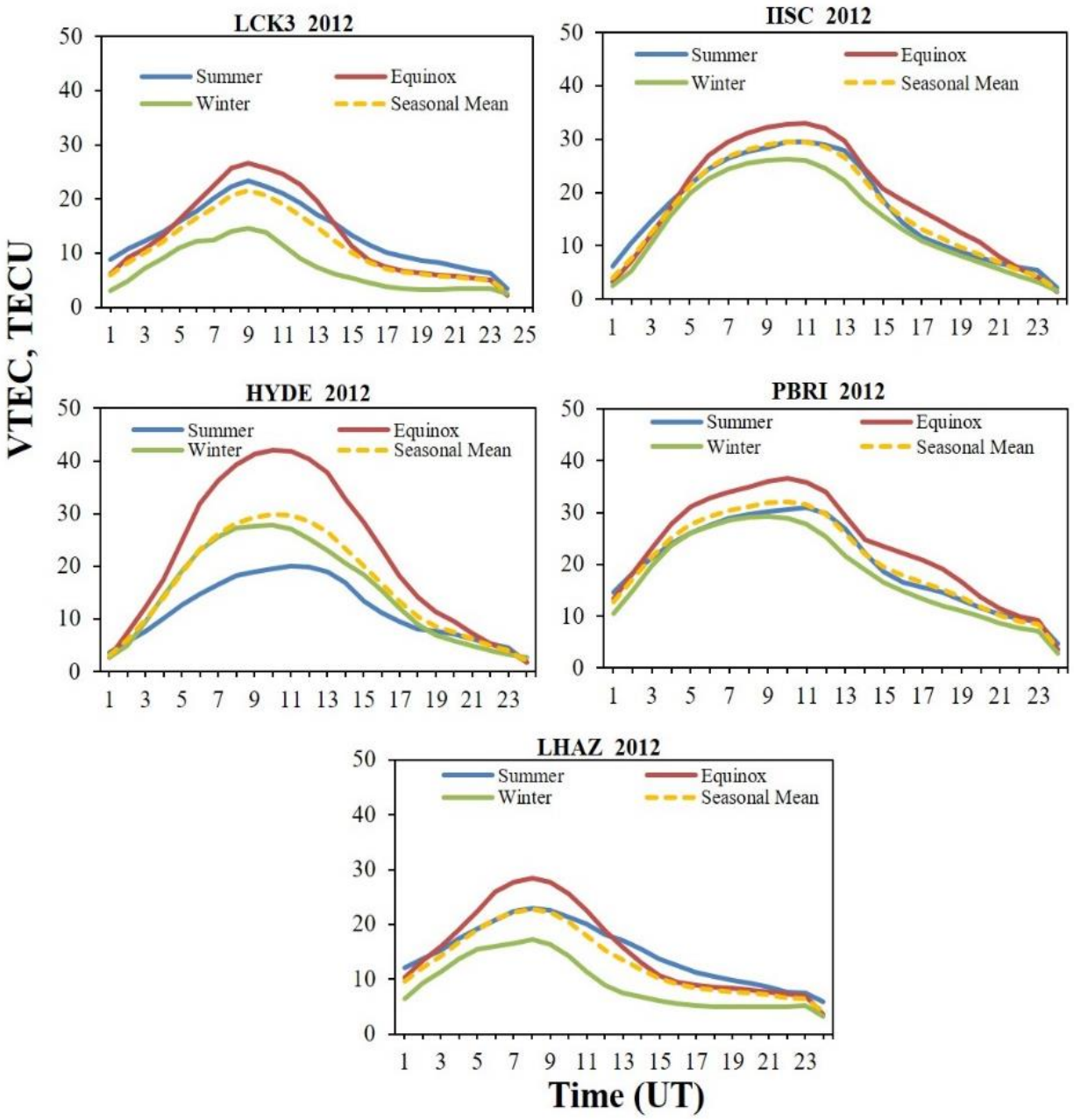

Figure 4a. Seasonal variations of VTEC (in TECU) data along with their seasonal means at five IGS stations for the year 2012. The seasonal variations are depicted by solid curves of different colours while their seasonal means are shown by dashed yellow curves.

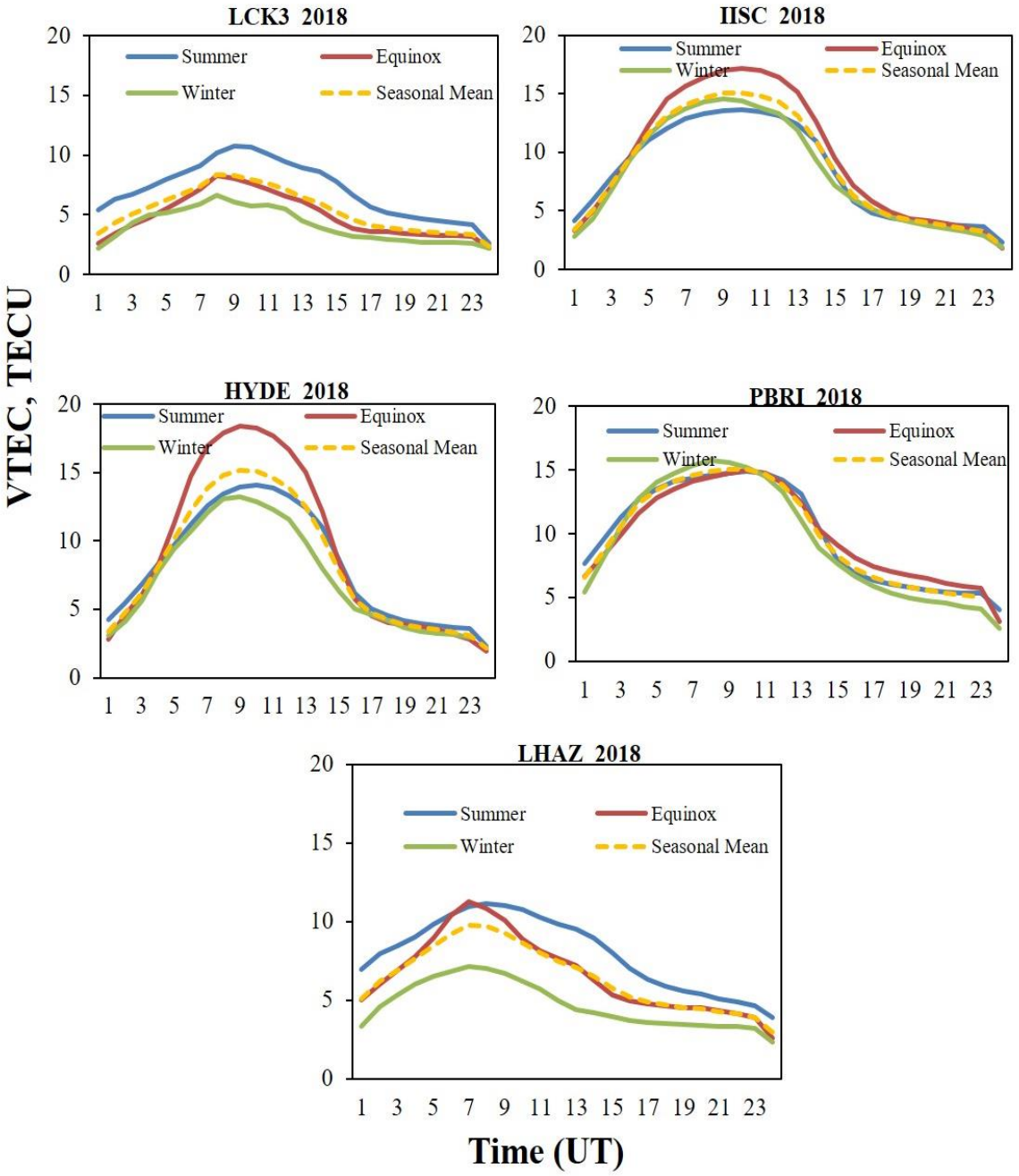

Figure 4b. Seasonal variations of VTEC (in TECU) data along with their seasonal means at five IGS stations for the year 2018. The seasonal variations are depicted by solid curves of different colours while their seasonal means are shown by dashed yellow curves.

Solar activity and magnetic storm dependence

Solar activity may affect the TEC data recorded at IGS low-latitude stations. For examining the impact of solar activity on TEC data, the solar flux index F10.7 cm and sunspot number (SSN) are considered here. The data for solar flux index F10.7 cm and sunspot number are procured from the National Aeronautics and Space Administration (NASA) through their website: http//omniweb.gsfc.nasa.gov/form/dx/.html. GPS-TEC data may also be affected by magnetic storms. For studying the effect of magnetic storms on TEC data, ΣKp data are considered which are downloaded from World Data Centre Kyoto, Japan through the website: http//swdcdb.kugi.kyotse.ac.jp

To examine the effect of solar activity on VTEC variations at all the stations under consideration during the high and low solar activity periods, sunspot numbers (SSN) and solar

flux index, F10.7 cm are plotted in the top and bottom panels of Figure 5. A large variation in SSN in the summer months is seen for period-I. The peak values of SSN are ≈ 175 and ≈ 55 in period-I and period-II, respectively. From the bottom panel of this figure, it can be seen that peak values of solar flux index F10.7cm are ≈ 185 for period-I and ≈ 85 for period-II. Here, a large difference in peak values of solar flux index F10.7 cm indicates a wide variation in solar activity in the two periods. This shows that solar activity during period-I, is more prominent than in period-II. The higher values of SSN and solar flux index in period-I in comparison to period-II, indicate that TEC should be more affected in period-I as compared to period-II. The higher values of TEC observed in period-I than in period-II give evidence of the same.

For examining the influence of geomagnetic storms on the GPS-TEC data, the correlation between the daily values of TEC data for all the five low latitude stations considered in the present analysis and ∑Kp data are studied both for the high as well as low solar activity periods (i.e. 2012 and 2018) for which correlation coefficients between the two data sets are computed. The results of the computation are shown in Figures 6a and b for both periods i.e. period-I and period-II. From these figures, it is clear that the correlation coefficient ranges between 0.18 – 0.23 during high solar activity while it ranges between 0.22 – 0.37 during the low solar activity period for all five IGS stations. These values of correlation coefficients for both periods are however low but positive. This indicates that the effect of magnetic storms at low latitudes is quite low.

While the correlation produces almost insignificant results, three cases of magnetic storms are chosen for the examining impact of magnetic storms on the TEC data of all the five stations that happened on 20 April, 26 August, and 11 September 2018. In each case, 10 days of TEC data are plotted along with the ∑Kp. For the first two cases, daily variations of VTEC data (upper 5 panels) are plotted with corresponding ∑Kp data (lower panels) for 10 days (in each case) from 18-27 April, 24 August-2 September 2018, and 9-18 September 2018, as shown in Figures 7 a, b, and c respectively, where 0 value of TEC data in the figures shows non-availability of data. Its significant enhancements (≈ 1-4 TECU) can be clearly seen in TEC data over all the stations on the day of the magnetic storm and after its occurrence can be seen. These perturbations in the TEC data are interpreted in terms of the delayed effect of the magnetic field which is penetrated from high latitude to low latitude.

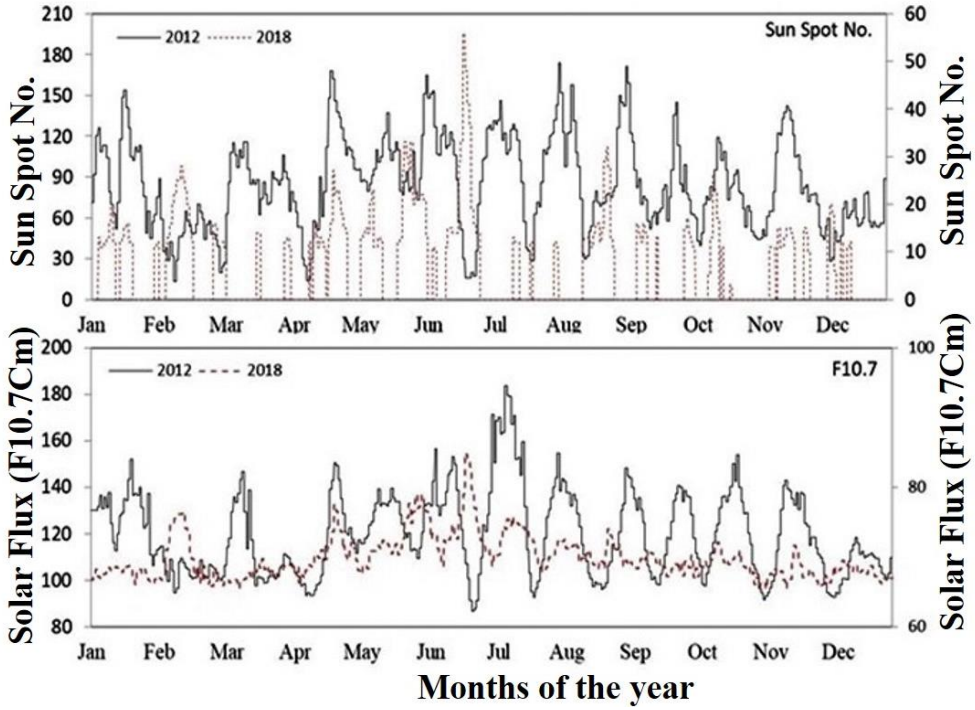

Figure 5. Variations of sunspot numbers for the years 2012 and 2018 by solid and dashed curves respectively (top panel). Variations of solar flux F 10.7 for the years 2012 and 2018 are shown by solid and dashed curves respectively (bottom panel).

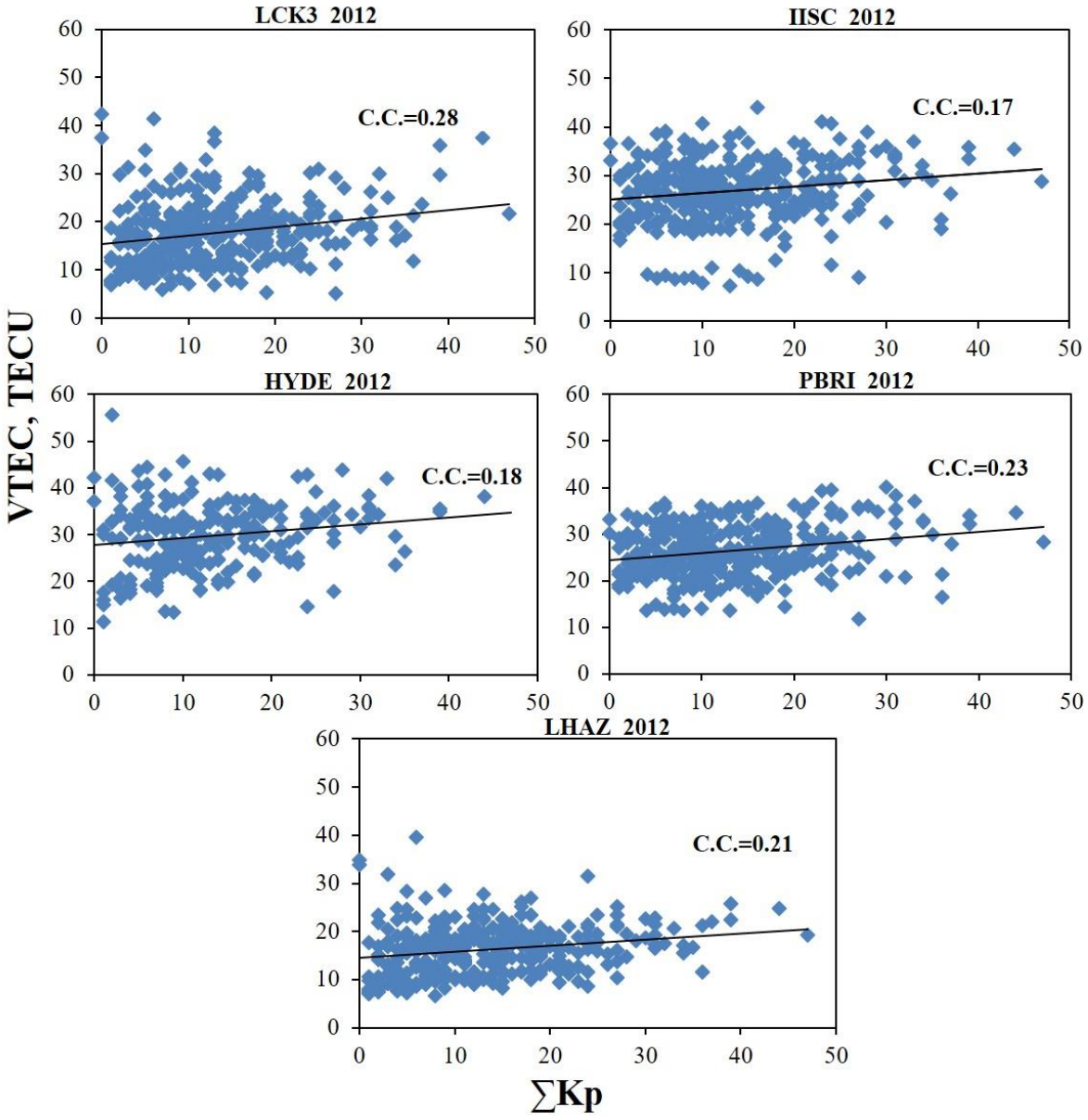

Figure 6a. Correlation plots between VTEC (in TECU) and geomagnetic activity factor (ΣKp index) during the period (2012).

It is very important to explain the changes in observed GPS-TEC by considering the possible suitable mechanism. Solar extreme UV ionization coupled with the upward vertical E × B drift, maybe the cause for the enhancements in GPS-TEC data. The stations under consideration are situated within the equatorial ionization anomaly region which consists of both the crests of ionospheric electron density. It usually depicts a minimum close to magnetic dips of 15° north and south (Appleton, 1946). The VTEC values are higher in period-I than in period II. The cause for this is the difference in solar activity during the two periods. In the present study, higher TEC values appear in equinoxes in comparison to both the winter and summer seasons for both periods. The cause for this is as follows. The Equator, in general, is hotter than the North and South poles during the daytime. This leads to the flow of meridional winds from the equator to the North Pole. The change in the neutral composition and reduction in the ratio of O/N_2 takes place over the equatorial region because of the flow of meridional winds. This reduction in the O/N_2 ratio is highest in equinoctial months which results in electron density. This is why equinox VTEC variations are noticed the highest (Bagiya et al., 2009; Kumar et al., 2012; Pundhir et al., 2017a).

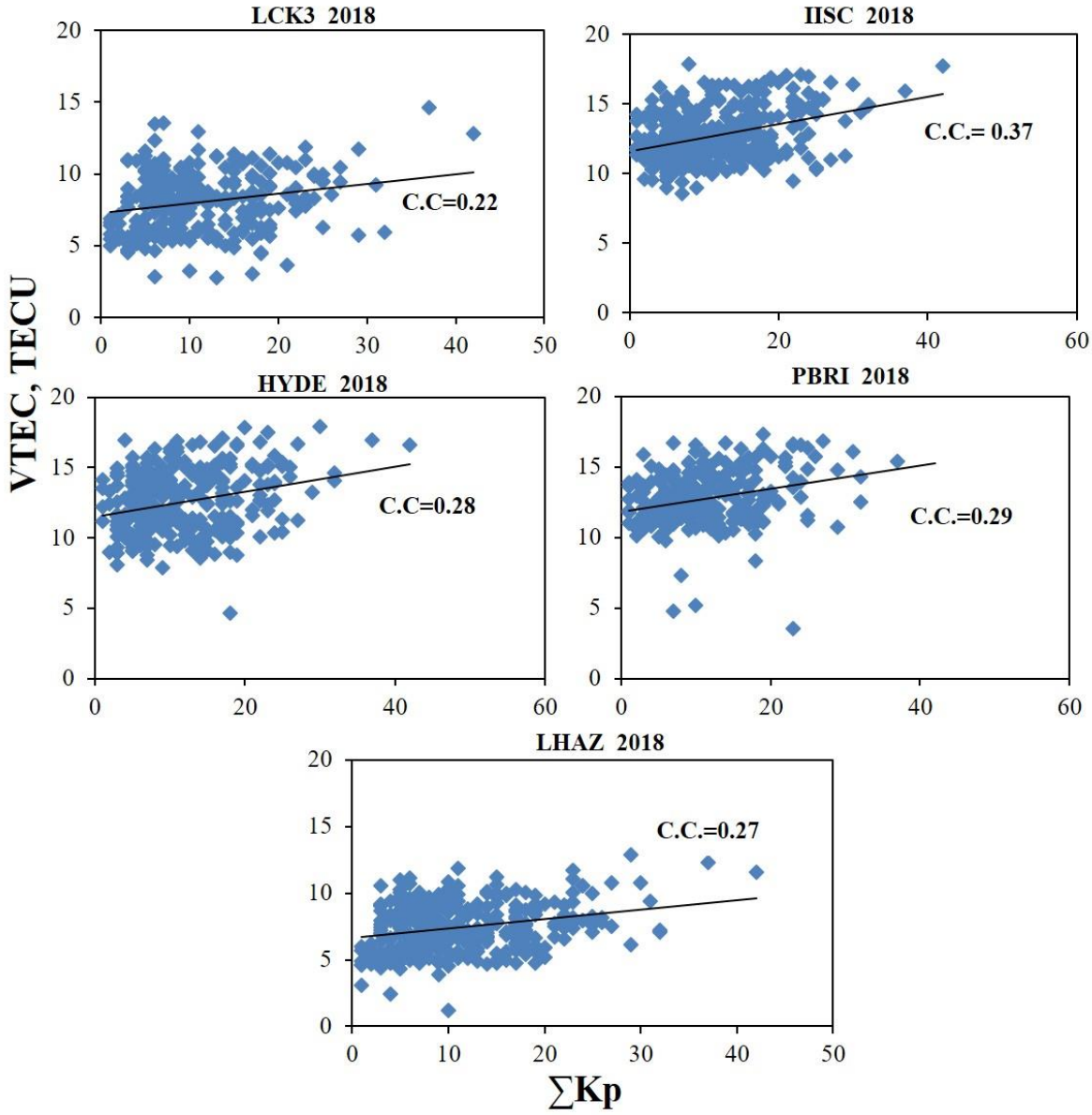

Figure 6b. Correlation plots between VTEC (in TECU) and geomagnetic activity factor (ΣKp index) during the period (2018).

Magnetospheric dynamics are affected by solar activity and perturb distribution of the plasma density in the ionosphere. Ionospheric VTEC variations are directly controlled by solar activity and this effect can be studied with the help of SSN and solar flux index F10.7 cm. These indicators are highly useful to understand ionospheric variations. The radio power of the sun observed in the solar flux unit (1 sfu = 10^{-22} Wm^{-2} Hz^{-1}) at the frequency of 2800 MHz describes the solar flux index. Generally, the ionization enhances in the high solar activity period and reduces in the low solar activity period. SSN is a temporary phenomenon that also measures the intensity of solar radiation. The changes in the TEC data observed at the stations considered may be due to variations in solar activity which variation is accounted for by the variations in solar activity factors (F10.7 and SSN). These variations of TEC with solar activity are in good agreement with the earlier studies (Kumar et al., 2012; Pundhir et al., 2017a, b).

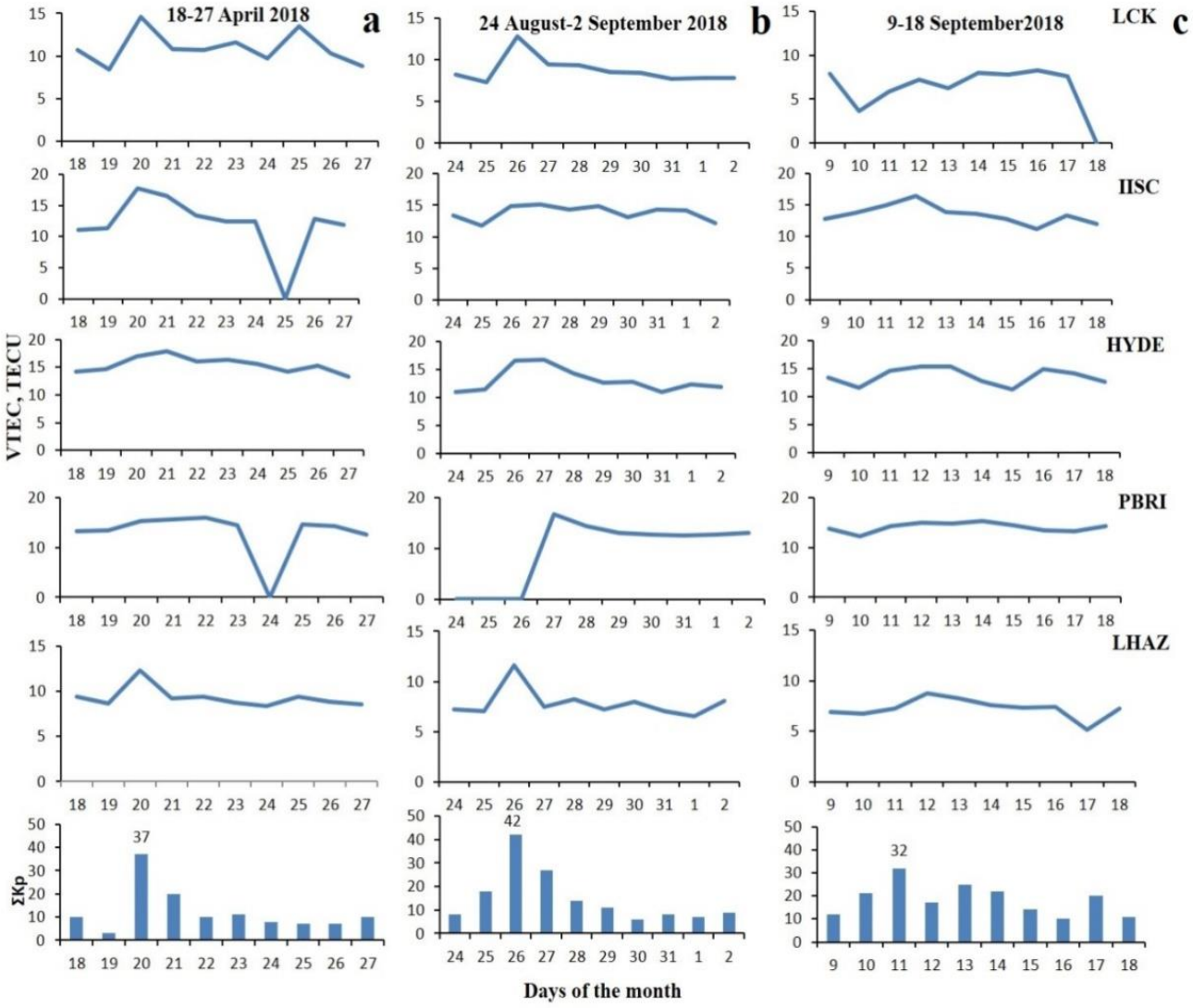

Figure 7a, b, and c. Upper five panels in each are shown the daily variation of VTEC (in TECU) over all the stations considered for the periods 18-27 April, 24 August-2 September, and 9-18 September in the year 2018, respectively. Histograms in the lower panel of each are shown the variations of ΣKp for the same periods.

Electric field induced by a magnetic storm may penetrate the low latitude ionosphere and magnetosphere and can cause TEC enhancements (Jain and Singh, 1977; Lakshmi et al., 1983, 1997; Rastogi and Klobuchar, 1990; Jain et al., 2010). The ionosphere is perturbed by two main factors that include (i) thermospheric heating, primarily generated due to thermospheric winds which are triggered by storms at low latitudes (Danilov and Latovicka, 2001) ionization level, enhances and produces changes in the ratio of atoms to molecules (Fuller- Rowell et al., 1996), and (ii) the penetration of eastward electric field at low latitudes produce enhancements in fountain effect and EIA poleward. The enhancements in TEC data observed at low latitudes are mainly due to the fountain effect.

CONCLUSIONS

The VTEC data of five different low latitudes IGS stations, Lucknow, Bangalore, Hyderabad, Port Blair, and Lhasa (China) for the two periods i.e. from 01 January-31 December 2012 and 01 January-31 December 2018, corresponding to high and low solar activity periods respectively, have been analyzed. Diurnal and seasonal variations of VTEC have been studied for both periods of observation. In diurnal variations, peak VTEC is found to lie between 08:00 and 10:00 hrs (UT) at all the stations and ranges from 25-50 TECU during period-I and it lies at the same time interval but within the range of 14-20 TECU during the period-II. In all seasons, seasonal peak VTEC values are noticed to vary between 14-42 TECU during

period-I and 7-18 TECU during period-II. In the majority of the cases, higher values of TEC variations are observed during equinoctial months. The peak VTEC values are found in the range of 14-42 TECU for all the seasons during period-I and 7-18 TECU during period-II. The effect of solar activity is studied in terms of sunspot number (SSN) and solar flux index, F10.7 cm variation, whose maximum values are 175 and 185 for period-I and 55 and 85 for period-II, respectively. Thus, it can be inferred that the TEC values are maximum during equinoxes which may be due to enhanced solar activity in both periods. The effect of magnetic storms on TEC data is also examined and it is found that TEC values enhance significantly on the day of the occurrence of a severe storm. Finally, this study provides a better understanding of the behavior of low latitude ionosphere during high and low solar activity periods. These studies are highly useful before the examination of TEC variations in relation to earthquakes because TEC is not only varied in different seasons, and locations but also by other anthropogenic phenomena like magnetic storms, solar activity, dust storms, volcanic eruptions, and human activity i.e. nuclear tests, artificial rain, etc.

ACKNOWLEDGMENTS

One of the authors D. Pundhir is highly grateful to the Ministry of Earth Sciences, Govt. of India, New Delhi for providing financial support in the form of a major research project. The authors are also thankful to the editor-in-chief of JIGU for his editing support which enhances the quality of the paper.

Compliance with Ethical Standards

The authors declare no conflict of interest and adhere to copyright norms.

REFERENCES

Adebiyi, S.J., Odeyemi, O.O., Adimula, I.A., Oladipo, O.A., Ikubanni, S.O., Adebesin, B.O. and Joshua, B.W., 2014. GPS derived TEC and foF_2 variability at an equatorial station and the performance of IRI-model. Adv. Space Res., 54(14), 565-575.

Akala, A.O., Seemala, G.K., Doherty, P.H., Valladares, C.E., Carrano, C.S., Espinoza, J. and Oluyo, S., 2013. Comparison of equatorial GPS-TEC observations over an African station and an American station during the minimum and ascending phases of solar cycle 24. Ann. Geophys., 31, 2085–2096.

Appleton, E.V., 1946. Two Anomalies in the Ionosphere. Nature, 157, pp. 691, doi:10.1038/157691a0.

Bagiya, M.S., Joshi, H.P., Iyer, K.N., Aggarwal, M., Ravindran, S. and Pathan, B.M., 2009. TEC variations during low solar activity period (2005–2007) near the Equatorial Ionospheric Anomaly Crest region in India. Ann. Geophys., 27, 1047–1057.

Bhuyan, P.K. and Borah, R.R., 2007. TEC derived from GPS network in India and comparison with the IRI. Adv. Space Res., 39, 830–840.

Chakraborty, M., Kumar, S., De, B.K. and Guha, A., 2014. Latitudinal characteristics of GPS derived ionospheric TEC: a comparative study with IRI 2012 model. Ann. Geophys., 57, 5, A0539.

Danilov, A.D. and Lastovicka, J., 2001. Effects of geomagnetic storms on the ionosphere and atmosphere. Int. J. Geomag. Aeron., 2, 209–224.

Dashora, N., Sharma, S., Dabas, R.S., Alex, S. and Pandey, R., 2009. Large enhancements in low latitude total electron content during 15 May 2005 geomagnetic storm in Indian zone. Ann. Geophys., 27, 1803–1820.

Fuller-Rowell, T. J., Codrescu, M.V. Moffett, R.J. and Quegan, S., 1996. On the seasonal response of the thermosphere and ionosphere to geomagnetic storms. J. Geophys. Res., 101, A2, 2343-2353.

Huy, M. Le, Amory-Mazaudier, C., Fleury, R., Bourdillon, A. and Lassudrie-Duchesne, P., et al., 2014. Time variations of the total electron content in the Southeast Asian equatorial ionization anomaly for the period 2006–2011. Adv. Space Res., 54, 355-368.

Jain, A., Tiwari, S., Jain, S. and Gwal, A.K., 2010. Study of TEC response during severe geomagnetic storms near the crest of the equatorial ionization anomaly. Ind. J. Radio Space Phys., 39, 11–24.

Jain, S.K. and Singh, B., 1977. Vertical motions of the low and equatorial-latitude F_2 layers during prolonged and isolated magnetic storms. J. Geophys. Res., 82, 723-726.

Karia, S.P., Patel, N.C. and Pathak, K.N., 2015. Comparison of GPS based TEC measurements with the IRI-2012 Model for the period of low to moderate solar activity (2009-2012) at the crest of equatorial anomaly in Indian region. Adv. Space Res., 55(8), 1965-1975.

Kumar, S., Priyadarshi, S., Krishna, S.G. and Singh, A.K., 2012. GPS-TEC variations during low solar activity period (2007-2009) at Indian low latitude stations. Astrophys & Space Sci., 339, 165–178.

Lakshmi, D.R., Reddy, B.M. and Sastri, S., 1983. A prediction model for equatorial low latitude HF communication parameters during magnetic disturbances. Ind. J. Radio Space Phys., 12, 1-18.

Lakshmi, D.R., Veenadhari, B., Dabas, R.S. and Reddy, B.M., 1997. Sudden post-midnight decreases in equatorial in F-region electron densities associated with severe magnetic storms. Ann. Geophysicae, 15, 306-313.

Lastovicka, J., 2002. Monitoring and forecasting of ionospheric space weather-effects of geomagnetic storms. J. Atmos. and Solar-Terr. Phys., 64, 5–6, 697–705.

Mukherjee, S., Sarkar, S., Purohit, P.K. and Gwal, A.K., 2010. Seasonal variation of total electron content at crest of equatorial anomaly station during low solar activity conditions. Adv. Space Res., 46, 291–295.

Mannucci, A.J., Wilson, B.D. and Edwards, C.D., 1993. A new method for monitoring the earth ionospheric total electron content using GPS global network. Institute of Navigation, 1323.

Natali, M.P. and Meza, A., 2011. Annual and semiannual variations of vertical total electron content during high solar activity based on GPS observations. Ann. Geophys., 29, 865–873.

Parwani, M., Atulkar, R., Mukherjee, S. and Purohit, P.K., 2019. Latitudinal variation of ionospheric TEC at Northern Hemispheric region. Rus. J. Earth Sci., 19 ES1003, 1-11.

Prasad, S.N.V.S., Rama Rao, P.V.S., Prasad, D.S.V.V.D., Venkatesh, K. and Niranjan, K., 2012. On the variabilities of the Total Electron Content (TEC) over the Indian low latitude sector. Adv. Space Res., 49, 898-913.

Pundhir, D., Singh, B., Singh, O.P. and Gupta, S.K., 2017a. A morphological study of low latitude ionosphere and its implication in identifying earthquake precursors. J. Ind. Geophys. Union, 21(3), 214-222.

Pundhir, D., Singh, B., Singh, O. P. and Gupta, S. K., 2017b. Morphological study of GPS -TEC during the ascending phase of solar cycle 24 at a low latitude station Agra, India. J. Sci. & Technological Res., 1(2), 6-15.

Rama Rao, P.V.S., Krishna, S.G., Niranjan, K. and Prasad, D.S.V.V.D., 2006. Prasad Temporal and spatial variations in TEC using simultaneous measurements from the Indian GPS network of receivers during the low solar activity period of 2004–2005. Ann. Geophys. 24, 3279-3292.

Rama Rao, P.V.S., Gopi Krishna, S., Vara Prasad, J., Prasad, S.N.V.S., Prasad, D.S.V.V.D. and Niranjan, K., 2009. Geomagnetic storm effects on GPS based navigation. Ann. Geophys., 27, 2101–2110.

Rastogi, R.G. and Klobuchar, J.A., 1990. Ionospheric electron content within the equatorial anomaly belt. J. Geophys. Res., 95, A11, 19045-19052.

Rathore, V.S., Kumar, S. and Singh, A.K., 2015. A statistical comparison of IRI TEC prediction with GPS TEC measurement over Varanasi, India. J. Atmos. Solar-Terr. Phys., 124, 1-9.

Sharma, K., Dabas, R.S. and Ravindran, S., 2012. Study of total electron content variations over equatorial and low latitude ionosphere during extreme solar minimum. Astrophys. Space Sci., 341, 277–286.

Seemala, G. K., 2011. "GPS-TEC analysis application." Technical Report.

Trivedi, R., Jain, A., Jain, S. and Gwal, A.K., 2011. Study of TEC changes during geomagnetic storms occurred near the crest of the equatorial ionospheric ionization anomaly in the Indian sector. Adv. Space Res., 48, 1617-1630.

Trivedi, R., Jain, S., Jain, A. and Gwal, A.K., 2013. Solar and magnetic control on night time enhancement in TEC near the crest of the Equatorial Ionization Anomaly. Adv. Space Res., 51, 61-68.

Wu, Y., W., Liu, R.Y., Zhang, B.C., Wu, Z.S., Ping, J.S., Liu, J.M. and Hu, Z.J., 2012. Variations of the ionospheric TEC using simultaneous measurements from the China Crustal Movement Observation Network. Ann. Geophys., 30, 1423–1433.

Xu, J., Guoming, L. and Wu, J. et al. 2012. Recent unrest of Changbaishan volcano, northeast China: A precursor of a future eruption? Geophys. Res. Lett., 39, L16305.

Yadav, S.K., Karia, S.P. and Pathak, K.N., 2015. Anomalous Variation in GPS Based TEC Prior to the 5 Earthquakes in 2009 and 2010, Positioning, 6(4), 96-106.

Yasyukevich, A.S., Yasyukevich Y.V. and Mylnikova, A.A., 2017. Regular TEC variations in mid-latitude and polar regions, Progress In Electromagnetics Research Symposium-Spring (PIERS).

Received on: 30.12.2023; Revised on: 20.03.2023; Accepted on: 27.03.2023

Report of IGU- Student chapter in Adikavi Nannaya University, Rajahmundry

Indian Geophysical Union has inaugurated its 11th Student Chapter in the Department of Geo-Sciences, Adikavi Nannaya University, Rajahmundry, Andhra Pradesh on 5th January, 2023. Prof. M. Jagannadha Rao, Vice-Chancellor, Adikavi Nannaya University and Chief Guest of the function inaugurated the chapter and addressed gathering. Dr. V. M. Tiwari, Outstanding Scientist (HAG) and Vice-President, Indian Geophysical Union(IGU) has participated as a distinguished guest and declared the student chapter on behalf of IGU and introduced the IGU in his opening remarks. Prof. Y. Srinivasa Rao, Head, Dept. of Geo-Sciences, Adikavi Nannaya University welcomed the guests and presided over the function. Dr. ASSSRS Prasad, Organising Secretary, IGU has explained about activities of IGU for the benefit of the society and introduced Dr. B. P. K. Patro, Chief Scientist, CSIR-NGRI and IGU-Anni Talwani Memorial Prize Awardee to the gathering. Dr. Patro has delivered his IGU-Anni Talwani Memorial Prize Award lecture on "Magnetotellurics role in the exploration of Geothermal targets". Dr. K. V. Swamy, Associate Professor and coordinator of the program proposed vote of thanks. The Dept. of Geosciences has conducted poster presentation competition to the students of Earth Science programs on "Global Warming - Climatic Change". Researchers and Students from Dept. of Geosciences, Adikavi Nannaya University and its affiliated colleges viz., Sir CR Reddy College, Eluru and DNR College, Bhimavaram participated. The Chief Guest and the Distinguished Guest have distributed certificates to the best poster presenters of the competition.






Report of IGU student Chapter at Department of Geophysics, Osmania University, Hyderabad

Indian Geophysical Union (IGU) Student chapter was inaugurated in Department of Geophysics, Osmania University, during the student chapter a IGU-Sri LN Kailasam Memorial Lecture organized at Prof. VLB Bhimasankaram Seminar hall, Osmania University, Hyderabad on 30th January 2023.

Dr. G. Udaya Laxmi, Assistant Professor and Executive member of IGU welcomed the dignitaries viz., Dr. Prakash Kumar, Director, CSIR-NGRI, Dr. V. M. Tiwari, Vice-President, Indian Geophysical Union(IGU) & Outstanding Scientist(HAG), Prof. B. Veeraiah, Principal, UCS and Head, Centre for Exploration Geophysics, Osmania University, Dr. Abhey Ram Bansal, Hon. Secretary, IGU & Chief Scientist, CSIR-NGRI. She also welcomed Dr.DV Ramana, IGU-Sri LN Kailasam memorial lecture awardee with his Family members, Dr. N. Chandra Babu, Retired Scientific Officer, ONGC, Rajahmundry, faculty members, Alumni members, research scholars, post graduate students, IGU members and eminent scientists from CSIR-NGRI.

The program starts with the lightening of the lamp by the dignitaries on the dais. Dr. V. M. Tiwari, Vice-President, Indian Geophysical Union (IGU) declared open the student chapter and deliberated his opening remarks followed by Dr. Prakash Kumar, Director, CSIR-NGRI, Guest of Honour addressed the gatherings. A poster session was organized during the student chapter. Certificates distributed to students for best poster presenters for their research work.

During the function dignitaries were honoured by Vice-President, IGU and Head, Department of Geophysics.

Dr. Abhey Ram Bansal, Hon. Secretary, IGU & Chief Scientist, CSIR-NGRI informed the audience about IGU activities and about IGU- Sri LN Kailasam Memorial Awardee. Dr.Ramana delivered Sri L N Kailsam memorial lecture on "Data Science in Earth science and Challenges".

Dr. Udaya Laxmi proposed vote of thanks and the program concluded with National Anthem.

GUIDE FOR AUTHORS

The Journal of Indian Geophysical Union (JIGU), published bimonthly by the Indian Geophysical Union (IGU), is an inter disciplinary journal from India that publishes high-quality research in earth sciences with special emphasis on the topics pertaining to the Indian subcontinent and the surrounding Indian Ocean region. The journal covers several scientific disciplines related to the Earth sciences such as solid Earth geophysics, geology and geochemistry, apart from marine, atmosphere space and planetary sciences. J-IGU welcomes contributions under the following categories:

*Research articles, short notes and students section reporting new findings, results, etc.

*Review articles providing comprehensive overview of a significant research field.

In addition, JIGU also welcomes short communications, after communications and report on scientific activity, book reviews, news and views, etc.

The manuscript should be submitted electronically as a single word format (.doc file) including the main text, figures, tables, and any other supplementary information along with the signed "Declaration Letter". The manuscript should be submitted by email (jigul1963@ gmail.com) to the Chief Editor.

After acceptance of the manuscript the corresponding author would be required to submit all source files (text and Tables in word format) and figure in high resolution standard (*.jpg, *.tiff, *.bmp) format. These files may be submitted to JIGU as a single *.zip file along with the "Copyright Transfer Statement".

IMPORTANT INFORMATION

Ethics in publishing; J-IGU is committed to ensuring ethics in publication and takes a serious view of plagiarism including self-plagiarism in manuscripts submitted to the journal, Authors are advised to ensure ethical values by submitting only their original work and due acknowledgement to the work of others used in the manuscript. Authors must also refrain from submitting the same manuscript to more than one journal concurrently, or publish the same piece of research work in more than one journal, which is unethical and unacceptable. Editor of JIGU is committed to make every reasonable effort to investigate any allegations of plagiarism brought to his attention, as well as instances that come up during the peer review process and has full authority to retract any plagiarized publication from the journal and take appropriate action against such authors if it is proven that such a misconduct was intentional.

Similarly, Editor and Reviewers are also expected to follow ethical norms of publishing by ensuring that they don't use any unpublished information, communicated to them for editorial or review purpose, in their own research without the explicit written consent of the author. They are also expected to keep manuscript' data/ observations/ any other information related to the peer review confidential to protect the interest of the authors. Reviewers should refrain from reviewing the manuscripts in which they have conflicts of interest resulting from competitive, collaborative, or other relationships or connections with any of the authors, companies, or institutions connected to the manuscript.

Conflict of interest

All authors are requested to disclose any actual or potential conflict of interest including any financial, personal or other relationships with other people or organizations within three years of beginning the submitted nor that could inappropriately influence, or be perceived to influence, their work.

Submission declaration

Submission of a manuscript implies that the work has not been published previously and it is not under consideration for publication elsewhere, and that if accepted it will not be published elsewhere in the same or any other form, in English or in any other language, without the written consent of the publishers. It also implies that the authors have taken necessary approval from the competent authority of the institute/organization where the work was carried out.

Copyright

After acceptance of the manuscript the corresponding author would be required to sign and submit the "Copyright Transfer Statement".

MANUSCRIPT PREPARATION

The corresponding author should be identified (include E-mail address, Phone/Mobile number). Full affiliation and postal address must be given for all co-authors.

Abstract:

An abstract of not more than 300 words must be included.

Text:

The manuscript should be structured to include a front page containing the title, Author(s) name, affiliation and address of the institute, where the work was carried out, and 5-to-6 Key words. Author(s) present address, if different from the above mentioned address, may be given in the footnote. The corresponding author should be identified with an asterisk and his/her email ID should be provided. This page should be followed by the main text consisting of Abstract, Introduction, Methods/ Techniques/ Area description, Results, Discussion, Conclusions, Acknowledgements, and References. Tables and Figures with captions should be inserted at the end of main text. It should not be inserted in the body of the text.

Figures/ Illustrations:

figures should be provided in camera-ready form, suitable for reproduction (which may include reduction) without retouching. Figures in high-resolution (at least 300 dpi) standard formats (*.jpg, * tiff, *.bmp) are acceptable. Figures should be numbered according to their sequence in the text. References should be made in the text to each figure. Each figure should have a suitable caption.

Tables:

Authors should take note of the limitations set by the size and layout of the journal. Table should not exceed the printed area of the page. They should be typed on separate sheets and details about the tables should be given in the text. Heading should be brief. Large tables should be avoided and may be provided as supplementary information, if required.

Equations:

Equations should be numbered sequentially with Arabic numerals and cited in the text. Subscripts and Superscripts should be set off clearly.

Equation writing software that presents each equation as an object in MS Word will be accepted. Style and convention adopted for the equations should be uniform throughout the paper.

References:

All references to publications cited in the main text should be presented as a list of references in order following the text and all references in the list must be cited in the text. References should be arranged chronologically, in the text. The list of references should be arranged alphabetically at the end of the paper.

References should be given in the following form:

Kaila, K.L., Reddy PR., Mall D.M., Venkateswarlu, N., Krishna V.G. and Prasad, A.S.S.S.R.S., 1992, Crustal structure of the west Bengal el eon deep seismic sounding investigations. Geophys. J. Int., 1,45-66.

REVIEW PROCESS:

All manuscripts submitted to the journal are peer-reviewed. It is advisable to send the contact details of 4 potential reviewers along with the manuscript to expedite the review process. Editor has the option to select reviewers from the list or choose different reviewers. The review process usually takes about 3 months. All enquiries regarding the manuscript may be addressed to the Chief Editor.

GALLEY PROOF:

Technical editing of manuscripts is performed by the editorial board. The author is asked to check the galley proof for typographical errors and to answer queries from the editor. Authors are requested to return the corrected proof within two days of its receipt to ensure uninterrupted proceedings The editor will not accept new material in proof unless permission from the editorial board has been obtained for the addition of a "note added in proof". Authors are liable to be charged for excessive alterations to galley proof.

PUBLICATION CHARGES:

There are no page charges for publication. The corresponding author will receive a soft copy (pdf format) of his/her published article. Should the author desire to purchase reprints of his/her publication, he/she must send the duly signed Reprint Order Form (accompanies the galley proof and contains price details) along with the corrected galley proof to the Editor. The reprint charges must be paid within one month of sending the Reprint Order Form.

Any payment related to printing or purchase of reprints should be made in the form of a Demand Draft in the name of Treasurer, Indian Geophysical Union, payable at Hyderabad.

You may download the pdf file from:
http://iguonline.in/journal/instructions.php